Sheffield Hallam University

A Sheffield Hallam University thesis

REFERENCE

Numerical and Experimental Optimisation of a High Performance Heat Exchanger

Lik Fang Sim

A thesis submitted in partial fulfilment of the requirements of
Sheffield Hallam University
for degree of Doctor of Philosophy

November 2007

This thesis is dedicated to my beloved parents and Teresa Lim, who have been giving me endless love and absolute support through life.

Abstract

The aim of this research is to numerically and experimentally scrutinise the thermal performance of a typical heat exchanger fitted in a domestic condensing boiler. The optimisation process considered the pins' geometry (circular pins and elliptical pins), pins' spacing, pitch distance, the pressure drop across the heat chamber and the occurrence of thermal hot spots. The first part of the study focused on the effect of altering the circular pins spacing and pins pitch distance of the heat exchanger. Computational Fluid Dynamics (CFD) is used to scrutinise the thermal performance and the air flow properties of each model by changing these two parameters. In total, 13 circular pin models were investigated. Numerical modelling was used to analyse the performance of each model in three-dimensional computational domain. For comparison, all models shared similar boundary conditions and maintained the same pin height of 35 mm and pin diameter of 8 mm. The results showed that at a given flow rate, the total heat transfer rate is more sensitive to a change in the pins spacing than a change of the pins pitch. The results also showed that an optimum spacing of circular pins can increase the heat transfer rate by up to 10%.

The second part of the study, focused on investigating the thermal performance of elliptical pins. Four elliptical pin setups were created to study the thermal performance and the air flow properties. In comparison with circular pins, the simulation results showed that the optimum use of eccentricity of elliptical pins could increase the total energy transfer by up to 23% and reduce the pressure drop by 55%.

To validate the acquired CFD results, a Thermal Wind Tunnel (TWT) was designed, built and commissioned. The experimental results showed that the numerical simulation under predicted the circular pin models' core temperatures, but over predicted the elliptical models core temperatures. This effect is due to the default values of the standard $k - \varepsilon$ transport equations model used in the numerical study. Both numerical and experimental results showed that the elliptical models performed better compared to its circular pins counter parts.

The study also showed that heat exchanger optimisation can be carried out within a fixed physical geometry with the effective use of CFD.

Acknowledgements

CONTENTS

Table of Figures

Table of Tables

Nomenclature

u	x - momentum, (kg·m/s)
v	y – momentum, (kg·m/s)
w	z – momentum, (kg·m/s)
S_m	Mass added to the continuous phase from the dispersed second phase and any user defined sources, (kg)
p	Static pressure, (Pa)
k_{eff}	Effective conductivity, (W/ m·K)
$\overline{J_j}$	Diffusion flux, (mol/ m^2 s)
S_h	Heat of chemical reaction and other volumetric heat sources from user, (W)
h	Enthalpy, (J/kg)
Y_j	Mass fraction of species j
I	Unit tensor
k	Turbulence kinetic energy, (m^2/s^2)
G_k	Generation of turbulence kinetic energy due to the mean velocity gradients
G_b	Generation of turbulence kinetic energy due to buoyancy
Y_M	Fluctuating dilation in compressible turbulence to the overall dissipation rate
S_k	User defined source term for turbulence kinetic energy, (m^2/s^2)
S_ε	User defined source term for turbulence dissipation rate, (m^2/s^3)
D_h	Hydraulic diameter, (m)
m	Mass to be heated, (kg)
C_p	Specific heat capacity of the fluid, (kJ/kg·K)
$\varDelta T$	Temperature difference, (K)
t	Temperature rise time, (hrs)
U	Overall heat transfer coefficient, (W/ m·K)
A	Wind tunnel surface area, (m^2)
BSP	British Standard Pipe
Re	Reynolds Number
P_o	Pressure head at fan outlet, (Pa)
v_o	Outlet velocity, (m/s)
v_i	Inlet velocity, (m/s)
P_i	Pressure head at fan inlet, (Pa)
h_{o-i}	Sum of total pressure head loss between fan outlet and inlet, (Pa)
Q	Volume flow rate, (m^3/s)
P_a	Fan power, (W)
C_u	Coefficient of uniformity
V_{max}	Maximum air velocity, (m/s)
V_{min}	Minimum air velocity, (m/s)
V_{avg}	Average air velocity, (m/s)
V	Voltage, (V)
T_h	Measured temperature, (°C)
EMF	Electro Magnetic Field
V_H	Hall effect voltage, (V)

I	Current, (A)
B	Magnetic field, (N s)
d	Depth of the plate, (m)
e	Electron charge, (m kg s)
n	Bulk density of carrier electrons, (m^{-3})
f	Frequency, (Hz)
n	Number of cycles of the repetitive signal
t	Time, (s)
P	Pulses per minute
K	Pulses per litre
RPM	Revolution Per Minute
f	Supplied frequency to the motor, (Hz)
p	Number of motor poles
P_{out}	Proportional term
K_p	Proportional gain
$\bar{e}$	Measured error
t	Process time, (s)
I_{out}	Integral term
K_i	Integral gain
D_{out}	Derivative term
K_d	Derivative gain
p_t	Measured total pressure , (Pa)
p_s	Measured static pressure, (Pa)
V	Defined velocity, (m/s)
ΔP	Pressure difference, (Pa)
$P_{upstream}$	Upstream pressure, (Pa)
$P_{downstream}$	Downstream pressure, (Pa)

Greek symbol

$\vec{v}$	Fluid flow velocity, (m/s)
ρ	Local density, (kg/m^3)
$\rho\vec{g}$	Gravitational body force, ($kg/ m^2 s^2$)
$\bar{\bar{\tau}}$	Stress tensor, (N/m^2)
μ	Molecular viscosity, (Pa s)
ε	Turbulence dissipation rate, (m^2/s^3)
σ_k	Turbulent Prandtl number for turbulence kinetic energy
σ_ε	Turbulent Prandtl number for energy dissipation rate
τ	Time in the past contributing in the integral response, (s)

Chapter 1   Introduction

Research shows that the earth's surface temperature increased by 0.6 ±0.2°C during the 20th century. This caused the global mean sea level to increase at an average annual rate of 1 to 2 mm [1]. By the year 2010, the United Kingdom's (UK) Government pledges to reduce the carbon emissions from British homes by 20% compared with the average emission rate of the year 1990 [2]. Domestic home boilers have direct impact on the domestic emissions target, thus it is important to design more efficient and intelligent boilers.

Overview

The majority of UK homes utilise gas fired central heating to supply hot water and heating around the house. As depicted in Figure 1-1, a conventional central heating system consists of the following:

1. Conventional boiler
2. Timer
3. Room thermostat
4. Cold water storage tank
5. Cylinder
6. Expansion tank/ vessel
7. Radiators
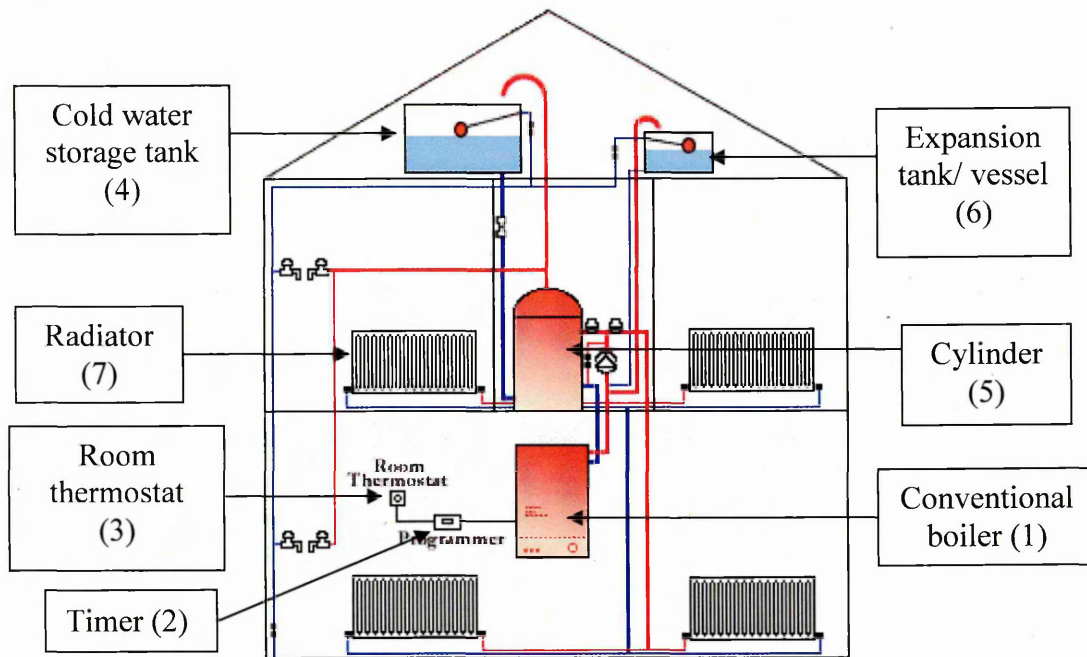
Figure 1-1: Conventional central heating system [3]

Cold water from the storage tank or mains supply, replenishes the cylinder when water has been released from the cylinder. A conventional boiler is used to raise the water temperature inside the cylinder for household usage and home heating. A pump is used to circulate the water from the cylinder to the radiators. As illustrated, a conventional central heating system utilises more heating space in the house. If the cylinder does run out of hot water it will usually take 25 to 30 minutes for the water to recover. Another disadvantage of a traditional boiler is that a large quantity of excessive heat is wasted when there is no demand for hot water.

Figure 1-2 shows a modern condensing boiler supply hot water and heating around the house without using any cylinder or cold water tank. Unlike conventional central heating, hot water is supplied on demand basis. A modern condensing boiler converts more than 90% of fuel into heat, compared to 78% using a conventional boiler. Any conventional boiler over 15 years old is considered inefficient because it only converts 50% of fuel into heat [4].
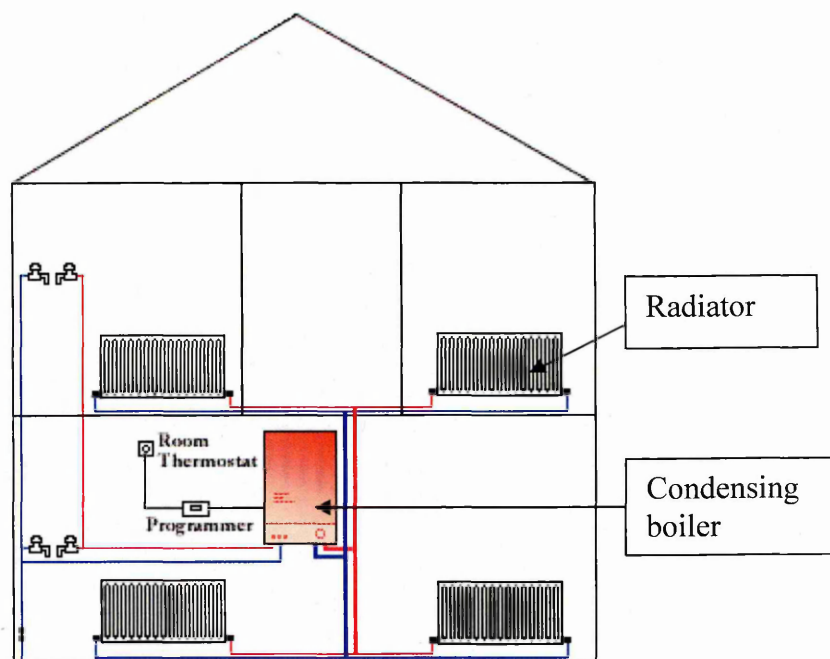
Figure 1-2: Modern central heating system [3]

A high efficiency condensing boiler burns natural gas in a heat chamber surrounded by a water jacket as illustrated in Figure 1-3. This unit is known as the heat exchanger. The heat exchanger plays a vital role within the boiler, as it is where the energy conversion and exchange would occur. The heat exchanger is a device in which energy is transferred from one fluid to another across a solid surface. The solid surface usually contains large quantities of pins to increase the total surface area available for heat exchanging process. Water channels or waterways externally encase the heat chamber to pick up the generated heat and transfer it to the water side.

Hot gas inlet

Water outlet

Water inlet

Hot gas outlet
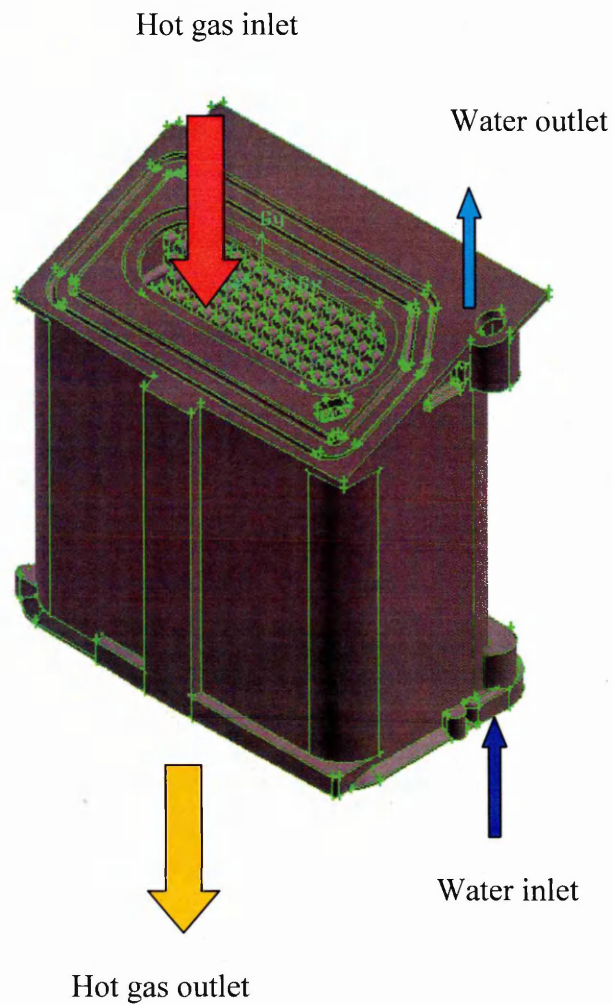
Figure 1-3: Heat exchanger in condensing boiler [courtesy of Vaillant Group]

The principle behind a condensing boiler is to recover as much heat as possible from the gas and further absorb the sensible heat from the condensate water before rejecting it to the atmosphere. In natural gas (methane CH_4), the simplified combustion equation can be written as:

$$CH_4 + 2\,O_2 + 7.2\,N_2 \rightarrow 2\,H_2O + CO_2 + 7.2N_2 + 30\,\text{kW of heat} \qquad \text{Equation 1-1}$$
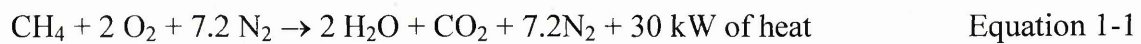
Fuel: CH_4 = 16 kg/k mol

Air: $2\,O_2 + 7.2\,N_2$ = 274.6 kg/k mol

Products: $2\,H_2O + CO_2 + 7.2N_2$ = 290.6 kg/k mol

If the wall temperatures at the heat chamber fall below the water vapour dew point, condensation will occur. Figure 1-4 illustrates that the water vapour dew point is approximately 57 °C. Currently, for natural gas (95% CH_4) condensing boilers exiting temperature is between 50°C to 60°C compared with 120 to 180 °C in current non-condensing boilers. Figure 1-4 also shows that the lower the sensible heat from the water vapour that is drawn out, the lower the carbon dioxide content released to the atmosphere.
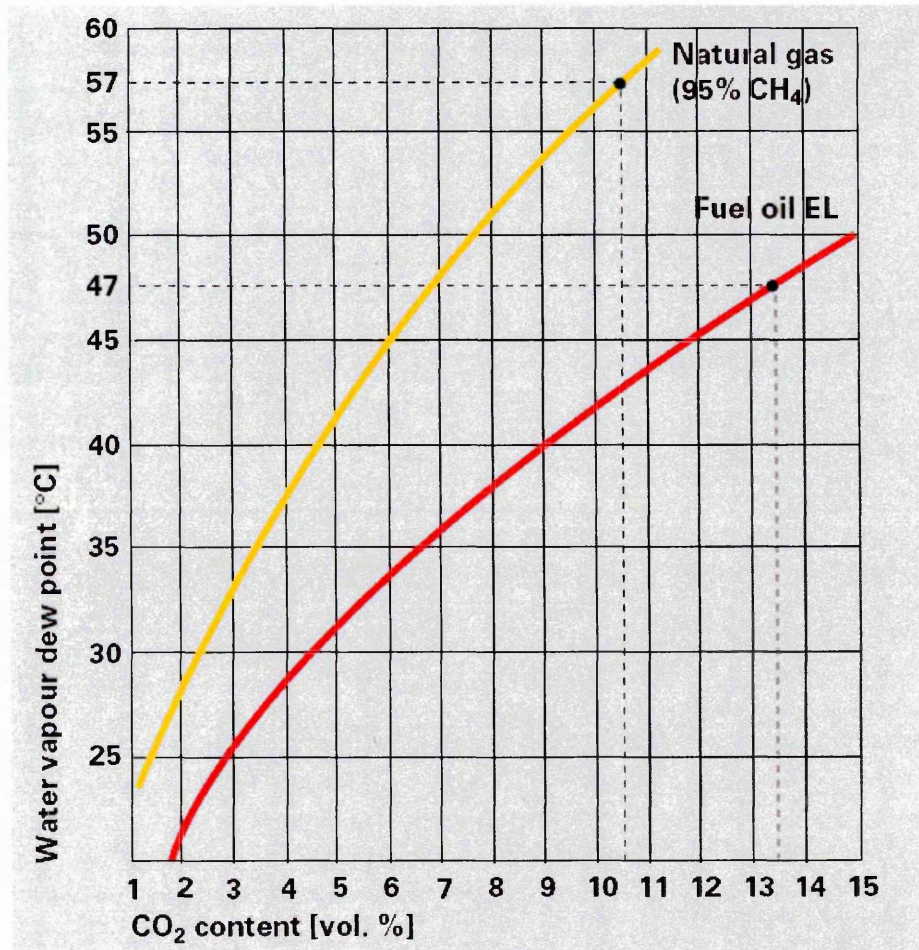
Figure 1-4: Natural gas and fuel oil water vapour dew point [5]

1.1 Research Objectives

The aim of this research was to numerically and experimentally scrutinise the thermal performance of a typical heat exchanger fitted in a domestic condensing boiler. The optimisation process took into account the pins' geometry (circular and elliptical pins), pins' spacing, pins pitch, the pressure drop across the heat chamber and the occurrence of thermal hot spots.

The main objectives of this research on current heat exchangers are to:
1. Scrutinise the sensitivity of the geometrical performance of circular pins
2. Scrutinise the sensitivity of the geometrical performance of elliptical pins
3. Design, build and commission a thermal wind tunnel
4. Validate numerical simulation results against experimental results
5. Improve the thermal efficiency of a current heat exchanger taken as a benchmark without physically altering the size, weight and volume of the unit.

The first stage of this research investigates the thermal and fluid flow performance of fixed diameter circular pins. In total 13 models with different pins' spacing or pitch distance were investigated. The second stage of the research evaluates the performance of the conventional circular pins' thermal performance against elliptical pins.

The third stage of the research introduces the experimental equipment used. A thermal wind tunnel was designed and enhanced using Computational Fluid Dynamics (CFD) tool. The thermal wind tunnel was then built and commissioned to experimentally validate the acquired numerical results. Direct Metal Laser-Sintering (DMLS) technology was used to build the pin models out of copper alloy which was tested on the thermal wind tunnel. Experimental data acquired from the thermal wind tunnel were then used to validate the numerical results.

1.2 Research Methodology

Both computational and experimental methods were used to study the thermal performance of the heat exchanger. Figure 1-5 illustrates the methodology and the logical thread structure used in this research. The first stage of the study focuses on the thermal and fluid flow performance of 4 x 4 staggered circular pins, with different spacing and pitch distance in a fixed channel. The numerical studies were conducted using commercially available CFD code, FLUENT 6.2. A model taken from a current market production heat exchanger was used as a benchmark design. From this model, several different pins configuration models with the same boundary conditions were then compared on the basis of maximising the total energy transfer from the pins to the water and reduce the pressure loss within the hot air channel.

The second stage of the research focused on the thermal and fluid flow performance of 4 x 4 staggered elliptical pins with different eccentricities. All elliptical models have the same material volume as their circular pins counterparts.

The third stage of this research shows the design, building and commissioning of a thermal wind tunnel. Due the specific application requirements, the thermal wind tunnel had to be custom made to suit the experimental tests. The initial design focuses on the flow quality within the thermal wind tunnel. Furthermore, the thermal wind tunnel design enhancement was carried out using CFD code, FLUENT 6.2. The specimens are then experimentally assessed in the thermal wind tunnel. Experimental results obtained from the thermal wind tunnel gave the thermal distribution of the pins' core temperature and thermal performance of each model. The experiment data was used to validate the numerical models.

The acquired data for numerical validation provides confidence in concluding the justification.
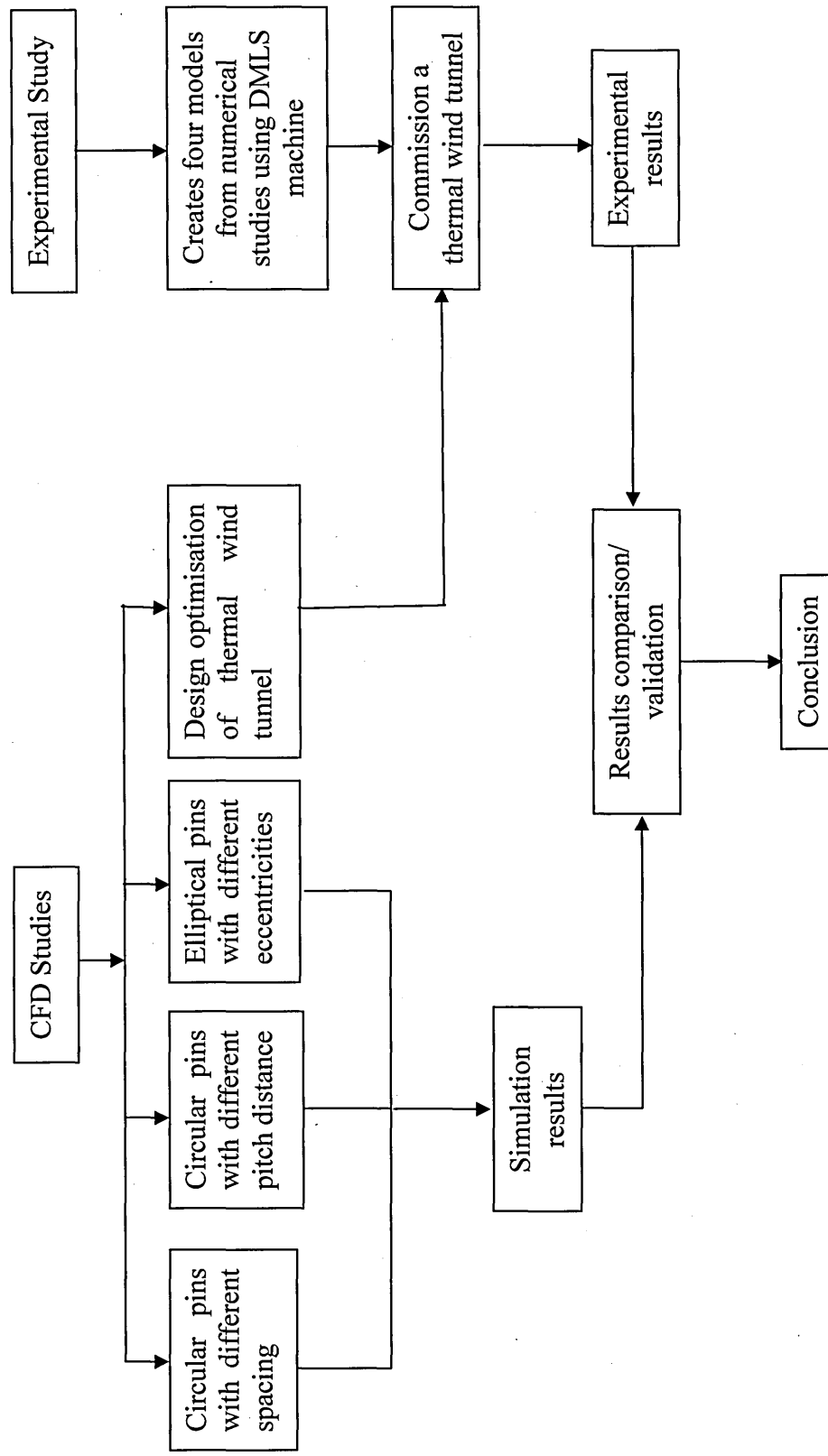
Figure 1-5: Research methodology and structure

Summary

This thesis is divided into 11 chapters. Each chapter covers a topic deemed necessary for this research. A summary of each chapter is listed below:

Chapter 1 provides an introduction of present domestic heating system and conventional heating system. This chapter also summarises the research objectives and methodology used in this research.

Chapter 2 presents previous related publications that have been published in different journals. Topics selected ranging from heat exchanger classification to the design parameters of heat exchanger.

Chapter 3 introduces CFD and its solution algorithms as a design tool used in this research. The chapter covers the theory of CFD and the modelling methods employed.

Chapter 4 summarises the numerical modelling methods employed in this research. The chapter covers the topics from computational meshing to solution convergence.

Chapter 5 introduces the design criteria of the thermal wind tunnel. A summary of the thermal wind tunnel numerical calculations is given in the chapter. A further design optimisation of the thermal wind tunnel is also discussed in the chapter.

Chapter 6 introduces the manufacturing process used to create the generic models namely, Direct Metal Laser Sintering (DMLS) technology. The chapter also introduces the instruments used throughout the experimental tests. Specimen preparation and water loop pressure testing were also described in the chapter.

Chapter 7 summarises the numerical simulation results.

Chapter 8 evaluation and analysis of the flow pattern and heat transfer results acquired from computer simulation is given.

9

Chapter 9 summarises the flows conditions and data acquired from the experimental tests.

Chapter 10 evaluates and validates the numerical results using the data acquired from the experimental tests.

Chapter 11 concludes this research and presents future work that could be carried out.

Chapter 2   Literature Review

A literature review has been carried out in this study to gather the previous related work on heat exchanger design and optimisation.

2.1 Introduction to Heat Exchangers

A heat exchanger is a device, which is used to transfer thermal energy from hotter fluid to a colder fluid [6]. Heat exchangers can be operated in three different ways and they are recuperation, regeneration and direct contact [7]. The most common heat exchanger is the recuperation heat exchanger, which transfers heat between two fluids separated from each other by a wall or a partition. Regeneration heat exchangers consist of either a moving wheel or fixed matrix. They are often found in gas turbines, where they are used to preheat combustion gases by the exhaust stream. Direct contact heat exchangers are commonly found in the metal sheet drawing industry. For example, cooling metal sheet by water droplets as it leaves a rolling press and in cooling towers where water droplets are cooled by an up draught of air [7].

2.2 Heat Exchangers Classification

Heat exchangers can be classified according to the flow arrangement. The flow arrangements can be parallel flow, counter flow, cross flow or multiple passes. In parallel flow heat exchangers, both fluids flow in from the same direction into the heat exchanger [8]. Conversely with counter-flow, two fluids at different temperature enter the heat exchanger at opposite ends and heat is transferred continuously from the hotter fluid to the colder fluid along the length of the heat exchanger [6]. Both flow characteristics can be found in Figure 2-1 and Figure 2-2. When two working fluids flow paths are perpendicular then the process is known as cross flow. In complex heat exchangers, multiple passes are used to increase the heat transfer rate because fluid transverse the heat exchanger several times before exiting. The operating principle of multiple passes can be found in Figure 2-3.

11
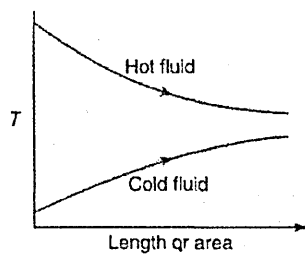
Figure 2-1: Parallel flow [6]
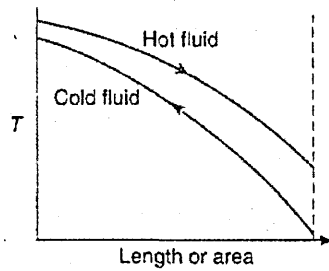
Figure 2-2: Counter flow [6]
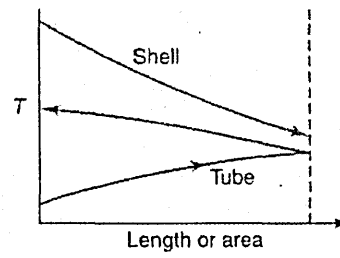
Figure 2-3: Multiple flows [6]

2.3 Changing Pins Geometries

Research [9 - 18] has been carried out to discover the most efficient pins geometry for each individual heating application. The common pins geometry used in the heating industry ranges from convectional circular pins to hexagonal pins. This research conducted a thorough review on different pins geometries. Behnia *et al.* [9] used computational fluid dynamics software to analyse the thermal performance of circular, square, elliptical and parallel plate fins heat sinks. The authors also used both inline and staggered arrays on each geometry studied. All geometries in the study were compared based on air velocity between 0.5 to 5 m/s and equal wetted area of the fins per unit base area. The authors concluded that at a given pressure drop, the staggered plate and staggered elliptical heat sink performed better than other geometries. The authors concluded that at lower values of pressure drop and pumping power, elliptical fins work best.

Christopher *et al.* [10] used an experimental approach to study elliptical pins, cross cut pins and straight fins. The authors conducted a series of tests on different air velocities ranging from 0.5 m/s to 1 m/s in a wind tunnel. Their report showed that the heat transfer on elliptical pins is much better than cross cut pins and straight fins. In open or confined flow, straight fin showed less effect on the pressure drop.

Kyoungwoo *et al.* [11] studied the flow and heat transfer of staggered cone shape pins geometry (spacing and pitch) and its shape (upper and lower diameter of the cone pin) in two-dimensional form. The flow and thermal characteristics of the reference staggered cone pins were first analysed using Finite Volume Method (FVM). Later, a Sequential Linear

12

Programming (SLP) algorithm method was used to optimise the design. They concluded that the most dominant factor for pressure drop and heat transfer rate is the lower diameter D_2, as depicted in Figure 2-4, of the cone pin and the pins' spacing. The research work showed that increasing the pins' spacing is more efficient than altering the pins pitch distance. The authors also concluded that the total heat transfer is more sensitive on the change of the heat exchanger area than the temperature gradient.

Similar study, but in three-dimensional form was found using four dimensionless geometric parameters to study cone pins in a fixed channel by Lee *et al.* [12]. Four dimensionless geometric parameters of the pins were selected as an important design variables in the study, namely the pins' spacing (L), pin volume (V), the angle (β) and pitch distance (G) as depicted in Figure 2-4.
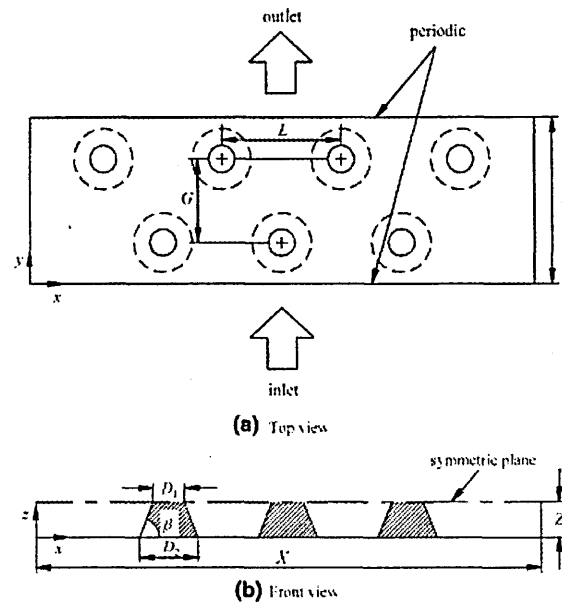
Figure 2-4: (a) top view of computational domain, (b) side view of computational domain [11, 12]

The authors affirmed that when increasing the cone spacing, the heat transfer rate increases and the pressure drop reduces. The study also showed that changing pitch distance does not give any significant improvements on heat transfer and pressure drop because most of the flow passes through both sides of the channel as in the case of small pins' spacing. The authors also carried out an optimisation process to minimise a global objective function

consisting of the correlation between the Nusselt number and the friction factor. The authors concluded that the optimum geometric parameters obtained can be applied to Reynolds number ranging between 500 and 1500. The most influencing parameters to the thermal and flow performance in the highest sensitivity order is pins' spacing, volume, cone angle and pitch distance.

2.4 Inline and Staggered Pins Configuration

The most common pin configurations can be inline or staggered configurations. Some research has been carried out to study the effectiveness of both configurations. Previous study was found from Jang et al. [13] who used computational and experimental methods to study the fluid flow and heat transfer of a multi row plate-fin and tube heat exchanger. The study focused on two different arrangements; inline and staggered pin configuration as illustrated in Figure 2-5.

| (a) Staggered arrangement | (b) In-lined arrangement |
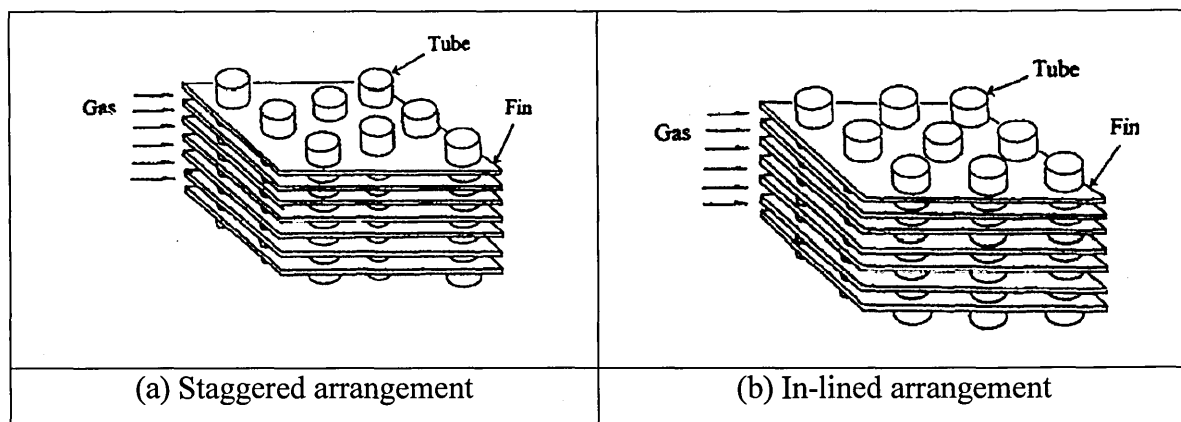
Figure 2-5: Multi row plate-fin and tube heat exchanger used in Jang et al. study [13]

The authors found that the average heat transfer coefficient of the staggered arrangement is 15% to 27% higher than the inline arrangement but it suffered from high-pressure drop. The pressure drop was 20% to 25% higher than the inline arrangement. In the staggered array, the authors detected a small recirculation zone behind each tube, due to repeated blockage of the staggered tube bank. On the inline array, the flow separates at the rear portion of a tube and reattaches at the front portion of the following tube to form a larger stationary recirculation region between the two adjacent tubes, causing a stagnant zone. This work showed that the staggered array outperformed the inline array.

14

2.5 Comparative Study of Circular and Elliptic Tubes

More direct comparison studies between circular and elliptic tubes were found through out this review. Rocha *et al.* [14] analysed the heat transfer performance of one and two rows of circular and elliptical tubes. Throughout their studies, elliptical configuration showed better efficiency than a circular counterpart. The maximum relative efficiency gain on elliptical tube was 18% on eccentricity of 0.5. A further study from Matos *et al.* [15] was found, which used numerical approach to investigate a two-dimensional heat transfer performance of circular and elliptic tube heat exchangers. The study used Finite Element Method (FEM) to define the model's fluid flow and heat transfer. The study focused on the optimal spacing of staggered circular and elliptical tubes in a fixed volume. The circular and elliptical arrangements with the same flow obstruction cross-sectional area were compared. They concluded that elliptical arrangement heat transfer was about 13% more than the circular counter parts. The authors also stated that the flatter the ellipses are, the higher the overall heat transfer will be.

Recently, Matos *et al.* [16] presented another study on circular and elliptical tubes fins' thermal performance. The study focused on three-dimensional numerical and experimental geometric optimisation. The optimisation parameters were tube to tube spacing, eccentricity and fin to fin spacing as shown in Figure 2-6.
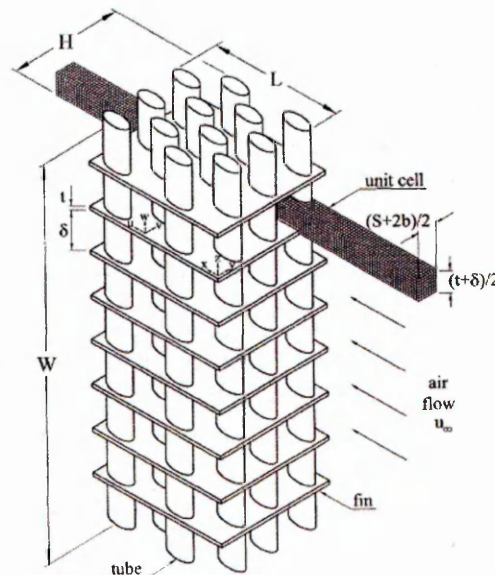
Figure 2-6: Elliptical tubes and fins used on Matos *et al.* studies [16]

15

The investigations were based on laminar regime for Re = 100 and 125. The study concluded that the three-dimensional elliptical model has a relative heat transfer gain up to 19% in comparison with circular tubes. The results also showed that fin's temperature on elliptical tubes is more uniform than the one on circular tubes.

2.6 Design Parameters of Heat Exchanger

Recently, Sahin *et al* [17] studied the heat transfer and pressure drop characteristics of rectangular fins by changing the fins width (*b*), stream wise distance between slices (*e*), span wise distance slices (*f*), angle of attack (α), heights of the fins (h_k), stream wise distance between fins (*c*), span wise distance between fins (a) and flow velocity as shown in Figure 2-7.
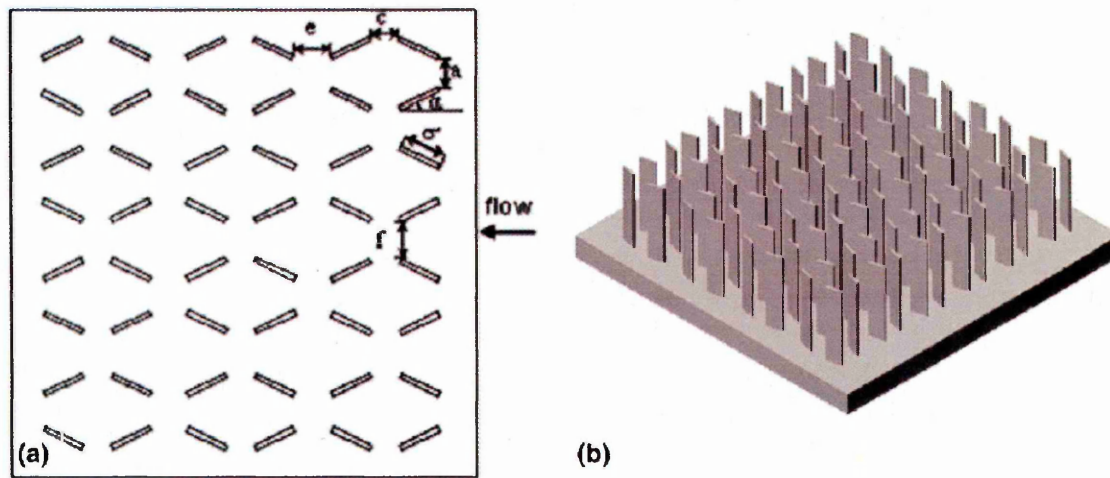
Figure 2-7: Rectangular fins used on Sahin *et al.* studies [17]

The authors used experimental techniques to analyse the identified design factors. According to their argument, the most influential parameters on heat transfer rate were identified as follows: fin height, fluid velocity, stream-wise distance between slices, span wide distance between slices, fin width, span wise distance between fins, angle of attack and stream wise distance between fins. The results also showed that when increasing the fin height, the heat transfer surface increases but the heat transfer coefficient decreases. As for the most influencing pressure drop factors were: angle of attack, fin width, fluid velocity

and span wise distance between slices where, the rest of the parameters does not show any significant changes in friction factor. Overall, the optimisation priorities among all these factors were found to be the fin width, angle of attack, fin height and span wise distance between fins.

A study carried out by Yakut *et al.* [18] examined the design parameters of hexagonal pins heat exchangers. As depicted in Figure 2-8, the effect of the height, widths of the hexagonal pins, streamwise and spanwise distance between pins and flow velocity on thermal resistance and pressure drop were investigated. The study concluded that the most important parameters affecting the heat resistance and pressure drop are pin height, pin width, spanwise distance between pins and streamwise distance between pin.
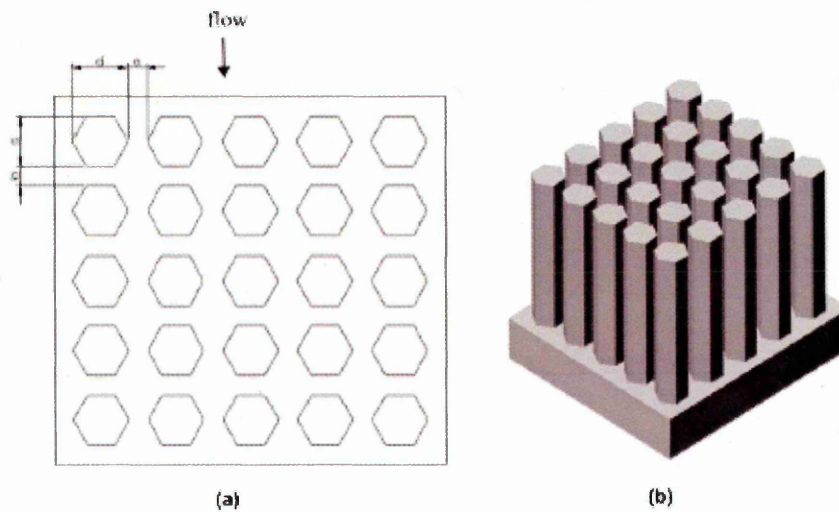
Figure 2-8: (a) Arrangement of hexagonal pins, (b) Isometric view of hexagonal pins. [18]

Summary

After reviewing previous related published works, it is evident that most previous studies only focused on the effects of different pins geometries, for example square pins or elliptical pins. Although, Sahin *et al.* [17] studied the effects of the fin stream-wise and spam-wise distance, rectangular fins were used instead of circular pins in their study. Furthermore, Matos *et al.* [16] investigations were very similar to this research but the authors only focused on laminar flow scenario. To the author's knowledge no publication was found, studying heat transfer from the solid phase to fluid phase.

Using Kwan-Soo Lee *et al.* [6] publication as a reference material, this research will focus more on pins' spacing to improve the heat exchanger performance rather than focusing on the pins pitch. This research differs from Kwan-Soo Lee *et al.* [6] as they only focused on laminar flow on cone pins and further more, the authors did not utilise any coolant or water in their study.

Consequently, this research will focus on:

- Air flow on circular and elliptical pins at Reynolds number of 1.7×10^4.
- Using two different fluids on test models. Air temperature of $200^{\circ}C$ and cold water of $17^{\circ}C$ as the heat carrier.

Chapter 3   Introduction to Computational Fluid Dynamics (CFD)

Introduction

During the earlier twentieth century, physicists and scientists used experimental and theoretical methods to study fluid dynamics. However, the advancement of high speed computing power and mathematical modelling introduced an important new approach in fluid dynamics known as Computational Fluid Dynamics (CFD). CFD is a scientific tool of predicting fluid flow, heat transfer, mass transfer, phase change, chemical reaction, mechanical movement, stress or deformation of related solid structure and related phenomena by solving the mathematical equations that govern processes using a numerical algorithm on a computer [19]. CFD is an important tool in modern research. Numerous fluid dynamics problems have been studied and optimised using computational studies before any experimental work was carried out. Sometimes CFD simulation permits the investigation to be carried out, where controlled experiments are difficult to achieve. For example, temperature at a particular point inside the heat chamber of the heat exchanger. CFD simulations are most useful in predicting the trends of how shape changes affect the flow field and heat transfer of the system. The ultimate advantage of the CFD over experiment is practically the unlimited level of detail of results it has.

This chapter presents a brief introduction of the theories behind CFD and modelling steps using CFD codes. Only relevant numerical models for this study will be presented here. The numerical simulation steps described in this study are based on FLUENT 6.2 CFD code.

3.1 Theory of Computational Fluid Dynamics (CFD) Modelling

There are several commercially available CFD codes on today's market. The most commonly used CFD codes are FLUENT, STAR-CD, CFX and CFD-FASTRAN. CFD simulations are summarised in three main steps:

1. Pre-processing
2. Solving equations
3. Post - processing

Each step will be discussed briefly within this chapter.

3.1.1 Pre-processing

Pre-processing can be carried out using different Computer Aided Design (CAD) or Computer Aided Engineering (CAE) package for example Pro/Engineer Wildfire, SolidWorks or Gambit. The activities involved in pre-processing are:

1. Defining the physical geometry of the region of interest
2. Mesh generation
3. Mesh independent solutions and refinement
4. Define appropriate boundary conditions at boundaries

Defining the physical geometry

Before any CFD models can be solved, the geometry of the interested system must be defined. All CFD codes require a geometrical model as a starting point. A geometrical model of a system is also known as the physical domain. A geometrical model can be created in any CAD package that is available on the market.

Mesh generation

Mesh generation is one of the most important and most time consuming processes in CFD simulation. It is also known as grid generation. Mesh generation is the approximation of the continuous surfaces of the object and the continuous physical volume through a set of discrete x, y, z coordinates. The quality of mesh plays a significant role on the results accuracy and solution stability. The attributes associated with mesh quality including node point distribution, smoothness and skewness of mesh. An improper mesh can affect the physics of the flow simulated, solution stability and computing time. There are two types of mesh generation schemes to represent the model in computational domain. They are:

1. Structured mesh
2. Unstructured mesh.

Structure mesh can be divided into two types:

1. Algebraic methods
2. Partial Differential Equation (PDE) mapping methods.

As shown in Figure 3-1, in algebraic methods, geometric data of the Cartesian coordinates in the interior of a domain are generated from the values specified at the boundaries through interpolations or specific functions of the curvilinear coordinates [20]. PDE mapping methods are more complicated than algebraic methods but provide smoother mesh generation. PDE mapping methods use partial differential equations to transfer physical domain to computational domain. The partial differential equations can be elliptic, hyperbolic, or parabolic. The mesh generated using PDE mapping methods is shown in Figure 3-2.
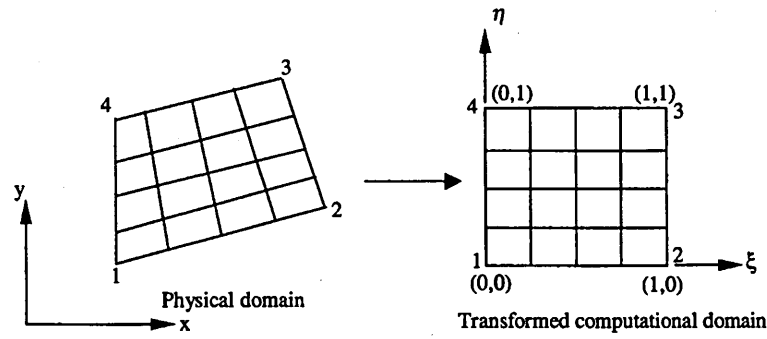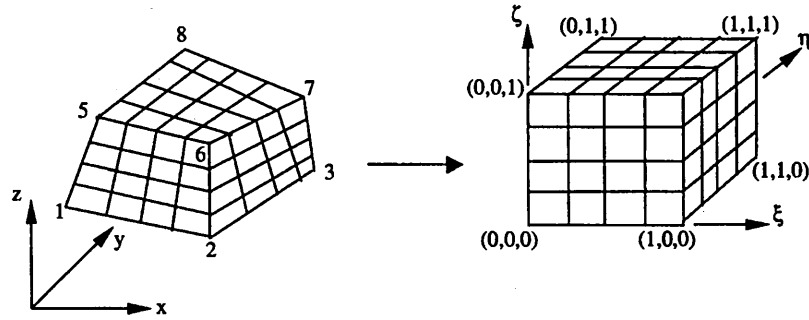
Figure 3-1: Algebraic methods transfer from physical domain to computational domain (a) two dimension (b) three-dimension [20]
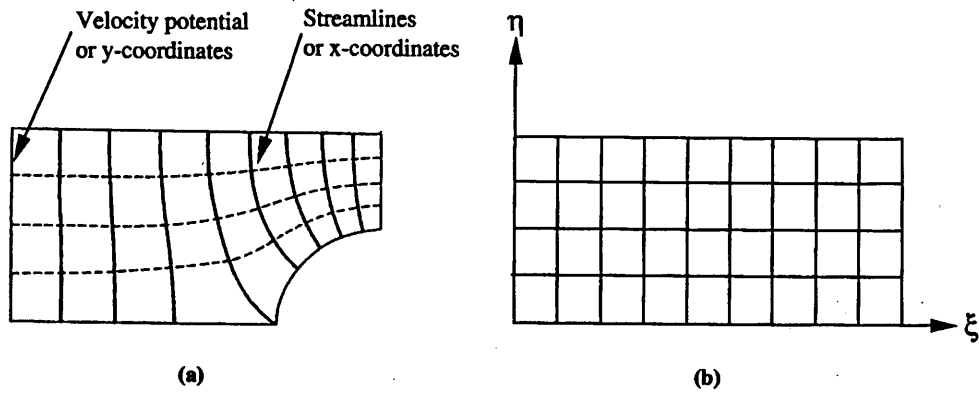
Figure 3-2: PDE mapping methods (a) physical domain, (b) computational domain [20].

Unstructured mesh offers more flexibility on complex and irregular geometry. Structured mesh is restricted to where physical domain can be transformed into computational domain through one to one mapping. There are two major unstructured mesh generation methods: (a) Delaunary-Voroni Methods (DVM) and (b) Advancing Front Methods (AFM) for triangles in two dimensional and tetrahedral in three dimensional. In DVM a two

22

dimensional domain may be triangulated as shown in Figure 3-3. Each side line of the triangles can be bisected in a perpendicular direction such that these three bisectors join a point within the triangle forming a polygon surrounding the vertex of each triangle. DVM prefer triangle close to an equilateral triangle than distorted triangular shapes.

(a)   (b)
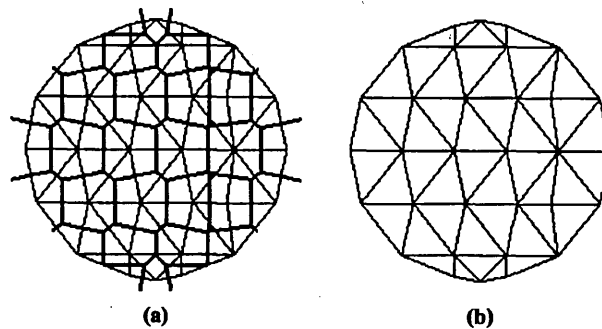
Figure 3-3: (a) Polygon bisected by triangles (b) DVM meshing on computational domain [21]

AFM use internal nodal formation and triangulation to generate mesh. As shown in Figure 3-4, simple domains with six nodes are used as initial active front face. Node 7 is created to form a triangular 1-2-7 and then side 1-2 is deleted so that now two new front faces 1-7 and 2-7 are created. The process continues until all front faces are deleted as shown in Figure 3-4. The deleted sides then represent the generated mesh [21]. This type of mesh generation method is more controllable on the node spacing especially when coarse and fine meshes are together. This type of meshing can also cause cells to be skewed for example cells collapse on other cells. In some CFD codes, the quality of the generated mesh as a function of its skewness can be shown after meshing.

(a) Given domain

1(0, 1)   5(6, 3.5)
2(2.5, 0.5) 6(2, 5)
3(5, 0)   7(3, 2.5)
4(10, 2)   8(7, 2)
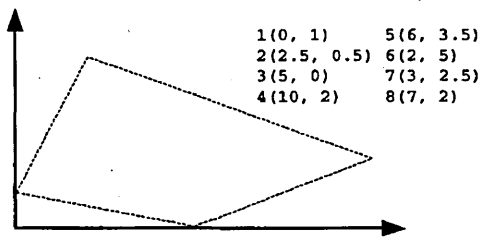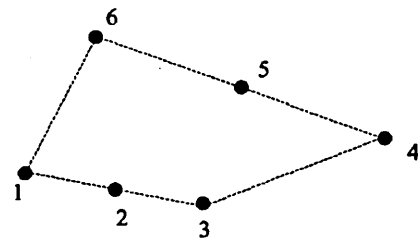
(b) Background boundary nodes (initial fronts)
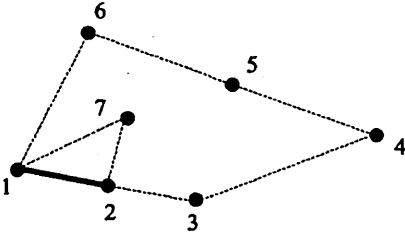
(c) Choose new node (7), delete side (1-2), new active fronts (1-7, 2-7)
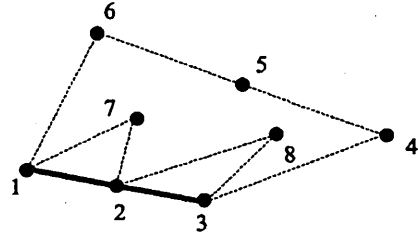
(d) Choose new node (8), delete side (2-3), new active fronts (2-8, 3-8)
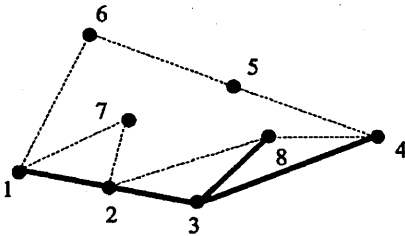
(e) Delete sides (3-8, 3-4), new active front (8-4)
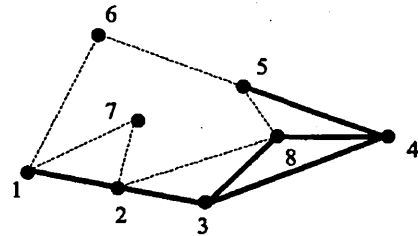
(f) Delete sides (4-8, 4-5), new active front (5-8)
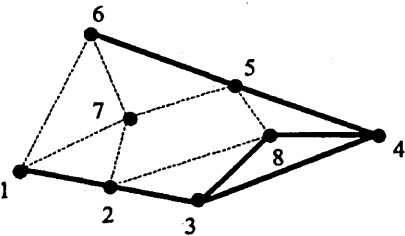
(g) Delete side (5-6), new active fronts (5-7, 6-7)
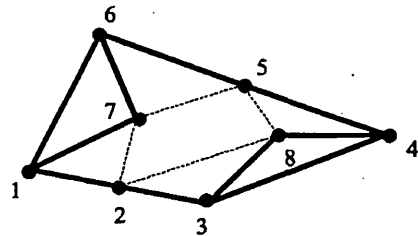
(h) Delete sides (6-7, 6-1, 1-7), no new active front
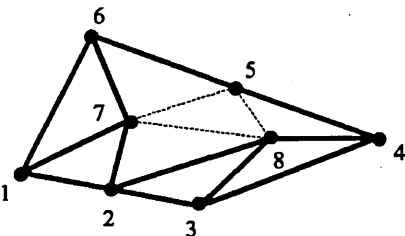
(i) Delete sides (2-7, 2-8), new active front (7-8)
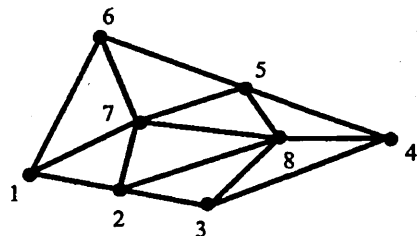
(j) Delete sides (7-8, 7-5, 8-5), no new active front

Figure 3-4: Advancing front methods (AFM) meshing construction [21]

24

Mesh independent solutions and refinement

The aim of CFD simulation is to obtain acceptable results while minimising the requirements of computing power. In general, the larger the number of cells used in a model the better the representation of the physical domain and hence the better the accuracy. In many cases, CFD users want to achieve accuracy and efficiency at the same time. Thus, mesh independent methods are utilised to assess both accuracy and efficiency at the same time. Depending on which mesh generation scheme used, a suitable mesh independent method could be selected. Structured mesh scheme can use (1) control function methods or (2) variation function approach. Both methods use redistribution method to move the grid points in accordance with the weight or control functions on the gradients of the variable. More details of these two methods can be found in reference [22].

Due to flexibility on node spacing, unstructured mesh scheme allows users to adopt more than two different mesh independent methods. The mesh independent methods used on unstructured method are:

1. Mesh refinement methods (h - methods)
2. Mesh movement methods (r – methods)
3. Mesh enrichment methods (p- methods)
4. Combined mesh refinements and movements (hr - methods)
5. Combined mesh refinements and enrichments (hp – methods) [22].

This Chapter will focus on unstructured mesh independent methods because it is adopted in this research. Mesh refinement methods (h - methods) is to refine the mesh based on an error indicator. An error indicator is the solution gradient variables for example density, pressure or temperature. It indicates how fast the error changes as the refinement changes. This refinement is carried out until the solution reaches the user specified tolerance. Mesh movement methods (r – methods) is slightly different compared with mesh refinement methods (h – methods) because instead of mesh refinement, grid point can be moved around to more sensitive areas. This method can reduce the number of cells, but also increase the results accuracy. This method also use error indicator to reach user specified tolerance. Mesh enrichment methods (p- methods) is different from the above methods.

Geometry is assigned with a fixed mesh and the solutions are expected to improve by running higher polynomials or higher order functions. If the solution fails to reach the user specified tolerance, the relating order must be raised. Combined mesh refinements and movements (*hr* - methods) is the most flexible mesh improvement method. It refines and moves around the grid points to more sensitive areas to achieve better accuracy in simulation results. If a simulation model is involved in a shock wave interacting with turbulent boundary layers, combined mesh refinements and enrichments (*hp* – methods) is not recommended [22]. This method begins with lower polynomial or order until *h* – methods reach to a certain level i.e. shock discontinue, then followed by *p* - enrichment.

Defining Boundary conditions

Boundary conditions specify the fluid flow and thermal variables on the boundaries of the computational domain. Consequently, they are a critical component of any CFD simulation and are crucial that they are effectively enforced. The fluid flow boundary conditions are classified as follows:

1. Flow inlet and exit boundaries: pressure inlet, velocity inlet, mass flow rate inlet, inlet bent, intake fan, pressure outlet, pressure far field, outflow, outlet vent, exhaust fan.
2. Wall, repeating and pole boundaries: wall, symmetry, periodic, axis.
3. Internal cell zones: fluid, solid.
4. Internal face boundaries: fan, radiator, porous jump, interior wall.

3.1.2 Solving equations

There are few standard equations that need to be solved on every simulation process. The fundamental aspects of fluid flow are governed by three conservation laws of physics:

1. Conservation law of mass
2. Newton' second law. The rate of change of momentum equals the sum of the forces on a fluid particle
3. First law of thermodynamics. The rate of change of energy is equal to the sum of the rate of heat addition to and the rate of work done on a fluid particle [23].

Other equations used on this study are Navier-Stokes equations for Newtonian fluid, energy equation to solve the heat transfer and turbulence model.

Continuity equation

The continuity equation is also known as the mass conservation equation. The principle of the mass conservation equation is that the mass of a controlled volume will remain constant, regardless of any process acting inside the system. The controlled volume can change form, but cannot be created or destroyed. The partial differential equation form of the continuity equation can be written as follows [19]:

$$\frac{\partial \rho}{\partial t} + \nabla \left(\rho \vec{v} \right) = S_m$$
Equation 3-1

Where,

$$\nabla = \frac{\partial}{\partial x} + \frac{\partial}{\partial y} + \frac{\partial}{\partial z}$$
Equation 3-2

S_m is the mass added to the continuous phase from the dispersed second phase and any user defined sources.

Momentum conservation equation

Newton's second law stated that the rate of change of momentum of a fluid particle equals to the sum of the forces on the particle. In this case, there are two types of forces on fluid particles:

1. Body forces - gravity force, centrifugal force and electromagnetic force.
2. Surface forces – pressure force, viscous force, shear and normal force.

The rate of increase of x, y, z momentum per unit volume of a fluid particle are given by

$$\rho\frac{Du}{Dt} \qquad \rho\frac{Dv}{Dt} \qquad \rho\frac{Dw}{Dt} \qquad\qquad \text{Equation 3-3}$$

The body forces overall effect is by the source S_{Mx}, S_{My}, S_{Mz} of the x-component, y-component and z- component of the momentum equation. Based on the principle above the momentum conservation equation can be written as follow [23]:

The x-component of the momentum equation is given by:

$$\rho\frac{Du}{Dt} = -\frac{\partial p}{\partial x} + \frac{\partial \tau_{xx}}{\partial x} + \frac{\partial \tau_{yx}}{\partial y} + \frac{\partial \tau_{zx}}{\partial z} + S_{Mx} \qquad\qquad \text{Equation 3-4}$$

The y-component of the momentum equation is given by:

$$\rho\frac{Dv}{Dt} = -\frac{\partial p}{\partial y} + \frac{\partial \tau_{xy}}{\partial x} + \frac{\partial \tau_{yy}}{\partial y} + \frac{\partial \tau_{zy}}{\partial z} + S_{My} \qquad\qquad \text{Equation 3-5}$$

The z-component of the momentum equation is given by:

$$\rho\frac{Dw}{Dt} = -\frac{\partial p}{\partial z} + \frac{\partial \tau_{xz}}{\partial x} + \frac{\partial \tau_{yz}}{\partial y} + \frac{\partial \tau_{zz}}{\partial z} + S_{Mz} \qquad\qquad \text{Equation 3-6}$$

Navier-Stokes equations for a Newtonian fluid

The Navier-Stokes equations are used to define the fluid flow viscous stress τ_{ij}, derived independently by two scientists during the 19th century. In three dimensional flows, the local rate of the deformation is composed of the linear deformation rate and the volumetric deformation rate. The three linear deformation components are:

$$e_{xx} = \frac{\partial u}{\partial x} \qquad e_{yy} = \frac{\partial v}{\partial y} \qquad e_{zz} = \frac{\partial w}{\partial z} \qquad\qquad \text{Equation 3-7}$$

The six shearing linear deformation components are:

$$e_{xy} = e_{yx} = \frac{1}{2}\left(\frac{\partial u}{\partial y} + \frac{\partial v}{\partial x}\right), \ \ e_{xz} = e_{zx} = \frac{1}{2}\left(\frac{\partial u}{\partial z} + \frac{\partial w}{\partial x}\right), \ \ e_{yz} = e_{zy} = \frac{1}{2}\left(\frac{\partial v}{\partial z} + \frac{\partial w}{\partial y}\right) \quad \text{Equation 3-8}$$

The volumetric deformation is given by

$$\frac{\partial u}{\partial x} + \frac{\partial v}{\partial y} + \frac{\partial w}{\partial z} = \nabla V \qquad\qquad \text{Equation 3-9}$$

Where, the x-component of Navier-Stokes equation is:

$$\rho \frac{Du}{Dt} = -\frac{\partial p}{\partial x} + \nabla\left(\mu\, grad u\right) + S_{Mx} \qquad\qquad \text{Equation 3-10}$$

The y-component of Navier-Stokes equation is:

$$\rho \frac{Dv}{Dt} = -\frac{\partial p}{\partial y} + \nabla\left(\mu\, grad v\right) + S_{My} \qquad\qquad \text{Equation 3-11}$$

The z-component of Navier-Stokes equation is:

$$\rho \frac{Dw}{Dt} = -\frac{\partial p}{\partial z} + \nabla\left(\mu\, grad w\right) + S_{Mz} \qquad\qquad \text{Equation 3-12}$$

Energy equation

The energy equation is derived from Newton's first law. The law states that the rate of change of energy inside a fluid element is equal to the rate of heat added to the fluid particles and rate of work done on the fluid particles. The energy equation used in this study can be written as follow [19]:

$$\frac{\partial}{\partial t}(\rho E) + \left(\vec{v}(\rho E + p)\right) = \nabla\left(k_{eff}\nabla T - \sum_j h_j \overline{J_j} + \left(\overline{\overline{\tau_{eff}}} \times \vec{v}\right)\right) + S_h \qquad \text{Equation 3-13}$$

Where,

k_{eff} is the effective conductivity,

$\overline{J_j}$ is the diffusion flux of j.

S_h include the heat of chemical reaction and other volumetric heat source that the user defined.

Where,

$$E = h - \frac{p}{\rho} + \frac{v^2}{2} \qquad \text{Equation 3-14}$$

enthalpy h is defined for ideal gas as [19]:

$$h = \sum_j Y_j h_j \qquad \text{Equation 3-15}$$

and for incompressible flow h is

$$h = \sum_j Y_j h_j + \frac{p}{\rho} \qquad \text{Equation 3-16}$$

30

k- ε transport equation

The k − ε transport equation is used to define the turbulence kinetic energy and flow dissipation rate within the model. It is the simplest turbulence model, which only initial or boundary conditions are needed to apply. Additionally, it is also the most widely used and validated turbulence model. In here, k is the turbulence kinetic energy and ε is the dissipation rate. The equations can be written as [19]:

$$\frac{\partial}{\partial t}(\rho k) + \frac{\partial}{\partial x_i}(\rho k u_i) = \frac{\partial}{\partial x_j}\left[\left(\mu + \frac{\mu_t}{\sigma_k}\right)\frac{\partial k}{\partial x_j}\right] + G_k + G_b - \rho\varepsilon - Y_M + S_k \qquad \text{Equation 3-17}$$

and

$$\frac{\partial}{\partial}(\rho\varepsilon) + \frac{\partial}{\partial x_i}(\rho\varepsilon u_i) = \frac{\partial}{\partial x_i}\left[\left(\mu + \frac{\mu_t}{\sigma_\varepsilon}\right)\frac{\partial\varepsilon}{\partial x_i}\right] + C_{1\varepsilon}\frac{\varepsilon}{k}(G_k + C_{3\varepsilon}G_b) - C_{2\varepsilon}\rho\frac{\varepsilon^2}{k} + S_\varepsilon$$

$$\text{Equation 3-18}$$

Where,

G_k represents the generation of turbulence kinetic energy due to the mean velocity gradients,

G_b is the generation of turbulence kinetic energy due to buoyancy

Y_M represents the contribution of the fluctuating dilatation in compressible turbulence to the overall dissipation rate,

$C_{1\varepsilon} = 1.44$,

$C_{2\varepsilon} = 1.92$,

$\sigma_k = 1.0$,

$\sigma_\varepsilon = 1.3$ [19]

31

The turbulent viscosity μ_t can be written as follow:

$$\mu_t = \rho C_\mu \frac{k^2}{\varepsilon}$$

Equation 3-19

Where,

$$C_\mu = 0.09 \,[19]$$

This model requires an initial value, which is the hydraulic diameter. The equation of hydraulic diameter can be written as follow:

$$D_h = \frac{4 \times inlet\ area}{wetted\ perimeter}$$

Equation 3-20

3.1.3 Post – processing

Most CFD codes come with a post – processing tool, which allow the user to visualise and present the results. The tool functions include:

1. Flow velocity vectors visualisation
2. Results showed in colour contours
3. Grid display
4. Particles tracking
5. View manipulation for examples scaling and translation.
6. Results summary
7. XY plot

Additional post – processor software are available on the market. For example Tecplot, can be used with many CFD codes to improve presentation and visualisation of simulation results.

3.2 Computational Fluid Dynamics (CFD) Codes

FLUENT is a general purpose commercial CFD package for modelling fluid flow and heat transfer in complex geometries. It supports different mesh types include 2D triangular, quadrilateral, 3D mesh including tetrahedral, hexahedral, pyramid, wedge and hybrid meshes. FLUENT uses client and server architecture, which allows it to run as separate simultaneous processes on client desktop workstations or powerful computer clusters. All functions required to compute a solution and display the results are accessible in FLUENT through an interactive, menu driven interface. The package includes the following programs:

1. FLUENT, the solver and postprocessor
2. GAMBIT, the pre-processor for geometry modelling and mesh generation.
3. TGrid, an additional pre-processor that can generate 2D or 3D meshes from existing boundary meshes.
4. Filters (translators) for importing of surface and volume meshes from other CAD/ CAE packages such as ANSYS, CGNS, I-DEAS, NASTRAN and PATRAN in IGES, STEP, STL and Parasolid file format.

3.2.1 Continuous phase modelling in FLUENT

Figure 3-5 illustrates the CFD simulation procedure as adapted by FLUENT. The three CFD simulation basic steps; namely pre-processor, solver and postprocessor, appeared as coloured arrows on the flowchart left hand side to assist in understanding the technique followed. The pre-processor step starts with an attempt to create a CAD wire frame geometry for the fluid flow physical domain. Normally GAMBIT is used to construct the model wire frame geometry. However, GAMBIT has the ability to import an initial graphics exchange specification files (IGES). This feature facilitates importing the geometry wire frame constructed using other CAD packages. Once the physical domain

33

geometry is represented in GAMBIT editor as a wire frame, a surface generation procedure is carried out to construct solid surfaces or skin using the wire frame geometry or so called body skeleton. Next, is stitching the subsequent solid surfaces into integrated volume sub-blocks. Gambit allows users to select different sort of mesh elements and type for grid generation. Table 3-1 and Table 3-2 listed the options available in Gambit.

```
                              ┌──────────┐
                              │  Start   │
                              └────┬─────┘
                                   │
                    ┌──────────────▼──────────────┐
                    │ Create geometry on CAD or Gambit │
                    └──────────────┬──────────────┘
                                   │
                    ┌──────────────▼──────────────┐
                    │  Surface generation (Gambit) │
                    └──────────────┬──────────────┘
                                   │
                    ┌──────────────▼──────────────┐
                    │ Volume blocks generation (Gambit or TGrid) │
                    └──────────────┬──────────────┘
                                   │
                    ┌──────────────▼──────────────┐
                    │ Grid generation and grid     │
                    │ smoothing/check              │
                    └──────────────┬──────────────┘
                                   │
                    ┌──────────────▼──────────────┐
                    │  Import mesh file into FLUENT │
                    └──────────────┬──────────────┘
                                   │
                    ┌──────────────▼──────────────┐
                    │ Set case file: Grid scale, equations, physical │
                    │ properties, boundary conditions │
                    │ (FLUENT)                      │
                    └──────────────┬──────────────┘
                                   │
                    ┌──────────────▼──────────────┐
                    │ Initialise the flow field/ calculate a solution │
                    │ (FLUENT)                      │
                    └──────────────┬──────────────┘
```

Preprocessor

Solver

Postprocessor

Is solution converging ?

No — No — Yes

Run more iterations until convergence

Save case and data file. Display and print simulation results (FLUENT)
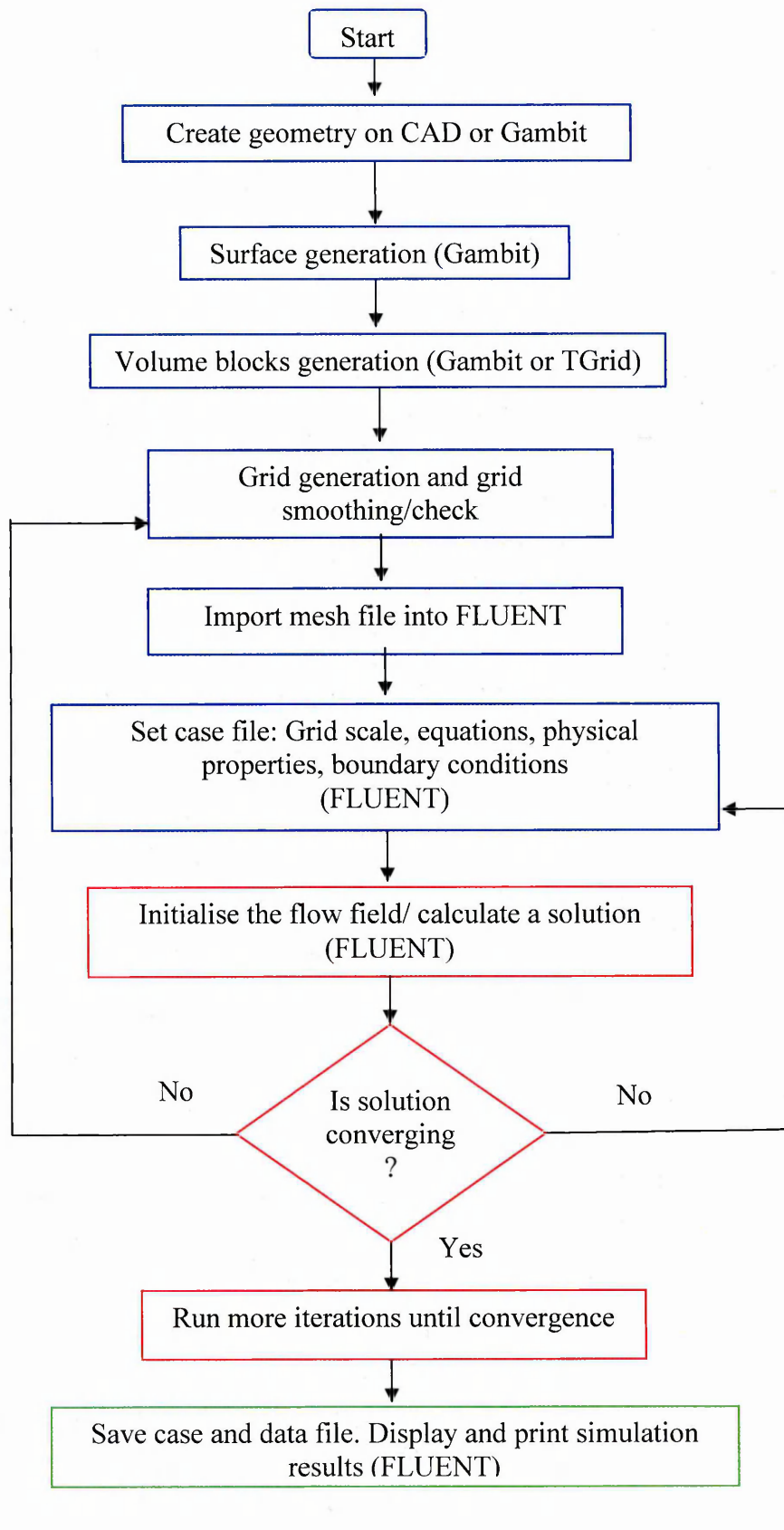
Figure 3-5: FLUENT simulation structure.

Table 3-1: Gambit face meshing elements options [24]

Option	Description
Quad	Specifies that the mesh includes only quadrilateral mesh elements
Tri	Specifies that the mesh includes only triangular mesh elements
Quad/Tri	Specifies that the mesh is composed primarily of quadrilateral mesh elements but includes triangular corner elements at user specified location

Table 3-2: Gambit face meshing type options [24]

Option	Description
Map	Creates a regular, structured grid of mesh elements
Submap	Divides an unmappable face into mappable regions and creates structures grids of mesh elements in each region
Pave	Creates an unstructures grid of mesh elements
Tri Primitive	Divides a three-sided face into three quadrilateral regions and creates a mapped mesh in each region
Wedge Primitive	Creates triangular elements at the tip of a wedge shaped face and creates a radial mesh outward from the tip

After all surfaces have been meshed, an additional software called TGrid can be used to carry out volume meshing. TGrid is a pre-processor for unstructured surface wrapping and volume mesh generation. It can be used to create unstructured tetrahedral and HexCore meshes for larger and complex shapes. It also offers better flexibility and quality meshing than Gambit. Hence, the physical boundary conditions are assigned to the required surfaces to simulate the fluid flow conditions on the physical domain. The boundary conditions assigned to certain surfaces can be changed later on the FLUENT solver editor. The last step in the grid generation procedure comprises a visual and mesh skewness check. In FLUENT, skewness must be maintained below 0.85 to be considered as a good mesh. If the mesh skewness is between 0.85 and 1, it is considered to be high level of skewness within the geometry. This could undermine the accuracy of the simulation results. Later, the developed mesh file must be saved and imported into FLUENT, the solver and postprocessor editor.

After successfully reading the meshed file within FLUENT solver editor, essential steps must be taken to rescale and check the grid. Grid rescaling is necessary if the model is made using different units. FLUENT provides different numerical models to solve the fluid flow, heat transfer and turbulence. An appropriate numerical model must be selected to represent the flow. Hence, the fluid properties and the boundary conditions can be identified and implemented for example, the fluid type, the fluid physical properties, fluid velocity and temperature. Before performing the calculations, the fluid flow initialisation must be carried out on the computational domain. This step enforcing an initial guess for the solution flow field. While performing calculations, the solution convergence status can be monitored by checking the plotted and printed scaled residuals. If the solution is satisfactorily converging, the solver is allowed to perform calculation until meeting the prescribed convergence criteria. The default convergence criteria in FLUENT requires that the scaled residuals decrease below 1×10^{-3}. However, if the solution is diverging, the calculations can be automatically or manually stopped. A thorough revision of the grid quality and the selected boundary conditions must be carried out. The suitability of the selected numerical model is also scrutinised. After acquiring a converged solution, further checks must be carried out to validate the numerical results. Usually the numerical results are validated against experimental data or against any previously published related data. FLUENT as a postprocessor offer a wide range of graphical and numerical data manipulation. For example, FLUENT editor offers domain geometry and grid display, velocity vector plots, contour plots and particle tracking. Finally, the case and data files can be saved for further calculations or refinement.

3.2.2 FLUENT Solution Algorithms

FLUENT solver has two solving methods:

1. Segregated solver
2. Coupled solver.

Both solving techniques consist of the following:

1. Division of the domain into discrete control volume using a computational grid.
2. Integration of the governing equations on individual volumes to construct algebraic equation for the discrete dependent variables such as velocity, pressure, temperature and the dependent variables.
3. Linearisation of the discretised equation and solution of the resultant linear equation system to yield values of the dependent variables [19].

Each solver will now be discussed.

Segregated solver

Segregated solution method is a very common solver. It is widely used on wide range of industrial flow applications. This type of solver is a non-linear solver. Consequently, several iterations of solution loop must be performed before a converged solution is obtained. Below are solution steps that segregated solver used:

1. Fluid properties are updated, based on the current solution. If the calculation has just begun, the fluid properties will be updated from the initialised solution.
2. The u, v and w momentum equations are each solved using current values for pressure and face mass fluxes, in order to update the velocity field.

3. If the velocities obtained in Step 2 do not satisfy the continuity equation, a 'Poisson type' equation for the pressure correction is derived from the continuity equation and the linearised momentum equations. This pressure correction equation is then solved to obtain the necessary corrections to the pressure and velocity fields and the face mass fluxes such that continuity is satisfied.

4. Where appropriate, equation for scalars such as turbulence and energy are solved using the previous updated values of the other variables.

5. A check for convergence of the equation set is made [19].

All these steps continue until the solutions converge as shown in Figure 3-6.
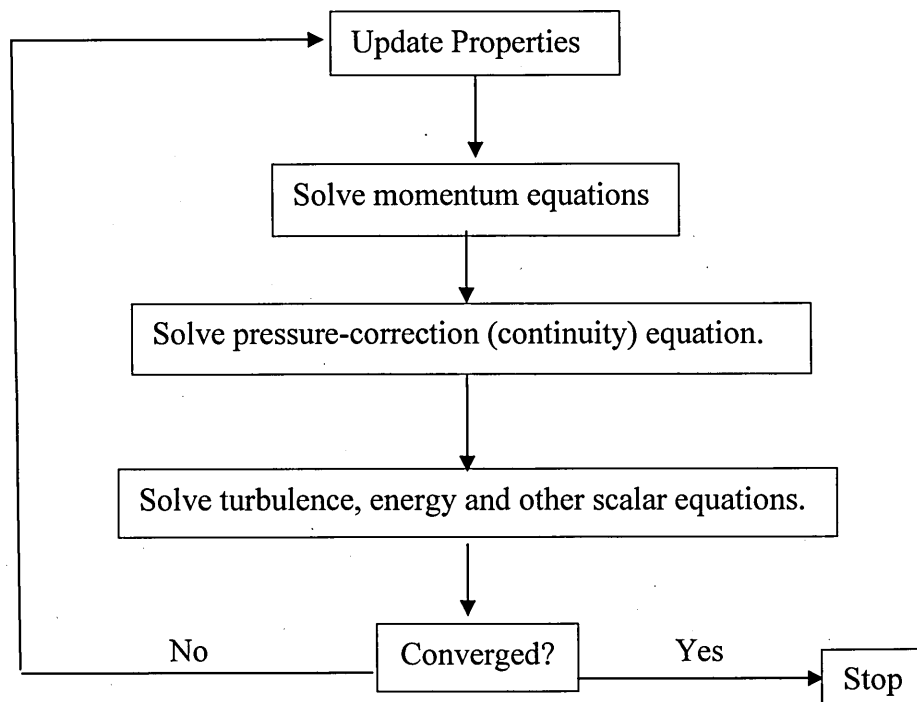
Figure 3-6: Segregated solution method [19].

Coupled Solver

The difference between segregate solver and coupled solver is that the conservation equations are solved sequentially. The details of the solver method are listed as follows:

1. Fluid properties are updated, based on the current solution. If the calculation has just begun, the fluid properties will be updated from the initialised solution.

2. The continuity, momentum, energy and species equations are solved simultaneously.

3. Where appropriate, equation for scalars such as turbulence and energy are solved using the previous updated values of the other variables.

4. A check for convergence of the equation set is made [19].

The solver sequence is shown in Figure 3-7.
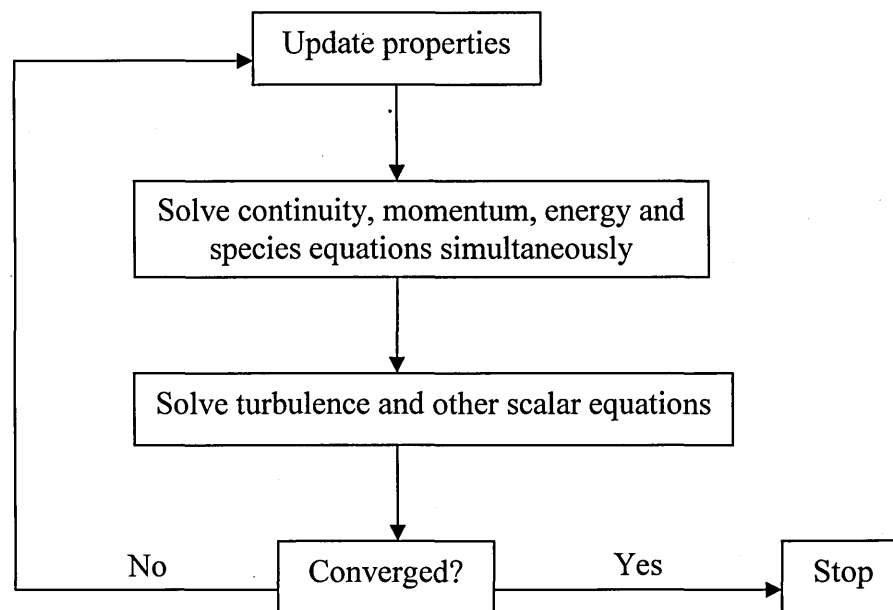
Figure 3-7: Coupled solver method [19].

These two solvers are non-linear solvers. Therefore, both methods are linearised using either implicit or explicit form to solve its variables. For a given variable, the unknown value in each cell in computed using both the existing and unknown values from neighbouring cells. This appeared to have two equations in the system. These equations must be solved simultaneously to give the unknown quantity, which is known as implicit [19].

Explicit form is known as at a given variable, the unknown value in each cell is computed using the relation that includes only existing values. In this case, only one equation in the system and the equations for the unknown values in each cell can be solved one at a time to give the unknown quantities [19]. In summary, segregate solver solve one variable for example momentum by considering all cells at the same time then solve another variable on all cells at same time again. Segregate solver can only use implicit linearisation on FLUENT code. Coupled solver with implicit form solves all variables for example pressure, velocity momentum in all cells at the same time. When coupled with explicit, it solves all variables one cell at a time.

Summary

This chapter introduced the theory behind CFD simulation. It covered the meshing methods and associated meshing assessment techniques such as mesh independent solutions. This chapter also introduced the numerical models utilised in this research. This research utilised FLUENT CFD codes in the numerical studies. The meshing options and solution algorithms of FLUENT CFD codes were also described in this chapter.

Chapter 4   Computational Fluid Dynamics (CFD)
Modelling

Introduction

A medium size heat exchanger on a current condensing boiler contains over 500 pins as depicted in Figure 1-3 in Chapter 1. It would be very complicated and inefficient if optimisation was carried out on the whole heat exchanger. Its complications would increase the simulation time, require more computing power and complex meshing making it difficult to achieve mesh independence. In order to avoid all these complications, this research considered a generic 4 x 4 staggered model. This model is considered to be the benchmark model. This chapter is focused on the methodology used from creating a physical domain of the generic model to the process of simulations. Topics covered in this chapter include:

1. Defining the physical domain
2. Creating the computational domain
3. Defining boundary conditions
4. Selecting solvers and equations
5. Solution convergence

4.1 Defining the Physical Domain

4.1.1 Circular Pins Setup

A benchmark model taken from a medium size current heat exchanger on a condensing boiler is used as the initial thrust for this research. A section view of the whole heat exchanger is shown in Figure 4-1. It is crucial to select a comparable benchmark model to represent the physical boundaries within the heat exchanger. As shown in Figure 4-1, a 4 x 4 staggered cylindrical pins model was created based on the actual heat exchanger's heat chamber size and water channel width. All sixteen pins are located inside the hot gas channel where the hot gas travels along the Y-axis as illustrated in Figure 4-2. The water inlet is positioned opposite the hot air channel to create counter-flow.
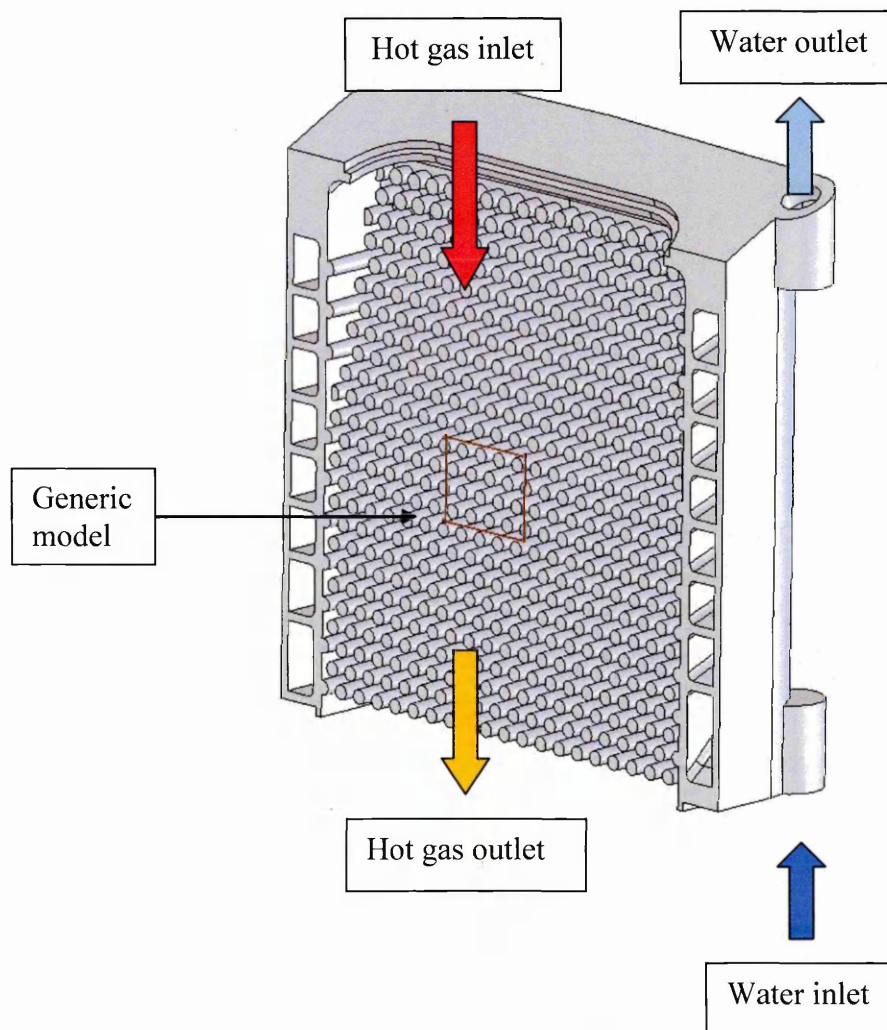
Figure 4-1: Section view of the whole heat exchanger.
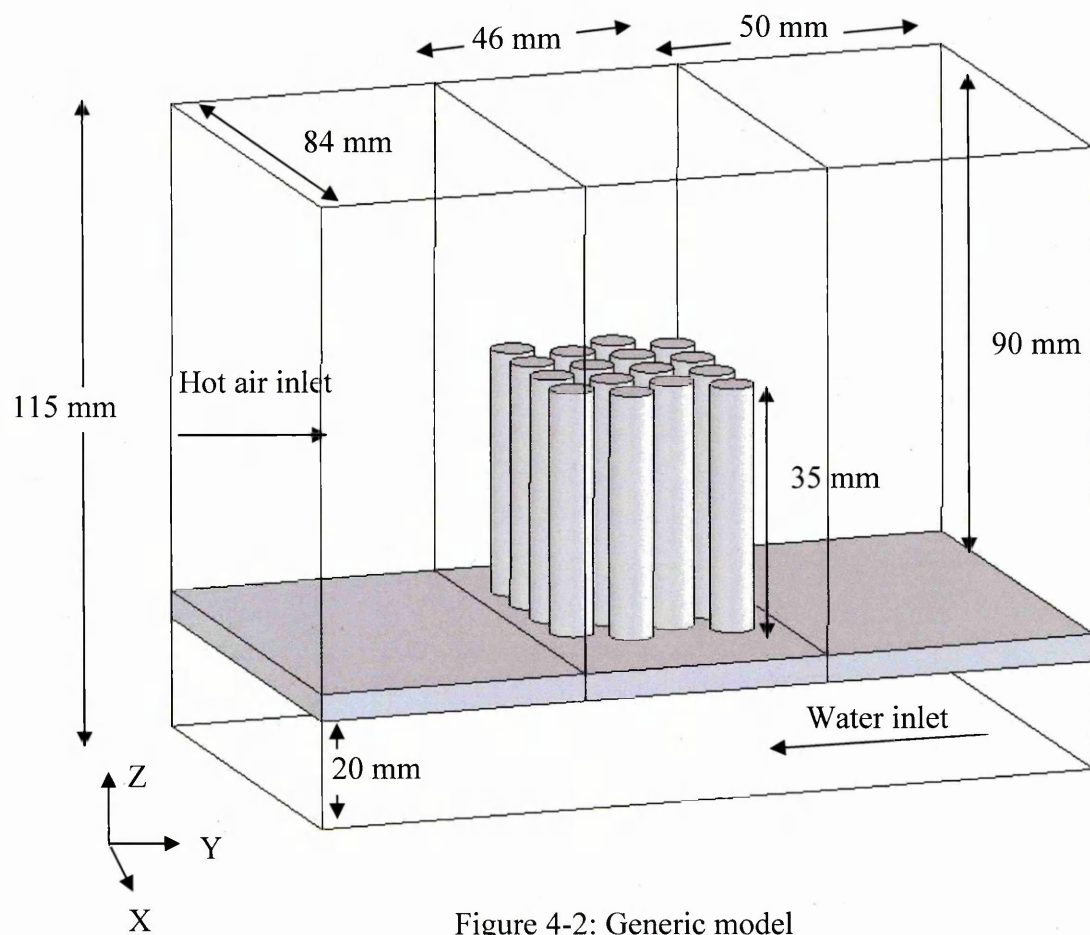
Figure 4-2: Generic model

Table 4-1: Benchmark model's geometric parameters

Model geometry	Dimensions
Pin spacing	11.00 mm
Pin pitch	9.50 mm
Pin diameter	8.00 mm
Pin height	35.00 mm
Plate length	46.00 mm
Plate width	84.00 mm
Plate thickness	5.00 mm
Hot air channel height	90.00 mm
Water channel height	20.00 mm

The benchmark model's physical parameters are given in Table 4-1. The pins' spacing is 11 mm and the pitch distance between rows is 9.5 mm. Pins' pitch is defined as the distance between two consecutive rows and spacing is defined as the distance between two pins as showed in Figure 4-3. The pins diameter and height is 8 mm and 35 mm, respectively. Previous related published works show that pins optimisation on heat sink is more sensitive on spacing rather than pitch distance. Hence, more longitudinal space is allocated for the plate length (X-axis).
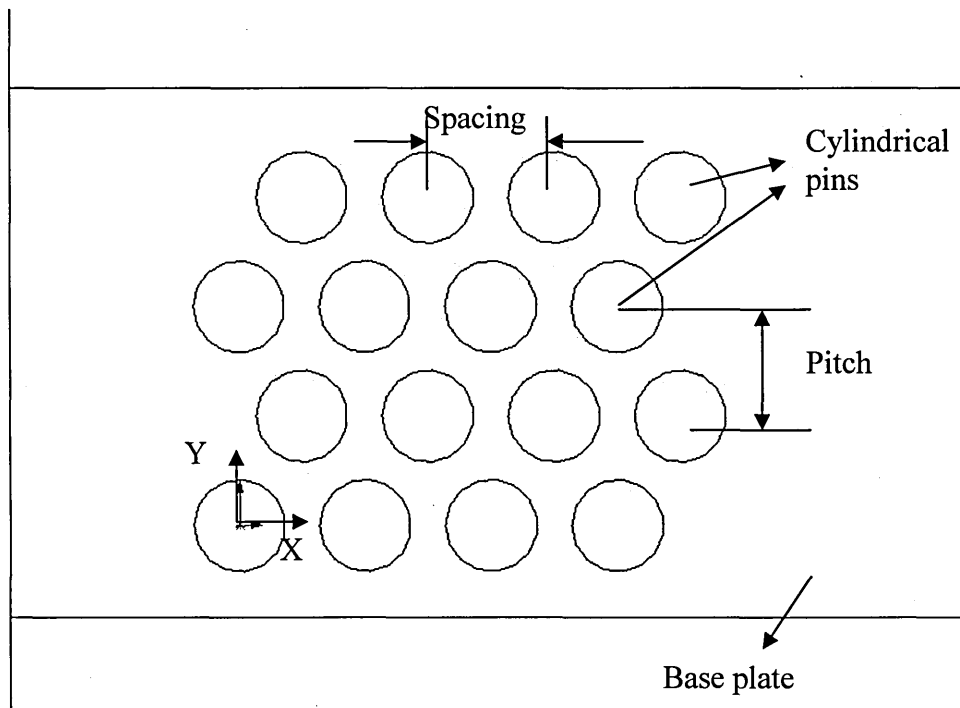
Figure 4-3: Pins' spacing and pitch distance

Based on the benchmark model, a further 12 models with different pins' spacing or pitch were created. Table 4-2 shows the spacing and pitch of each model. The first eight models have eight different spacing but they all maintain the same pitch distance as the benchmark model. The rest of the models as shown in Table 4-3 have four different pitch distances but maintain the same pins' spacing. The purpose of this arrangement is to distinguish the sensitivity of these two factors. It can be seen in Table 4-2 and Table 4-3 that the spacing and pitch distance are either increased or decreased in 1.5 mm steps. The model's names

45

were given based on either the change of pins' spacing or pitch distance. As shown in Figure 4-2, 50 mm clearance was designed to establish the flow boundary conditions across the plate. This would improve visualisation on the flow performance on the upstream and downstream of the group of pins.

All geometries are created using FLUENT pre-processor software called Gambit version 2.0.

Table 4-2: Eight models with different spacing

Model	Pin spacing (mm)	Pin pitch (mm)
S09.5	9.5	9.5
S12.5	12.5	9.5
S14.0	14	9.5
S15.5	15.5	9.5
S17.0	17	9.5
S18.5	18.5	9.5
S20.0	20	9.5
S21.5	21.5	9.5

Table 4-3: Four models with different pitch distance

Model	Pin spacing (mm)	Pin pitch (mm)
P06.5	11	6.5
P08.0	11	8
P11.0	11	11
P12.5	11	12.5

4.1.2 Elliptical Pins Setup

As part of this investigation, the thermal performance of elliptical pins is compared to the thermal performance of conventional circular pins. In order to compare the energy and flow performance of elliptical pins with circular pins, both models must have the same pins' volume. The elliptical geometry is measured according to its major and minor axis as illustrated in Figure 4-4. The eccentricity can be written as follow:

$$e = \sqrt{1 - \frac{b^2}{a^2}}$$
Equation 4-1
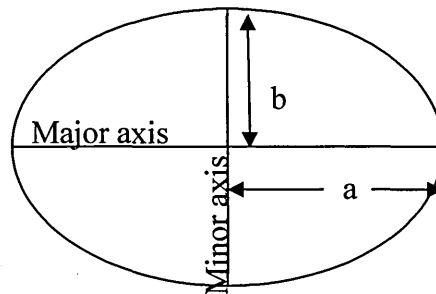
Figure 4-4: Ellipse and its mathematical properties.

Based on Equation 4-1, only four eccentricities were selected for comparison. The selected eccentricities are shown in Table 4-4. The elliptical model's names were given based on their major and minor axis.

Table 4-4: Elliptical models

Model Name	Major axis (a) mm	Minor axis (b) mm	Eccentricity (e)	Area (mm²)
Ellip(5.5, 2.9)	5.54	2.89	0.85	50.27
Ellip(6.4, 2.5)	6.40	2.50	0.92	50.27
Ellip(8.0, 2.0)	8.00	2.00	0.97	50.27
Ellip(10,1.6)	10.00	1.60	0.99	50.27

4.2 Creating the Computational Domain

Geometric meshing is an important process in CFD modelling. Unstructured mesh Advancing Front Method (AFM) is used to mesh all geometries. The meshing process is divided into three steps:

1. Creating surface meshing
2. Creating volume meshing
3. Mesh independent solutions

4.2.1 Creating surface meshing

All surface meshing was generated in Gambit. Triangular (Tri) mesh elements with Pave scheme were used on all models. This type of meshing scheme is widely used in different industries because it has no interval restriction on geometries vertexes or edges unlike Quad-Map meshing scheme which is restricted on certain faces and only suitable for mapping. On coarse mesh, the surface meshing skewness was between 0.44 and 0.47, which is within the tolerance scale.

4.2.2 Creating volume meshing

TGrid was used to complete the volumetric mesh. Unstructured tetrahedron type cells were used in volumetric meshing as shown in Figure 4-5. Most models were comprised of 874,000 - 3,216,000 cells. If a model had to be created for the whole heat exchanger, an acceptable mesh would have to contain approximately 10,000,000 cells.

2D Cell Types

Triangle   Quadrilateral

3D Cell Types

Tetrahedron   Hexahedron

Prism/Wedge   Pyramid
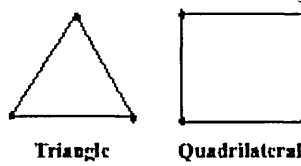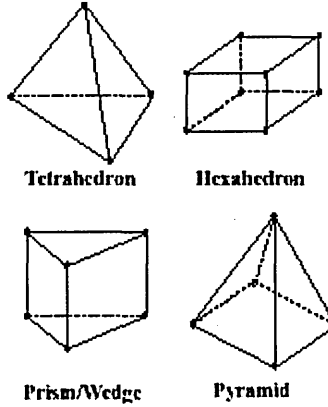
Figure 4-5: 2D and 3D cell types [24]

4.2.3 Mesh independent solutions

As mentioned in Chapter 3, the mesh independent process is a crucial task in CFD simulation. It can directly affect the results accuracy and computing time. In this research, combined mesh refinements and movement methods, also known as the *hr*-method was used in the meshing process. The *hr*-method was carried out separately on circular pin models and elliptical pin models. Figure 4-6 shows the circular pins mesh independent solution has been carried out based on the element size. The refinement process stopped at 874,00 cells, where the increase of the number of elements did not show any significant improvement in total energy transfer. The refinement process stopped when the total energy transfer deviation dropped to 2%.

Figure 4-7 shows the mesh independent solution has been carried out on elliptical pins based on different element size. Due to the extended surface area of elliptical pins, more cells were needed in the computational domain. The mesh independent process stopped at 3,216,00 cells, where total energy transfer deviation dropped to 2%.
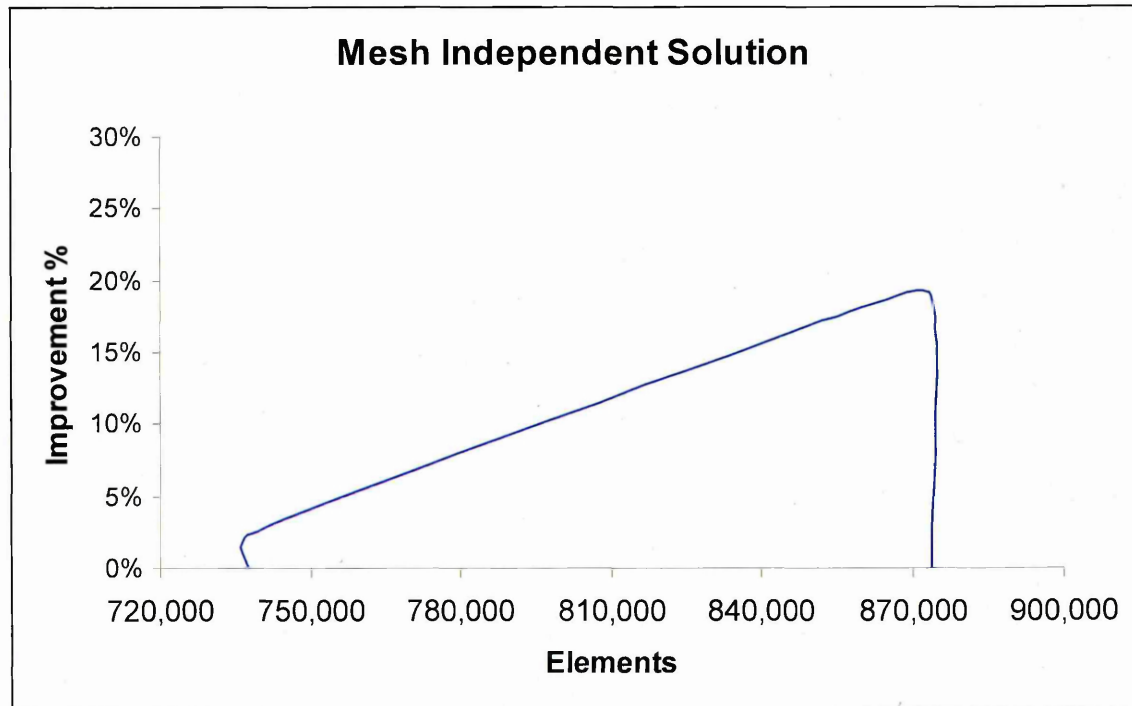
Figure 4-6: Circular pins mesh adaption
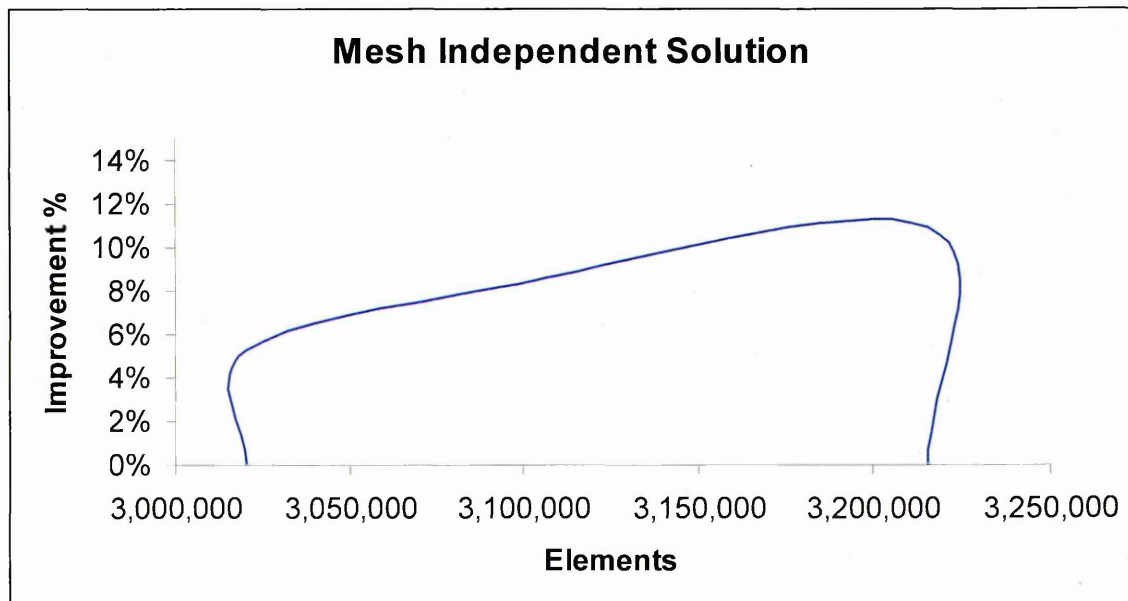
Figure 4-7: Elliptical pins mesh adaption

After performing the mesh independent method, the mesh quality was examined and considered to be fine enough to represent the geometry. Figure 4-8 and Figure 4-9 illustrates the mesh quality near the circular and elliptical pins. The average skewness of all the models is approximately 0.33.
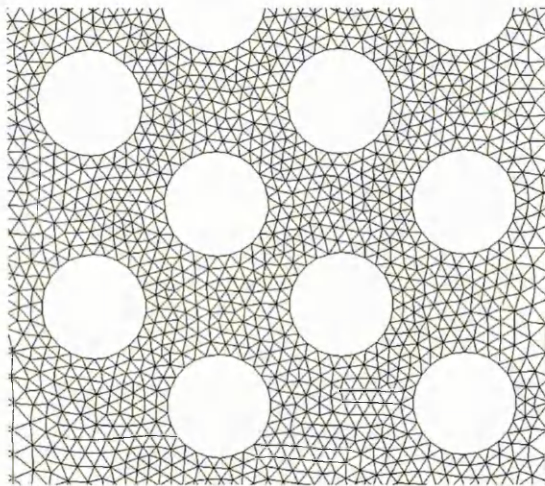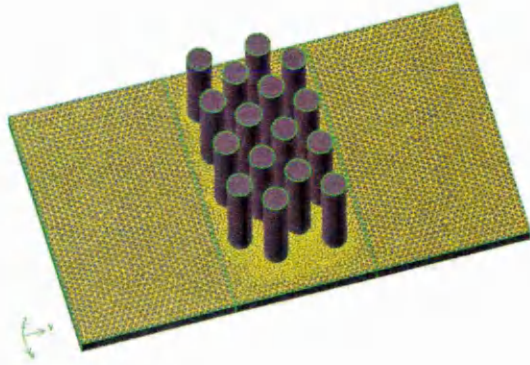
Figure 4-8: Mesh near circular pins
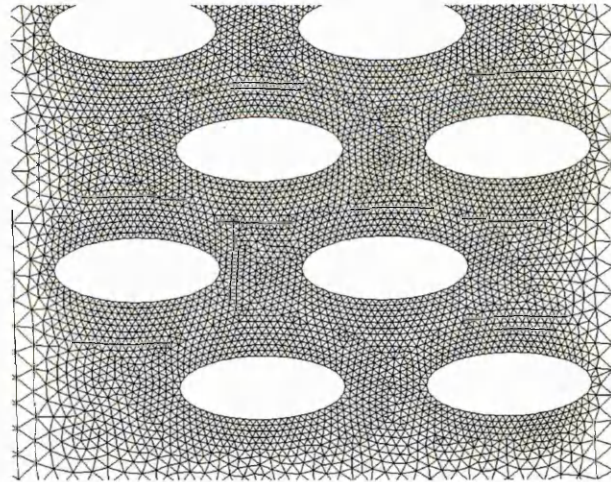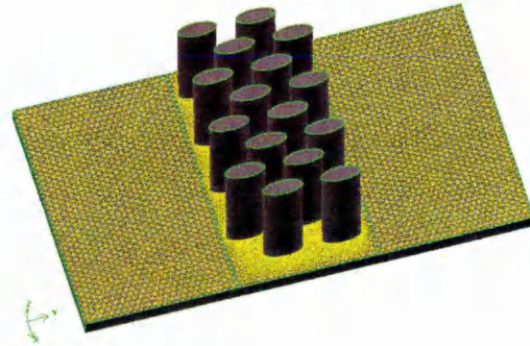
Figure 4-9: Mesh near elliptical pins

4.3 Defining Boundary Conditions

Boundary conditions must be specified before any simulation process can be carried out. The input values depend on the data that the user has. Initial values can be acquired from experimental tests or numerical calculations. In enforcing boundary conditions for the models used, most values were taken from experimental tests based on current heat exchangers. On all simulations, the following assumptions have been made:

1. The flow is steady-state and three-dimensional.
2. Wall and pin surfaces are smooth surfaces.
3. The flow is fully developed in both gas and water channel.
4. No structure transformation or phase change.

In this study, DirectMetal 20 was selected as the pins material in order to compare the numerical results with the experimental results. Hot air has been selected as the heat source and water as the heat carrier. The details of the used boundary conditions are given in Table 4-5.

Table 4-5: Initial boundary conditions

Boundary Conditions	Values
Hot air inlet velocity	4 m/s
Hot air temperature	473.5 K
Water mass flow rate	8.31×10^{-3} kg/s
Water inlet temperature	290.5 K
Gas channel hydraulic diameter	0.087m
Water channel hydraulic diameter	0.032 m

Hot air inlet velocity was set at 4 m/s on all models. The hot air inlet temperature was set at 473.5 K.

A pump has to overcome the pressure loss through the central heating system. In this study the benchmark model's water channel is relatively small in comparison to a heat exchanger channel. Therefore, smaller water mass flow rate is used in all generic models. The water

mass flow rate was set at 8.31×10^{-3} kg/s and the water inlet temperature was set at 290.5 K.

For laminar flow, the exact equations of continuity and momentum can be solved directly. For turbulent flow, using both equations directly can cause the results to be relatively insensitive. However, there are many methods to specify the turbulent quantities. For example turbulence intensity, turbulence, ratio, hydraulic diameter and turbulence length scale. This research used hydraulic diameter to specify each model's turbulence quantities. The hydraulic diameter equation, Equation 3-20 is given in Chapter 3. Hydraulic diameter of hot air channel can be calculated as follows:

Known, hot air channel height is 90 mm and width is 84 mm,

Hot air flow area can be calculated as:

$$Area_{(air)} = 84 \times 90 = 7560 mm^2 \qquad\qquad \text{Equation 4-2}$$

and the wetted perimeter at the channel is:

$$Perimeter_{(air)} = 2 \times (84 + 90) = 348 mm \qquad\qquad \text{Equation 4-3}$$

The hot air hydraulic diameter can be determined by substituting Equation 4-1 and 4-2 into Equation 4-1 and thus;

$$D_h = \frac{4 \times inlet\ area}{wetted\ perimeter} \qquad\qquad \text{Equation 3-20}$$

$$D_{h(air)} = \frac{4 \times 7560}{348} = 87 mm \approx 0.087 m$$

Known that, the water channel is 20 mm deep and 84 mm wide,

The water channel inlet area can be calculated as below:

$$Area_{(water)} = 20 \times 84 = 1680mm^2$$
<div align="right">Equation 4-4</div>

and the wetted perimeter at the channel is:

$$Perimeter_{(water)} = 2 \times (20 + 84) = 208mm$$
<div align="right">Equation 4-5</div>

The water channel hydraulic diameter can determined by substituting Equation 4-4 and 4-5 into Equation 3-20 and thus;

$$D_{h(water)} = \frac{4 \times 1680}{208} = 32mm \approx 0.032m$$

4.4 Selecting Solvers and Equations

Choosing an adequate solver for a particular flow problem is very important in fluid flow modelling. Segregate implicit solver is selected to study all flow phenomena on each model. This solver is more accurate for this particular flow in comparison to the coupled solver. Several equations were used to govern along with the solver. The equations used in this modelling process are:

1. Continuity equation.
2. Momentum conservation equation.
3. Navier-Stokes equations.
4. Kinetic and epsilon transport equation.
5. Energy equation.

4.5 Solution Convergence

The accuracy of CFD modelling results depends on three factors and they are:

1. Consistency
2. Stability
3. Convergence

Consistency is the selected numerical schemes, for example the segregate solver produces systems of algebraic equations which can be demonstrated to be equivalent to the original governing equation as the grid size and time step approach zero [23]. Stability is dependent on the numerical scheme used. Inappropriate solver, even round off, errors can cause wild oscillation or divergence of the solutions. Convergence is the term for a numerical method using iterations to produce a solution of the grid whereby the error approaches zeros. In this research, all model solutions converged after approximately 450 iterations. The convergence criteria on all models were below 1×10^{-4} and 1×10^{-6} on the energy equation.

Summary

In order to achieve accuracy of computational results with minimum computing power, this research utilised a generic model taken from a section of a current high performance heat exchanger. A 4 x 4 pins model was used to study the optimum pins' spacing and pitch distance at given flow conditions. Elliptical pins were also used in this research to study the heat transfer and pressure difference across the pins.

This chapter also described the meshing process used. The process started with surface meshing then volume meshing. After the initial mesh was created, a mesh independent method was used to ensure that the total energy transfer deviation is reduced to 2 %. Details of the boundary conditions were also given in this chapter. The specific solver and equations used in the numerical simulation were listed in the chapter. All simulation processes were carried out until the solutions convergence factors of 1×10^{-4} and 1×10^{-6} on energy equation, were achieved.

Chapter 5   Thermal Wind Tunnel Design

Introduction

The process of manufacturing a compact heat exchanger usually obliges long lead time and money. Due to the compact size of the heat exchanger, experimental results are very difficult to acquire. This research engaged on designing and commissioning a purpose built Thermal Wind Tunnel (TWT). Solely, to carry out experimental tests on different generic heat exchanger pin configurations in a controlled environment.

A wind tunnel is a research tool designed to study the effects of controlled moving fluid flow over and around solid objects. Every wind tunnel is designed and constructed to suit a certain application. There are many types of wind tunnel built around the world. They can be classified according to the prevailing average velocity as follows:

1. Subsonic.
2. Transonic.
3. Supersonic.
4. Hypersonic [25].

Wind tunnels can be built in two types of configurations. Namely, open loop or closed loop wind tunnels. Open loop wind tunnels draw air by fan through a contraction, test section and a diffuser all in a straight line. In general, an open loop wind tunnel is cheaper to build, but it is sensitive to its air entry conditions. Open loop wind tunnels suffer from the entry conditions because of the way air is being sucked in or blown out from the wind tunnel.

A closed loop wind tunnel re-circulates air inside the tunnel. Therefore requires more sections to form a loop. It is clear that a closed loop wind tunnel is usually more expensive to build. However, the advantages of a closed loop wind tunnel are significant. A closed loop wind tunnel provides more accurate results than an open loop wind tunnel because the flow quality can be controlled by turning vanes and screens.

56

This chapter explains the design parameters and requirements of the TWT. The design of the TWT started with a series of numerical calculations based on Bernoulli's equation. Guided by the numerical calculations, a three dimensional computational model was created to simulate the flow inside the wind tunnel. The flow simulation is based on the finite volume technique as implemented in Chapter 3 using the commercial CFD code FLUENT version 6.2. The TWT air flow is modelled using the k-ε transport equation. The 3D model consists of 390,000 tetrahedral cells dense model. Each section is then optimised to reduce the pressure loss and enhance the flow uniformity along the section. With the aid of the CFD tool, the 16 heaters were positioned in the most suitable section of the tunnel to maximise the heaters performance and minimise its impact on the air flow quality.

5.1 Thermal Wind Tunnel Design Parameters and Requirements

The TWT is designed to investigate the performance of the heat exchanger. When designing the tunnel features, an intensive survey of standard recommended practices and tests published by different organisations was made [26 -54]. The TWT design parameters, flow requirements and previous practices defined the expected tunnel capabilities as follows:

1. Closed loop wind tunnel.
2. Uniformity of the test section air velocity.
3. Heating elements selection.
4. High temperature bifurcated fan.
5. Specimen observation windows.
6. Water channel assembly and test section accessibility.
7. Tunnel insulation.

5.1.1 Closed loop wind tunnel

After surveying previous related publications, the decision was made to design a closed loop wind tunnel for this research. A closed loop wind tunnel is more efficient and able to provide more accurate test results than an open loop wind tunnel. Furthermore, a closed loop wind tunnel is more efficient to maintain the hot air temperature inside the TWT. Due to laboratory space restriction, the TWT was designed to operate in the vertical position. Figure 5-1 illustrates the CAD model of the vertical TWT with flow moving in a clockwise direction.
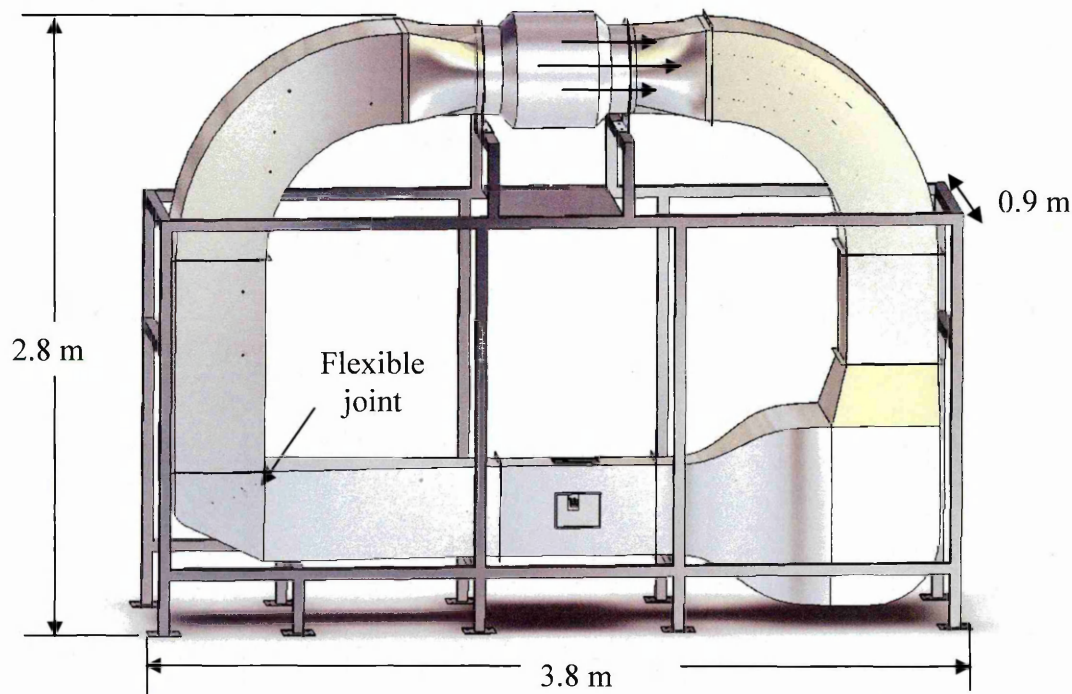
Figure 5-1: Vertical closed loop thermal wind tunnel

The TWT is fabricated from 1 mm, 305-grade stainless steel in order to sustain the elevated temperature levels. The wind tunnel is joined together in 13 sections and each section was connected using flanges at both ends. A flexible joint is made between the diffuser and third corner to accommodate the thermal expansion. The TWT is 3.8 m long × 2.8 m height × 0.9 m wide.

5.1.2 Uniformity of test section air velocity

All sections were carefully designed based on continuity equation and Bernoulli's equation to achieved 4 m/s air velocity at the test section. The design optimisation includes using wire mesh to straighten the air flow at the upstream of the test section.

5.1.3 Heating elements selection

The main requirements of the heating elements are capable to raise the air temperature inside the tunnel at a rate of 1°C every 10 seconds and the uniformity of heat distribution. The power required to raise the air temperature inside the tunnel was calculated using Equation 5.1 to 5.3. Several different types of heating elements were taken into consideration namely, a drum heater and a tubular element. Tubular elements were chosen in this research as they provide better heat distribution and efficiency for forced convection due to the additional surface area provided by the fins.

Power required to raise the air temperature:

$$q_1 = \frac{m \times Cp \times \Delta T}{t} \times 0.2778 \qquad \text{Equation 5-1}$$

Where,

m is mass of air to be heated

C_p is the specific heat capacity of the fluid

ΔT is the temperature difference

t is temperature rise time

Power required to overcome heat loss on surface area:

$$q_2 = U \times A \times \Delta T$$ Equation 5-2

Where,

U is the overall heat transfer coefficient,

A is the wind tunnel surface area

ΔT is the temperature difference.

Total power required to maintain the air temperature:

$$Q = q_1 + q_2$$ Equation 5-3

A total of 16 tubular heating elements were used to raise and maintain the air temperature inside the wind tunnel. Each element is 200 mm long with 24 mm diameter fins along the element and it provides approximately 974 W of energy. Figure 5-2 shows the actual dimension of the heating element. At the end of each element is a ¼″ BSP male compression fitting, which is utilised to secure the element to the tunnel duct work as shown in Figure 5-3.

Figure 5-2: Tubular heating element φ 9.53 mm x 200 mm long

Figure 5-3: 1/4″ BSP female lock nut fitting

5.1.4 High temperature bifurcated fan

Due to the extreme air temperatures inside the tunnel, a bifurcated fan was used to circulate the air inside the tunnel. Figure 5-4 shows the bifurcated fan used on the TWT. The bifurcated fan was from aluminium and powered by a 1.1 kW three phase AC motor. Figure 5-4 shows that the middle section has been enlarged to minimise the restriction of air flow. The casing ensures that the belt and the motor are isolated from the air stream as shown in Figure 5-5. The motor sits on top of the flow isolation chamber, which passes all the way through the casing. This ensures unrestricted air movement for motor cooling and easier for servicing. The fan performance graph can be found in Appendix A.
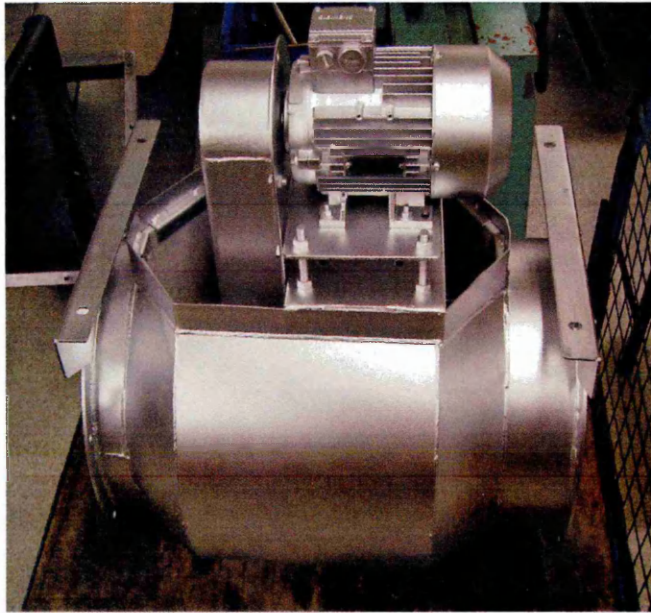
Figure 5-4: Bifurcated fan

Flow isolation chamber
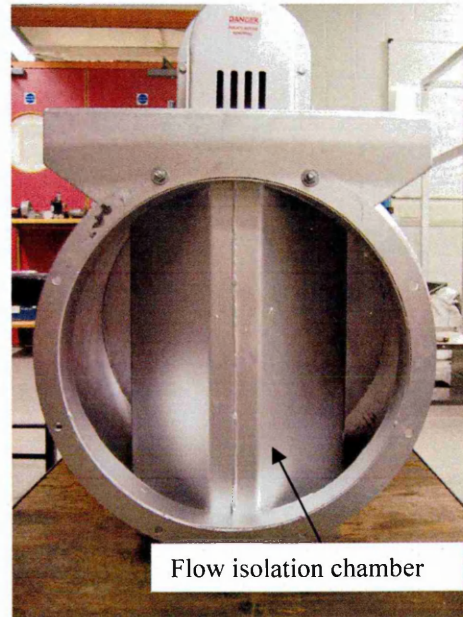
Figure 5-5: Side view of bifurcated fan

5.1.5 Specimen observation windows

Two observation windows were used to monitor the test specimen. Figure 5-6 shows the positions of the observation windows at the test section. The first observation window is 100 mm wide × 200 mm long, mainly to allow light through the test section area. The second observation window is 150 wide × 200 mm long and it can be used for flow and specimen monitoring.

Both windows were covered by 5 mm thick high temperature ceramic glass as shown in Figure 5-7. Each ceramic glass has a working temperature up to 700°C, which is also very resistant to differential temperature. Both ceramic glasses were secured in the window frame as shown in Figure 5-6.

Figure 5-6: Flow observation windows
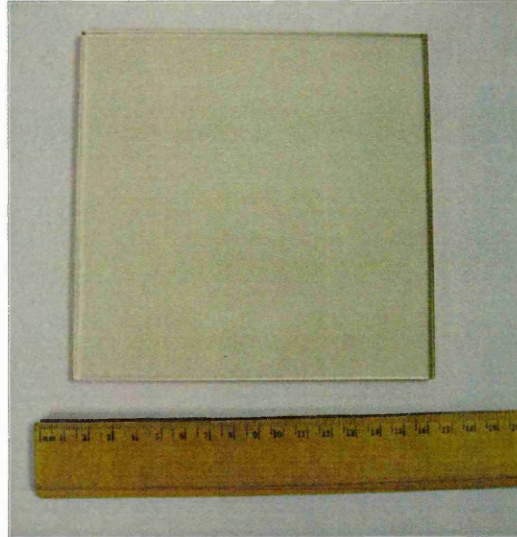
Figure 5-7: 5 mm thick ceramic glass

5.1.6 Water channel assembly and test section accessibility

Figure 5-8 illustrates the specimen access window. Each specimen was sealed using high temperature sealant on the water channel side. The water channel is assembled on the test section and secured by a mechanical clamp. Figure 5-9 shows the water channel in place on the test section.
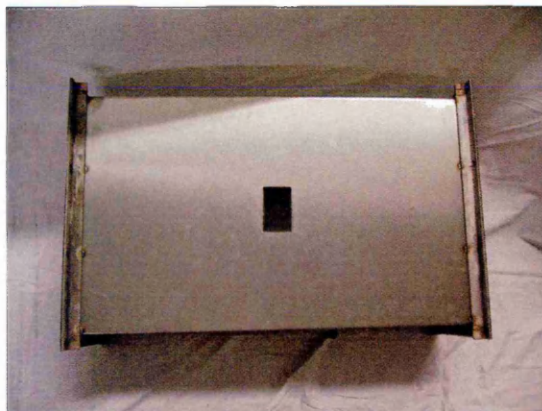
Figure 5-8: Specimen access window
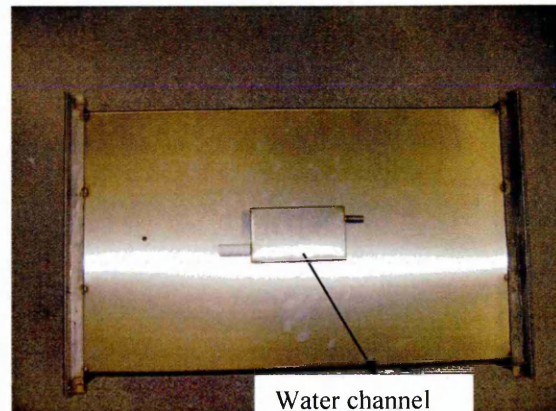
Water channel

Figure 5-9: Water channel in position

5.1.7 Tunnel insulation

In order to maintain the working air temperature inside the tunnel, two layers of insulation were wrapped around the tunnel exterior. The first layer of insulation utilised a Silicate wool blanket. It contained a pure raw material of Calcium-Magnesium Silicate and is specially designed to operate in high temperature applications. The wool blanket has a unique maximum operating temperature of 1100°C. A 6 mm thickness with density of 96 kg/m^3 Silicate wool blanket was used as the first layer of insulation.

The second layer of insulation utilised Rockwool industrial wired mat insulation. Its flexibility made it excellent for irregular surfaces. It has a 25 mm galvanised wire mesh stitched on one face so each piece was weaved together using soft iron wires. The industrial wire mat has a maximum operating temperature of 600°C. All sections including the bifurcated fan were insulated with a 50 mm thickness of industrial wired mat insulation as depicted in Figure 5-10. In order to protect the insulation from dust, a thin aluminium foil was used to wrap on the outside surface of the insulation as shown in Figure 5-11.

Figure 5-10: Industrial wire mat insulation without the protection foil

Figure 5-11: Tunnel insulation with protection foil

5.2 Thermal Wind Tunnel Design

The tunnel design started with a series of numerical calculations and then optimised using the CFD code, FLUENT version 6.2. The entire TWT is made up of 13 sections. Figure 5-12 shows an exploded view of the complete TWT. The TWT consist the following sections:

1. Annular inlet
2. First corner
3. Upstream straight duct
4. Expansion duct
5. Second corner
6. Contraction
7. Test section
8. Diffuser
9. Third corner
10. Downstream straight duct
11. Fourth corner
12. Annular outlet
13. Bifurcated fan
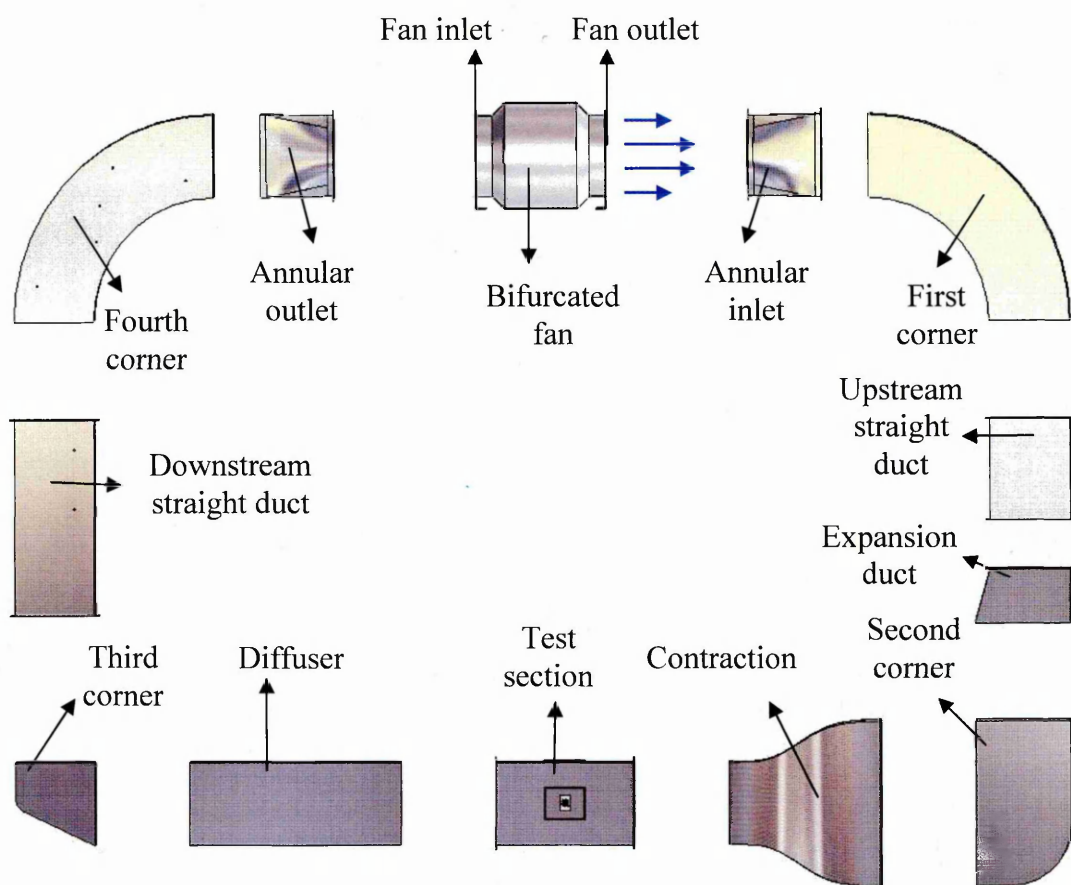
Figure 5-12: Exploded view of each section of the TWT

The pressure head loss was calculated from each section of the tunnel. The whole TWT total pressure loss is then used to determine the fan's specification. The purpose of the fan in the wind tunnel is to overcome the net pressure loss experienced by the air as it flows around the tunnel at the desired TWT average air velocity.

Figure 5-12 illustrates that the air flows in clockwise direction. Air first enters the annular outlet then past a 90° smooth bend into the upstream straight duct. Later, air flows into the expansion duct and settles down at the second corner before entering the three dimensional contraction section. A fine wire mesh was positioned between the contraction and the test section to straighten the flow.

Soon after the test section, the disturbed flow is then discharged through the diffuser into the third corner. Finally, cooled air is reheated at the downstream straight duct and the fourth corner, where heating elements were positioned, before entering the annular inlet.

5.2.1 Numerical calculations

The wind tunnel's design was based on energy equation and continuity equation. Bernoulli's principle states that for an incompressible ideal fluid, the increase in velocity occurs simultaneously with the decrease in pressure or change in the fluid's gravitational potential energy [55]. Applying Bernoulli's equation between fan inlet and outlet as depicted in Figure 5-12:

$$\frac{P_o}{\rho} + \frac{v_o^2}{2} + gz_o = \frac{P_i}{\rho} + \frac{v_i^2}{2} + gz_i + h_{o-i} \qquad \text{Equation 5-4}$$

Where,

P_o is the pressure head at fan outlet,

v_o is the outlet velocity,

P_i is the pressure head at fan inlet,

v_i is the inlet velocity

ρ is the local density

h_{o-i} is the sum of total pressure head loss between fan outlet and inlet

Known that $z_o = z_i$, $\frac{v_o^2}{2} = \frac{v_i^2}{2}$ and substituting into Equation 5-4

$$\therefore \quad \frac{P_o}{\rho} = \frac{P_i}{\rho} + h_{o-i}$$

$$h_{o-i} = \frac{P_o - P_i}{\rho}$$

Equation 5-5

The required fan power P_a can be obtained from the calculated total pressure head written as follow:

$$P_a = \rho \times Q \times h_p$$

Equation 5-6

Where,

ρ is the fluid density,

and Q is the air volume flow rate.

5.2.2 TWT preliminary calculation summary

The pressure head loss of each TWT section is summarised in Table 5-1. The table shows equations used on each section and its particular pressure loss coefficient. The table also presents the pressure head loss, with and without guide vanes. The calculation summarised that the TWT total pressure loss encountered within the tunnel is 70.88 Pa. The details of each section's calculation and fan's performance graph can be found in Appendix B and C.

Table 5-1: TWT net pressure loss calculation summary

Duct Section	Equation Used for Pressure Loss Calculation	Pressure Loss Coefficient k /with vanes	Pressure Head loss (m) without Guide Vanes	Pressure Head Loss (m) with Guide Vanes
Annular inlet	$$P_1 - P_2 = \dfrac{Q^2 \times \rho \times \left[1 - \left(\dfrac{A_2}{A_1}\right)^2\right]}{2 \times A_2^2}$$	N/A	0.17	0.17
Upstream wire mesh	$h = k \times \dfrac{v^2}{2g}$	0.48	0.47	0.47
First corner	$h = k \times \dfrac{v^2}{2g}$	0.15/ 0.14	0.03	0.03
Upstream straight duct	$h = k \times \dfrac{v^2}{2g}$	1.0	0.22	0.22
Expansion duct	$h = k \times \dfrac{v^2}{2g}$	0.99	0.22	0.22
Second corner	$h = k \times \dfrac{v^2}{2g}$	1.02	0.06	0.06
Contraction	$$\Delta p = \frac{1}{2}\rho v_{in}^2 \left[\left(\frac{A_{inlet}}{A_{outlet}}\right)^2 - 1\right]$$	N/A	0.75	0.75
Test section wire mesh	$h = k \times \dfrac{v^2}{2g}$	0.37	2.08	2.08
Test section	$h = k \times \dfrac{v^2}{2g}$	0.97	0.79	0.79
Diffuser	$h = k \times \dfrac{v^2}{2g}$	0.44	0.34	0.34
Third corner	$h = k \times \dfrac{v^2}{2g}$	0.98/ 0.13	0.22	0.03
Downstream straight duct	$h = k \times \dfrac{v^2}{2g}$	1.0	0.22	0.22
Downstream wire mesh	$h = k \times \dfrac{v^2}{2g}$	0.48	0.47	0.47
Fourth corner	$h = k \times \dfrac{v^2}{2g}$	0.15	0.03	0.03
Annular outlet	$h = k \times \dfrac{v^2}{2g}$	0.36	0.14	0.14
Total pressure loss in meter :			6.21	6.02
Known that, $P = \rho g h$ Total pressure loss in Pascal :			73.13	70.88

5.2.3 CFD optimisation

A commercial CFD code was used to aid the TWT design optimisation. Based on the initial calculation, the TWT geometry was first created in Gambit version 2.0. After that, the model was solved in FLUENT version 6.2. The main objective of the design optimisation was to enhance the flow quality at the test section. The design started without using any guide vanes or wire mesh screens. Figure 5-13 illustrates the middle plane pressure contours of the initial design. Uneven flow occurred at the first corner and reoccurred at the lower section of the contraction. This occurrence can directly affect the air flow quality at the test section as depicted in Figure 5-13. Figure 5-14 shows a large recirculation occurred at the down stream of the third corner and this is due to the inner 90° sharp bend.
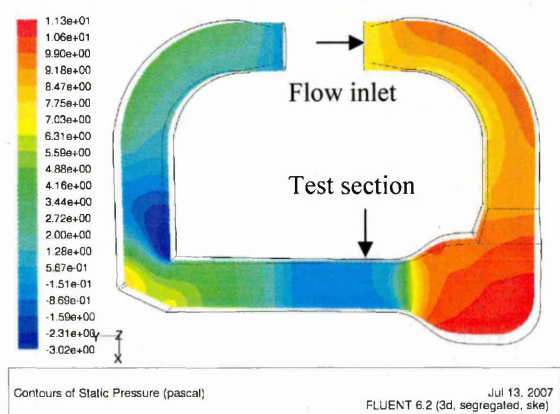
Figure 5-13: TWT without guide vanes and screens (pressure contours)
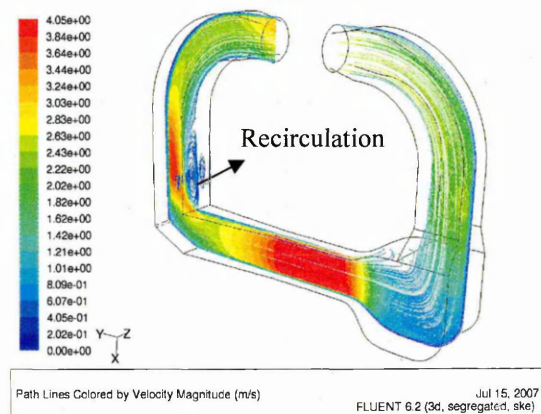
Figure 5-14: Velocity magnitude of the initial TWT design

In order to improve the air flow quality and minimise the pressure head loss, guide vanes were added at the first and third corners to enhance the air flow quality. Three guide vanes were installed in the first corner to enhance the flow quality around the bend as depicted in Figure 5-15. The figure shows that the guide vanes have improved the air flow quality at the first corner in comparison to Figure 5-13. In addition, the high pressure loss at the contraction was reduced.

69

As illustrated in Figure 5-15, 13 guide vanes were added into the third corner to direct the air flow through the bend. The additional vanes also discharged the large recirculation that occurred on the first design. The drawback of this design is that due to high quantity of air settled at the settling zone, large eddy flow started to occur at the inlet of the contraction as shown in Figure 5-16. This could affect the performance of the contraction. In order to reduce the large eddy at the settling zone, a wire mesh was added between the contraction outlet and test section. The wire mesh was modelled as a porous jump.
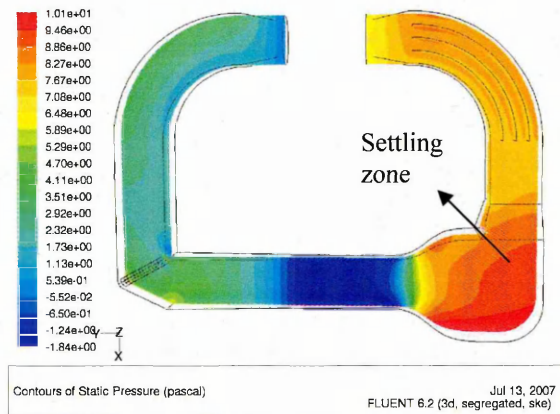
Figure 5-15: TWT design with guide vanes in first corner and third corner
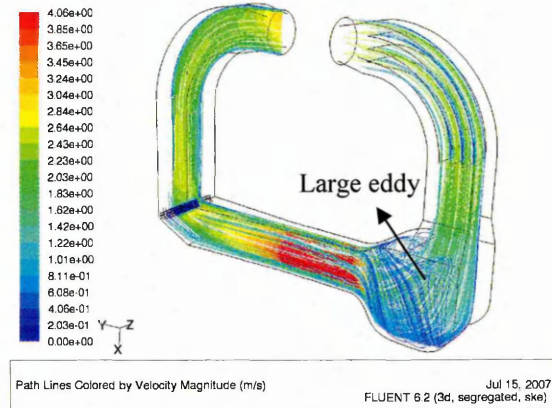
Figure 5-16: Large eddy occurred at settling zone

The final TWT design utilised additional wire mesh screen at the specific areas to straighten the air flow. The selected wire mesh diameter was 1.20 mm with 6 mm aperture. Three sets of wire mesh screens were added in the tunnel. The first wire mesh screen was placed between the annular inlet and the first corner. The second set of the wire mesh screen was placed between the contraction and the test section and the final set of wire mesh screen was located between the fourth corner and the annular outlet. Figure 5-17 illustrates the middle plane pressure contour across the TWT. The figure shows that pressure distribution is more uniform at the contraction and at the test section. The purpose of first set of the first wire mesh screen was to straighten the air flow due the construction of the bifurcated fan. The second set of wire mesh screen reduced the air velocity at the settling zone and straightens the air flow at the up stream of the test section. The purpose of the last set of wire mesh screen was to protect the fan in case of any loose debris within the

70

tunnel. Figure 5-18: illustrates the velocity magnitude across the whole TWT. It can be seen the wire mesh screen has taken the effect of settle down the air flow at the settling zone.
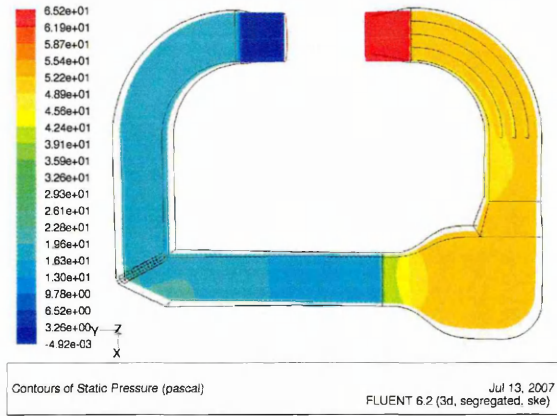
Figure 5-17: Final design of TWT with guide vanes and wire mesh screens
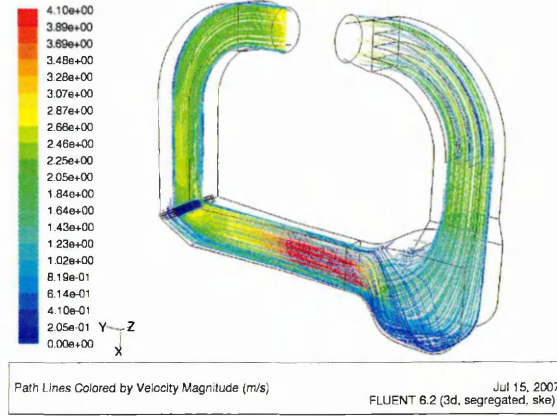
Figure 5-18: Velocity magnitude of the TWT

5.2.4 Tunnel air quality

The coefficient of uniformity is used to determine the quality of air velocity distribution at the TWT test section. The equation of coefficient of uniformity can be written as follows:

$$C_u = \left(V_{max} - V_{min}\right)/V_{avg} \qquad\qquad \text{Equation 5-7}$$

Where,

V_{max} is the maximum air velocity,

V_{min} is the minimum air velocity,

V_{avg} is the average air velocity.

The closer the value is to zero, the more uniform the air flow distribution. The design objective is to minimise the C_u to the lowest possible value. Table 5-2 shows the velocity coefficient of uniformity of each design. All values were recorded 150 mm from the test section inlet. It can be seen the first design has less uniformity at the test section due to uneven flow across the tunnel. With the advantage of guide vanes, the flow uniformity coefficient has been reduces to 0.13 as shown in Table 5-2. The final design shows that the coefficient of uniformity calculated at the test section is reduced to 0.07.

Table 5-2: Coefficient of uniformity of each design

	Vmin (m/s)	Vmax (m/s)	Vavg (m/s)	Cu
Design 1: without vanes and mesh screen	3.46	3.99	3.89	0.14
Design 2: with guide vanes only	3.52	4.03	3.90	0.13
Design 3: with guide vanes and mesh screens	3.67	3.95	3.89	0.07
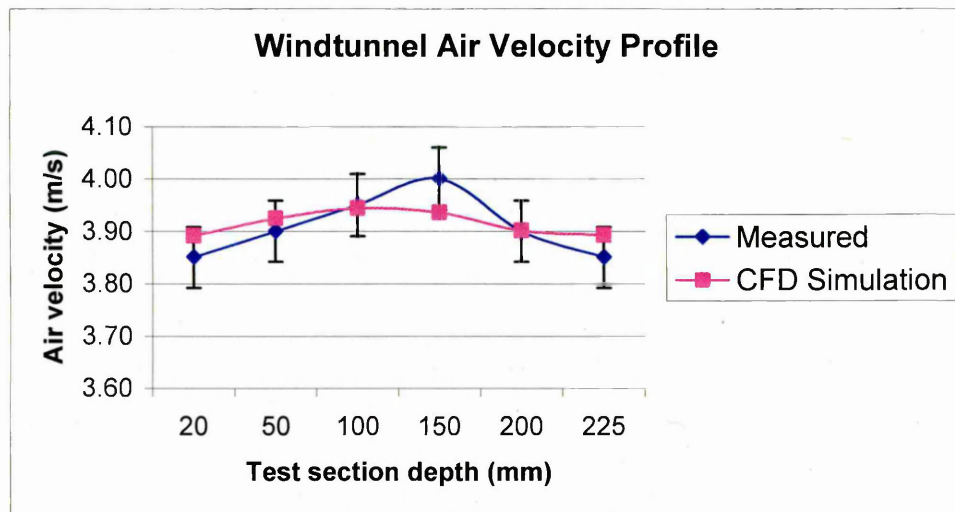
Figure 5-19: Wind tunnel air velocity profile

Figure 5-19 illustrates the wind tunnel air velocity profile measured using a Testo 521-3 meter with pitot tube measuring apparatus compared with the CFD simulation prediction. The figure shows that the numerical prediction is relatively close to the measure air velocity profile.

Summary

This chapter described the design parameters and requirements for the TWT. The design parameters including the temperature rise time and insulation were described in the chapter. The TWT was designed based on Bernoulli's equation and continuity equation. After a series of calculations, the design was optimised using the CFD tool to study the velocities uniformity at the test section. Guide vanes and wire meshes were utilised in the design of the TWT to achieve better flow uniformity.

Chapter 6   Specimens and Equipment

Introduction

This chapter introduces the design and manufacturing process of the test specimens. With the intention of validating the simulation results, all specimens were built identical to the numerical models. Six specimens were built to analyse against the numerical models. The chapter then introduces the Laser Sintering Technology and its use in building the tests specimens. This chapter also introduces the material properties of the specimens. All specimens were made out of DirectMetal 20 powder.

The chapter later introduces the equipment utilised in the experimental tests. Each equipment's operating principle was also introduced in this chapter. Before carrying out any experimental tests, specimen preparation and pressure testing process must be carried out. This chapter describes how to prepare the specimen for experimental testing. To ensure no water leakage from the water channel, the pressure testing process was carried out before the experimental test.

6.1 Specimen Geometry

All specimens were first numerically created in Gambit, the FLUENT pre-processor. In order to validate the simulation results, all specimens were manufactured using identical dimensions as the numerical models. Figure 6-1 illustrates the benchmark CAD model. The specimen consists of 16 pins with 8 mm in diameter and 35 mm in height. All 16 pins were manufactured on 54 × 84 mm base. In order to firmly secure the specimen on the test section, a 2 mm step was created on the 5 mm thick pins' base as shown in Figure 6-1. Due to the manufacturing technique requirement, the pins diameter to height ratio was over the recommended range, to firmly retain the pins on the base. Therefore a 65° chamfer angle was generated at the root of each pin.

Four models were selected for manufacturing and validation. The four models are:

1. Benchmark model
2. Model S18.5
3. Model Ellip(8.0, 2.0)
4. Model Ellip(10.0, 1.6)

As illustrated in Figure 6-1, each model has six circular channels in different row of pins to internally route in the thermocouples for temperature measurement. The thermocouple channels have a 2 mm diameter and are 35 mm deep from the base into the core of the selected pins.

Figure 6-1: Benchmark CAD model.

6.2 Specimens' Manufacturing Process

Laser sintering is a generative layer manufacturing technology [56]. The manufacturing principle is depicted in Figure 6-2. Laser sintering uses focused laser beam technology to fuse metal powder into a solid part by melting it locally. The system consists of lasers, scanner, part chamber and control system. Inside the part chamber consist a build platform, powder cartridge and level roller/ re-coater.

First, a thin layer of metal powder between 20 – 100 μm was spread across the platform where the laser traced a two dimensional cross section of the part and sintered the powder together. The build platform then descended one layer thickness to accommodate a layer of powder from the re-coater. As the re-coater sweep across the surface, a layer of powder is added to the top of the surface by the re-coater. At this point, the re-coater could fracture

76

the root of the pins. Thus, a small chamfer is generated at the root of the pins to ensure that the pins are secured on the base.

After the recoating process, the sintering process continues until the model is completed. Throughout the process the heat of the laser melts the powder under the guidance of the scanner. The entire part chamber is sealed and maintained at a temperature slightly above the melting temperature of the powder. Thus, only little heat from the laser beam is needed to cause sintering.

All specimens were manufactured using a EOSINT M 270 Direct Metal Laser Sintering (DMLS) machine as shown in Figure 6-3. The machine was equipped with Yb-fibre laser, which is able to produce 200 W of power. The part chamber was 250 mm long × 250 mm wide × 215 mm high. Its building speed ranged between 2 -20 mm^3/s depending on the material properties.

EOSINT Working Principle of Laser-Sintering
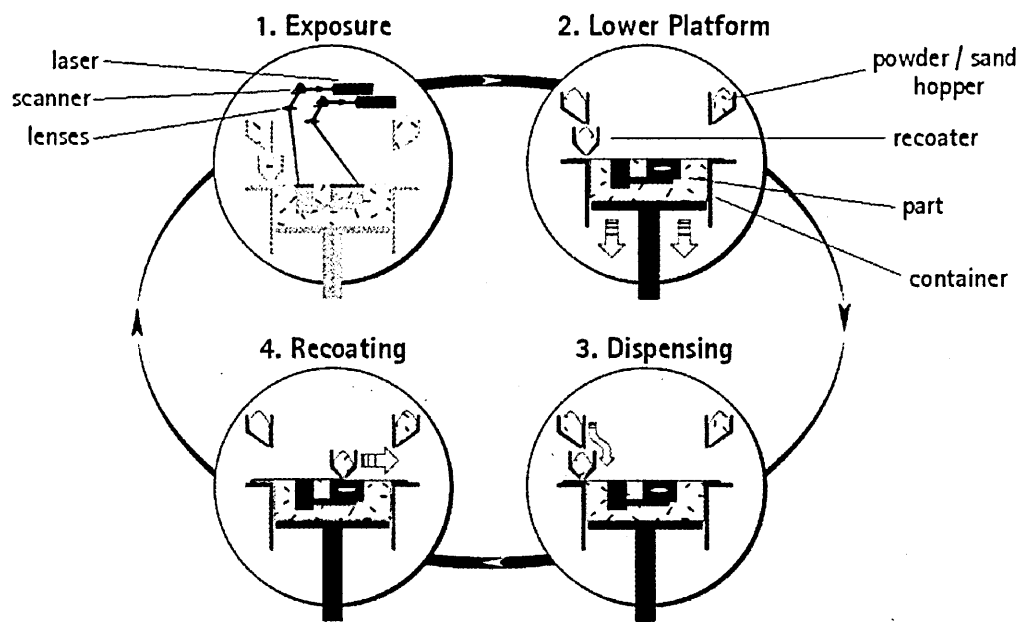
Figure 6-2: EOS laser sintering manufacturing process [56]
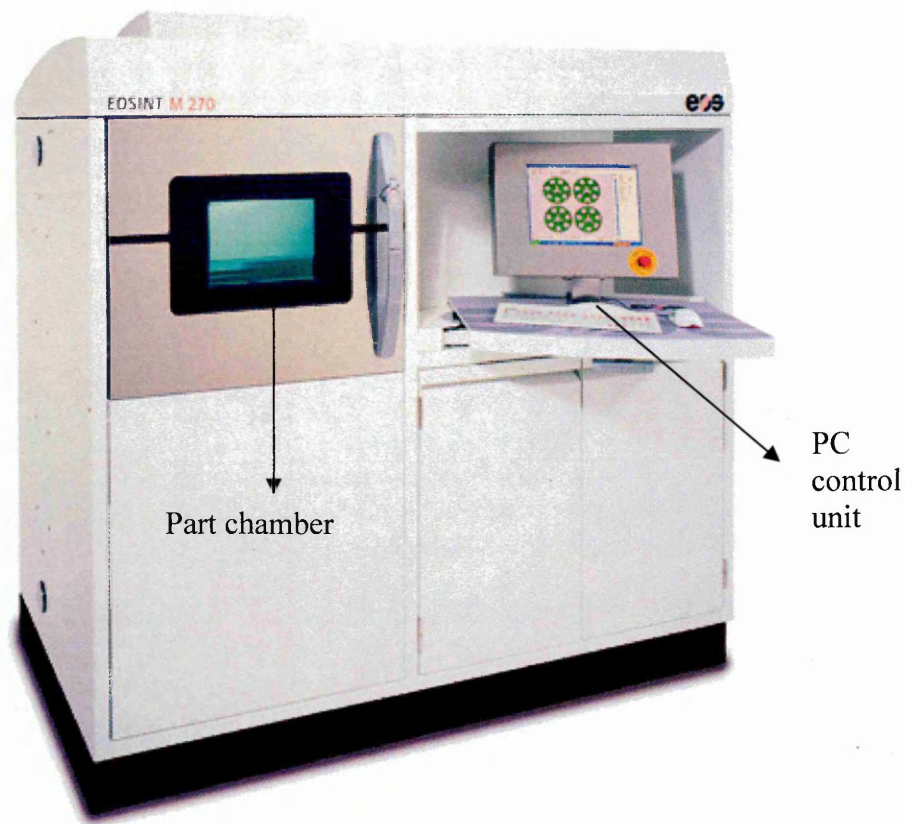
Figure 6-3: EOSINT M270 direct metal laser sintering machine. [57]

6.3 Specimen Material Properties

There are a number of different materials that could be used with EOSINT M 270 machine. The available materials were [58]:

1. DirectMetal 20 – very fine grained bronzed based metal powder.
2. DirectSteel 20 – very fine grained steel based metal powder.
3. DirectSteel H20 – very fine grained steel based metal powder, which has better strength, hardness, wear resistance and surface density of all above materials.

DirectMetal 20 was chosen to build the specimens because it has better thermal properties than the other two materials. DirectMetal 20 is a mixture of bronze and nickel powder. It offers good mechanical properties combined with excellent details resolution and surface quality. Its material properties are listed in Table 6-1.

Table 6-1: Material properties of DirectMetal 20

Material Properties	DirectMetal 20
Minimum recommended layer thickness (μm)	20
Typical achievable part accuracy (μm)	± 50
Minimum wall thickness (mm)	0.6
Density in skin areas (g/cm^3)	7.6
Density in core areas (g/cm^3)	6.3
Remaining porosity (min., %)	8
Tensile strength (MPa, MPIF 10)	Up to 400
Yield strength (MPa)	80
Young's Modulus (GPa)	80
Transverse rupture strength (MPa, MPIF 41)	700
Coefficient of thermal expansion (10^{-6}/K)	18
Thermal conductivity (W/mK)	55.5
Maximum operating temperature (°C)	400

Figure 6-4 shows all four specimens were manufactured out of DirectMetal 20 powder using EOSINT M 270 DMLS machine.

S18.5

Benchmark

Ellip(8.0, 2.0)

Ellip(10,1.6)
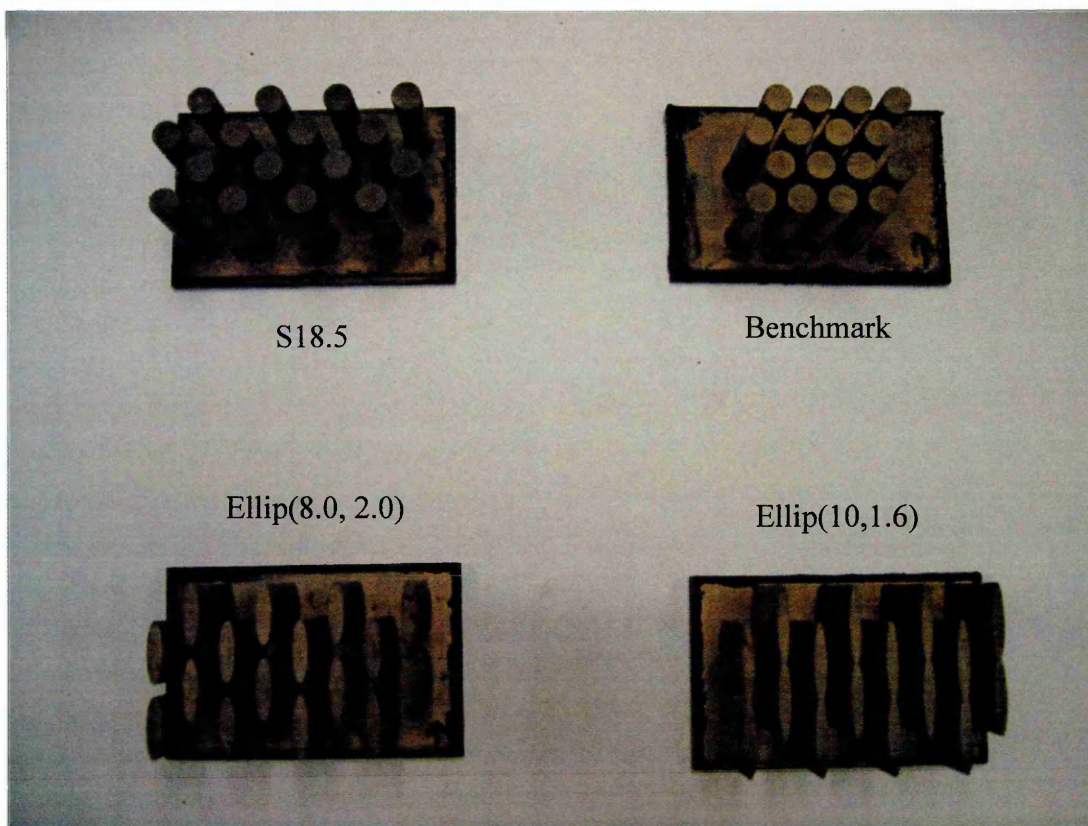
Figure 6-4: Elliptical and circular pins specimens

6.4 Experimental Equipment

Various equipment was utilised to acquire accurate experimental results. Some equipment was used to control and maintain the flow conditions inside the TWT and the water channel. Other equipment was used to measure and record the acquired data. The equipment utilised throughout the experimental tests are:

1. K- type thermocouples,
2. Pico TC-08 temperature data logger,
3. Water pump,
4. Water flow control valves,
5. Water flow rate sensor,
6. Water flow rate display unit,
7. Wind tunnel variable fan speed controller,
8. Heaters fuzzy logic PID controller,

9. Pitot tube,

10. Testo 521-3 flow measurement instrument.

6.4.1 K-type thermocouples

A thermocouple is the most commonly used temperature sensing device. It is usually relatively cheap and able to measure a wide range of temperature. In 1821, an Estonian physicist, Thomas Johann Seebeck discovered that when any conductor is subjected to a thermal gradient, it will generate a voltage. This effect is known as the thermoelectric effect or Seebeck effect [7].

Nickel Chromium

Measurement junction

Voltage difference

Nickel Auliminium
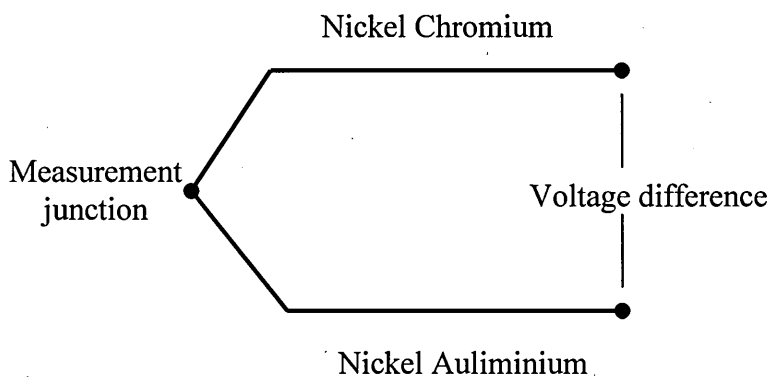
Figure 6-5: K-type thermocouple operation principle

If two similar conductor wires were used to measure the temperature gradient, it will develop a voltage of its own which opposes each other. Therefore, using dissimilar metal wire to complete the circuit as shown in Figure 6-5 will have a different voltage generated, leaving a small voltage difference to measure, which increases with temperature. Unfortunately, thermocouples only measure the temperature difference between two points, not the absolute temperature. The measured value from the thermocouple must be compared with a cold junction. Most cold junctions are incorporated into the circuit or the measurement equipment, which the thermocouple is connected to. Since the measured value is obtained in voltage, it has to be converted to temperature. This method is known as cold junction compensation. Cold junction compensation can be performed through look-up

tables or approximated using polynomial coefficients. The relationship between the temperature difference and the output voltage of a thermocouple is non-linear and is given by a polynomial interpolation as below [7].

$$T_h = aV^2 + bV$$
<div align="right">Equation 6-1</div>

Where,

V is voltage,

and a and b are coefficients found from calibration.

Thermocouples are available in different types. They are usually selected based on temperature range and sensitivity. Due to the extent of thermocouple types, this chapter only focuses on the characteristic of the K-type – Chromel (Nickel Chromium Alloy)/ Alumel (Nickel Aluminium Alloy) thermocouples, which have been used throughout the experimental tests. This type of thermocouple is the most common and widely used thermocouple. It is inexpensive and capable of measuring wide temperature ranges between –200°C to +1200°C. Sensitivity is approximately 41 µV/°C.

The most common wire insulation are Polyvinyl Chloride (PVC), Silicon rubber or Polytetrafluoroethylene (PTFE) insulator to be used in temperatures up to 250°C, above this temperature usually glass fibre or ceramic is used.

This research used K-type thermocouples with glass fibre wire insulation as shown in Figure 6-6. Each thermocouple is 2 m long with exposed junction and fitted with a miniature plug at the end of the wire. The thermocouple diameter is approximately 1.8 mm.
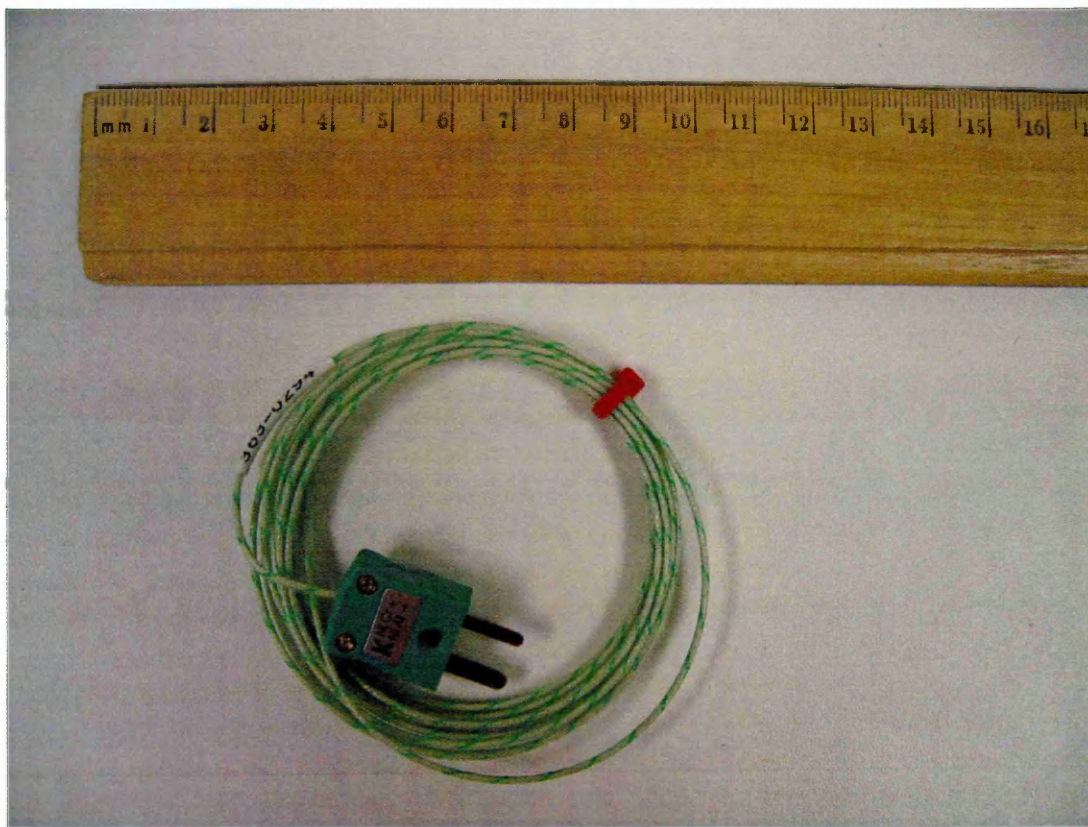
Figure 6-6: 2m K-type glass fibre thermocouple with miniature plug

6.4.2 Pico TC-08 temperature data logger

A data logger is an electronic instrument that records measurements from sensors over time. Modern data loggers can convert inputs, for example, raw voltage or current into meteorological variables. Typically, data loggers are small and powered by batteries or computers. Some data loggers have its own build-in data storage. Others can be attached with storage media or transmit the results to a computer through wireless connection.

This research utilised two Pico TC-08 data loggers to record all temperature values from the experimental tests. A TC-08 data logger is designed to record wide range of temperatures using any thermocouples that has a miniature connector. The data logger has built-in cold junction compensation, thus measured values can be displayed in voltage or Celsius. It has the capacity to link up eight thermocouples at the same time and take samples every second. Table 6-2 lists the specifications of the TC-08 data logger:

Table 6-2: Pico TC-08 data logger specifications [59]

Number of channels	8
Conversion time	100ms (thermocouple and cold junction compensation)
Temperature accuracy	Sum of ±0.2 % of reading and ±0.5°C
Voltage accuracy	Sum of ±0.2 % of reading and ±10μV
Overload protection	±30V
Maximum common mode voltage	±7.5 V
Input impedance	2 MΩ
Input range (voltage)	±70 mV
Resolution	20 bits
Noise free resolution	16.3 bits
Thermocouple types supported	B, E, J, K, N, R, S, T
Input connectors	Miniature thermocouple
Output connector	USB
PC connection	USB 1.1
Power supply	From USB port
Dimensions	201 × 104 × 34 mm
Supplied software	PicoLog (data logger), PicoScope (oscilloscope, spectrum analyser, meter), Drivers and examples

The supplied software has the function to display the measured values in listed tables or graph charts. All recorded values can be saved as a Microsoft Excel sheet or other spreadsheet software.

6.4.3 Water pump

The most common water pump is the centrifugal pump. Its operating principle is based on the first law of thermodynamics, which states that in a ideal system, energy can be neither created nor destroyed but can only be transformed from one form to another [60]. When fluid enters the centrifugal pump, the rotating impeller converts mechanical energy (kinetic energy) into pressure head (potential energy). The fluid velocity increases as the impeller speed increase. A water pump can be categorised by the pressure head and the volume flow rate it can deliver.

As the flow rate required to perform the test is relatively small, a EHIEM aquarium water pump is used to deliver water. The pump can deliver 4.5 L/min at 0.75 m head.

6.4.4 Water flow control valves

Flow valves control the flow rate by either throttling or diverting. Throttling involves in reducing the orifice size and diverting involves routing part of the flow to other channels. A flow control valve usually consists of an inlet port, outlet port and an adjustment handle as shown in Figure 6-7. The adjustment handle is used to control the flow area by restricting the amount of flow. Some sophisticated flow control valves might have a built-in sensor to monitor the flow through the valve. Two flow control valves were utilised to control the flow rate. Each valve has a 12 mm inlet and outlet diameter port with compression fitting.
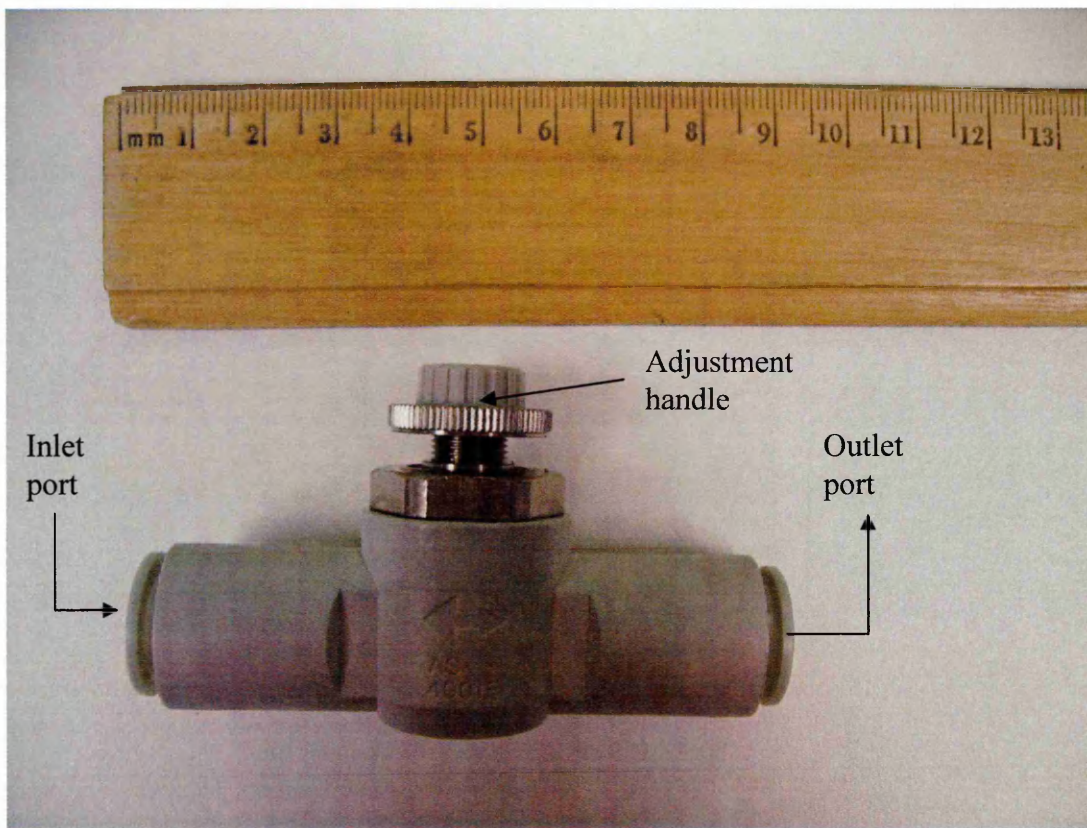
Figure 6-7: 12 mm diameter flow control valve

6.4.5 Water flow rate sensor

A flow rate sensor is a device sensing the rate of fluid flow. There are many types of flow rate sensors available on the market. Most flow sensors have vanes that are pushed by the fluid and drive a rotary potentiometer. The rotary potentiometer working principle is based on the Hall effect to determine the fluid flow rate.

Hall effect states that an electromotive force or Lorentz force is developed as a result of interaction when a steady state current flows in a steady state magnetic field. The direction of the Electro Magnetic Field (EMF) is at right angles to both the direction of the current and the magnetic field vector [61] as shown in Figure 6-8. The Hall voltage can be written as:

$$V_H = \frac{-IB}{ned}$$
Equation 6-2

Where,

V_H is the Hall voltage,

I is the current,

B is the magnetic field,

d is the depth of the plate,

e is the electron charge

and n is the bulk density of carrier electrons.
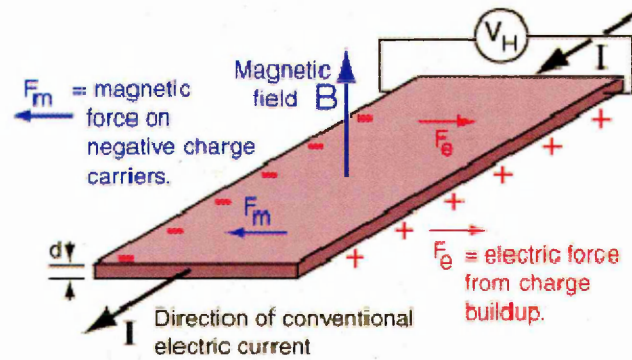
Figure 6-8: Hall effect principle [62]

This research used a fluid flow rate sensor based on the Hall effect principle. Figure 6-9 illustrates the fluid flow sensor that has been used throughout the experimental tests. The flow rate sensor is capable of measuring fluid flow rate between 0.05 and 10 L/min. The sensor has a working temperature range of -25 to +125°C. The sensor produces a pulse output frequency, which is proportional to the flow rate through the device.
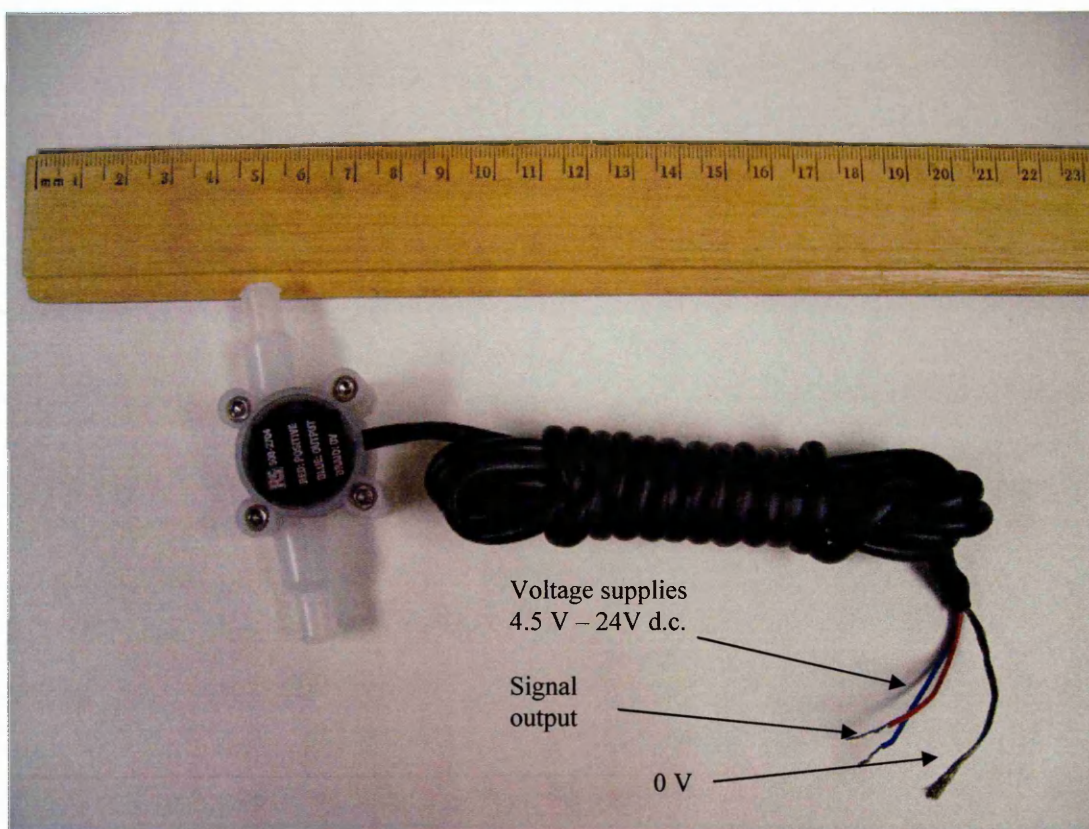
Figure 6-9: Fluid flow sensor

6.4.6 Water flow rate display unit

A flow rate display unit is a device which is used to translate the pulse of the flow rate sensor into displayed measured values. The unit works by using a counter to accumulate the frequency of received pulses occurring in a set period of time. After a set period of time, for example one second, the value in the counter is transferred to the digital display and reset to zero. The frequency equation can be written as follow:

$$f = \frac{n}{t}$$ Equation 6-3

Where,

n is the number of cycles of the repetitive signal that occurs in time interval, t

and t is the time in seconds.
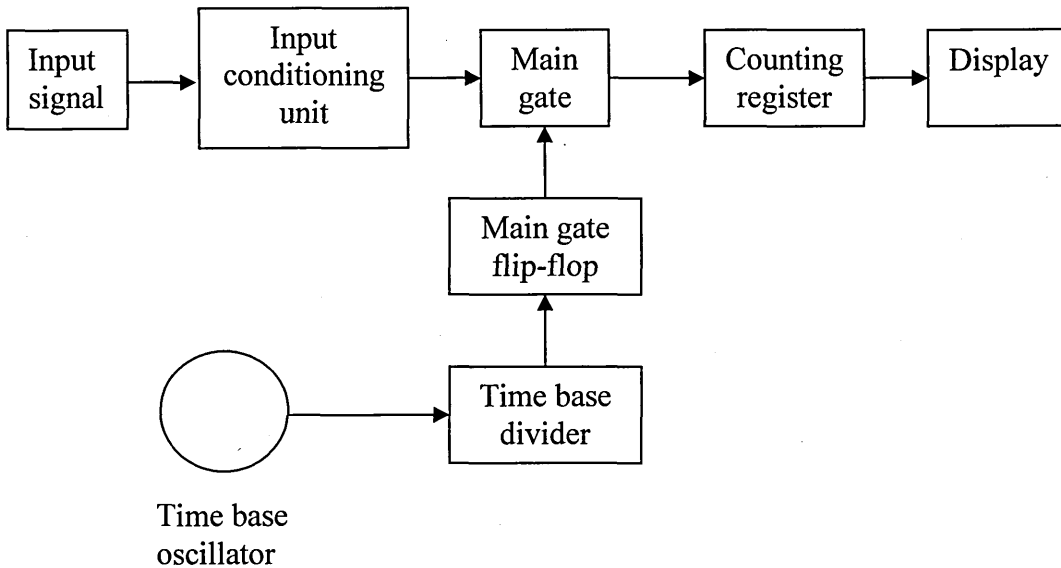
Figure 6-10: Frequency counter block diagram [63]

As illustrated in Figure 6-10, the input signal is initially conditioned to a form that is compatible with the internal circuitry of the counter. The conditioned signal appearing at the door of the main gate is in the form of a pulse train where each pulse corresponds to one cycle or event of the input signal. When the main gate opens, pulses are allowed to pass through and get totalised by the counting register. The time between the opening and the closing of the main gate is controlled by the time base oscillator. Equation 6-3 shows that the accuracy of the flow meter is dependant on the accuracy of the time base oscillator. The time base divider takes the time base oscillator signal as an input signal and provides an output to the main gate. The number of pulses totalled by the counting register for the selected gate time is the frequency of the input signal.

Figure 6-11 and Figure 6-12 show the top view and the front view of the digital flow rate display unit. It has the function to display the counted values in either 1/sec or 1/min. In order to define the amount of flow (L/min) that passes through the water channel, the following equation has been used:

$$Flow\ rate(L/\min) = \frac{P(\ pulses/\min)}{K(\ pulses\ /litre\ )}$$ Equation 6-4

Where,

P is the measured values from the flow meter

and K factor value can be acquired from the sensor manufacturer.

Figure 6-11: Top view of digital flow meter

Figure 6-12: Front view of digital flow meter

6.4.7 Wind tunnel variable fan speed controller

Variable fan speed controller is a device used for controlling the rotational speed of the fan induction motor. The device operates by controlling the frequency of the electric power supplied to the motor. The operating principle of the device is based on the following equation:

$$RPM = \frac{120 \times f}{p}$$

Equation 6-5

Where,

f is the supplied frequency from the device to the motor,

p is the number of motor poles

and RPM is the motor revolutions per minute.
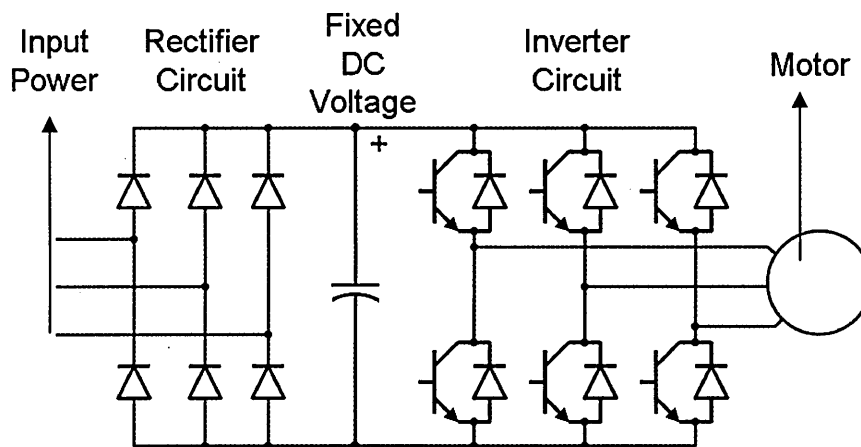
Figure 6-13: Three phase variable fan speed controller diagram [64]

All basic variable speed controllers contain three main components as shown in Figure 6-13. The first component is the rectifier circuit, which convert AC input power to DC power. The diodes reconstruct the negative halves of the waveform onto the positive half as shown in Figure 6-14 to produce DC power. Since, the half-wave or the full-wave waveform converted from the rectifier circuit cannot produce a constant DC voltage, a fixed DC voltage section must be added into the variable speed controller. This section

filters and smooth out the waveform produced by the rectifier circuit. Normally, a smoothing capacitor or filter capacitor is added in this section.

The last section inside the variable speed controller is known as the inverter circuit. It inverts the DC power back to AC but in variable voltage and frequency output.

Sinusoidal Signal

Half-wave Rectification

Full-wave Rectification
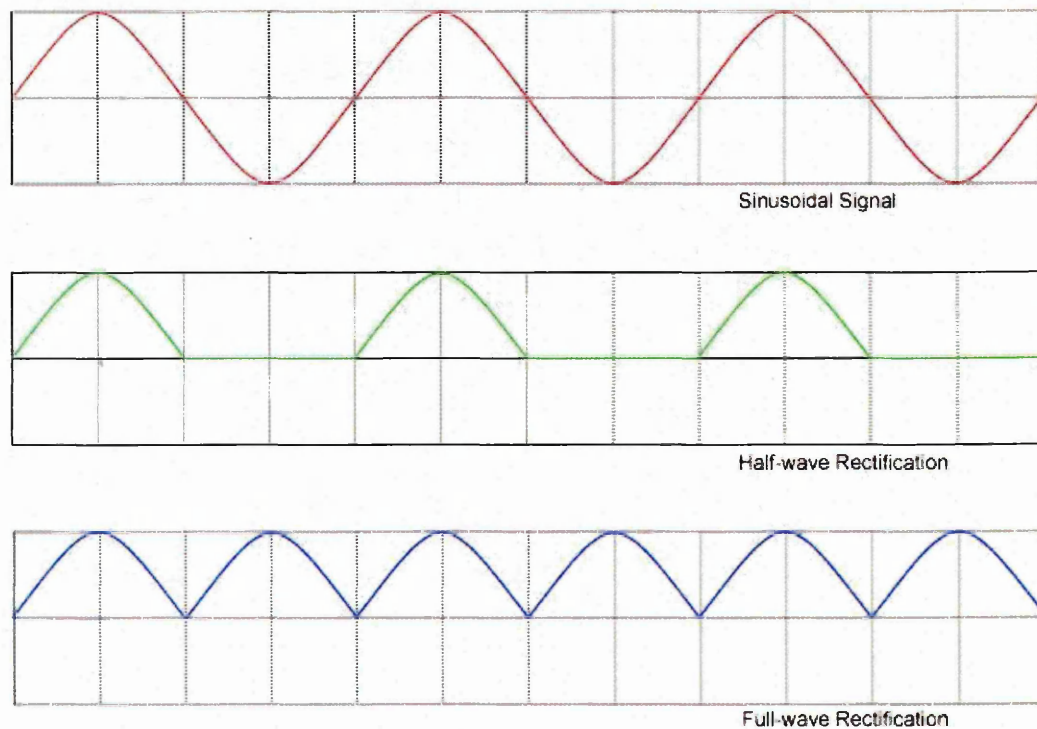
Figure 6-14: Single phase AC waveform rectification to DC waveform [65]

This research used a 1.1kW, three phase variable speed controller as shown in Figure 6-15 to control the wind tunnel fan speed. The device has a built-in potentiometer for variable speed control. The Liquid Crystal Display (LCD) display screen can display the operating signal in frequency, current or loading mode.

Potentiometer
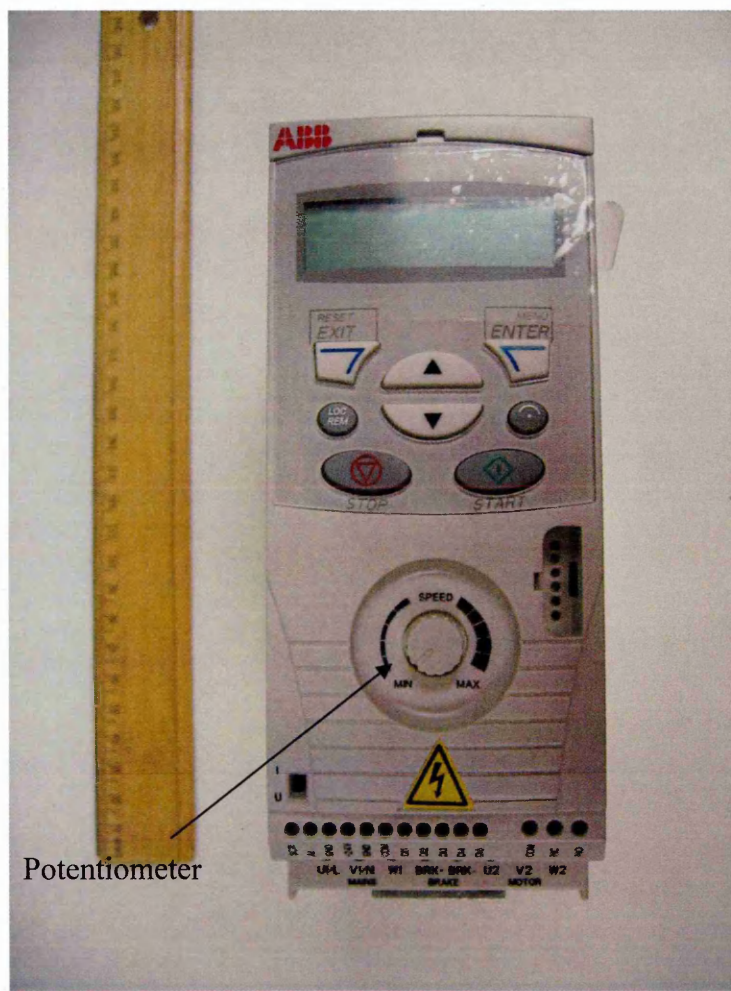
Figure 6-15: Three phase 1.1kW variable speed controller

6.4.8 Heaters fuzzy logic PID controller

Fuzzy logic Proportional-Integral-Derivative (PID) controller is a generic control feedback mechanism that has been used in industry. The PID controller operates by correcting the error between the measured process values and the set values by calculating the output then adjusting the process accordingly. Fuzzy logic is integrated in a PID controller to enhance the controller's performance from non-linear process.

Proportional Integral Derivative (PID) action

A PID controller has three terms. Proportional (P) corresponds to the proportional control. K_p is the proportional gain, which is selected for adequate rise time. The second term is the Integral (I), which controls the action that is proportional to the time integral of the error. K_i is selected for steady-state accuracy without making performance unacceptably poor. The third term is Derivative (D) term, which is to decrease the steady state errors. K_d is selected to overcome excessive oscillation or long settling time. The three combined algorithms can be written as follows [66]:

$$u(t) = K_p \bar{e}(t) + K_i \int_0^t \bar{e}(\tau)d\tau + K_d \frac{d\bar{e}}{dt} \qquad \text{Equation 6-6}$$

Where,

K_p is proportional gain,

$\bar{e}$ is measured error,

t is process time,

K_i is integral gain,

τ is time in the past contributing in the integral response,

and K_d is derivative gain.

The details of each term can be found in Appendix D.

Fuzzy logic control

The drawback of PID controllers is that it is most suitable for linear process. Some systems require non-linear control, for example Heating, Ventilation, Air-Conditioning (HVAC) systems. Therefore, most PID controllers are enhanced by integrating a fuzzy logic into the controller.

Fuzzy logic operating principle usually uses IF or THEN rules [67]. Taking the wind tunnel air temperature as example:

1. IF temperature is very low THEN turn on all elements.
2. IF temperature is low THEN reduce the total elements power.
3. IF temperature is normal THEN maintain the air temperature.
4. IF temperature is above normal THEN turn off all elements.

An integrated fuzzy logic PID control unit has been used to control the heating elements. The unit has a digital display unit and a circuit breaker located in front of the control panel as shown in Figure 6-16. The digital display has the ability to display the process value and the set value. All settings can be set through the digital display unit.
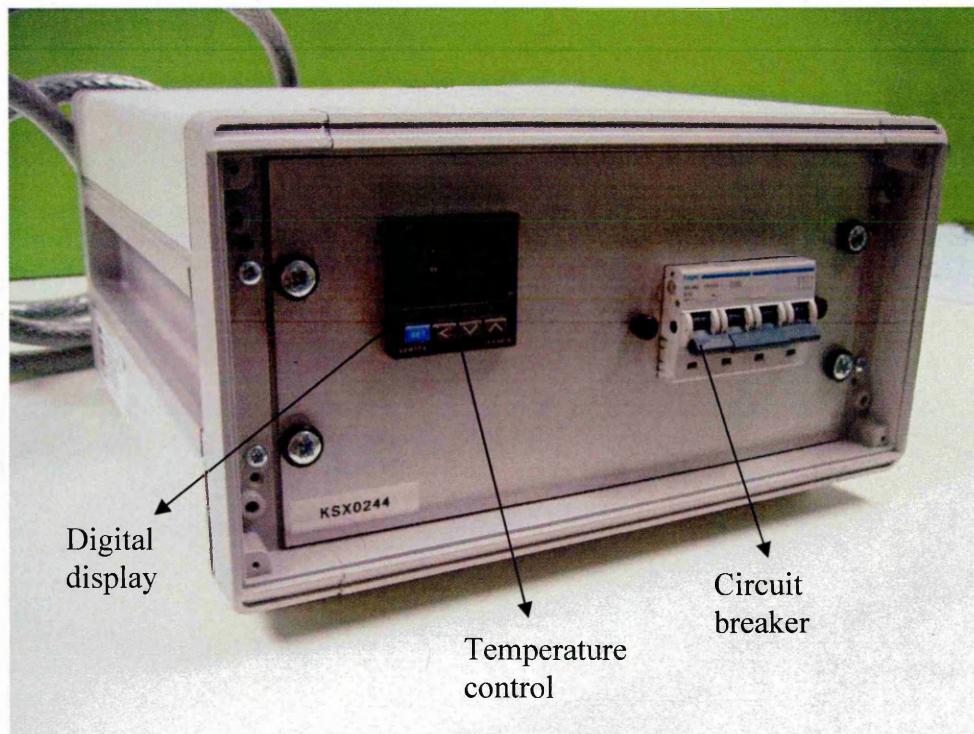
Figure 6-16: Fuzzy logic PID control unit

Figure 6-17 shows the inside of the control unit where the fuzzy logic PID controller, four solid state relays, circuit breaker and cooling fan are located. All 16 heating elements and one K type thermocouple is connected to the back of the control unit to form a closed loop system as depicted in Figure 6-18. The K-type thermocouple is inserted to feedback a measured value of the TWT air temperature.
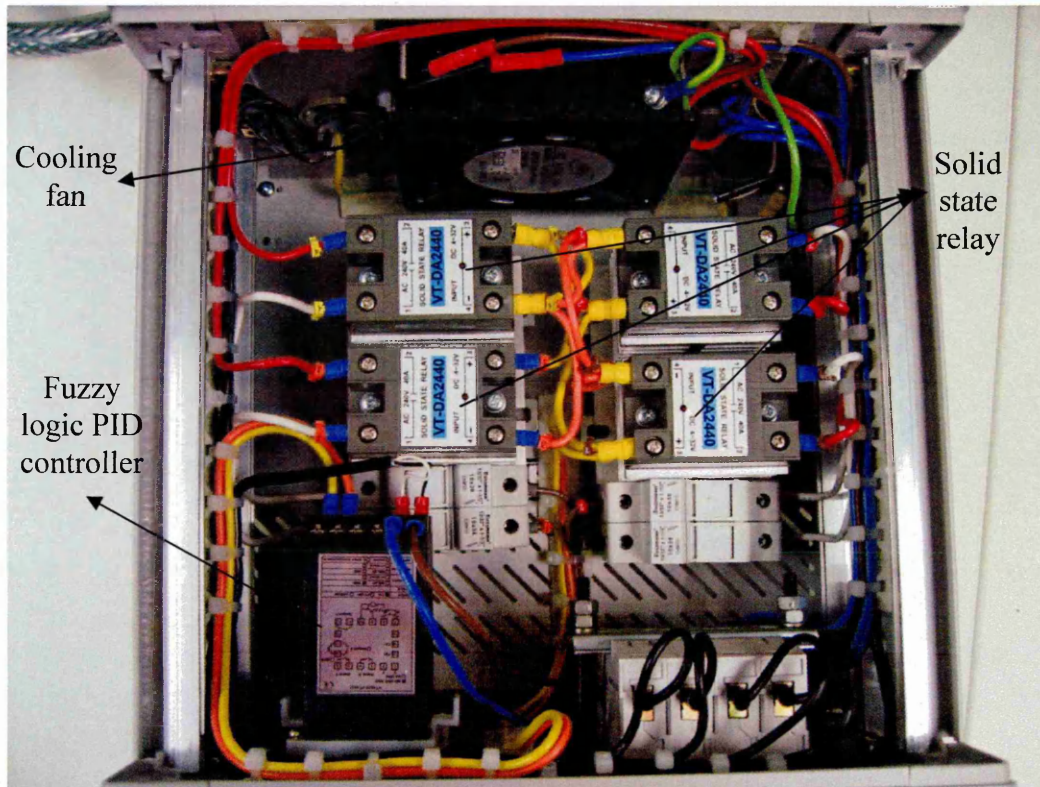
Figure 6-17: Inside the fuzzy logic PID control unit
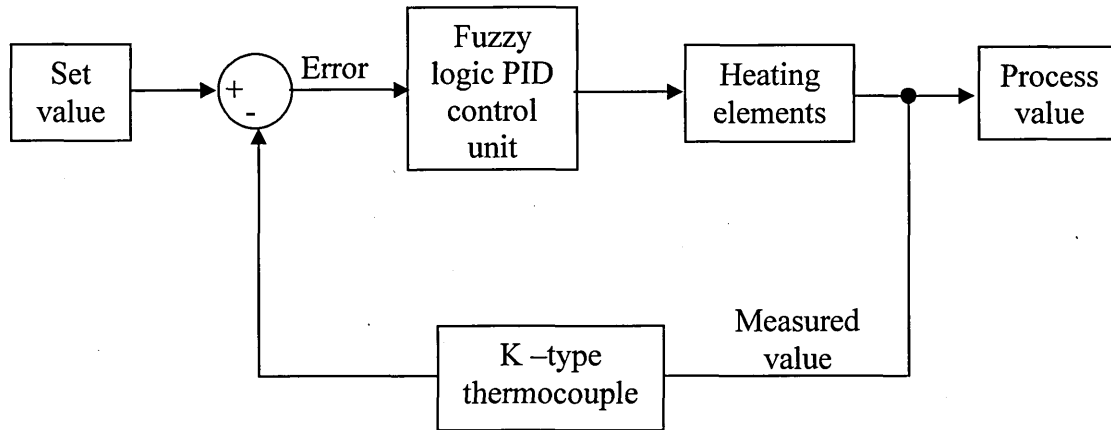
Figure 6-18: Wind tunnel air temperature control system

6.4.9 Pitot tube

A pitot tube is a measuring instrument used to measure fluid flow velocity by measuring the pressure difference of a moving fluid. Bernoulli's equation states that the total pressure is the sum of static pressure and dynamic pressure [68]. Inside a pitot tube are two individual tubes. The main tube is used to measure the total pressure difference as shown in Figure 6-19. The second tube is a static pressure measurement tube, which is perpendicular to the flow direction as depicted in Figure 6-20. Both ends of the tube are connected to silicone rubber hoses, which connect to a pressure measurement device such as the Testo 521-3.

Using the differential pressure measurement method, the sensor inside the measurement device can define the flow velocity based the equation below [69]:

$$V = \sqrt{\frac{2(p_t - p_s)}{\rho}}$$

Equation 6-7

Where,

V is defined velocity,

p_t is measured total pressure,

p_s is measured static pressure

ρ is the fluid density.
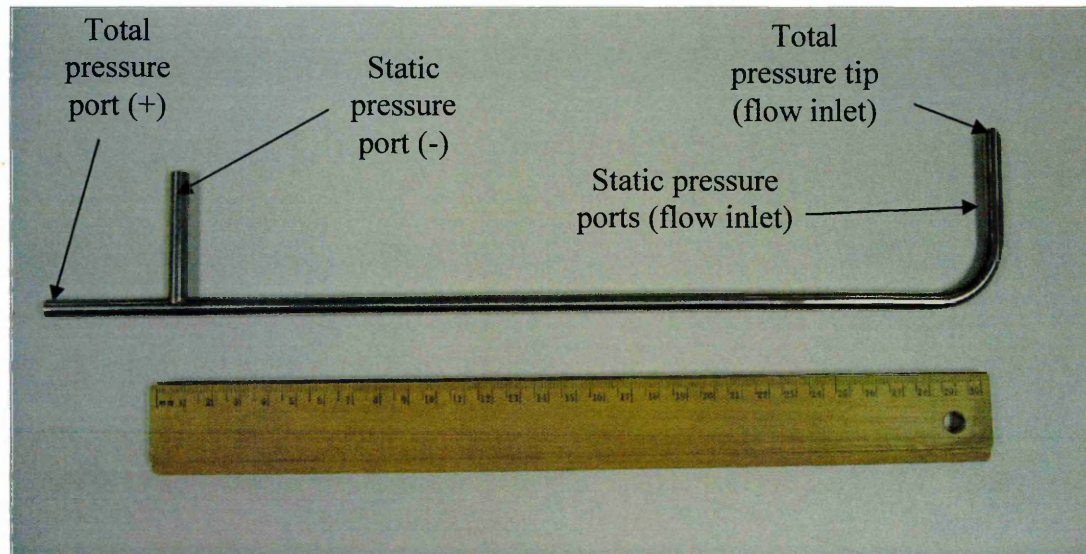
Figure 6-19: Pitot tube
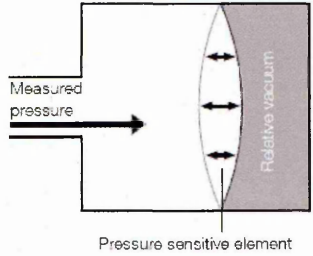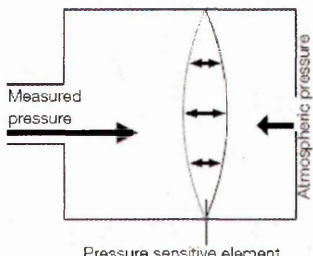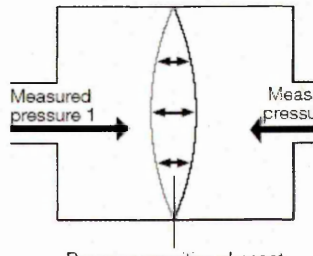
Figure 6-20: Section view of the pitot tube [70]

6.4.10   Testo 521-3 flow measurement instrument

Testo 521-3 is a pressure measurement device, which is utilised together with pitot tube to measure the TWT air velocity. The design of the device is based on the principle of the effect of pressure on a defined area.

There are three types of measurement methods. The first type of measurement is the absolute pressure measurement, which measure the pressure relative to the vacuum inside the device as depicted in Figure 6-21. The second measurement type is the gauge pressure measurement. It measures the external measurement relative to the atmospheric pressure as shown in Figure 6-22. The last measurement type is the differential pressure measurement, which is similar to the gauge pressure measurement but instead of measuring relative to the atmospheric pressure it measure a specific reference pressure as shown in Figure 6-23.

Figure 6-21: Absolute pressure measurement [72]	Figure 6-22: Gauge pressure measurement [72]	Figure 6-23: Differential pressure measurement [72]

Testo 521-3 as depicted in Figure 6-24 utilises a piezoelectric pressure sensor to measure pressure. The piezoelectric pressure sensor was designed based on the piezoelectric effect. The effect is a phenomenon where materials can generates an electric charge in response to applied mechanical stress. Quartz crystal material was found extremely stable and has been used in most sensors for pressure measurement.

Figure 6-24: Testo 521-3 flow measurement instrument

6.5 Specimens Preparation

In order to prevent water from entering into the thermocouple channels, high temperature folic graphite sealant was used to secure the thermocouples inside the core of the pins. Figure 6-25 shows that all six thermocouples were secured in position. The wires of the thermocouples were then fed out of the water channel through a hole as shown in Figure 6-26. A silicon sealant was used to prevent water from leaking out from the channel. Next, the specimen must be secured to the water channel to create heat convection. As the specimen is exposed to extreme air temperature, the same folic graphite sealant was used to secure the specimen in position on the water channel as shown in Figure 6-27. The sealant requires 24 – 30 hours to fully cure.
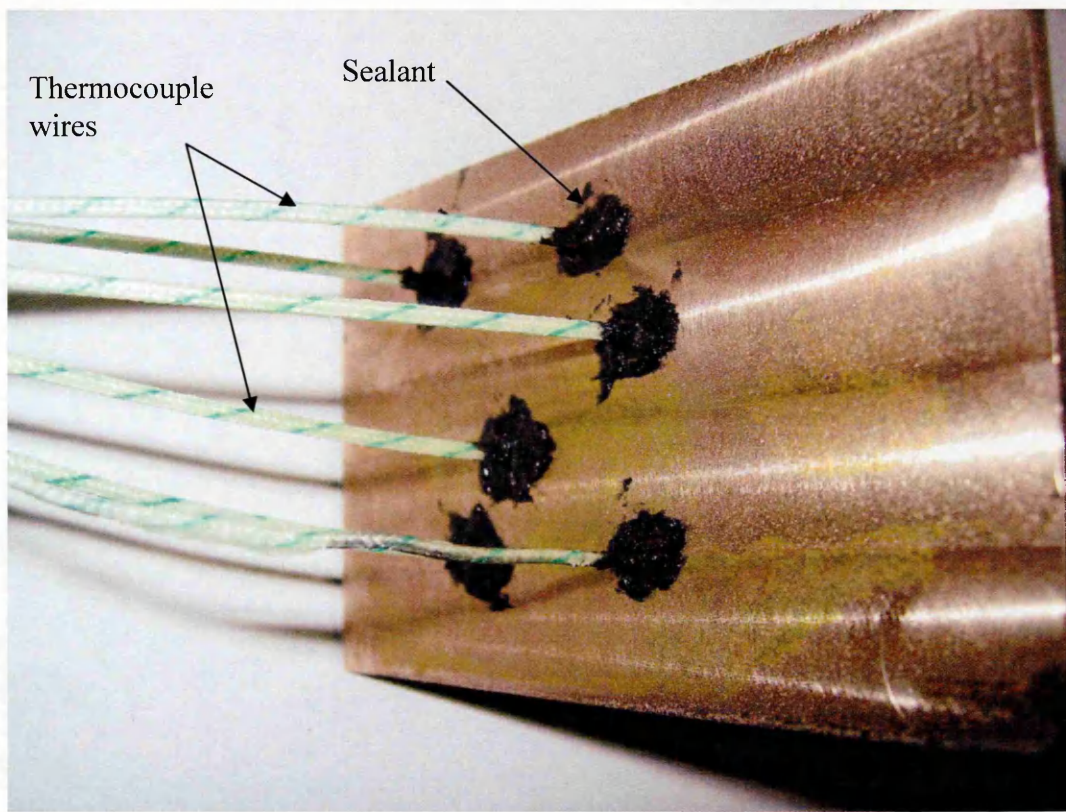
Figure 6-25: Thermocouples were sealed inside the core of the pins

Figure 6-26: Silicon sealant was used to fill in the hole and thermocouples position
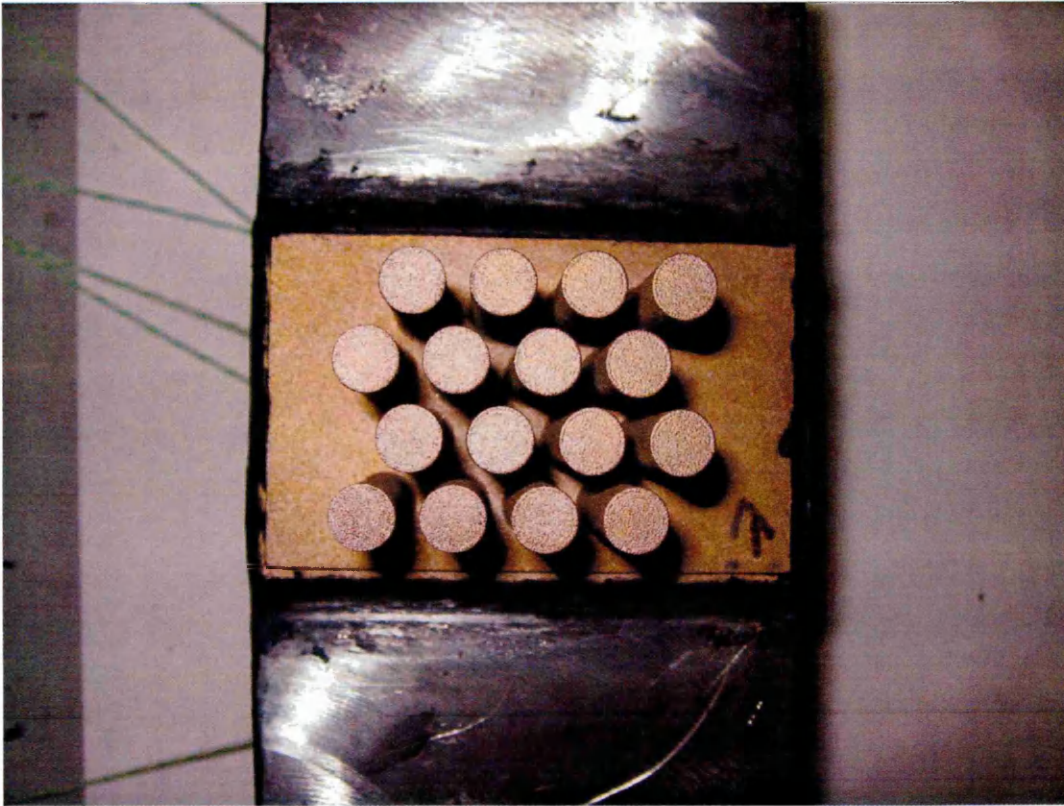
Figure 6-27: Folic graphite sealant was used to secure the specimen on the water channel

6.6 Water Loop Pressure Testing

Before conducting any experimental work, a water loop pressure testing procedure was carried out to ensure that the specimen is fully secured on the water channel without any water leakage. The water pathway consists of the following equipment:

1. Water supply tank
2. Water pump
3. Water flow valves
4. Water channel and specimen
5. Water flow rate sensor
6. 12 mm diameter water hose
7. Water collector tank
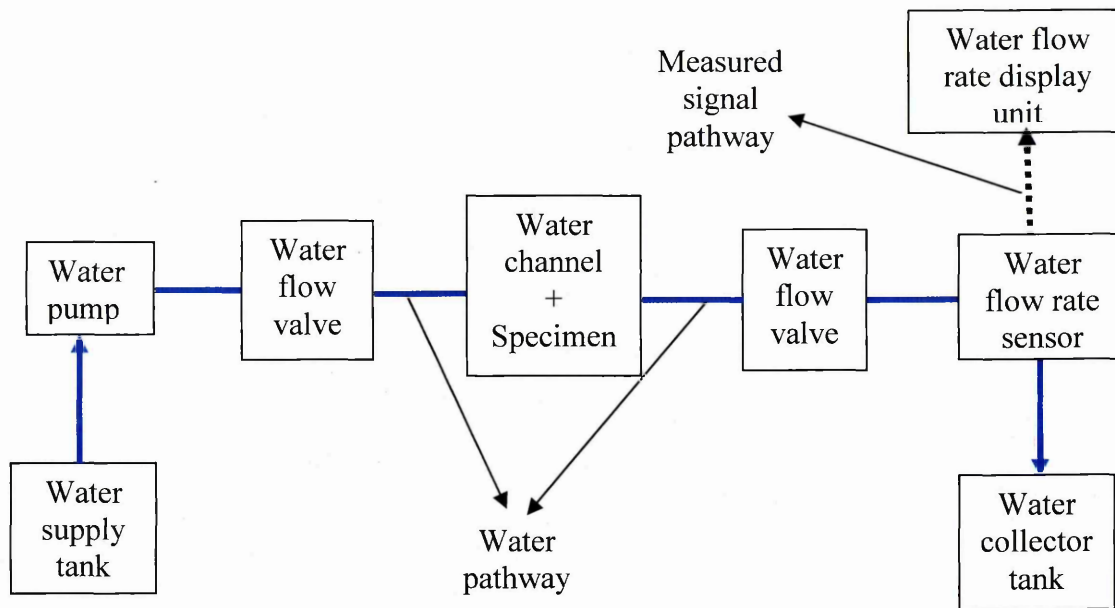
Figure 6-28: Water flow pathway

Figure 6-28 shows the water flow system. A water pump first feeds water from the supply tank to the water channel. In between the water pump and the water channel is a water flow control valve. This valve was used to isolate the water supply from the pump while replacing the water channel. Located downstream of the water channel are the water flow control valve and the flow sensor. The downstream water flow control valve was used to control the flow rate of the water. As water passes through the flow sensor, measured values are transferred to the water flow rate display unit. The whole water flow path was connected by 12 mm diameter rubber hose.

All valves were first fully opened during the flow testing operation and when the water flow rate reaches 1.9 ± 0.05 L/min, the downstream valve was used to reduce the flow rate to the experimental requirement flow rate of 0.5 L/min. This operation is carried out before each experimental test to ensure that no leakage occurred at the water channel. Figure 6-29 illustrates the pressure testing operation on Ellip(8.0, 2.0) specimen. The TWT operating procedures can be found in Appendix E.
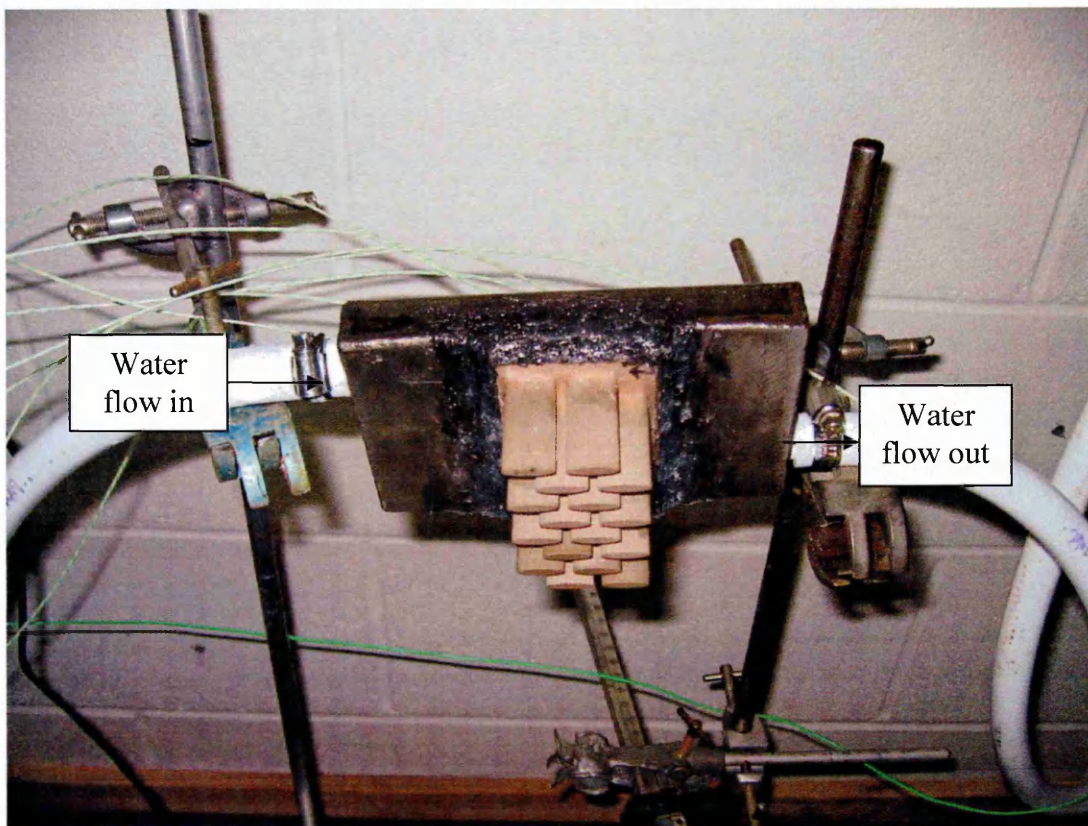
Figure 6-29: Pressure testing on specimen Ellip(8.0, 2.0) model

6.7 Accuracy of Equipment

All the equipment accuracy data supplied by the manufacturers is summarised in Table 6-3. The total equipment error was calculated in Table 6-3. The total error was used to set the error scale bar in Chapter 10.

Table 6-3: Equipment accuracy

Equipment	% error
K-type thermocouple	0.75
TC-08 data logger	0.20
Water flow-rate sensor	0.10
Water flow-rate display unit	5.00
Variable fan speed controller	1.00
Fuzzy logic PID controller	0.50
Testo 521-3 flow measurement unit	0.50
Total equipment error	8.05

Summary

This chapter describes the manufacturing process of the four models used in the experimental tests. All models were manufactured using DMLS method. The manufacturing process and material properties were given in the chapter. This chapter also introduced the operating principle of each piece of equipment used in the experimental tests. The water loop pressure testing procedure was also given in this chapter.

Chapter 7   Numerical Simulation Results

Introduction

This chapter summarises the results obtained from the CFD modelling. The CFD results were obtained from models which satisfied the mesh independent process. The process was carried out until the total energy transfer deviation dropped to 2-3%. Each models' numerical performance was judged by its total energy transfer and pressure difference across the pins. The energy transfer equation can be written as follows:

$$Q = \overset{\bullet}{m} \times C_p \times \left(T_{out} - T_{in} \right)$$
<div align="right">Equation 7-1</div>

Where,

$\overset{\bullet}{m}$ is hot air mass flow rate

C_p is the specific heat capacity of the fluid

T_{out} is the fluid outlet temperature

T_{in} is the fluid inlet temperature

The pressure difference on each model was measured from two central points located upstream and downstream of the bank of pins as depicted in Figure 7-1. The inlet pressure measurement point is located 25 mm from the hot air inlet channel and the same distance from the outlet channel measures the outlet pressure. The pressure difference can be calculated as follow:

$$\Delta P = P_{upstream} - P_{downstream}$$
<div align="right">Equation 7-2</div>

Where,

ΔP is pressure difference

$P_{upstream}$ is upstream pressure

$P_{downstream}$ is downstream pressure

<div align="center">106</div>
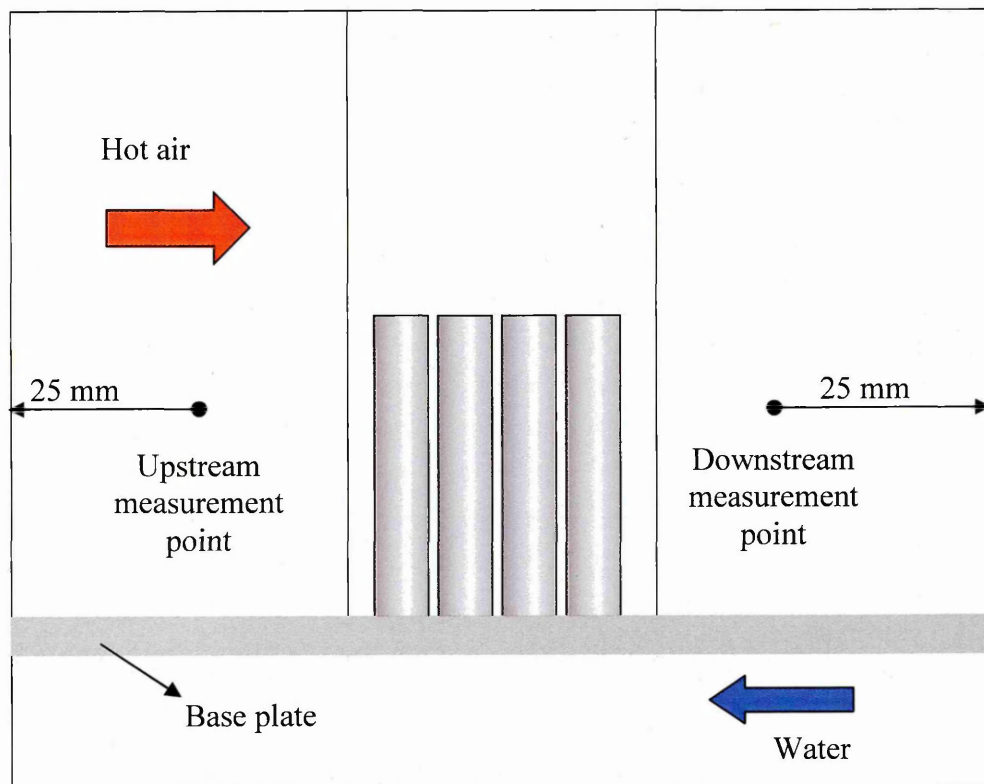
Figure 7-1: Pressure difference measurement points

7.1 CFD Energy Transfer Results

7.1.1 Circular pins' spacing and pitch distance CFD energy transfer results

Table 7-1 and Table 7-2 show the total energy transfer of each model with either varied pins' spacing or pitch distance. Nine models were created with different pins' spacing and the other four models with different pitch distances. All models shared the same boundary condition as stated in Table 4-5. The inlet water temperature was set at 290.5 K on all models and the numerical simulation results of water outlet temperature were given in both tables. Using the Benchmark model as an example to calculate the total energy based on Equation 7-1. The total energy of the Benchmark model is:

$$Q = \dot{m} \times C_p \times (T_{out} - T_{in})$$
Equation 7-1

Known that $\dot{m} = 0.0083$ kg/s and $C_p = 4182$ J/kg. K

$Q_{Benchmark} = 0.0083 \times 4182 \times (296.7 - 290.5)$

$Q_{Benchmark} = 216.9$ W

Table 7-1 Total energy transfer of each model with different pin spacing

Model Name	Spacing (mm)	Pitch (mm)	Water Outlet Temperature (K)	Total Energy Transfer (W)
S09.5	9.5	9.5	296.3	201.0
Benchmark	11	9.5	296.7	216.9
S12.5	12.5	9.5	296.9	222.5
S14.0	14	9.5	297.1	228.6
S15.5	15.5	9.5	297.2	234.2
S17.0	17	9.5	297.3	236.2
S18.5	18.5	9.5	297.4	240.2
S20.0	20	9.5	297.4	241.5
S21.5	21.5	9.5	297.4	239.1

Table 7-2: Total energy transfer of each model with different pitch distance

Model Name	Spacing (mm)	Pitch (mm)	Water Outlet Temperature (K)	Total Energy Transfer (W)
P06.5	11	6.5	296.1	195.3
P08.0	11	8	296.6	212.3
Benchmark	11	9.5	296.7	216.9
P11.0	11	11	296.8	217.3
P12.5	11	12.5	296.8	218.9

7.1.2 Elliptical pins CFD energy transfer results

Table 7-3 summarised the total energy transfer of elliptical pins. The table presented the major and minor axis of each model and also the numerical simulation results of the water outlet temperature. In order to compare the performance of elliptical pins with the circular pins, both designs had the same volume of material. Hence, only four eccentricities were selected for this research. Ellip(5.5, 2.9) eccentricity is 0.853 followed by Ellip(6.4, 2.5) with eccentricity of 0.921. Ellip(8.0, 2.0) and Ellip(10, 1.6) are thinner than both previous models and have an eccentricity of 0.968 and 0.987, respectively. The total energy transfer of the elliptical models can be calculated using Equation 7-1. Using Ellip(8.0,2.0) as an example, the total energy transfer can be calculate as follow:

Known that $\overset{\bullet}{m} = 0.0083$ kg/s and $C_p = 4182$ J/kg. K

$Q_{Ellip(8.0,2.0)} = 0.0083 \times 4182 \times (298.7 - 290.5)$

$Q_{Ellip(8.0,2.0)} = 285.6$ W

Table 7-3: Elliptical pins energy transfer

Model Name	Major Axis (a) (mm)	Minor Axis (b) (mm)	Water Outlet Temperature (K)	Total Energy Transfer (W)
Ellip(5.5, 2.9)	5.54	2.89	298.4	275.2
Ellip(6.4, 2.5)	6.4	2.5	298.6	280.0
Ellip(8.0, 2.0)	8	2	298.7	285.6
Ellip(10,1.6)	10	1.6	299.0	295.8

7.2 CFD Pressure Difference Results

7.2.1 Circular pins' spacing and pitch distance pressure difference results

Pressure differences across each group of pins have also been documented in this study. As shown in Figure 7-1, two points were selected to calculate the pressure drop between those points. Table 7-4 summarised the numerical simulation results of the upstream and downstream pressure. The pressure differences of circular pins can be calculated using Equation 7-2. Taking the Benchmark as an example, the pressure drop between the pins can be calculated as follows:

$$\Delta P = P_{upstream} - P_{downstream}$$

Equation 7-2

$$\Delta P_{Benchmark} = 17.4 - (-2.5)$$
$$\Delta P_{Benchmark} = 19.9 \text{ Pa}$$

Table 7-4: Pressure difference at hot air channel (circular pins)

Model Name	Upstream Pressure (Pa)	Downstream Pressure (Pa)	Pressure Loss (Pa)
S09.5	16.3	-2.6	18.9
Benchmark	17.4	-2.5	19.9
S12.5	18.3	-0.8	19.1
S14.0	18.9	0.3	18.6
S15.5	19.1	1.2	17.9
S17.0	19.5	1.7	17.8
S18.5	19.7	2.3	17.4
S20.0	20.1	3.0	17.1
S21.5	20.7	4.0	16.6
P06.5	17.3	-3.1	20.3
P08.0	17.1	-3.1	20.2
Benchmark	17.4	-2.5	19.9
P11.0	17.6	-2.2	19.8
P12.5	17.7	-2.1	19.8

7.2.2 Elliptical pins CFD pressure difference results

The same measuring points were used to calculate the elliptical pins' pressure difference as shown in Table 7-5. The pressure difference on each model was measured in Pascal. Using Ellip(8.0,2.0) as an example, the pressure drop between the pins can be calculated as follow:

$$\Delta P_{Ellip(8.0,2.0)} = 14.5 - 6.7$$

$$\Delta P_{Ellip(8.0,2.0)} = 7.9 \text{ Pa}$$

Table 7-5: Total pressure difference at hot air channel (elliptical pins)

Model Name	Upstream Pressure (Pa)	Downstream Pressure (Pa)	Pressure Difference (Pa)
Ellip(5.5, 2.9)	16.5	4.4	12.1
Ellip(6.4, 2.5)	15.5	5.3	10.2
Ellip(8.0, 2.0)	14.5	6.6	7.9
Ellip(10,1.6)	13.9	7.1	6.8

Summary

This chapter summarised the obtained numerical simulation results of all models presented in total energy transfer and pressure drop. All models were listed under two categories, namely, the total energy transfer and pressure difference. All numerical models' inlet water temperature was set at 290.5 K and the total energy transfer of each model was listed in the tables. The total energy transfer of each model was calculated based on the water temperature differences. Each models' pressure difference was calculated using the pressure difference between the upstream and downstream of the pins. The calculated total energy transfer and pressure difference will be used in next chapter to analyse the performance of each model.

Chapter 8   Numerical Simulation Results Analysis

Introduction

This chapter presents an analysis of the circular and elliptical pins' thermal and fluid flow performance. Temperature contours and velocity vector plots were used to assess the thermal and the fluid flow performance of each setup. This chapter is divided into six sections as listed below:

1. Thermal performance of circular pins
2. Pressure drop across circular pins
3. Circular pins performance summary
4. Thermal performance of elliptical pins
5. Pressure drop across elliptical pins
6. Elliptical pins performance summary

8.1 Thermal Performance of Circular Pins

Table 7-1 showed that the total energy transfer of the benchmark model is 216.9 W. Figure 8-1 shows the total energy transfer of different circular pins' spacing. The figure illustrates that the total energy transfer of each circular pins model on the Y-axis. In general, larger pin spacing setups outperformed smaller pin spacing setups as shown in Figure 8-1. The graph also summarises that spacing below 11 mm has less energy transfer rate than the benchmark model. The simulation results confirm that model S18.5 outperformed all the other models. This performance can be explained when comparing the velocity vectors on the benchmark model against S18.5 model. Figure 8-2 and Figure 8-3 are the velocity vector plots. The colour map on the left of the graph represents the velocity values of each vector and the colour map one the right represents the temperature values of each pins in Kelvin. It can be seen on Figure 8-2, flow has been redirected to both sides and the top of the channel thus leaving lower air velocity around the central pins. This effect is due to the smaller spacing on the benchmark model. Hot air is prevented from flowing through the pins. Hence, hot air has been re-directed to both sides of the channel. When increasing the pins' spacing as shown in Figure 8-3, flows are able to penetrate through to the middle pins and therefore energy transfer rate increases as recorded in simulation results. Fourier's Law stated that the heat transfer is directly proportional to the surface area. Due to less hot air being in contact with the pins, the benchmark model is cooler than the rest of the models. It can be seen from the temperature contour graphs on Figure 8-4 and Figure 8-5 that the model S18.5 is more efficient that the benchmark model. Pins' temperatures on model S18.5 are more even on each row, unlike the benchmark model, which has high temperature concentrated on the first two rows. When high temperature occurs on one area, it creates hot spots and may cause the material to deform quickly and generally increase pressure drops.

Table 7-1 summarised the total energy transfer through the water, which increases gradually as the pins' spacing increase until spacing reaches 20 mm. Energy transfer started to decrease after increasing the pins' spacing by 20 mm. When pin spacing increased over the limits, hot air started to accelerate through the spacing. Therefore, CFD simulation results show that model S21.5 hot air outlet temperature is 4 °C more than model S18.5.

Although Table 7-1 shows that model S20.0 has a higher energy transfer rate than model S18.5, the measured gas outlet temperature is 1.2 °C more than the optimum spacing model S18.5.

The next section of this research looked at the effect of altering the thermal performance of the pitch distance. Figure 8-6 illustrates the total energy transfer of different circular pins pitch distance. Each model's name is listed on the X-axis and the total energy transfer of each model is listed on the Y-axis. It can be seen in Figure 8-6 that, changing the pitch distance does not increase the thermal performance extensively. The simulation results agreed with the results published by Sahin *et al.* [17]. They claimed that on their rectangular fins heat exchanger, pitch distance was not an important parameter affecting the heat transfer. This study shows that circular pins shared the same behaviour when changing the pitch distance as the rectangular fins. Spacing of the pins is crucial for the flow to penetrate through from one row to another irrespective of the pitch distance. Unless an optimum spacing is selected, otherwise, changing pitch distance can only marginally improve the heat transfer on a heat exchanger.
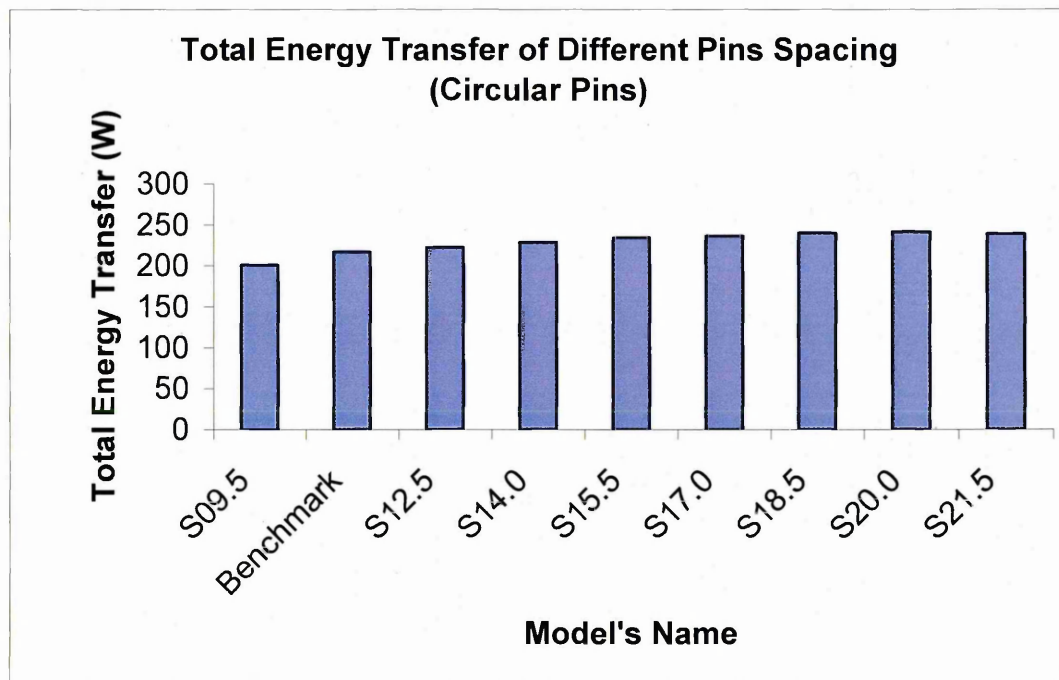
Figure 8-1: The effects of total energy transfer to the water side when altering the pins' spacing
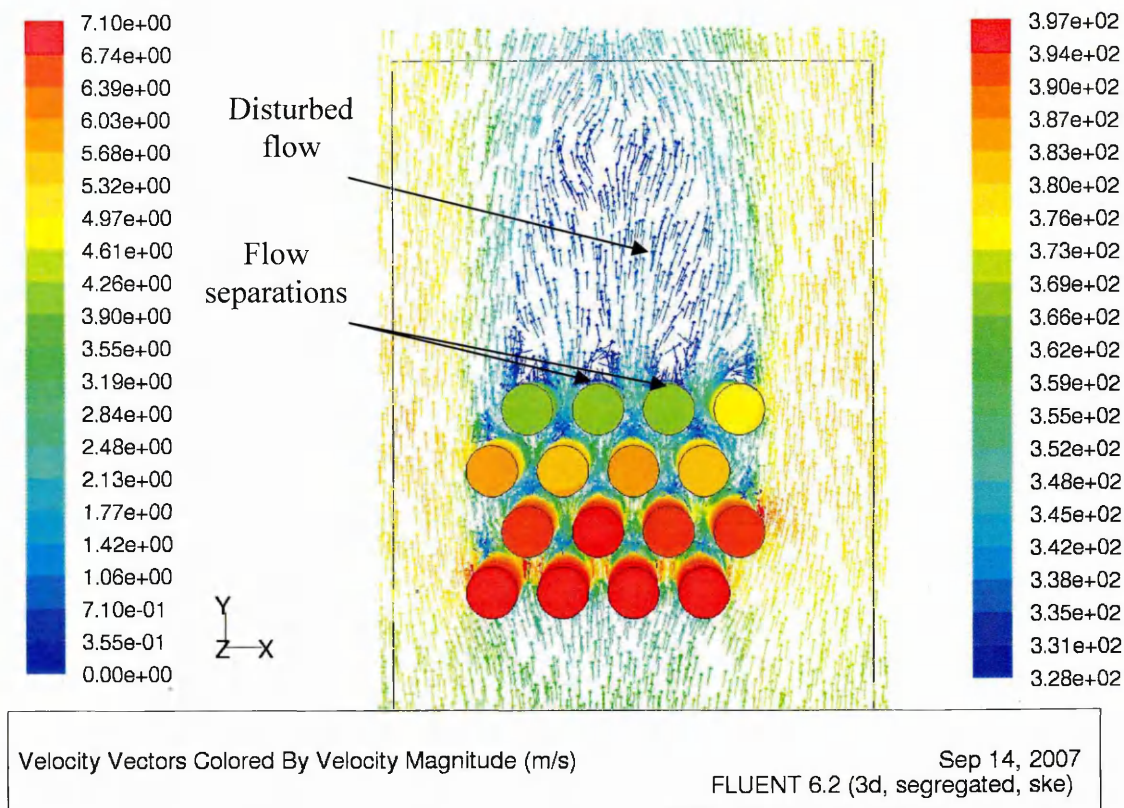
Figure 8-2: Benchmark model's velocity vector graph
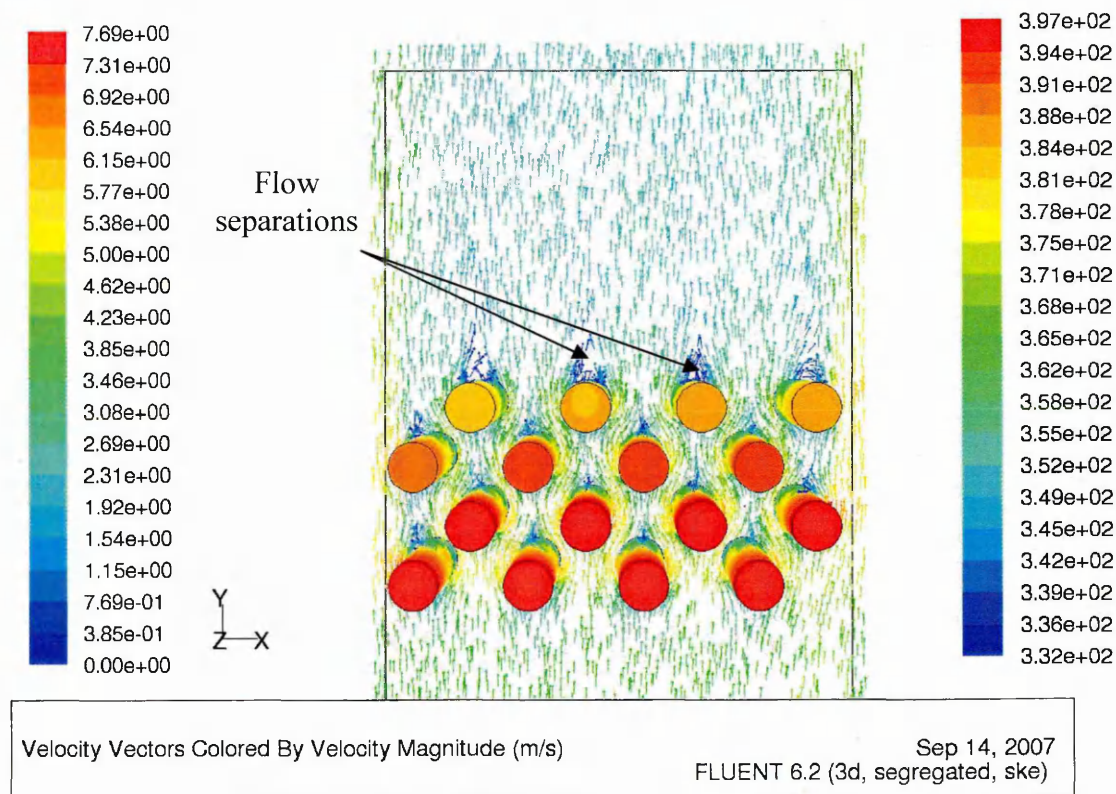
Figure 8-3: Model S18.5 velocity vector graph
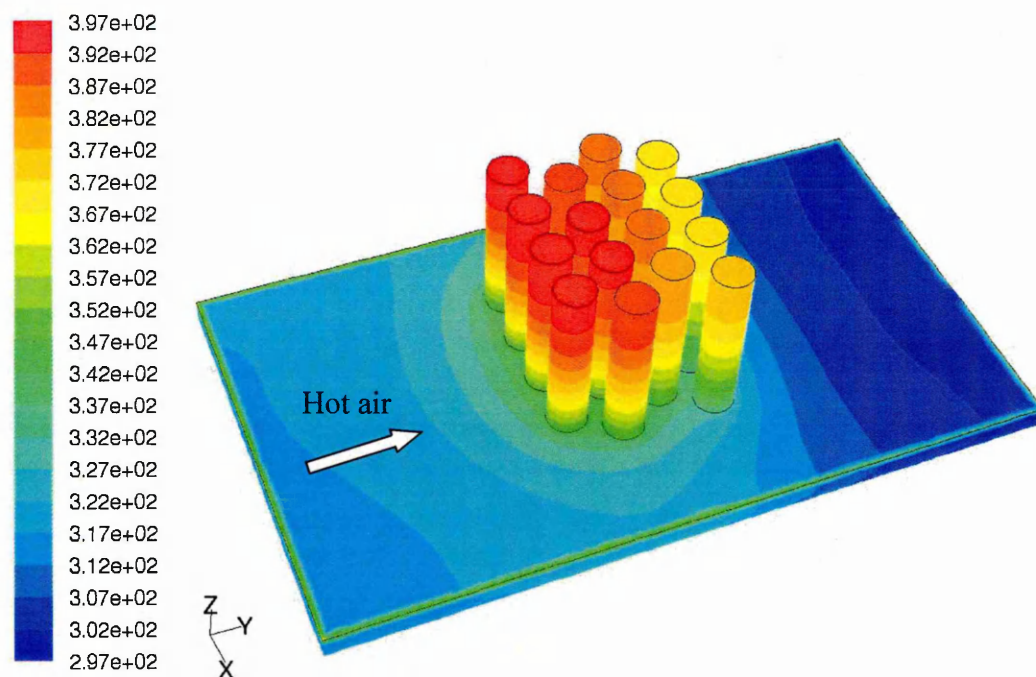
Figure 8-4: Benchmark model's pins temperature contour
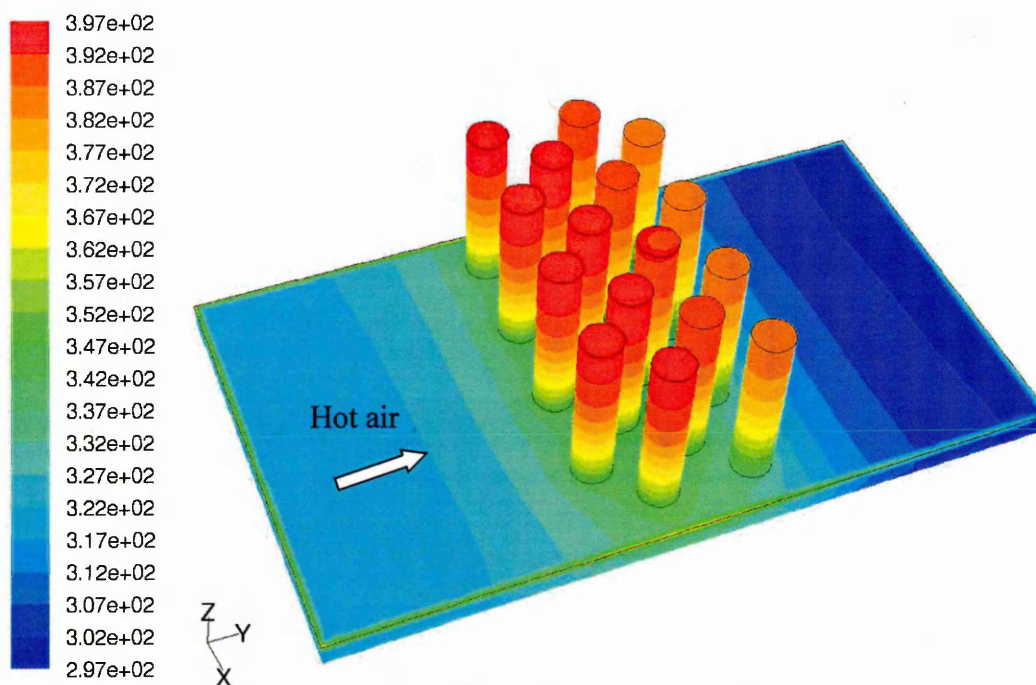
Figure 8-5: S18.5 model's pins temperature contour

116

Total Energy Transfer of Different Pitch Distance (Circular Pins)
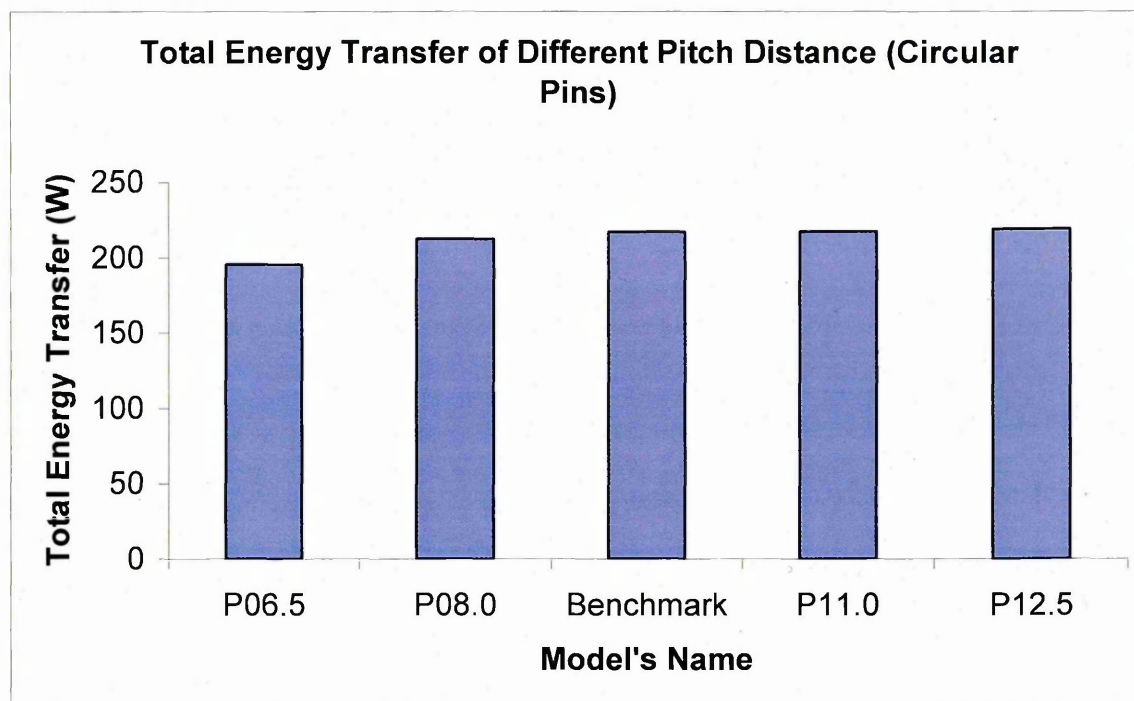
Figure 8-6: The effects of total energy transfer to the water side when altering the pins pitch distance

8.2 Pressure Drop Across Circular Pins

At a given flow rate, small pin spacing restricted the air flowing through. Thus air flow path is redirected to the sides of the channel. Figure 8-7 shows the pressure contours around the pins. It can be seen in the figure that the pressure difference between the upstream (18.3 Pa) and the downstream (-2.5 Pa) is relatively large. Highly packed pins restricted the air flow through, therefore a high pressure area occurred at the upstream of the channel. At the downstream of the channel, back pressure was detected because of the recirculation flow generated behind the pins as depicted in Figure 8-8. The figure illustrates that recirculation occurred at the downstream further away from the pins therefore it does not enhance the heat transfer at the final row nevertheless, it increased the pressure drop. Larger pins' spacing permits more air flow to flow through and therefore, the pressure loss across those pins are smaller as illustrated in Figure 8-9. Table 7-4 showed that models with smaller spacing would create back pressure. This is due to flow separation which occurred at the downstream of the channel as depicted in Figure 8-2. Flow separation occurred when the air flow is divergent [73]. On larger spacing, air is able to flow through the spacing and

117

thus, the streamlines would diverge more slowly and the tendency for separation could be reduced. Figure 8-10 illustrates the velocity vectors of a horizontal plane across model S18.5. The figure shows that the downstream air velocity is much more uniform compared to Figure 8-8. Figure 8-11 summarised the pressure difference of different pin spacing models. The model which caused the highest pressure drop is the Benchmark model and the lowest pressure drop is the model S21.5. The simulation results show that the pressure difference gradient reduces as the spacing increases as depicted in Figure 8-11. As air decelerates, the pressure increases cause a high pressure area to occur at the upstream of the channel.
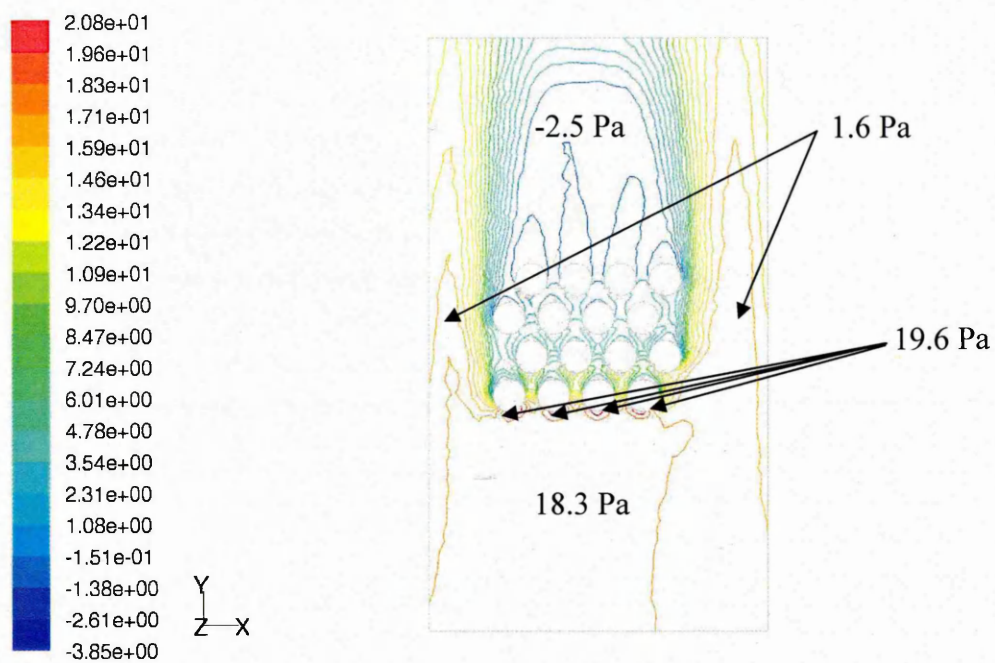
Contours of Total Pressure (pascal)

Sep 14, 2007
FLUENT 6.2 (3d, segregated, ske)

Figure 8-7: Pressure contours on benchmark model
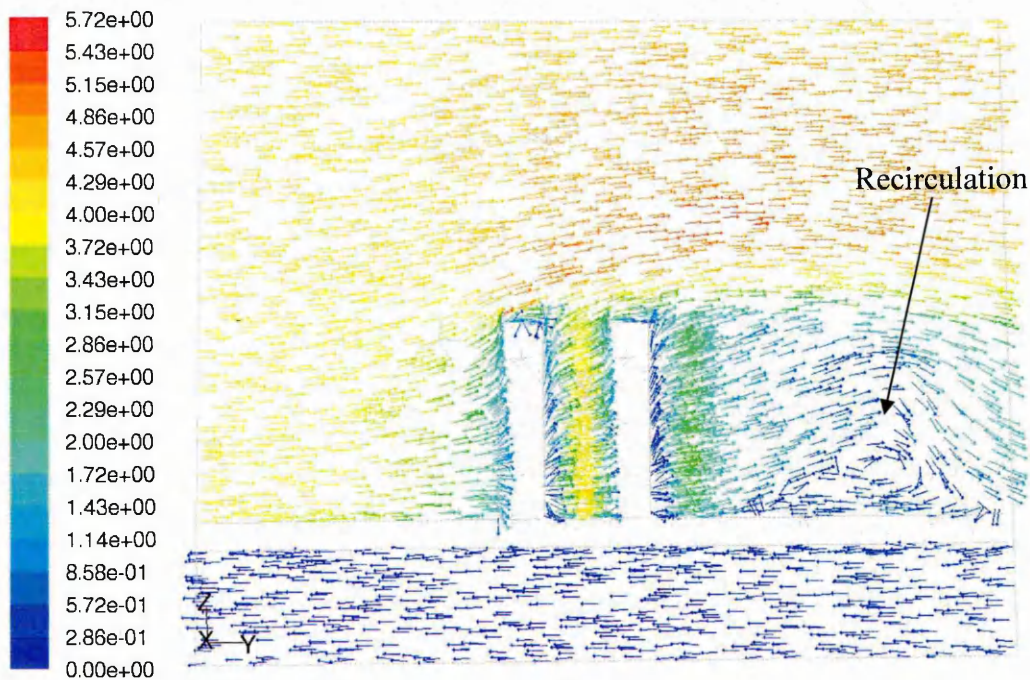
Velocity Vectors Colored By Velocity Magnitude (m/s)

Dec 07, 2007
FLUENT 6.2 (3d, segregated, ske)

Figure 8-8: Benchmark model's velocity vectors (horizontal plane)

119
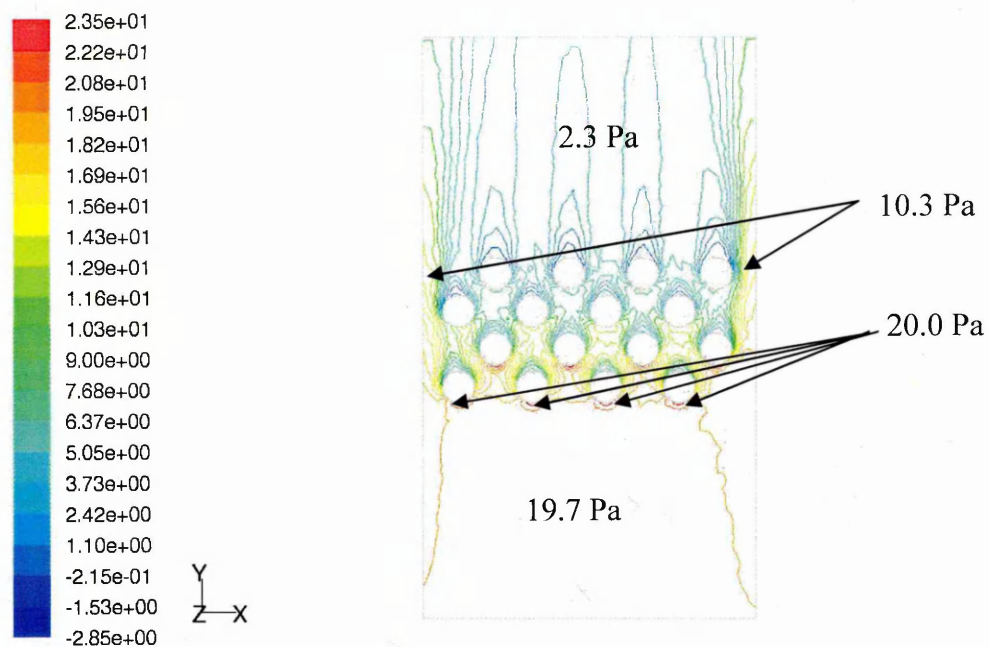
Contours of Total Pressure (pascal)   Sep 14, 2007
                                              FLUENT 6.2 (3d, segregated, ske)

Figure 8-9: Pressure contours on S18.5 model
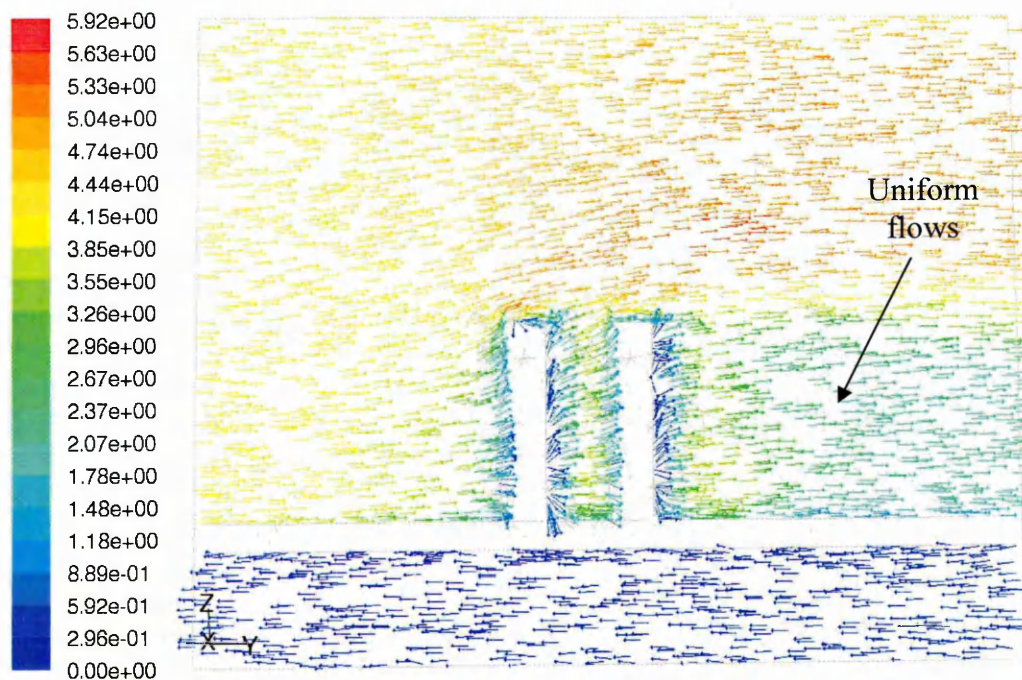
Velocity Vectors Colored By Velocity Magnitude (m/s)   Dec 07, 2007
                                              FLUENT 6.2 (3d, segregated, ske)

Figure 8-10: Velocity vectors of model S18.5 (horizontal plane)

120
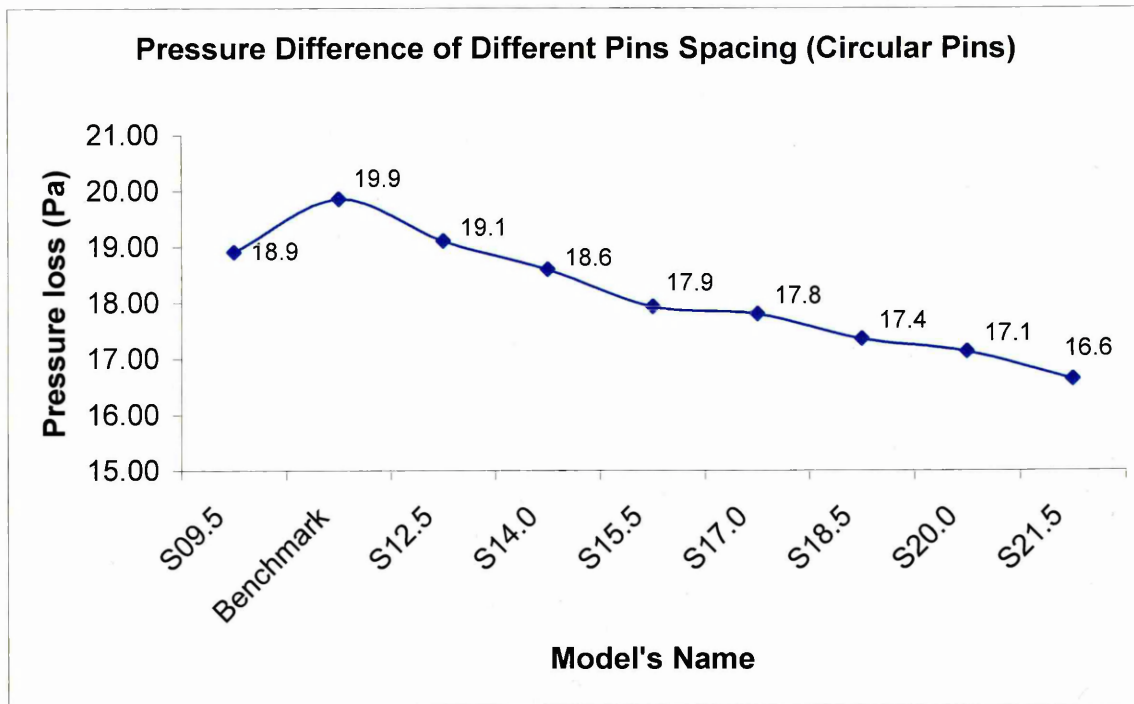
Figure 8-11: Pressure difference of different pins' spacing
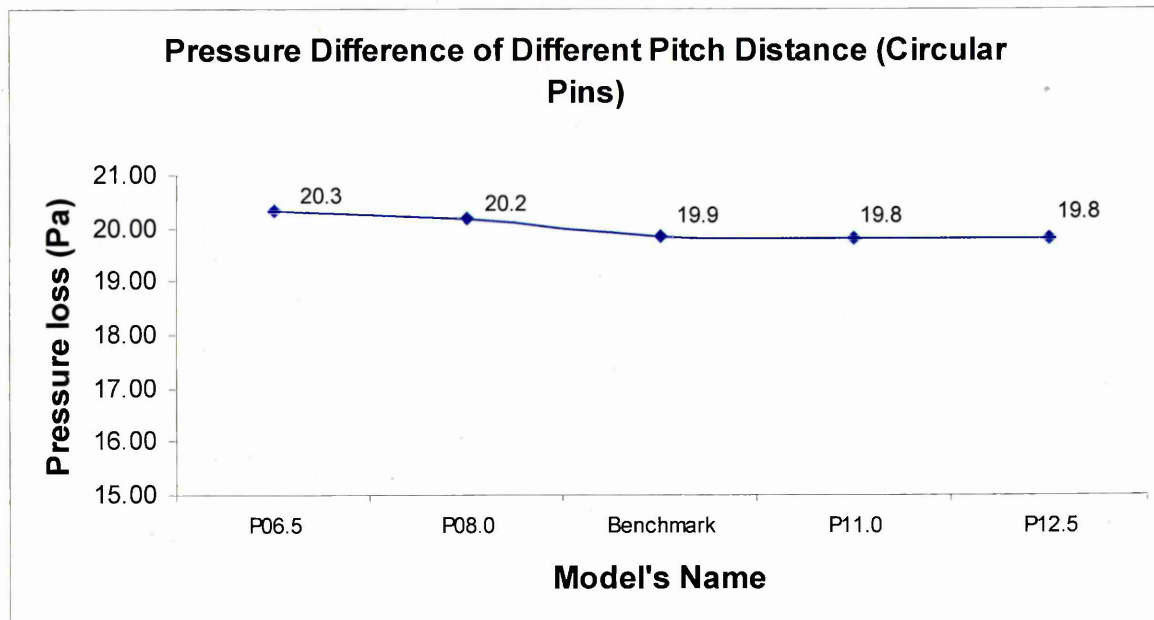
Figure 8-12: Pressure difference of different pitch distance

121

Figure 8-12 summarises the pressure difference across each model with different pitch distance. It can be seen that changing the pitch distance does not give any significant improvement on pressure loss. The highest pressure drop is 20.3 Pa in model P06.5 and the lowest pressure drop is 19.8 Pa with 12.5 mm pitch distance. Smaller pin spacing with larger pitch distance would not improve either the heat transfer or the pressure loss. This study shows that smaller pin spacing with larger pitch distance creates high back pressure behind the pins. This is due to the extent of divergent regions as depicted in Figure 8-13. This effect not only creates high back pressure at the downstream of the pins but it also affects the heat transfer on the last row of pins.
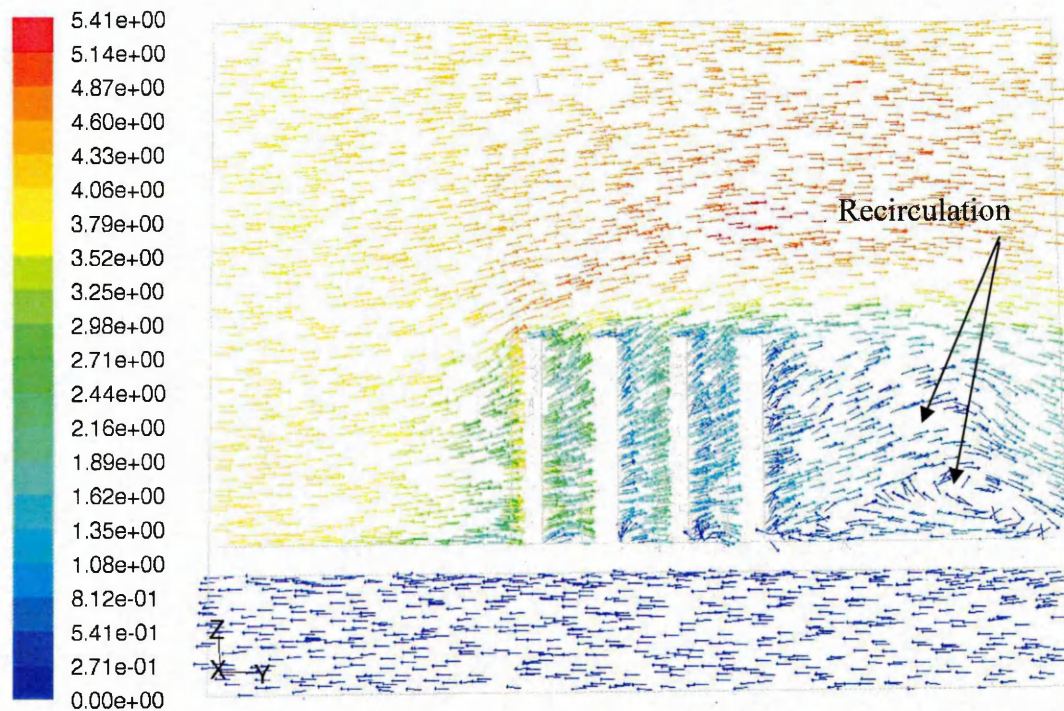
Figure 8-13: Velocity vectors of model P12.5 (horizontal plane)

8.3 Circular Pins Performance Summary

This research shows that heat transfer and pressure loss across a bank of pins is more sensitive to a change in pins' spacing. Whereas altering the pitch distance is not an effective parameter to improve the heat transfer rate or pressure loss on a heat exchanger. A further study was conducted to justify the effectiveness of changing the pins' spacing. A benchmark model with an extra 10 pin evenly distributed across the hot air channel was created to be compared with model S18.5. Table 8-1 summarises the improvement of Benchmark-26 against S18.5 model. The table shows that the 10 extra pins on Benchmark-26 can increase the heat transfer up to 26%, but the pressure difference also increased to almost double the fan demand of 44%.

Although model S18.5 can only produce an extra 10% improvement in total energy transfer compared to the benchmark model, pin temperatures across each row is more uniformly distributed. Figure 8-14 illustrates the Benchmark-26 model's temperature contours across each row of the pins. It clearly illustrates that high temperature is concentrated on the first two rows of the pins. In order to compare the temperature distribution in model S18.5, the same scale colour map was used in Figure 8-15. The figure shows that the temperature distribution is more uniform than the Benchmark-26 model.

Figure 8-16 illustrates that the upstream pressure increased dramatically to 27.5 Pa at the upstream of the pins. This effect can be analysed by studying the hot air flow velocity vectors in Figure 8-17. The colour map on the left represents the velocity values and the colour map on the right represents the temperature values of each pins. The upstream air velocity reduces to 2.5 m/s compared with 3.9 m/s in model S18.5. Based on Bernoulli's equation pressure loss is inversely proportional to the velocity. Therefore, when hot air velocity reduced dramatically, high pressure occurred. The disadvantage of this effect is that it requires a larger fan or pump to overcome the pressure loss across the bank of the pins and thus generates noise.

Table 8-1: Comparison between pins' spacing and number of pins

Model's Name	Spacing (mm)	Pitch (mm)	Number of Pins	Pressure Different (Pa)	Total Energy Transfer (W)	Improvement %
Benchmark	11	9.5	16	19.9	216.9	N/A
Benchmark-26	11	9.5	26	28.6	274.0	26%
S18.5	18.5	9.5	16	17.4	240.2	11%

This extended study shows that although the Benchmark-26 model has higher total energy transfer, hot spots also occurred at the front rows of the pins. This part of the research concluded that pins' spacing is one of the important parameters on design optimisation. At a given flow rate, an optimum pins' spacing and pitch distance must be defined to maximise the heat exchanger performance.
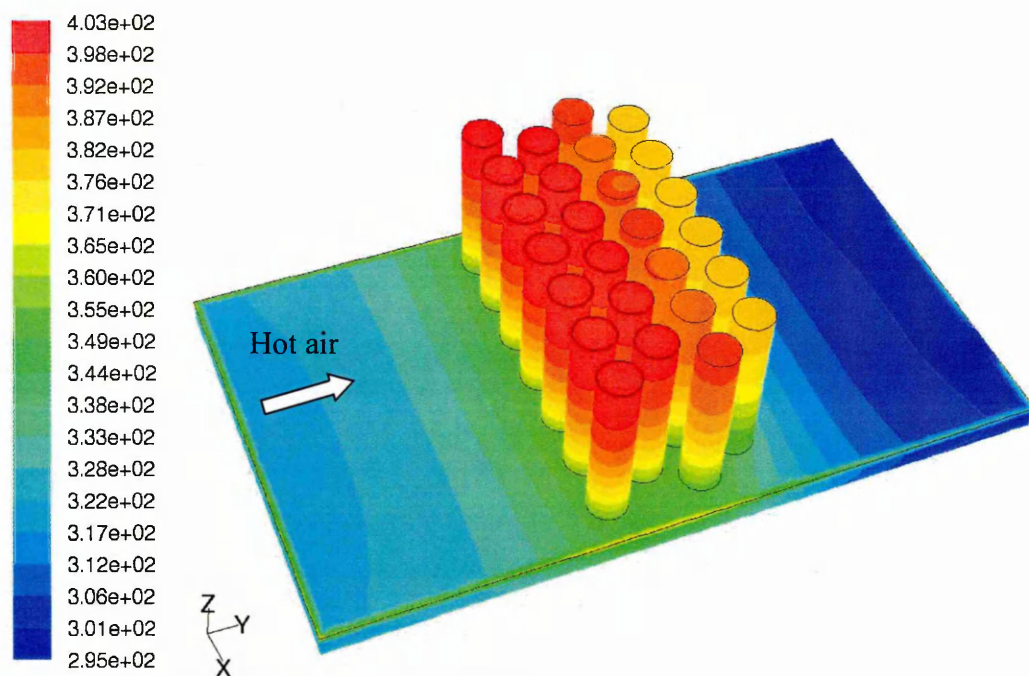
Figure 8-14: Temperature contours of Benchmark-26 model
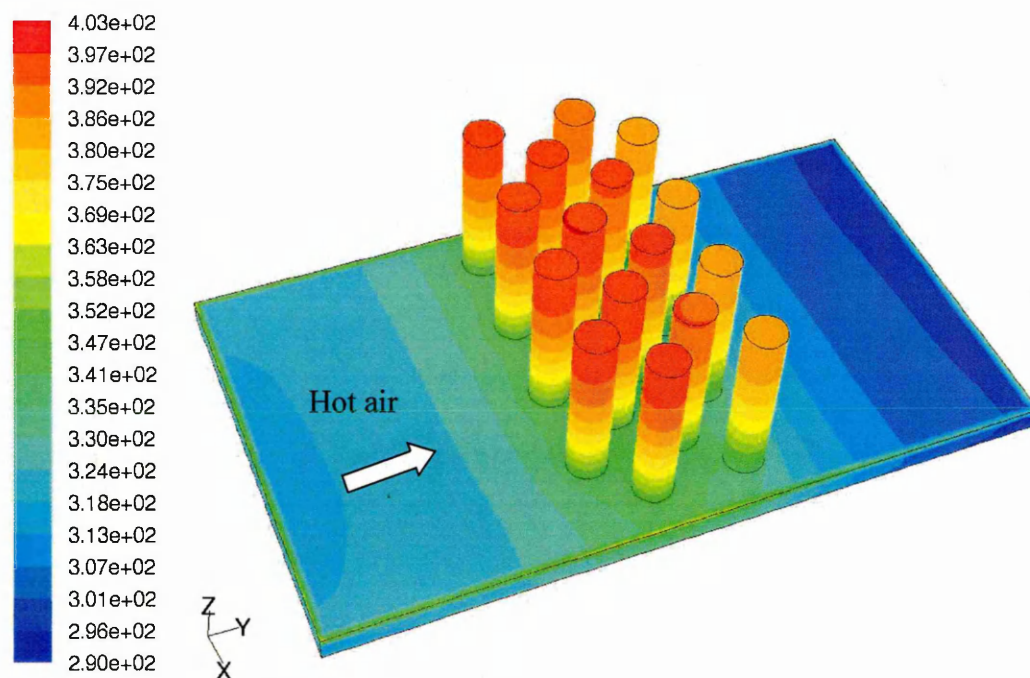
Figure 8-15: Temperature contours of model S18.5
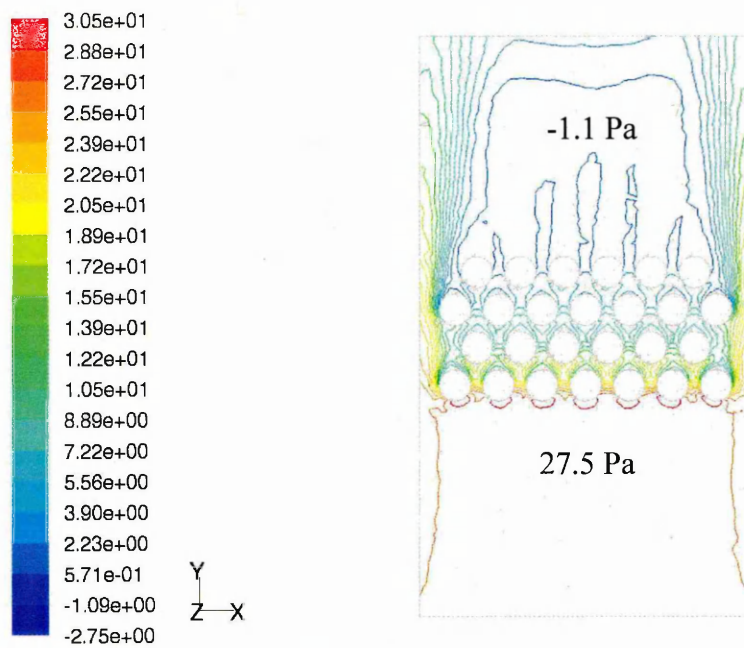
125

Figure 8-16: Total pressure contours of Benchmark-26 model
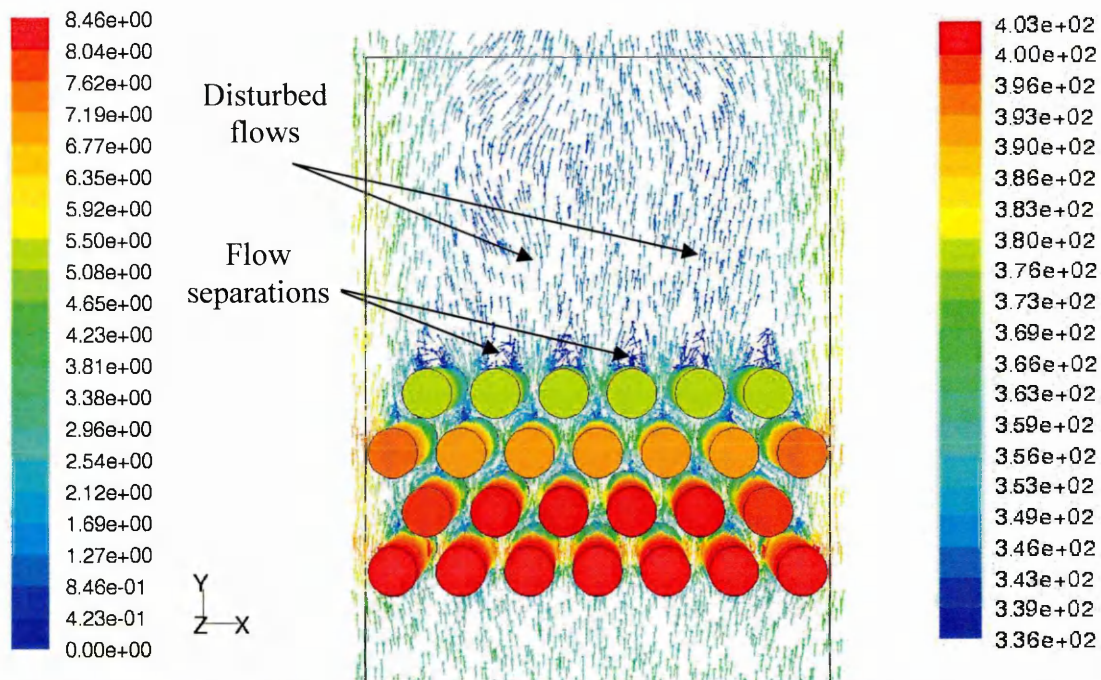
Figure 8-17: Velocity vectors of Benchmark-26 model

126

8.4 Thermal Performance of Elliptical Pins

In order to compare the thermal and fluid flow performance of model S18.5 with elliptical models, all models must maintain the same volume, pins' spacing and pitch. Table 7-3 was generated to show the major and minor axis of each elliptical model. Four elliptical models were created for comparison. The smaller the minor axis is, the thinner the pins will be. It can be seen in Table 7-3, elliptical models' thermal performance outperform all circular pins in this study. Figure 8-18 summarised the elliptical pins' total energy transfer. The figure shows that the flatter the ellipses are the higher the total heat transfer will be. Study shows that the Ellip(6.4, 2.5) gained extras 17% in total energy transfer and Ellip(10.0, 1.6) gained up to 23 % in total energy transfer in comparison with model S18.5. These results agreed with Matos *et al.* [16] published work. They claimed that the thinner the pins, the higher the heat transfer will be.
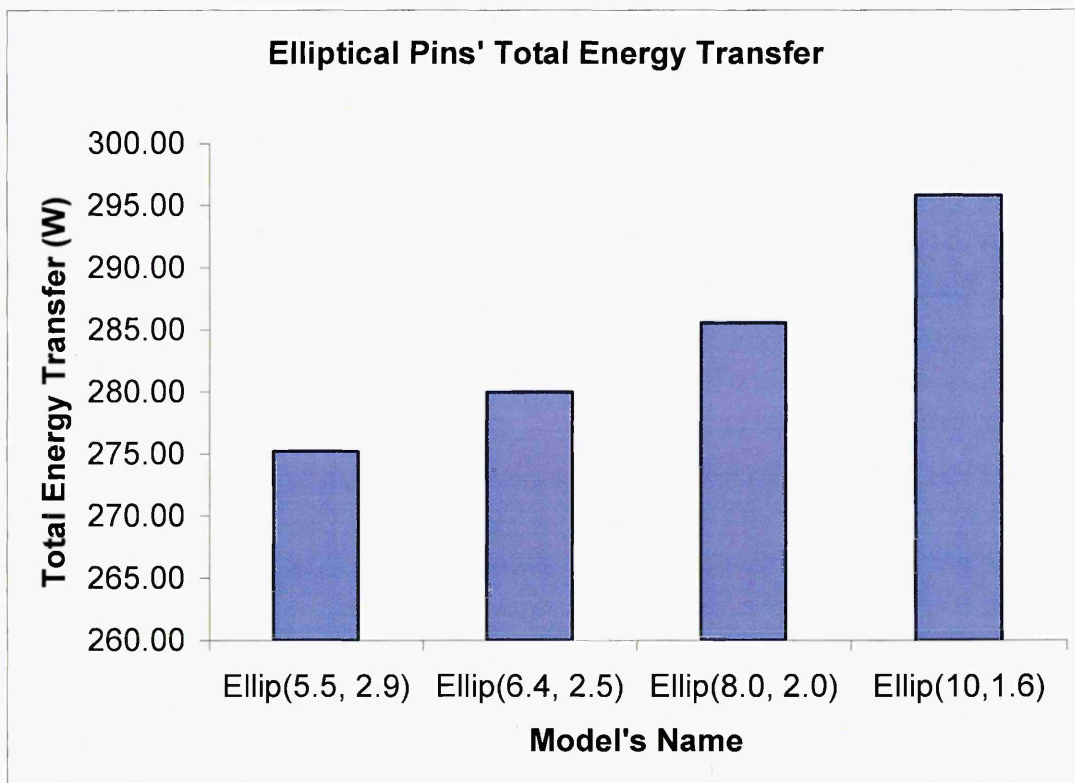
Figure 8-18: Total energy transfer of different eccentricity

Elliptical pins outperform circular pins because the tendency of flow separation on elliptical pins is lower than circular pins. As discussed earlier, fluids tend to leave the boundary whenever the streamlines are divergent and this is known as flow separation. It can be seen on Figure 8-19, Ellip(5.5, 2.9) model is slightly thinner than the circular pins. Therefore the flow separation occurred near to the end of the pins instead of the middle as on circular pins. The colour map on the left represents the velocity values and the colour map on the right represents the temperature values of each pins. When thinner elliptical pins were used as shown in Figure 8-20, fluid has more surface contact area and thus heat transfer rate increases. On circular pin the main heat transfer occurs at the frontal area of the pin. Furthermore, flow separation starts to occur at the middle of the pin. Whereas, on elliptical pin an extended surface area exposed to the heat source therefore, heat transfer rate increase.
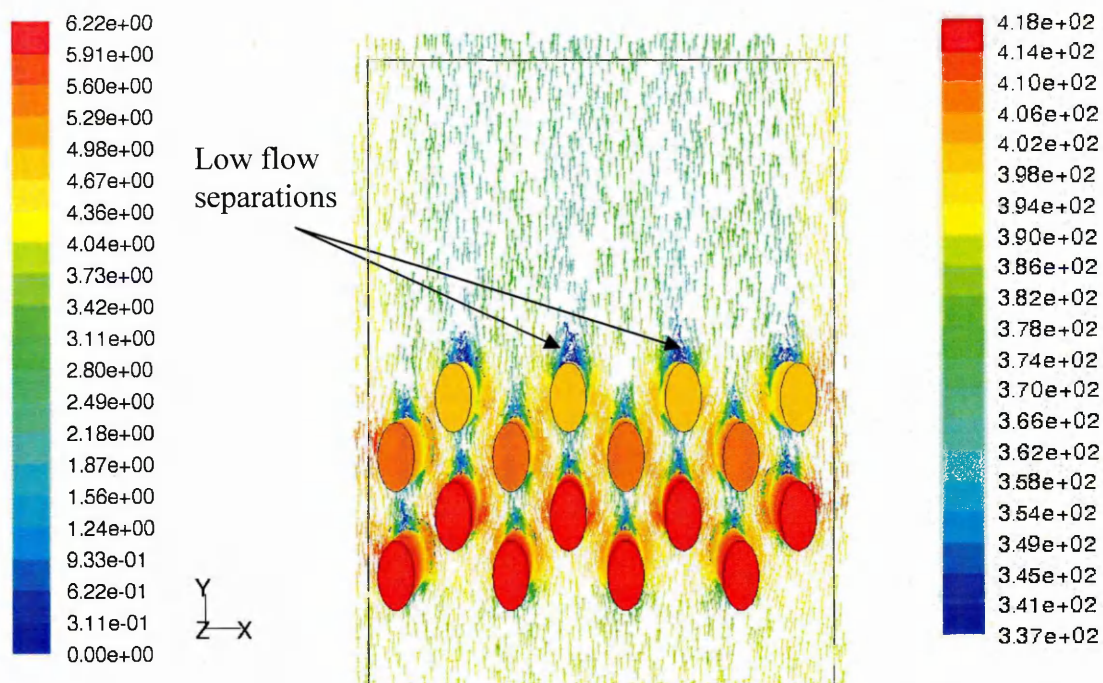
Figure 8-19: Velocity flow vectors of Ellip(5.5, 2.9)
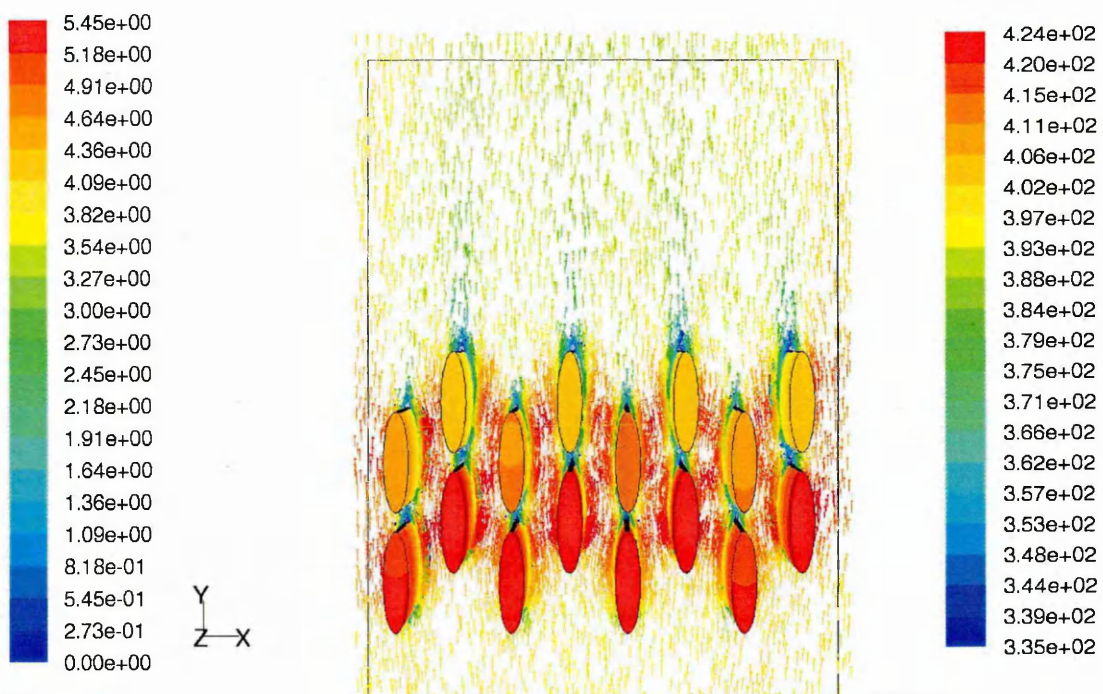
Figure 8-20: Model Ellip(8.0, 2.0) velocity flow vectors

129

Table 7-3 shows that the Ellip(10.0, 1.6) model has the largest major axis. Due to the extended major axis of 10 mm, it makes Ellip(10.0, 1.6) distinctive from other elliptical models as shown in Figure 8-21. Large major axis connected the first row to the third row and second row to the fourth row. Hence, heat transfer increased towards the back rows of pins. This model also shows that smaller minor axis reduces the flow separation rate. This research shows that Ellip(10.0, 1.6) has the best heat transfer compared to the other elliptical models.
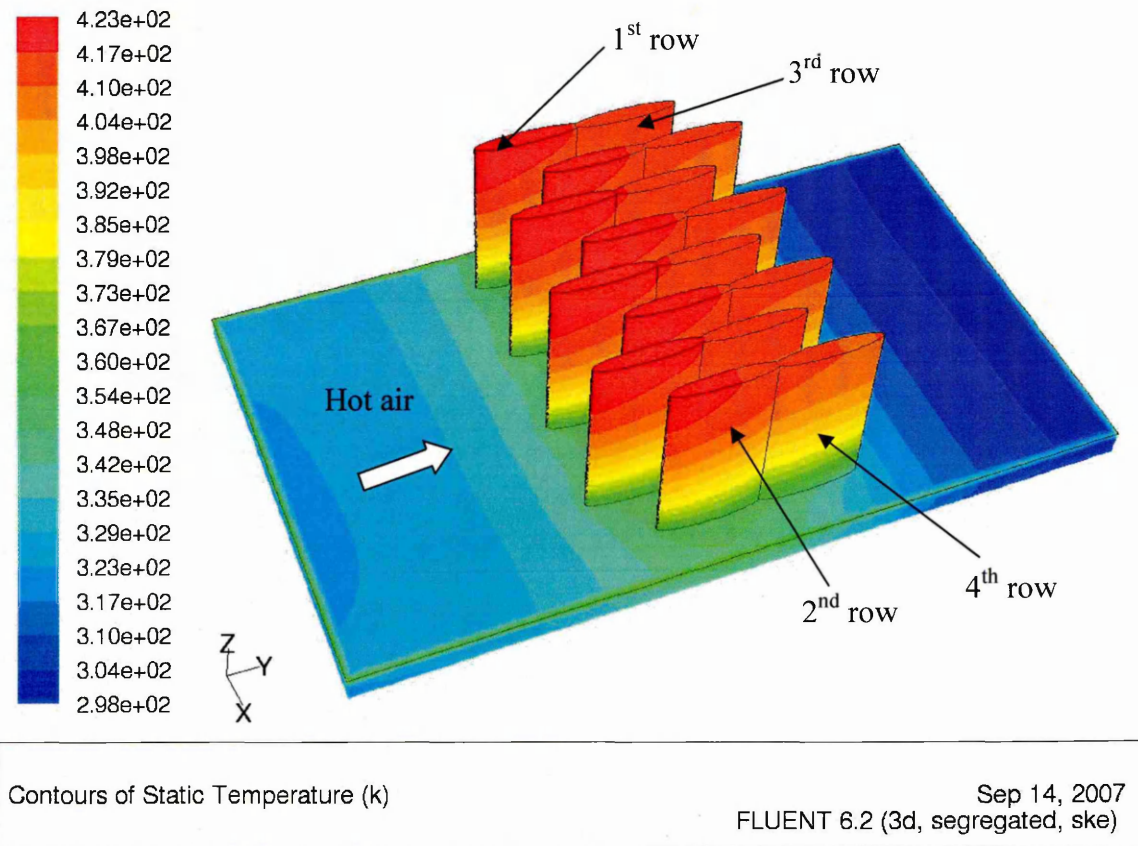
Figure 8-21: Model Ellip(10.0, 1.6) pins temperature contours

130

8.5 Elliptical Pins – Pressure Difference

Simulation results on Table 7-5 shows that the elliptical models have less pressure drop than the circular pin models. The highest pressure difference occurred on elliptical model is Ellip(5.5, 2.9) because it has the largest minor axis of 2.9 mm. Figure 8-22 shows the pressure difference measured on the upstream and downstream of the channel on model Ellip(5.5, 2.9). Comparing this figure with Figure 8-23, the pressure contours plot shows that less mechanical power is required for thinner elliptical pins. Due to the aerodynamic shape, thinner elliptical pins generate less flow separation at the downstream of the channel. Furthermore, pressure behind those elliptical pins in Figure 8-23 is more uniform compared to circular pins. Figure 8-24 summarised the pressure difference of each elliptical model. The figure shows that Ellip(5.5,2.9) has the highest pressure drop of 12.1 Pa among the elliptical models and Ellip(10,1.6) has the lowest pressure drop of 6.9 Pa. The graph shows that the thinner the pins, less fan power required the overcome the pressure loss.
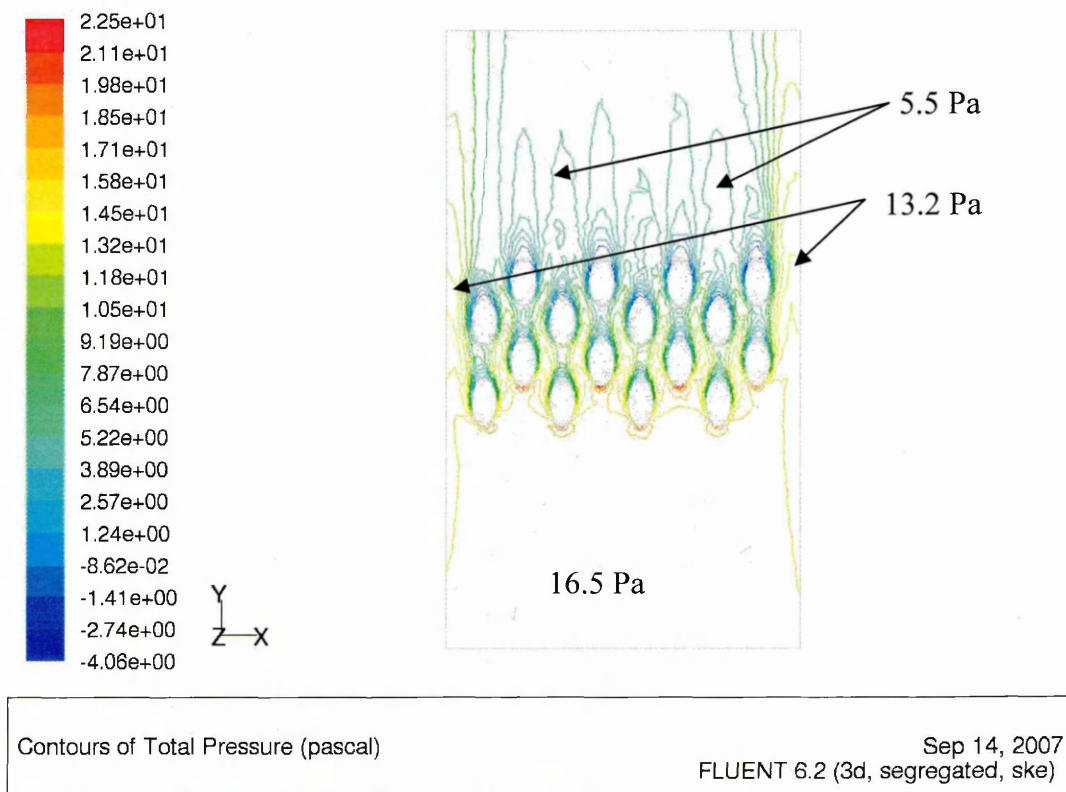
Figure 8-22: Pressure contours of Ellip(5.5, 2.9) model

Contours of Total Pressure (pascal)

Sep 14, 2007
FLUENT 6.2 (3d, segregated, ske)
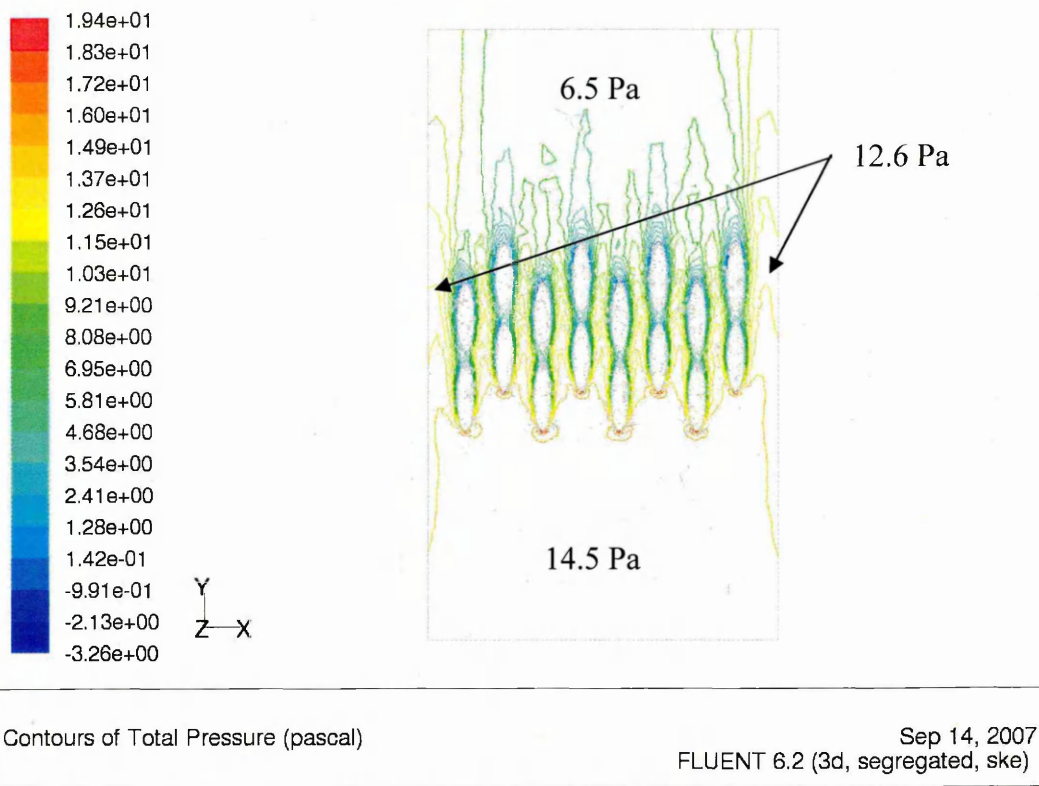
Figure 8-23: Pressure distribution on Ellip(8.0, 2.0) model
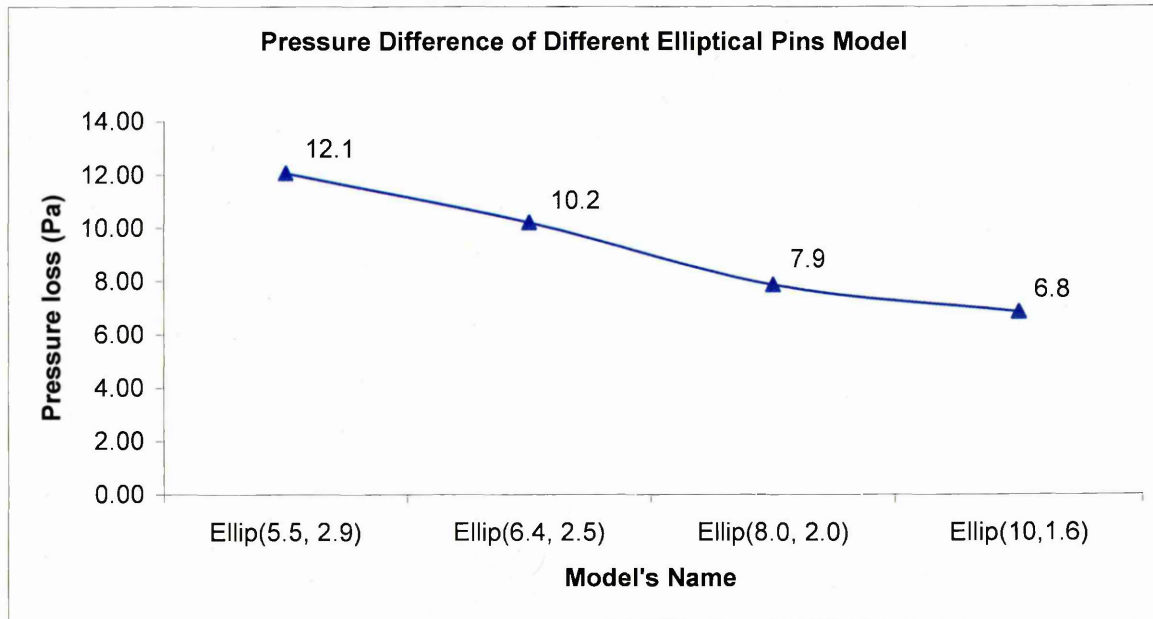
Figure 8-24: Pressure difference of different elliptical pins model

8.6 Pins' Performance Summary

Figure 8-25 summarises the total energy transfer and pressure difference of all the models. On the left hand side of the Y-axis summarised the total energy transfer of each models and on the right hand side of the Y-axis summarised the pressure loss of all models. It can be seen that elliptical pins have the highest total energy transfer and the lowest pressure difference. It outperformed circular pins with either larger spacing or pitch distance. The simulation results show that smaller spacing and pitch distance could not effectively increase the heat exchanger efficiency. This study also shows that smaller spacing or pitch distance causes higher pressure drop compared to the benchmark model. The optimum circular pins' spacing is 18.5 mm where, total energy transfer increased by 11 % compared to the benchmark model. This study showed that the elliptical model reduced the pressure difference up to 36% compared with circular pins. Although only four models were used to study the thermal and fluid flow performance of elliptical pins, it is certain that elliptical pins can replace conventional circular pins' heat exchangers in the near future.
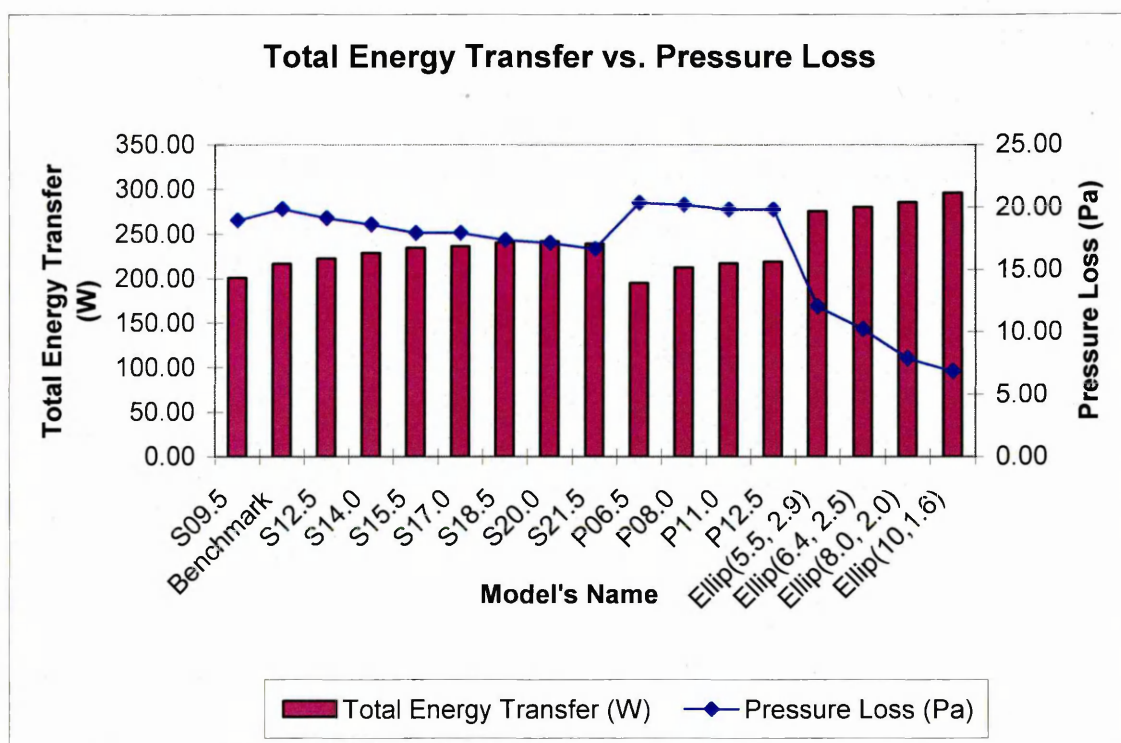
Figure 8-25: Heat transfer and pressure difference performance graph

Chapter 9   Experimental Results

Introduction

Due to high manufacturing costs and time consuming to manufacture all 17 models, only four distinctive models are selected for experimental testing. The elected models are:

1. Benchmark model
2. Model S18.5
3. Model Ellip(8.0,2.0)
4. Model Ellip(10,1.6)

The Benchmark model is selected because it is used in the sponsor's current heat exchanger's heat chamber. Numerical simulation results presented in Table 7-1 showed that 18.5 mm is the optimum configuration for circular pins. Therefore, model S18.5 was selected for experimental testing.

Model Ellip(8.0,2.0) was elected for experimental testing due to its high heat transfer rate in comparison to the circular pins. Model Ellip(10,1.6) has a very distinctive geometry than other elliptical pin models as the first row and third row was joined together. Therefore, model Ellip(10,1.6) was selected for experimental testing.

This chapter describes the experimental conditions and results acquired from the experimental tests. Each experimental test results were recorded at three different air flow temperatures. The experimental test results were recorded when the air flow temperature within the tunnel reached 50°C, 100°C and 200°C. The only data used for the numerical validation are when air flow temperature reached and maintained at 200°C.

When reaching the set experimental test conditions, pin core temperatures, water inlet and outlet temperatures were recorded during the experimental tests for the duration of 13 minutes. In order to validate the numerical simulation results, all the numerical models

were set to similar boundary conditions as the experimental tests. Each model was experimentally tested three times to assess repeatability, minimise errors and uncertainties.

9.1 Experimental Testing Parameters

The wind tunnel hot air temperature is maintained at 474 ± 2.4 K, average air velocity is maintained at 4 ± 0.06 m/s. The water flow rate and the water inlet temperature were maintained at 0.5 ± 0.05 L/min and 295 ± 1.5 K respectively. The data loggers were set to record data every second for a period of 13 minutes for each test.

9.2 The Benchmark Model Experimental Results

Table 9-1 summarises the experimental results acquired for the Benchmark model. Figure 9-1 illustrates the location of the embedded thermocouples within the Benchmark model. Measured pin core temperatures are recorded in Table 9-1. The table also lists the numerical simulation results of the pin core temperatures. Guided by the measured water inlet temperature from the experimental test, a water inlet temperature of 295.3 K boundary condition was imposed on the numerical simulation. The table also lists the calculated total energy transfer using Equation 7-1. The last column summarises the percentage difference between the experimental data and numerical simulation.

Table 9-1: Experimental and numerical simulation results of the Benchmark model

Pins' Position	Experimental Results (K)	Numerical Simulation (K)	%
P(1,2)	424.9	394.9	7%
P(1,4)	407.8	393.6	3%
P(2,2)	425.0	384.2	10%
P(3,3)	396.9	370.3	7%
P(4,2)	387.7	370.3	4%
P(4,4)	372.7	369.2	1%
Water inlet temperature	295.3	295.3	N/A
Water outlet temperature	302.5	301.4	0%
Total energy transfer (W)	247.9	211.1	15%
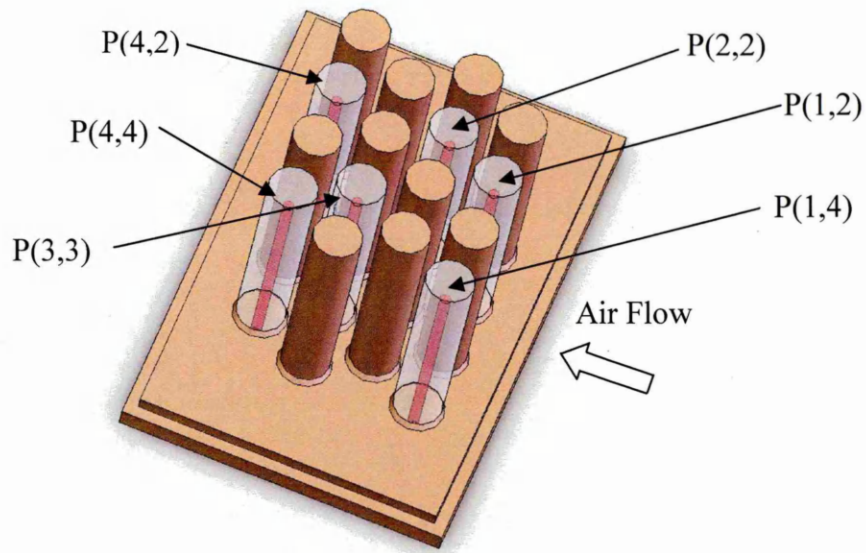
Figure 9-1: Thermocouples positions in Benchmark model

9.3 Model S18.5 Experimental Results

Table 9-2 summarises the experimental and numerical results of the model S18.5. The pin core temperatures, water inlet and outlet temperatures and percentage difference are listed in the table. The total energy transfer was calculated using Equation 7-1. The results given below are based on **Error! Reference source not found.** experimental test conditions. Figure 9-2 illustrates the position of the thermocouples in model S18.5.

Table 9-2: Experimental and numerical simulation results of model S18.5

Pins' Position	Experimental Results (K)	Numerical Simulation (K)	%
P(1,2)	399.6	396.1	1%
P(1,4)	373.8	395.2	-6%
P(2,2)	400.7	397.2	1%
P(3,3)	398.4	392.6	1%
P(4,2)	390.1	385.1	1%
P(4,4)	380.1	384.2	-1%
Water inlet temperature	295.2	295.2	N/A
Water outlet temperature	302.2	301.9	0%
Total energy transfer (W)	244.0	233.1	4%
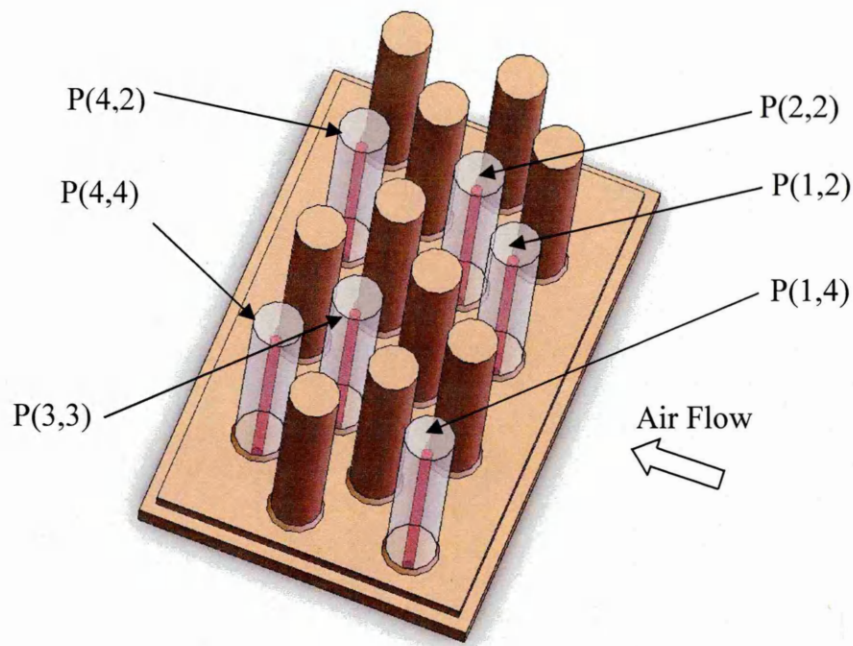
Figure 9-2: Thermocouples positions in model S18.5

9.4 Model Ellip(8.0, 2.0) Experimental Results

Table 9-3 summarises the experimental and numerical simulation results of the Ellip(8.0, 2.0) model. Pin core temperatures were recorded during the experimental test in order to validate the numerical simulation results. The thermocouples positions within the model are depicted in Figure 9-3.

Table 9-3: Experimental and numerical simulation results of Ellip(8.0, 2.0) model

Pins' Position	Experimental Results (K)	Numerical Simulation (K)	%
P(1,2)	418.3	420.2	0%
P(1,4)	404.8	419.7	-4%
P(2,2)	425.6	422.1	1%
P(3,3)	384.3	410.8	-7%
P(4,2)	404.2	404.1	0%
P(4,4)	374.4	403.7	-8%
Water inlet temperature	294.9	294.9	N/A
Water outlet temperature	302.5	302.9	0%
Total energy transfer (W)	263.1	278.2	-6%

137
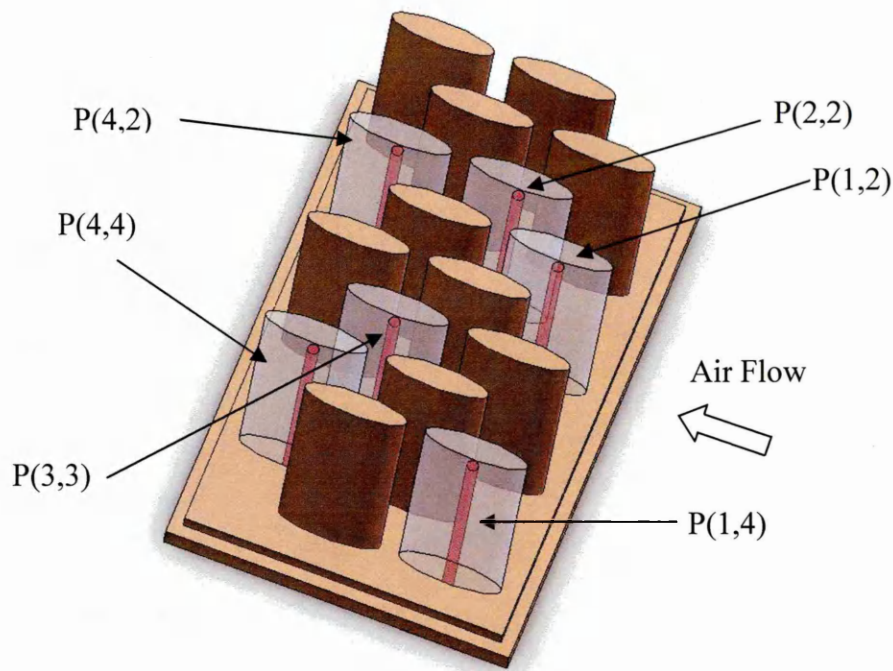
Figure 9-3: Thermocouples positions in model Ellip(8.0, 2.0)

9.5 Model Ellip(10.0, 1.6) Experimental Results

Table 9-4 summarises the numerical and experimental pins and water temperatures of Ellip(10.0, 1.6) model. Due to the small minor axis of the elliptical pins, thermocouples could not be used in this model to experimentally measure the pin core temperatures. Therefore, only numerical results of the pin core temperatures are presented in the table along with the water inlet and outlet temperatures. The table also gives the calculated total energy transfer of model Ellip(10.0,1.6).

Table 9-4: Experimental and numerical simulation results of Ellip(10.0, 1.6) model

Pins' Position	Experimental Results (K)	Numerical Simulation (K)	%
P(1,2)	N/A	420.0	N/A
P(1,4)	N/A	418.9	N/A
P(2,2)	N/A	419.3	N/A
P(3,3)	N/A	415.0	N/A
P(4,2)	N/A	412.2	N/A
P(4,4)	N/A	411.5	N/A
Water inlet temperature	295.9	295.9	N/A
Water outlet temperature	303.6	304.2	0%
Total energy transfer (W)	267.1	287.5	-8%

Summary

This chapter listed the operational flow conditions used in the experimental tests. This chapter also summarised the experimental data acquired from the TWT for the Benchmark model, model S18.5, model Ellip(8.0,2.0) and model Ellip(10.0,1.6). The data acquired includes the pin core temperatures, water inlet and outlet temperatures of each model. In order to validate the numerical results, all models retained the same boundary conditions as the experimental test conditions.

Chapter 10   Experimental Results Analysis

Introduction

This chapter presents an analysis of the experimental data acquired from the TWT. The experimental data acquired from the TWT is used to validate the numerical results. Four models are selected to study the heat transfer from the pins side to the water side. The four models are:

1. Benchmark model
2. Model S18.5
3. Model Ellip(8.0, 2.0)
4. Model Ellip(10, 1.6)

This chapter utilised pin core temperatures, water inlet and outlet temperatures from the experimental tests to validate the numerical results. To further understand the models' performance, the increase of water outlet temperature and pins core temperatures against time were recorded.

10.1 Benchmark Model Experimental Results Analysis

Figure 10-1 illustrates the benchmark model's pins core temperature against time. The graph presents the measured temperatures recorded by the embedded thermocouples on P(1,2), P(1,4), P(2,2), P(3,3), P(4,2) and P(4,4). The thermocouple locations were shown in Figure 9-1. The graph shows that temperatures at P(1,2), P(1,4) and P(2,2) are relatively high compared to the third row and fourth row of pins. The average temperature of P(1,2) is 424.9 K, and the average temperatures of P(1,4) and P(2,2) are 407.8K and 425.0 K, respectively. The high temperatures concentration at one area is known as a hot spot. The numerical results presented in Chapter 8 also captured the occurrence of the hot spot at the same locations as the experimental tests. Due to the small spacing, hot air is limited to flow through the pins and thus increased the front rows pin temperatures. In contrast with the last row pins, the core temperature is relatively low. The average temperature of P(4,4) is 372.7 K.

The experimental average water inlet and outlet temperatures were recorded during the test. The measured average water outlet temperature was 302.5 K, which resulted in a total energy transfer of 247.9 W using Equation 7-1. In the numerical simulation, the predicted water outlet temperature was 301.4 K, which gives the total energy transfer of 211.1 W. It is clear that the numerical simulation under predicted the water outlet temperature. At steady state, the numerical simulation under predicted the total energy transfer by 15% compared to the experimental results. This phenomenon was analysed by studying the heat transfer from the pins to the water side during the experimental tests.

Figure 10-2 illustrates the experimental result of the Benchmark model's water outlet temperature against time. The water outlet temperature increased linearly from 301.1 K to 302.5 K in 779 seconds. The water inlet temperature was relatively low for the first 400 seconds. This is due to the small pins' spacing restricted the hot air to flow through the consecutive rows. After the first 400 seconds, the water outlet temperature started to increase linearly and the pins temperature started to drop as depicted in Figure 10-1.
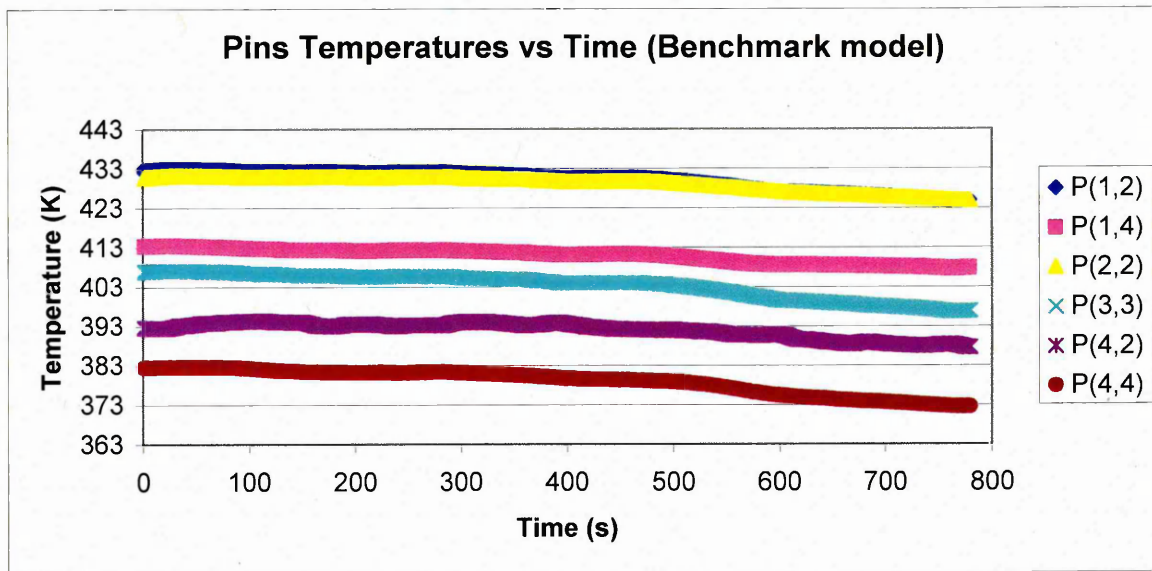
Figure 10-1: Benchmark model's pins core temperature with time
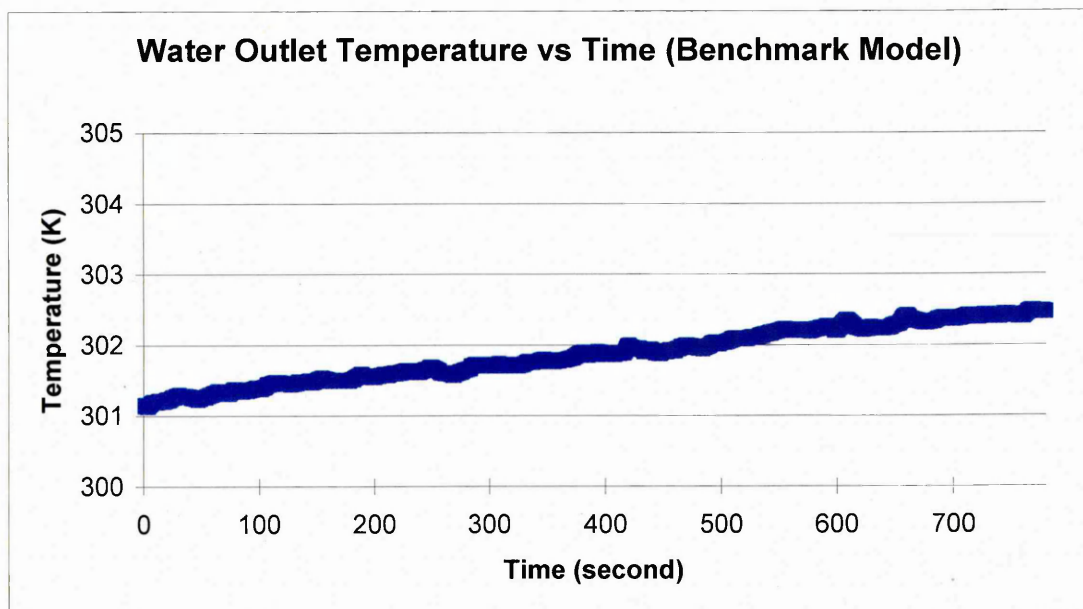
Figure 10-2: Benchmark model's water outlet temperature with time

Figure 10-3 illustrates the pin core temperatures acquired from the experimental tests and its counter part acquired from the numerical predictions. The numerical results under predicted the experimental pin temperatures. Nevertheless, the numerical results sit well within the error scale. The error scale bar shown was calculated in Chapter 6 using a total experimental error of 8%. The figure shows that the experimental results of the pin P(2,2)

drop outside the error scale bar. This could be the cause of air trapped inside the water channel when the experimental test was carried out.
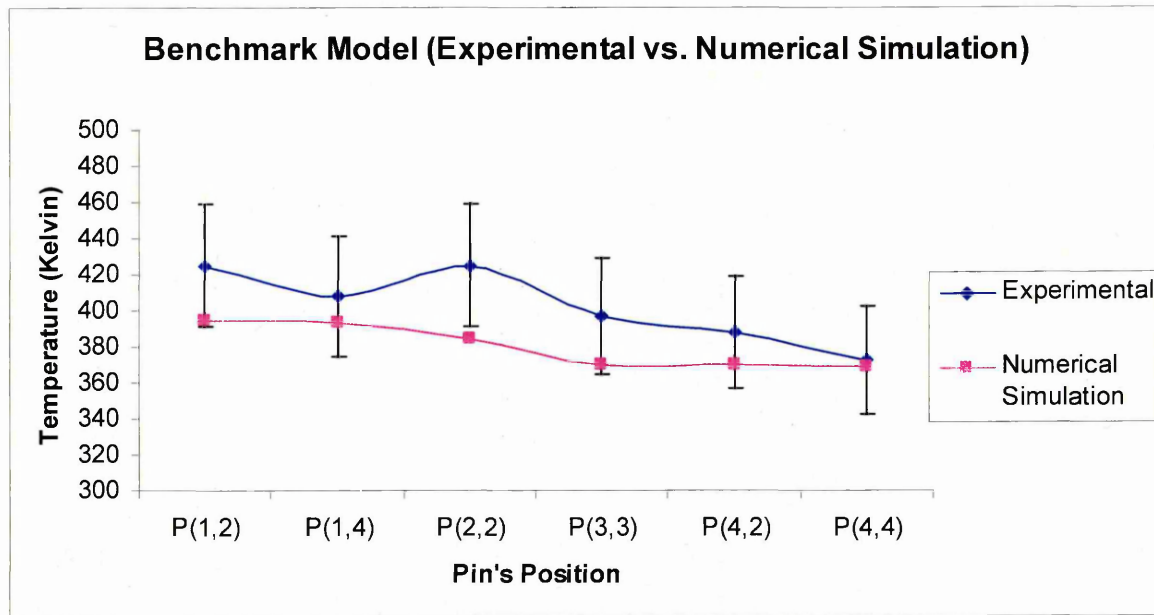
Figure 10-3: Benchmark pins' core temperature

10.2 Model S18.5 Experimental Results Analysis

Figure 10-4 illustrates the pin temperatures of model S18.5 with time. Pin temperatures between 75 - 150 seconds and 300- 500 seconds were not considered due to vacillation of hot air temperature inside the tunnel. The figure showed that the pins core temperature is relatively constant throughout the experimental test period.

The numerical study presented in Chapter 8 highlighted that model S18.5 is more sensitive to the heat source compared to the Benchmark model because is able to penetrate through the bank of pins. Therefore, Figure 10-5 shows that the water outlet temperature started at 302.2 K which is 1.1 K more than the Benchmark model. The water outlet temperatures were between 302 K and 303 K throughout the experimental test.

It can be seen in the figure that there was a trough in between 400 to 550 seconds, this mainly is due to the hot air temperature drop inside the TWT. This section of data was not considered when the total energy transfer was calculated.
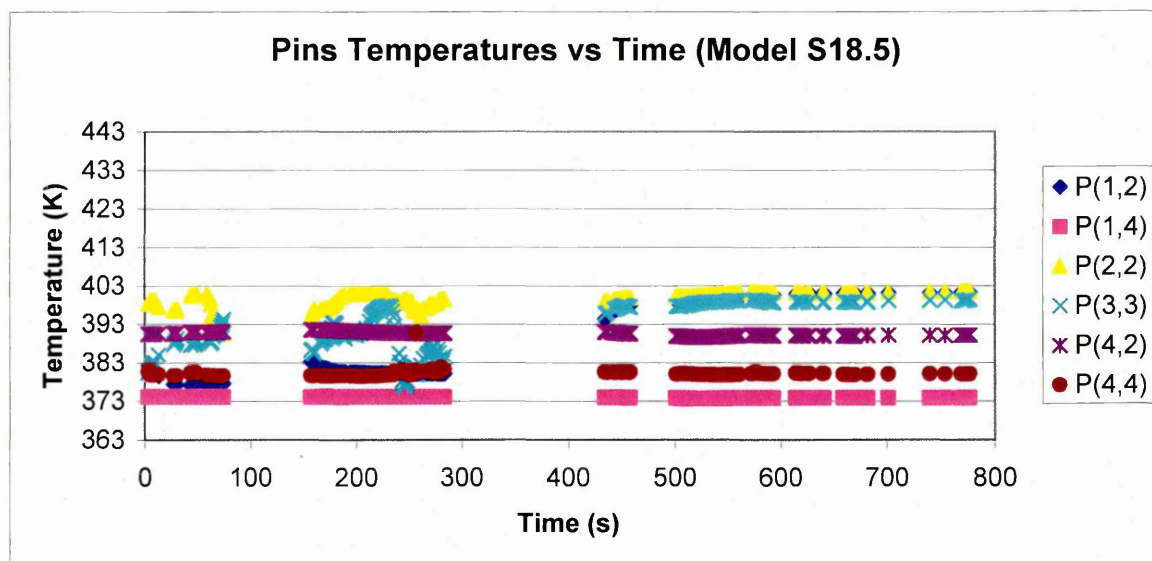
Figure 10-4: Model S18.5 pins temperatures with time
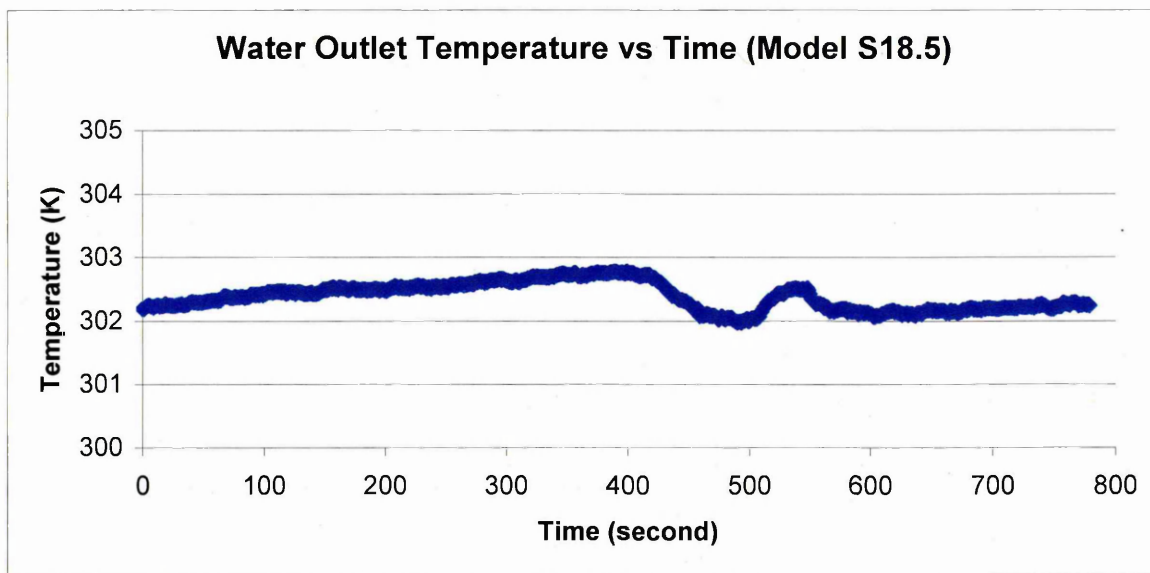
Figure 10-5: Model S18.5 water outlet temperature against time

Figure 10-6 illustrates the pin core temperatures from the experimental data and numerical simulation results. It can be seen the numerical predictions are relatively close to the experimental data acquired from the TWT. Chapter 8 showed that model S18.5 pins' temperature is relatively uniform, unlike the Benchmark model.

Table 9-2 summarises the water inlet and outlet temperatures obtained from the experimental tests and numerical predictions. The measured water outlet temperature was 302.2 K, which gives a total energy of 244 W. Based on the same water inlet temperature taken from the experimental tests, the numerical simulation predicted the water outlet temperature of model S18.5 was 302 K, which gives a total energy of 233.1 W. Once again the experimental data shows that the numerical simulation predictions are valid. The numerical simulation under predicted the total energy transfer by 4%.
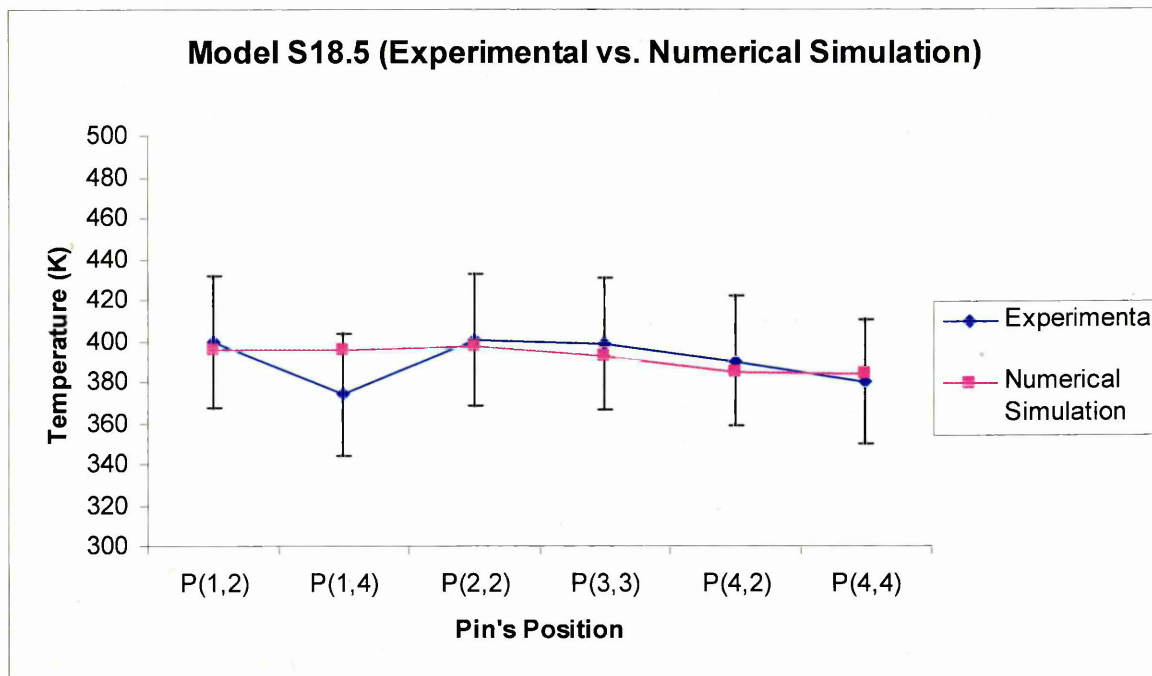
Figure 10-6: Model S18.5 pins' core temperature

10.3 Model Ellip(8.0, 2.0) Experimental Results Analysis

Figure 10-7 illustrates the pin core temperatures of model Ellip(8.0,2.0) with time. The figure shows that the pins core temperatures are constant in comparison with the benchmark model. Although the pins average temperature difference between each row is slightly higher than model S18.5, it generates higher heat transfer as presented in Chapter 8.

To further study the Ellip(8.0, 2.0) model, water outlet temperature against time is depicted in Figure 10-8. The water outlet temperatures remained constant around 302.5 K.

The numerical prediction of the pins core temperatures was almost identical on P(1,2), P(2,2) and P(4,2) as shown in Figure 10-9. Although the other three pin core temperatures were numerically over predicted, they all sit well in the error scale bar.

On this model the average experimental water outlet temperature is 302.5 K, which gives a total energy transfer of 263.1 W. From Table 9-3, the numerical simulation water outlet temperature was 302.9 K and the calculated total energy transfer is 278.2 W. These results show that the numerical prediction is relatively close to the experimental data. The numerical simulation is over predicted the total energy transfer by 6%. The experimental results show that model Ellip(8.0,2.0) is 8% more efficient than the circular model S18.5. The experimental data also validates the numerical predicted results.
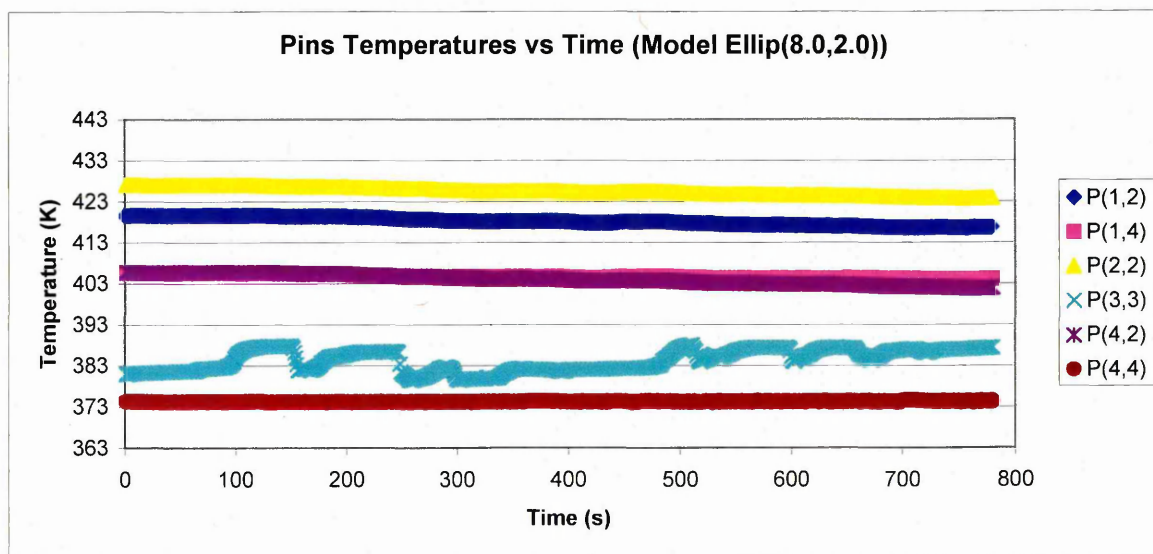
Figure 10-7: Model Ellip(8.0,2.0) pins core temperature with time
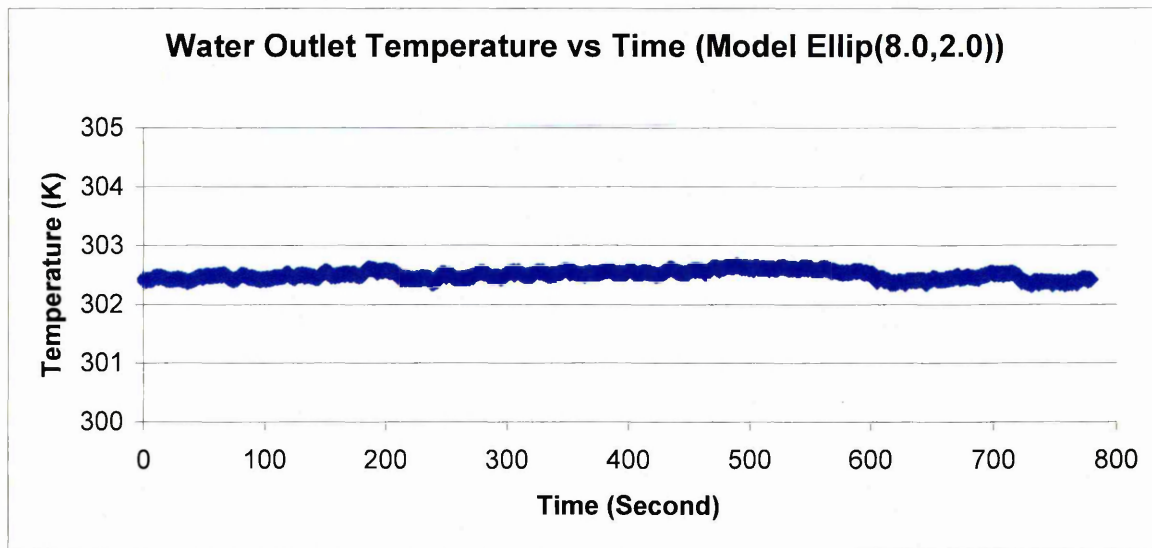
Figure 10-8: Ellip(8.0, 2.0) model's water outlet temperature with time
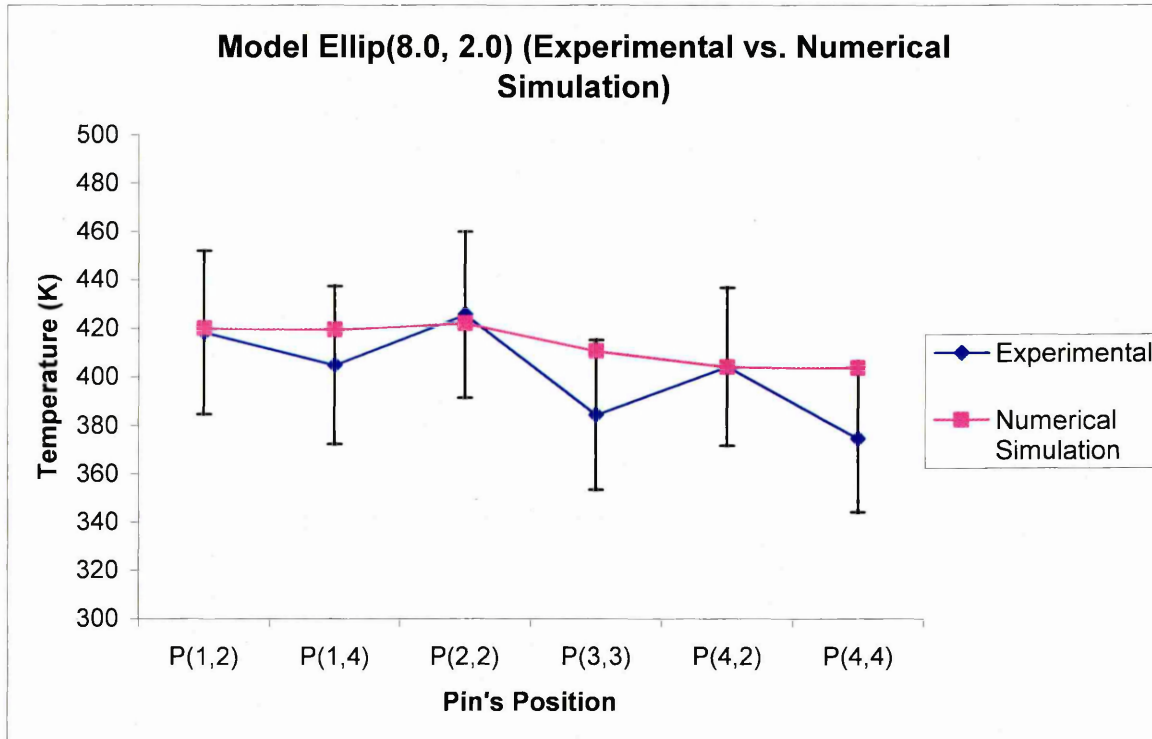
Figure 10-9: Model Ellip(8.0, 2.0) pins' core temperature

148

10.4 Model Ellip(10, 1.6) Experimental Results Analysis

The Ellip(10, 1.6) model is slightly different from the other selected models. Due to the small minor axis of the elliptical pins, the first row united with the second row pins as depicted in Figure 8-21. An experimental test has been carried out on this model to measure the water inlet and outlet temperatures. In Table 9-4, the measured water outlet temperature was 303.6 K and the calculated total energy transfer was 267.1 W. The numerical simulation predicted the water outlet temperature to be 304.2 K and the calculated total energy transfer was 287.5 W. The numerical prediction over predicted the total energy transfer by 7% compared to the experimental data.

Due to the extended surface area of model Ellip(10, 1.6), heat conduction occurred between the first row of pins to the fourth row of pins as seen in Figure 8-21. Figure 10-10 shows the water outlet temperature against time. The water outlet temperature increased linearly from 302.7 K to 304.3 K in 779 seconds. It must be pointed that the model has the highest water outlet temperature at the start of any models. Numerical predictions as depicted in Figure 10-11 shows that the pin core temperatures is relatively uniform compared to other models. If this configuration was applied to a heat exchanger, it would perform better at cold start and reduce the operating time.
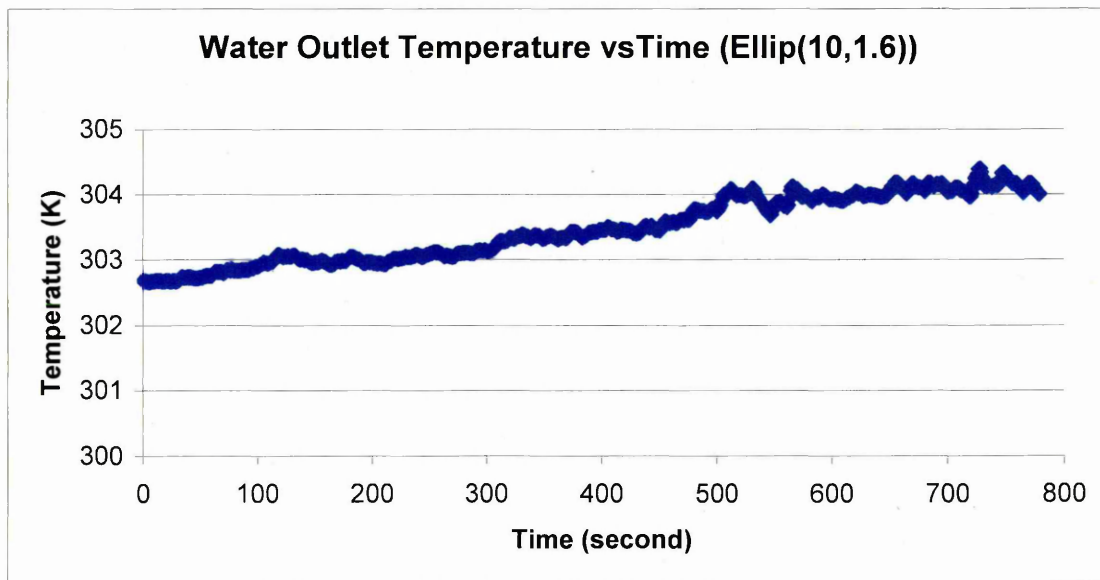
Figure 10-10: Model Ellip(10,1.6) water outlet temperature against time
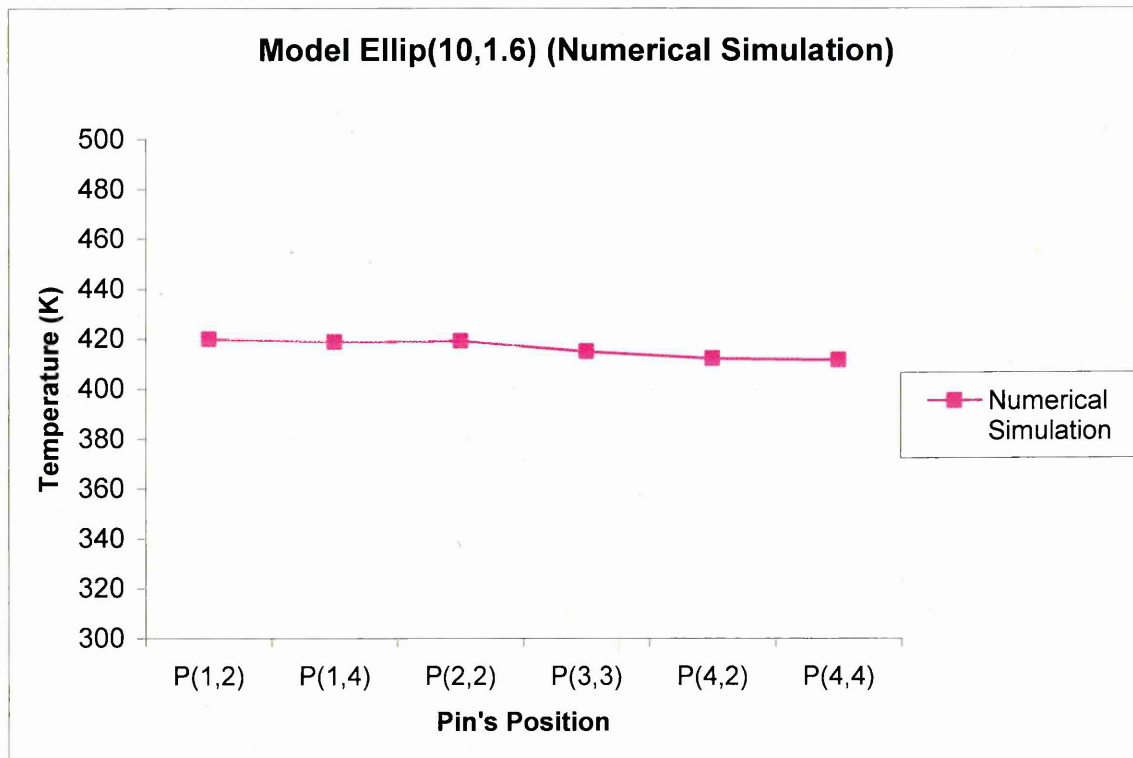
Figure 10-11: Ellip(10, 1.6) model pins' core temperature

Summary

This chapter analysed and validated the numerical predicted results using the data acquired from the experimental tests. Table 10-1 summarises the total energy transfer of each model. Based on the experimental results, the numerical simulation under predicted the Benchmark model's performance by 15 %. The experimental results also showed that the numerical simulation under predicted the S18.5 model's performance by 4 %.

Table 10-1: Total energy transfer of each model

	Experimental Total energy transfer (W)	Numerical Total energy transfer (W)	Percentage Difference (%)
Benchmark	247.9	211.1	15
S18.5	244.0	233.1	4
Ellip(8.0,2.0)	263.1	278.2	-6
Ellip(10,1.6)	267.1	287.5	-8

The table also shows that both elliptical models performed better compared to its circular pins counter parts in both numerical and experimental results. The experimental results showed that the numerical simulation over predicted the total energy transfer of both elliptical models. In summary, the simulation under predicted the circular pins but over predicted the elliptical pins. This is due to the default values of the $k - \varepsilon$ transport equations in Equation 3-19, employed in the numerical simulation. In the numerical study, the default values for turbulence viscosity were used as discussed in Chapter 3. The $k - \varepsilon$ transport equations constant can be tuned to match the experimental results.

A further study was conducted by fine tuning the constant of C_μ. The default value of constant C_μ is 0.09. When $C_\mu = 0.085$ as shows in Table 10-2, the pins' temperature increased by 1-2 °C on the Benchmark model. This study shows that when turbulent viscosity μ_t has been reduced in circular pins model, the heat transfer between the pins and the air stream increased.

Table 10-2: Numerical simulation results of Benchmark model when $C_\mu = 0.085$

Pins' Position	Experimental Results (K)	Numerical Simulation Cμ = 0.085 (K)	%
P(1,2)	424.9	397.5	6%
P(1,4)	407.8	395.0	3%
P(2,2)	425.0	393.7	7%
P(3,3)	396.9	384.3	3%
P(4,2)	387.7	370.3	4%
P(4,4)	372.7	369.3	1%
Water inlet temperature	295.3	295.3	N/A
Water outlet temperature	302.5	301.4	0%
Total energy transfer (W)	247.9	211.1	15%

The experimental and numerical results showed that Ellip(10,1.6) model outperformed the circular and elliptical models. Joining the first row to the third row enhanced the conduction between pins and it also created more surface area.

The experimental data acquired from the TWT validated the numerical studies in this research.

Chapter 11   Conclusions and Future Work

11.1 Conclusions

The aim of this research was to numerically and experimentally scrutinise the thermal performance of a typical heat exchanger fitted in a domestic condensing boiler. This research scrutinised the sensitivity of the geometrical performance of both circular pins and elliptical pins in a heat exchanger. The optimisation process took into account the pins geometry (circular pins and elliptical pins), pins' spacing, pitch distance, the pressure drop across the heat chamber and the occurrence of thermal hot spots. Clear research objectives and methodology were planned and listed at the beginning of the introduction chapter. After carrying out an intensive research on different previous studies, it was clear that design optimisation of current heat exchangers can be carried out without altering the physical size of the heat exchanger using thermal wind tunnel (TWT) and CFD as design tools. It was evident that no previous research was done using:

1. Air flow on circular and elliptical pins at higher Reynolds number of 1.7×10^4.
2. Two separate fluids as heat source and heat carrier on a single test model.

The numerical modelling method used in this research was given in Chapter 3 and 4. In order to study the pins performance effectively a total of 17, 4×4 pins models were used.

A custom made TWT was designed, built and commissioned to carry out experimental tests on different pin configurations under a controlled environment. The main design criteria of the TWT were to achieve a uniform air velocity across the test section and ability to raise and maintain the air temperature at a desired operational temperature. The TWT experimental results were used to validate results acquired from the numerical study.

All specimens were manufactured using DMLS technology. The experimental test utilised a fuzzy PID controller to control all of the 16 heating elements to raise and maintain the air temperature inside the TWT. K-type thermocouples and Pico TC-08 data logger were used to measure and record the pins' core temperatures and water temperatures. Before carrying

out any experimental test, water loop pressure testing was performed on each specimen to ensure no water leakage at the water loop system.

The numerical study found that at a given flow rate, optimum pins configuration is a major factor affecting the heat exchanger's performance. This research showed that heat exchanger optimisation can be carried out within a fixed volume without physically increasing the heat exchanger's size. Circular pins numerical studies concluded that, altering the pins' spacing is more efficient than altering the pins pitch distance. This research showed that optimising circular pins' spacing can increase the heat transfer rate up to 10%. It also concluded that changing the circular pins pitch distance should be the last parameter to consider due to its low effect on the heat transfer rate. This research showed that at a flow rate of 4 m/s of hot air, the optimum circular pins configuration was 18.5 mm pins' spacing and 9.5 mm in pitch distance. This configuration provided better heat transfer relative to pressure drop.

The second part of the research focused on different eccentricities of elliptical pins based on the optimum circular pins' spacing. This research showed that all elliptical models outperformed circular pins models. This phenomenon was attributed to the low tendency of hot air flow separation and the increased surface area presented to the flow. Elliptical pins increase the energy transfer up to 23% at a reduced pressure drop of 55% compared to its circular counter part.

Experimental tests were carried out to validate the obtained numerical results. All specimens were tested three times to minimise errors and uncertainties. The experimental data showed that the numerical simulation under predicted the Benchmark model and model S18.5 but over predicted the elliptical models' water outlet temperatures. This effect is due to the default values of the k − ε transport equations used in the numerical study. Results showed that numerical simulation successfully predicted the S18.5, Ellip(8.0, 2.0) and Ellip(10,1.6) models' pin core temperatures and water outlet temperatures within an error of 8%. The experimental study demonstrated that the elliptical pins showed significant improvements compared to circular pins. This research concluded that elliptical pins have better thermal performance at a lower pressure drop than the circular pins counter

154

part. It is certain that the utilisation of elliptical pins could replace the circular pins in the near future.

11.2 Future Work

- This research highlighted the effectiveness of elliptical pin configurations in comparison with circular pin configurations. An extended study could be carried out to control the porosity of the pins. For example non uniform pin's diameter to direct the hot air closer to the roots of the pin.

- Numerical and experimental studies are needed to investigate the effect of changing the angle of attack of the elliptical pins. Elliptical pins angle of attack could be used to control the hot gas flow path within the heat chamber to increase the heat transfer rate.

- Introducing pins or fins in the water channel to enhance the heat transfer performance from the pins to the water.

- Investigate the use of novel materials such as Aluminium foams. Aluminium foams could be used in crucial areas inside the heat chamber to enhance the heat transfer. Aluminium foams are known to have large surface areas, which could improve the heat transfer rate and further reduce the size of current heat exchangers.

- Since heat transfer is inversely proportional to the wall thickness, different manufacturing techniques and materials selection can also be carried out in the future to reduce the wall thickness between the gas chamber and water channel. This can enhance the heat exchanger performance and also reduce the size and material costs of the heat exchanger.

References

1. DEPARTMENT OF TRADE & INDUSTRY, (2006). *DTI - energy white paper: Our energy future - creating a low carbon economy.* [online]. Last accessed on 01/08/2006 at URL: http://www.dti.gov.uk/energy/policy-strategy/energy-white-paper/page21223.html.

2. THE CARBON TRUST, *Carbon trust | across the UK.* [online]. Last accessed on 10/29 2006 at URL: http://www.carbontrust.co.uk/climatechange/policy/uk.htm.

3. GAS CONNECT HEATING, (2004). Conventional (traditional) gas central heating boilers in Essex - gas connect quality central heating from ex-British gas trained engineers [online]. Last accessed on 10/15/2006 at URL: http://www.gasconnect.co.uk/central/conventional.html.

4. ENERGY SAVING TRUST, *Efficient condensing boiler - save on heating bills - energy saving trust* [online]. Last accessed on 14/08/2007 at: http://www.energysavingtrust.org.uk/home_improvements/heating_and_hot_water/is_my_boiler_a_high_efficiency_condensing_boiler

5. VIESSMANN, (2006). *Brochures & technical documents: Viessmann - more than heat!.* [online]. Last accessed on 06/18/2006 at URL: http://www.viessmann.co.uk/products/technical-documents.php.

6. KAMINSKI, D. A. and JENSEN, M. K. (2005). Introduction to thermal and fluids engineering. International ed., United States of America, John Wiley & Sons, Inc.

7. LONG, C. (1999). Essential heat transfer. 1st ed., United Kingdom, Longman.

8. HAUSEN, H. and WILLMOTT, A. J. (1983). Heat transfer in counter-flow, parallel flow and cross flow. 2nd ed., United States of America, McGraw-Hill.

9. BEHNIA, M., COPELAND, D. and SOODPHAKDEE, D. (1998). A Comparison of Heat Sink Geometries for Laminar Forced Convection: Numerical Simulation of Periodically Developed Flow [online]. In: *Proceedings of the 1998 6th Intersociety Conference on Thermal and Thermomechanical Phenomena in Electronic Systems, ITHERM,* Seattle, WA, USA, Institute of Electrical and Electronic Engineers.

10. CHAPMAN, C. L., SERI L., and SCHMIDT, B. L. (1994). Thermal performance of an elliptical pin fin heat sink. In: *Proceeding of the 10th IEEE Semiconductor Thermal Measurement and Management Symposium, 1-3 Feb 1994,* Published by IEEE, Piscataway, NJ, USA. 24-31.

11. KYOUNGWOO, P. D., CHOI, D. H. and LEE, K. S. (2004). Optimum Design of Plate Heat Exchanger with Staggered Pin Arrays. *Numerical Heat Transfer*; Part A: Applications **45** (4), 347-361.

12. LEE, K. S, KIM, W. S. and SI, J. M. (2001). Optimal Shape and Arrangement of Staggered Pins in the Channel of a Plate Heat Exchanger. *International Journal of Heat and Mass Transfer* **44** (17), 3223-3231.

13. JANG, J. Y., WU, M. C. and CHANG, W. J., (1996). Numerical and Experimental Studies of Three-dimensional Plate-fin and Tube Heat Exchangers. *International Journal of Heat and Mass Transfer* **39** (14), 3057-3066.

14. ROCHA, L. A. O., SABOYA, F. E. M. and VARGAS, J. V. C. (1997). A comparative study of elliptical and circular section in one and two row tubes and plate fin heat exchangers. *International journal of heat and fluid flow,* **18** (2), 247 – 252.

15. MATOS, R. S., VARGAS, J. V. C., LAURSEN, T. A. and SABOYA, F. E. M. (2001). Optimization study and heat transfer comparison of staggered circular and elliptic tubes in forced convection. *International journal of heat and mass transfer,* **44** (20), 3953-3961.

16. MATOS, R. S., VARGAS, J. V. C., LAURSEN, T. A. and BEJAN A. (2004). Optimally staggered finned circular and elliptic tubes in forced convection. *International Journal of Heat and Mass Transfer* **47** (6-7), 1347-1359.

17. SAHIN, B., YAKUT, K., KOTCIOGLU, I. and CELIK, C. (2004). Optimum Design Parameters of a Heat Exchanger. *Applied Energy* **82** (1), 90-106.

18. YAKUT, K., ALEMDAROGLU, N., KOTCIOGLU, I. and CELIK, C. (2006). Experimental investigation of thermal resistance of a heat sink with hexagonal fins. *Applied thermal engineering.* **26** (17-18), 2262- 2271.

19. FLUENT/UNS 6.2 User's Guide, Fluent Incorporated, Lebanon, New Hampshire, 2006

20. CHUNG, T. J. (2002) Structured Grid Generation. In: *Computational Fluid Dynamic.* First edition, Cambridge, United Kingdom: Cambridge University Press. 533 – 570.

21. CHUNG, T. J. (2002) Unstructured Grid Generation. In: *Computational Fluid Dynamic.* First edition, Cambridge, United Kingdom: Cambridge University Press. 581 – 593.

22. CHUNG, T. J. (2002) Adaptive Methods. In: *Computational Fluid Dynamic.* First edition, Cambridge, United Kingdom: Cambridge University Press. 607 – 637.

23. VERSTEEG, H. K. and MALALASEKERA, W. (1995). Introduction. In: *An introduction to computational fluid dynamics: The finite volume method.* Longman Scientific and Technical. 4-6.

24. Gambit 2.0 User's Guide, Fluent Incorporated, Lebanon, New Hampshire, 2006.

25. GORLIN, S. M (1966). Wind tunnels and their instrumentation. Jerusalem, Israel Program for scientific Translations Ltd.

26. BELL, J. H. and MEHTA, R. D. (1989). Boundary-layer predictions for small low-speed contractions. *AIAA journal,* **27** (3), 372-374.

27. BELL, J. H. and MEHTA, R. D. (1988). *Contraction Design for Small Low-Speed Wind Tunnels.* [online]. Report from Joint Institute for Aeronautics and Acoustics, last accessed 15/07/2006 at: http://www.engineeringvillage2.org/

28. BRASSARD, D. and FERCHICHI, M. (2005). Transformation of a polynomial for a contraction wall profile. *Journal of fluids engineering, transactions of the ASME,* **127** (1), 183-185.

29. BRYSON, S. and LEVIT, C. (1992). The virtual wind tunnel. *IEEE computer graphics and applications,* **12** (4), 25-34.

30. CHARITY JR., D. D., SMITH, S. T. and BURGE III, L. L. (2003). Virtual tool development for exploring the virtual wind tunnel (VWT). In: *Proceedings of the International Conference on Imaging Science, Systems and Technology, CISST'03,* 23-26 Jun 2003. Las Vegas, NV, United States, CSREA Press, Bogart, GA 30622, United States, 352-357.

31. FANG, F., CHEN, J. C. and HONG, Y. T. (2001). Experimental and analytical evaluation of flow in a square-to-square wind tunnel contraction. *Journal of wind engineering and industrial aerodynamics,* **89** (3), 247-262.

32. FANG, F. M. and FARELL, C. (1996). Turbulent boundary layer characteristics along the centreline of a contracting wall. *Journal of wind engineering and industrial aerodynamics,* **61** (2), 131-151.

33. GAN, G. H. and RIFFAT, S. B. (1996). Measurement and computational fluid dynamics prediction of diffuser pressure-loss coefficient. *Applied energy,* **54** (2), 181-195.

34. GHANI, S. A. A. A., AROUSSI, A. and RICE, E. (2001). Simulation of road vehicle natural environment in a climatic wind tunnel. *Simulation practice and theory,* **8** (6), 359-375.

35. GORDON, R. and IMBABI, M. S. (1998). CFD simulation and experimental validation of a new closed circuit wind/water tunnel design. *Journal of fluids engineering, transactions of the ASME,* **120** (2), 311-318.

36. GUIRGUIS, N. M., HASSAN, M. A., SHAALAAN, M. R. and HANNA, G. B. (1996). Construction and testing of a wind tunnel for in-door investigation of environmental effects on buildings. *Renewable energy,* **8** (1), 186-189.

37. JOHL, G., PASSMORE, M. and RENDER, P. (2004). Design methodology and performance of an indraft wind tunnel. *Aeronautical journal,* **108** (1087), 465-473.

38. KATO, M. and HANAFUSA, T. (1996). Wind tunnel simulation of atmospheric turbulent flow over a flat terrain. *Atmospheric environment,* **30** (16), 2853-2858.

39. LAGHROUCHE, M., ADANE, A., BOUSSEY, J., AMEUR, S., MEUNIER, D. and TARDU, S. (2005). A miniature silicon hot wire sensor for automatic wind speed measurements. *Renewable energy,* **30** (12), 1881-1896.

40. LINDGREN, B., OESTERLUND, J. and JOHANSSON, A. V. (1998). Measurement and calculation of guide vane performance in expanding bends for wind-tunnels. *Experiments in fluids,* **24** (3), 265-72.

41. LIU, G., XUAN, J. and PARK, S. U. (2003). A new method to calculate wind profile parameters of the wind tunnel boundary layer. *Journal of wind engineering and industrial aerodynamics,* **91** (9), 1155-1162.

42. MATHEW, J., BAHR, C., CARROLL, B., SHEPLAK, M. and CATTAFESTA, L. (2005). Design, fabrication, and characterization of an anechoic wind tunnel facility. In: *Collection of Technical Papers - 11th AIAA/CEAS Aeroacoustics Conference,* Mar 23-25 2005. Monterey, CA, United States, American Institute of Aeronautics and Astronautics Inc., Reston, VA 20191, United States, 3142-3152.

43. MATHEW, J., BAHR, C., SHEPLAK, M., CARROLL, B. and CATTAFESTA, L. (2005). Characterization of an anechoic wind tunnel facility. In: *2005 ASME International Mechanical Engineering Congress and Exposition, IMECE 2005,* Nov 5-11 2005. Orlando, FL, United States, American Society of Mechanical Engineers, New York, NY 10016-5990, United States, 281-285.

44. MEHTA, R. D. (1985). Turbulent boundary layer perturbed by a screen. *AIAA journal,* **23** (9), 1335-42.

45. MEHTA, R. D. and BRADSHAW, P. (1979). Design rules for small low speed wind tunnels. *Aeronautical journal,* **83** (827), 443-449.

46. MOONEN, P., BLOCKEN, B., ROELS, S. and CARMELIET, J. (2006). Numerical modelling of the flow conditions in a closed-circuit low-speed wind tunnel. *Journal of wind engineering and industrial aerodynamics,* **94** (10), 699-723.

47. OHYA, Y., TATSUNO, M., NAKAMURA, Y. and UEDA, H. (1996). A thermally stratified wind tunnel for environmental flow studies. *Atmospheric environment,* **30** (16), 2881-2887.

48. SHONO, H., OJIMA, A. and KAMEMOTO, K. (2003). Development of a virtual two-dimensional wind tunnel using a vortex element method. In: *4th ASME/JSME Joint Fluids Engineering Conference,* 6-10 July 2003. Honolulu, HI, United States, American Society of Mechanical Engineers, New York, NY 10016-5990, United States, 1657-1662.

49. SU, Y. X. (1991). Flow analysis and design of three-dimensional wind tunnel contractions. *AIAA journal,* **29** (11), 1912-1920.

50. WOLF, T. (1995). Design of a variable contraction for a full-scale automotive wind tunnel. *Journal of wind engineering and industrial aerodynamics,* **56** (1), 1-21.

51. SARGISON, J., WALKER, G. and ROSSI, R. (2004) Design and calibration of a wind tunnel with a two dimensional contraction. In: *15th Australasian Fluid Mechanics Conference,* 13-17 December 2004, University of Sydney, Sydney, Australia.

52. UNIVERSITY OF WASHINGTON, *Technical guide for Kirsten wind tunnel* [online]. last accessed on 05/1/2006 at http://www.aa.washington.edu/uwal/

53. LINDGREN, B. and JOHANSSON, A. V. (2004). Evaluation of a new wind tunnel with expanding corners. *Experiments in fluids,* **36** (1), 197-203.

54. KNIGHT, I. K. (2001). The design and construction of a vertical wind tunnel for the study of untethered firebrands in flight. *Fire technology,* **37** (1), 87-100.

55. NAKAYAMA, Y. and BOUCHER, R. F. (1999). *Introduction to fluid mechanics.* London, Arnold.

56. *EOS technology* [online]. Last accessed on 02/08/2007 2007 at: http://www.eos.info/products/technology.html?L=1.

57. *EOS metal laser-sintering* [online]. Last accessed on 02/08/2007 2007 at: http://www.eos.info/products/metal-laser-sintering.html?L=1.

58. *EOS materials* [online]. Last accessed on 02/08/2007 2007 at: http://www.eos.info/products/metal-laser-sintering/materials.html?L=1.

59. *TC-08 thermocouple data logger* [online]. Last accessed on 07/08/2007 2007 at: http://www.picotech.com/thermocouple.html.

60. DUFOUR, J. W. and NELSON, W. E. (1992). Centrifugal pump sourcebook. United State of America. Mc-Grill Hill.

61. *IICA dictionary [H]* [online]. Last accessed on 07/08/2007 2007 at: http://www.control.co.kr/dic/dic-h.htm.

62. *Hall Effect* [online]. Last accessed on 07/08/2007 2007 at: http://hyperphysics.phy-astr.gsu.edu/hbase/magnetic/hall.html.

63. WIKIPEDIA CONTRIBUTORS, *Frequency counter* [online]. Last accessed on 07/08/2007 2007 at: http://en.wikipedia.org/wiki/frequency_counter?oldid=149697046.

64. WIKIPEDIA CONTRIBUTORS, *Variable-frequency drive* [online]. Last accessed on 08/08/2007 2007 at: http://en.wikipedia.org/wiki/variable-frequency_drive?oldid=149199729.

65. WIKIPEDIA CONTRIBUTORS, *Rectifier* [online]. Last accessed on 08/08/2007 2007 at: http://en.wikipedia.org/wiki/rectifier?oldid=145957219.

66. ASTROM, K. J. and HAGGLUND, T. (1994). *PID controllers*. 2nd ed. United States of America, Instrument Society of America.

67. *An Introduction to Fuzzy Logic* [online]. Last accessed on 10/08/2007 2007 at: http://www.seattlerobotics.org/encoder/mar98/fuz/fl_part1.html#INTRODUCTION

68. NAKAYAMA, Y. and BOUCHER, R. F. (1999). Characteristics of a Fluid. In: *Introduction to fluid mechanics*. 1st ed., London, Arnold. 64 - 68.

69. *Pitot-static (prandtl) tube* [online]. Last accessed on 11/08/2007 2007 at: http://www.grc.nasa.gov/WWW/K-12/airplane/pitot.html.

70. WIKIPEDIA CONTRIBUTORS, *Pitot tube* [online]. Last accessed on 11/08/2007 2007 at: http://en.wikipedia.org/wiki/pitot_tube?oldid=149338502.

71. BOSCH, R. (2004) *Automotive handbook.* 6th ed. England, Bury St Edmunds, Professional Engineering.

72. TESTO LIMITED, *Testo limited - portable measuring instruments, calibration and seminars* [online]. Last accessed on 11/08/2007 2007 at: http://www.testo.co.uk/online/

73. KNUDSEN, J. and KATZ, D. (1958) Flow of non-viscous fluids. *Fluid dynamics and heat transfer.* International student edition, Tokyo, Japan, McGraw-Hill, 66-68.
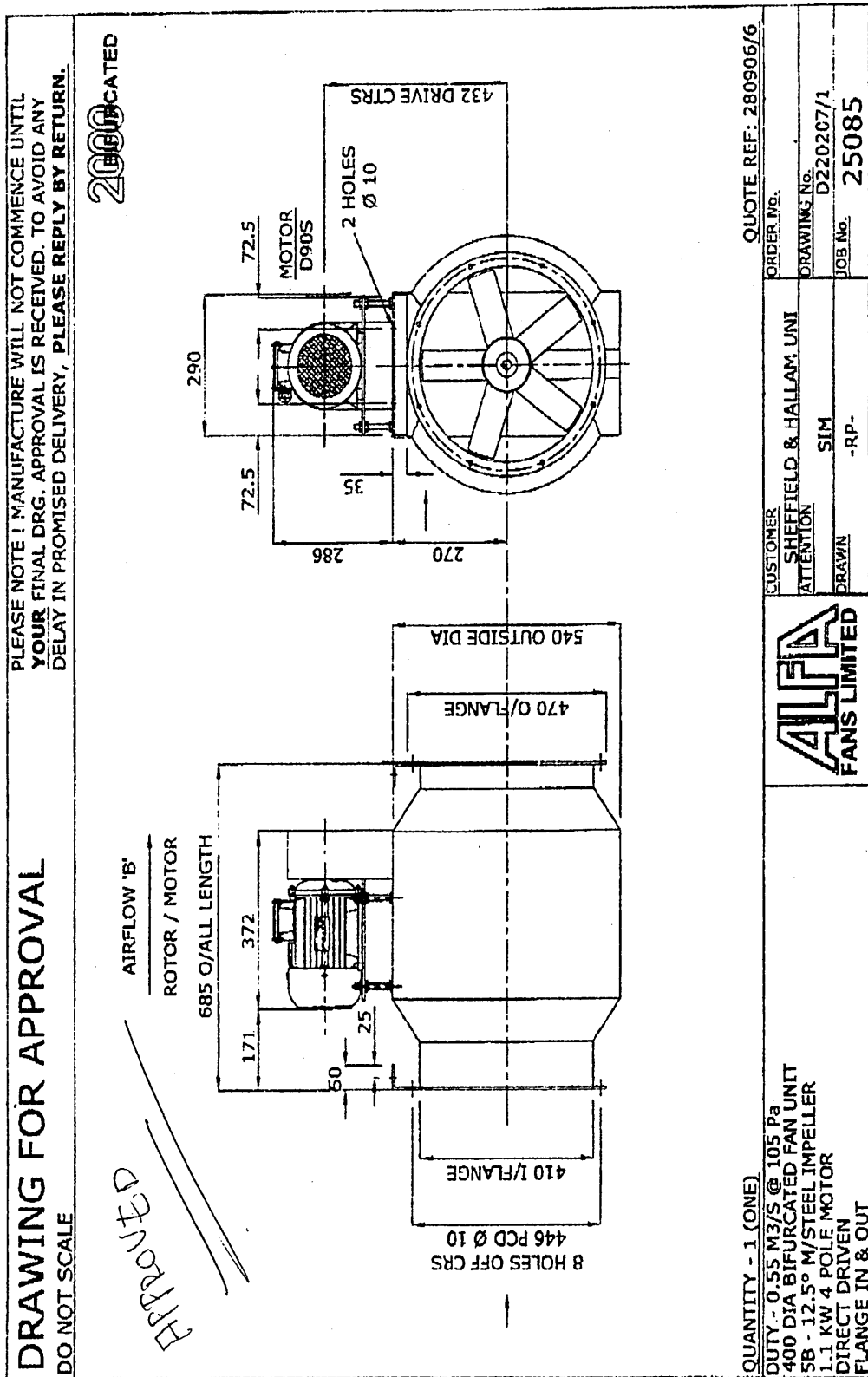
Bibliography

- STANESCU, G., FOWLER, A. J. and BEJAN, A. (1995). The Optimum Spacing of Cylinder in free-stream Cross-flow Forced Convection. *International Journal of Heat and Mass Transfer* **122** (3), 430-449.

- ANDERSON, J. D., Jr. (1995) Philosophy of computational fluid dynamics. In: *Computational fluid dynamics: the basics with applications.* Singapore, McGraw-Hill, 23-25.

- .BARLOW, J. B., RAE, W. H. and POPE, A. (1999). Low-speed wind tunnel testing. 3rd ed., Canada, John Wiley & Sons, Inc.

- *CTM: PID tutorial* [online]. Last accessed on 10/08/2007 2007 at: http://www.engin.umich.edu/group/ctm/PID/PID.html.

- NATIONAL INSTRUMENT Co., *Measuring pressure with pressure sensors-developer zone - national instruments* [online]. Last accessed on 11/08/2007 2007 at: http://zone.ni.com/devzone/cda/tut/p/id/3639.

- NELIK, Lev (1999). Centrifugal and rotary pumps: Fundamentals with applications. 1st ed., United States of America, CRC Press.

- ANDERSON, J. D. Jr. (1995). Computational fluid dynamics: The basics with applications. 1st ed., New York, McGraw-Hill.

- ASTROM, K. J., HAGGLUND, T. and Instrument Society of America (1988). Automatic tuning of PID controllers. 2nd ed., United States of America, Instrument Society of America.

- BOLEY, B. A. and WEINER, J. H. (1985). Theory of thermal stresses. 1st ed., United Stats of America, Krieger.

- BRATER, E. F. (1996). Handbook of hydraulics. 7th ed. United States of America, McGraw-Hill.

- CHEN, G. and PHAM, T. T. (2001). Introduction to fuzzy sets, fuzzy logic, and fuzzy control systems. 1st ed., Florida, CRC Press.

- DUCKWORTH, R. A. (1977). Mechanics of fluids. 1st ed., New York, Longman

- EASTOP, T. D. and CROFT, D. R. (1990). Energy efficiency: For engineers and technologists. 1st ed., United Kingdom, Longman.

- EVETT, J. B. and LIU, C. (1987). Fundamentals of fluid mechanics. 1st ed., United States of America, McGraw-Hill

- FINNEY, D. and Institution of Electrical Engineers (1988). Variable frequency AC motor drive systems. 1st ed., London, United Kingdom, Peter Peregrinus Ltd.

- FOX, R. W. and MCDONALD, A. T. (1994). Introduction to fluid mechanics. 4th ed., Canada, Wiley.

- HOLMAN, J. P. (1997). Heat transfer. 8th ed., United States of America, McGraw-Hill.

- INCROPERA, F. P. (2006). Fundamentals of heat and mass transfer. 6th ed. New Jersey, Wiley.

- KREITH, F. (1996) Principles of heat transfer. 2nd ed., United States of America, International Textbook Company.

- MANSON, S. S. (1966). Thermal stress and low-cycle fatigue. 1st ed., New York, R.E. Krieger Pub. Co.

- SIMONSON, J. R.(1975). Engineering heat transfer. Revised ed. London, United Kingdom, Macmillan.

- SONNTAG, R. E., BORGNAKKE, C. and VAN WYLEN, G. J. (2003). Fundamentals of thermodynamics. 6th ed. New York, Wiley.

- WHITE, F. M. (1999). Fluid mechanics. 4th ed. London, McGraw-Hill.

- ZHANG, Z. and LI, Y. Z. (2003). CFD simulation on inlet configuration of plate-fin heat exchangers. *Cryogenics,* **43** (12), 673-678.

- COLEMAN, H. W. (2005). Verification and validation in computational fluid dynamics and heat transfer using experimental uncertainty analysis concepts. In: *2005 ASME Summer Heat Transfer Conference, HT 2005,* 17-22 July 2005. San Francisco, CA, United States, American Society of Mechanical Engineers, New York, NY 10016-5990, United States, 1009-1010.

- GEORGE, P. L., BOROUCHAKI, H. and LAUG, P. (2000). An efficient algorithm for 3D adaptive meshing. In: *Fifth International Conference on Computational Structures Technology and the Second International Conference on Engineering Computational Technology,* 6-8 Sept. 2000. Leuven, Belgium, Civil-Comp Press, 1-11.

- HAMDAN, M. H. (1998). A note on computational uncertainty. *Applied mathematics and computation,* **94** (2), 285-91.

- OBERKAMPF, William L. and TRUCANO, Timothy G. (2002). Verification and validation in computational fluid dynamics. *Progress in aerospace sciences,* **38** (3), 209-272.

- PELLETIER, D., TURGEON, E., LACASSE, D. and BORGGAARD, J. (2003). Adaptivity, sensitivity, and uncertainty: Toward standards of good practice in computational fluid dynamics. *AIAA journal,* **41** (10), 1925-1933.

- AHMAD, E. H. and BADR, H. M. (2001). Mixed convection from an elliptic tube placed in a fluctuating free stream. *International journal of engineering science,* **39** (6), 669-93.

- BORDALO, S. N. and SABOYA, F. E. M. (1999). Pressure drop coefficients for elliptic and circular sections in one, two and three-row arrangements of plate fin and tube heat exchangers. *Revista brasileira de ciencias Mecanicas/ Journal of the Brazilian society of mechanical sciences,* **21** (4), 600-610.

- BOURIS, D., PAPADAKIS, G. and BERGELES, G. (2001). Numerical evaluation of alternate tube configurations for particle deposition rate reduction in heat exchanger tube bundles. *International journal of heat and fluid flow,* **22** (5), 525-536.

- ELSAYED, A. O., IBRAHIM, E. Z. and ELSAYED, S. A. (2003). Free convection from a constant heat flux elliptic tube. *Energy conversion and management,* **44** (15), 2445-2453.

- ELSHAZLY, K., MOAWED, M., IBRAHIM, E. and EMARA, M. (2005). Heat transfer by free convection from the inside surface of the vertical and inclined elliptic tube. *Energy conversion and management,* **46** (9), 1443-63.

- KIBBOUA, R. and AZZI, A. (2005). Laminar film condensation on an elliptical tube embedded in porous media. *Energy conversion and management,* **46** (15), 2359-72.

- LEE, S. (1995). Optimum design and selection of heat sinks. *IEEE transactions on components, packaging, and manufacturing technology, part A,* **18** (4), 812-17.

- LI, Q., CHEN, Z. FLECHTNER, U. and WARNECKE, H. (1998). Heat transfer and pressure drop characteristics in rectangular channels with elliptic pin fins. *International journal of heat and fluid flow,* **19** (3), 245-250.

- MISSIRLIS, D., YAKINTHOS, K. PALIKARAS, A., KATHEDER and K., GOULAS, A. (2005). Experimental and numerical investigation of the flow field through a heat exchanger for aero-engine applications. *International journal of heat and fluid flow,* **26** (3), 440-458.

- MOAWED, M., ELSHAZLY K., IBRAHIM, E. and EMARA, M. (2006). Experimental investigation of natural convection inside horizontal elliptic tube with different angles of attack. *Energy conversion and management,* **47** (1), 35-45.

- PRSTIC, S., IYENGAR, M. and BAR-COHEN, A. (2001). Bypass effect in high performance heat sinks. *Strojniski Vestnik/ Journal of mechanical engineering,* **47** (8), 441-448.

- SABOYA, S. M. and SABOYA, F. E. M. (2001). Experiments on elliptic sections in one-and two-row arrangements of plate fin and tube heat exchangers. *Experimental thermal and fluid science,* **24** (1), 67-75.

- YANG, S. and HSU, C. (1997). Free and forced-convection film condensation from a horizontal elliptic tube with a vertical plate and horizontal tube as special cases. *International journal of heat and fluid flow,* **18** (6), 567-574.

- HILBERT, R., JANIGA, G., BARON, R. and THEVENIN, D. (2006). Multi-objective shape optimization of a heat exchanger using parallel genetic algorithms. *International journal of heat and mass transfer,* **49** (15), 2567-2577.

- GOLDSTEIN, R. J., ECKERT, R. G., IBELE, W. E., PATANKAR, S. V., SIMON, T. W., KUEHN, T. H., STRYKOWSKI, P. J., TAMMA, K. K., HEBERLAIN, J. V. R. and DAVIDSON, J. H.(2003). Heat transfer - A review of 2001 literature. *International journal of heat and mass transfer,* **46** (11), 1887-1992.

Appendix A   Fan Drawing

DRAWING FOR APPROVAL
DO NOT SCALE

APPROVED

AIRFLOW 'B'

ROTOR / MOTOR

685 O/ALL LENGTH

540 OUTSIDE DIA

470 O/FLANGE

410 I/FLANGE

8 HOLES OFF CRS
446 PCD Ø 10

372

171

25

50

PLEASE NOTE ! MANUFACTURE WILL NOT COMMENCE UNTIL
YOUR FINAL DRG. APPROVAL IS RECEIVED. TO AVOID ANY
DELAY IN PROMISED DELIVERY, PLEASE REPLY BY RETURN.

2000 BIFURCATED

432 DRIVE CTRS

MOTOR
D90S

72.5

290

72.5

2 HOLES Ø 10

35

286

270

QUANTITY - 1 (ONE)
DUTY - 0.55 M3/S @ 105 Pa
400 DIA BIFURCATED FAN UNIT
5B - 12.5° M/STEEL IMPELLER
1.1 KW 4 POLE MOTOR
DIRECT DRIVEN
FLANGE IN & OUT

QUOTE REF: 280906/6

ORDER No.

DRAWING No. D220207/1

JOB No. 25085

CUSTOMER SHEFFIELD & HALLAM UNI
ATTENTION SIM
DRAWN -RP-

ALFA FANS LIMITED

167

Appendix B   Thermal Wind Tunnel (TWT) Design and Calculations

B.1 Introduction

A wind tunnel is a research tool designed to study the effects of controlled moving fluid flow over and around solid objects. Every wind tunnel is designed and constructed according to suit a certain application. There are many types of wind tunnel built around the world. They can be classified according to the prevailing average velocity as follows:

5. Subsonic - mach number from 0 to 0.7.
6. Transonic - mach number from 0.7 to 1.2.
7. Supersonic - mach number from 1.2 to 5.
8. Hypersonic - mach number above 5.

Wind tunnels can be built in two types of configurations. Namely, open loop or closed loop wind tunnels. Open loop wind tunnels draw air by fan through a contraction, test section and a diffuser all in a straight line. In general, an open loop wind tunnel is cheaper to build, but it is sensitive to its air entry conditions. Open loop wind tunnels suffer from the entry conditions because of the way air is being sucked in or blown out from the wind tunnel.

A closed loop wind tunnel re-circulates air inside the tunnel. Therefore requires more sections to form a loop. It is clear that a closed loop wind tunnel is usually more expensive to build. However, the advantages of a closed loop wind tunnel are significant. A closed loop wind tunnel provides more accurate results than an open loop wind tunnel because the flow quality can be controlled by turning vanes and screens.
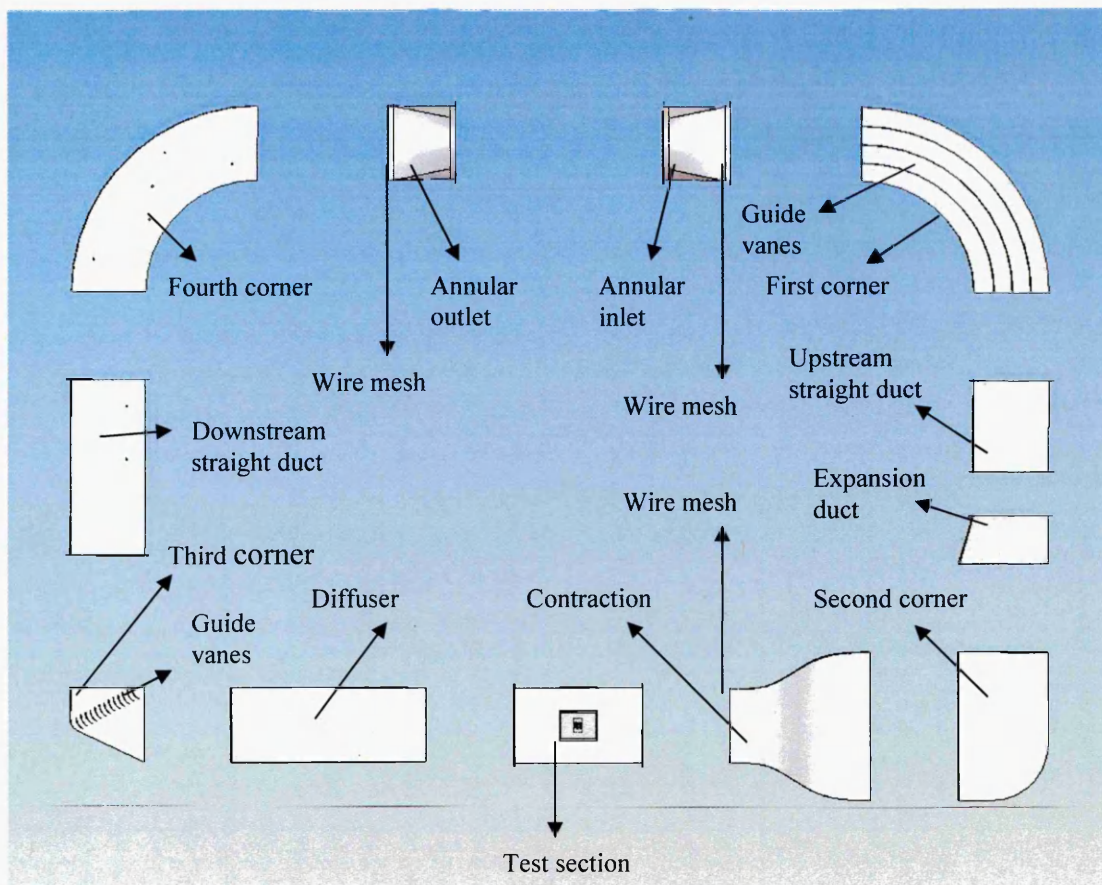
Figure B-1: Exploded view at every section of the wind tunnel

The tunnel design started with a series of numerical calculations and then optimised using the CFD code FLUENT version 6.2. Figure B-1 shows an exploded view of the whole TWT. The TWT consist the following components:

1. Annular inlet
2. Upstream wire mesh
3. First corner
4. First corner guide vanes
5. Upstream straight duct
6. Expansion duct
7. Second corner
8. Contraction
9. Test section wire mesh
10. Test section
11. Diffuser
12. Third corner
13. Third corner guide vanes
14. Downstream straight duct
15. Fourth corner
16. Downstream wire mesh
17. Annular outlet

Figure B-2 illustrates that the air flows in clockwise direction. Air first enters the annular outlet then past a 90° smooth bend into the upstream straight duct. Later, air flows into the expansion duct and settles down at the second corner before entering the three dimensional contraction section. A fine wire mesh was positioned between the contraction and the test section to straighten the flow.

Soon after the test section, the disturbed flow is then discharged through the diffuser into the third corner. Finally, cooled air is reheated at the downstream straight duct and the fourth corner, where heating elements were positioned, before entering the annular inlet.
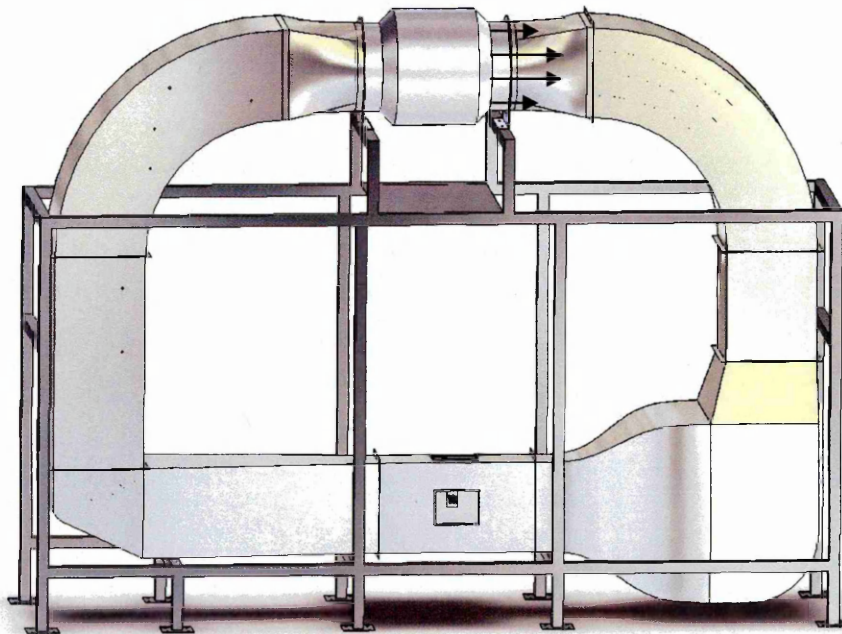

Figure B-2: Bird's eye view at the thermal wind tunnel

B.2 Test section

The initial design of the TWT started with the test section because it is the most important section within the tunnel. The size of the test section is depends on the specimen size. The test section must able to accommodate one specimen without any disturbing flow generated by three sides of the walls. In order to avoid flow been throttled through the test section, an aspect ratio of 2 on each side of the specimen was used to determined the test section size. Test section is 420mm wide × 225mm height × 730mm long as shown in Figure B-3 and Figure B-4.
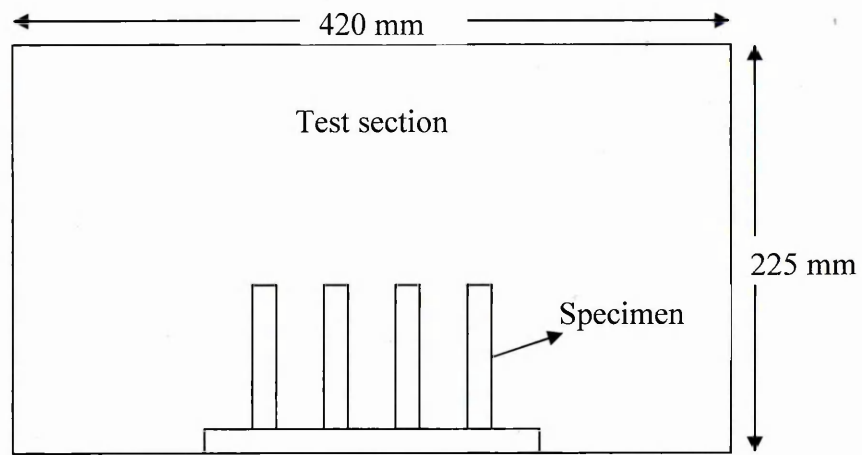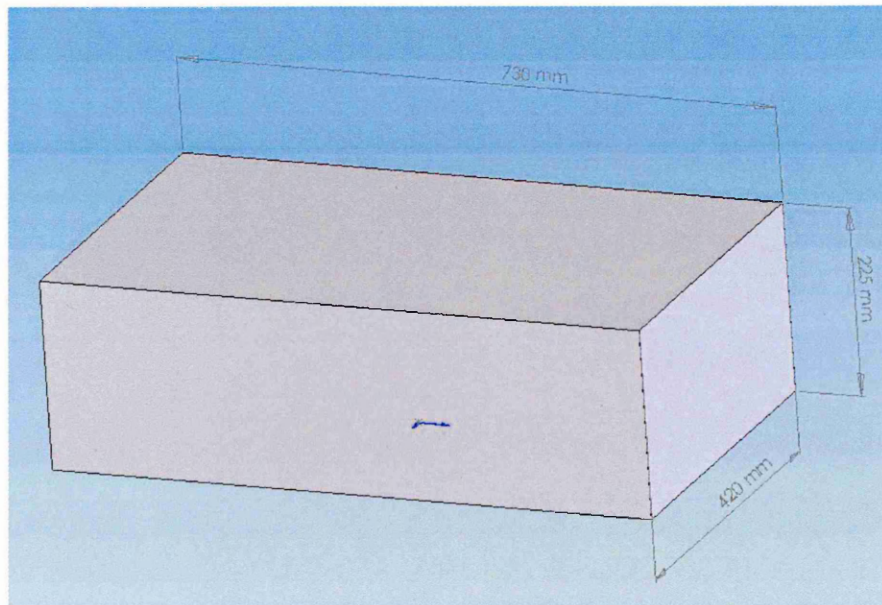
Figure B-3: Cross sectional view on test section

Figure B-4: Test section's dimension

Test section dimension:
Wide = 420 mm
Height = 225 mm
Length = 730 mm

Initial conditions:
1. Velocity = 4m/s at test section

2. Volume flow rate:

$$Q_{air} = (A_{test} - A_{speciment}) \times v \qquad \text{Equation B-1}$$

171

$$Q_{air} = (A_{test} - A_{specimen}) \times v$$
$$= (0.1 - 2.58 \times 10^{-3}) \times v$$
$$= 0.37 \text{ m}^3/\text{s}$$

Pressure loss coefficient

$$k = (1 - \frac{A_{speciment}}{A_{test}})$$

<div align="right">Equation B-2</div>

$$k = (1 - \frac{A_{specimen}}{A_{test}})$$
$$= (1 - \frac{2.58 \times 10^{-3}}{0.1})$$
$$= 0.97$$

Test section pressure loss

$$h = k \times \frac{v^2}{2g}$$

<div align="right">Equation B-3</div>

$$h = k \times \frac{4^2}{2 \times 9.81}$$
$$= 0.97 \times \frac{4^2}{2 \times 9.81}$$
$$= 0.79 \text{ m}$$

B.3 Wind tunnel diffuser

The design of the diffuser acts as a discharging duct. In this design, the area ratio is 1.87 with and incline angle of 10 degree. Figure B-5 shows the overall dimension of the diffuser.
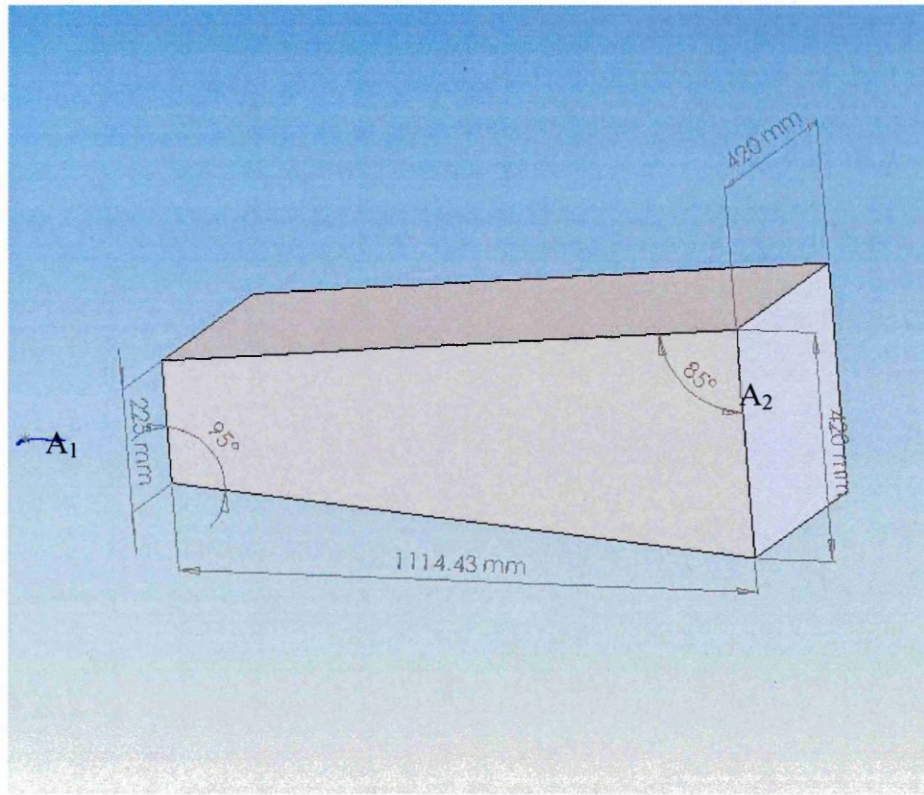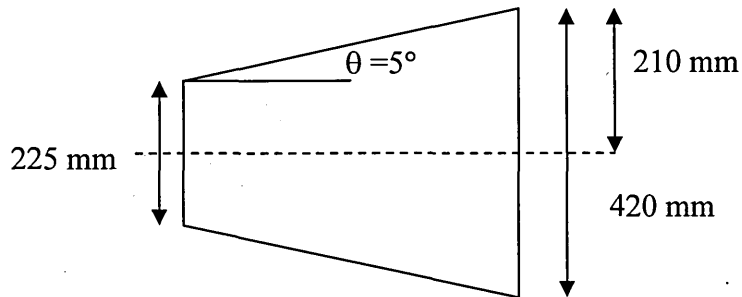

Figure B-5: Diffuser section's dimension

Area ratio

$$AR = \frac{\text{Outlet Area}}{\text{Inlet Area}}$$

Equation B-4

$$AR = \frac{x_2 \cdot y_2}{x_1 \cdot y_1}$$
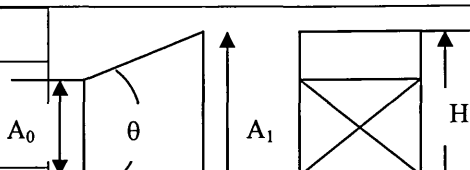$$= \frac{420 \cdot 420}{420 \cdot 225}$$
$$= 1.87$$

173

Defining the diffuser length

$$\tan 5° = \frac{97.5}{length}$$

$$= 1114.43 \text{ mm}$$

Therefore, diffuser length L = 1114.43 mm

Table B-1: Pressure loss coefficient for diffuser

A_1/A_0	C_0									
	θ, degrees									
	8	10	14	20	30	45	≥ 60			
1	0	0	0	0	0	0	0			
2	0.50	0.51	0.56	0.63	0.80	0.96	1.0			
4	0.34	0.38	0.48	0.63	0.76	0.91	1.0			
6	0.32	0.34	0.41	0.56	0.70	0.84	0.96			

From Table B-1, pressure loss coefficient k = 0.44217

Velocity at diffuser:

$$v = \frac{Q}{A}$$

Equation B-5

$$v = \frac{0.368}{\frac{(225 \times 420)}{1000^2}}$$

$$v = 3.89 \text{ m/s}$$

From Equation B-3

$$h = 0.44 \times \frac{3.89^2}{2 \times 9.81}$$

$$h = 0.34 \text{ m}$$

B.4 Third corner

The third corner was designed to direct the air flow around the bend into downstream straight duct. Figure B-6 shows that it has 420 mm cross section on both open ends.
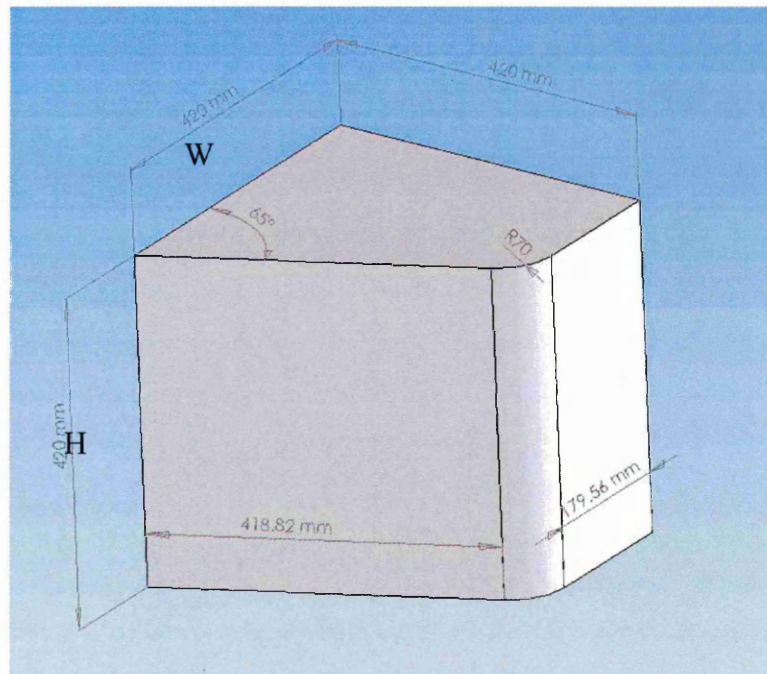

Figure B-6: Third corner's dimension

Table B-2: Pressure loss coefficient for elbow

Pressure loss coefficient for elbow Cp

r/W	H/W										
	0.25	0.5	0.75	1.0	1.5	2.0	3.0	4.0	5.0	6.0	8.0
0.5	1.3	1.3	1.2	1.2	1.1	1.0	1.0	1.1	1.1	1.2	1.2
0.75	0.57	0.5	0.48	0.44	0.4	0.39	0.39	0.4	0.42	0.43	0.44
1.0	0.27	0.3	0.23	0.21	0.19	0.18	0.18	0.19	0.20	0.21	0.21
1.5	0.22	0.2	0.19	0.17	0.15	0.14	0.14	0.15	0.16	0.17	0.17
2.0	0.2	0.2	0.16	0.15	0.14	0.13	0.13	0.14	0.14	0.15	0.15

Angle correction factor

θ	0	20	30	45	60	75	90	110	130	150	180
Af	0	0.3	0.45	0.6	0.78	0.9	1.00	1.13	1.2	1.28	1.4
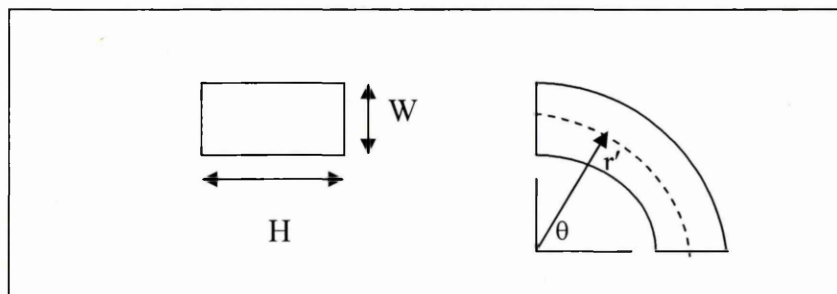
Known, H = W = 420 mm, θ = 65° and r = 70 mm. Using Equation B-5 v = 2.08 m/s

$$k = c_p \times A_f$$

<div align="right">Equation B-6</div>

From Table 2, c_p = 1.2 and A_f = 0.82. Therefore, k = 0.98

From Equation B-3

$$h = k \times \frac{v^2}{2g}$$
$$= 0.98 \times \frac{2.08^2}{2 \times 9.81}$$
$$= 0.22 \text{ m}$$

B.5 Guide vanes in third corner

Guide vanes have the function to improve air flow pressure loss around corners. In this design, the guide vane is 420 mm long with 70 mm radius creates an arc shape vane as illustrates in Figure B-7. In total of 13 guide vanes were used in the third corner to enhance the air flow around the bend.
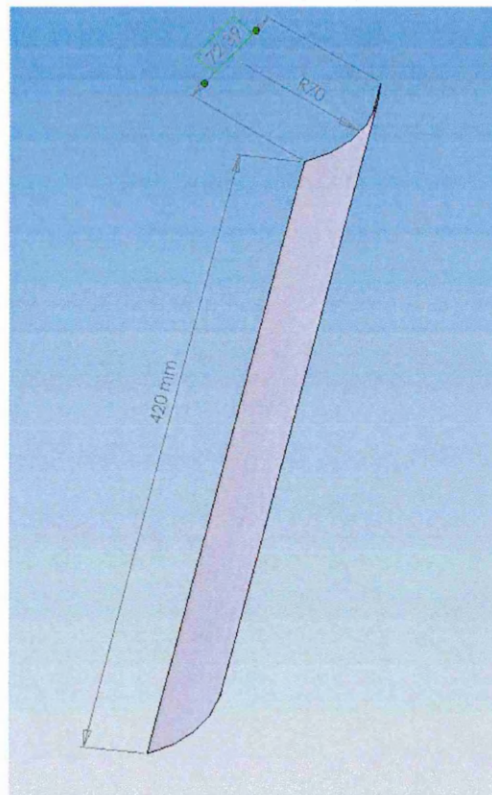

Figure B-7: Guide vane dimension

Known that, vanes spacing = 30 mm, vane radius = 70 mm, number of vanes = 13 and air velocity v = 2.08 m/s.

Using Equation B-3, pressure loss from vanes can be defined:

$$h = 0.13 \times \frac{2.08^2}{2 \times 9.81}$$
$$= 0.03 \text{ m}$$

B.6 Downstream straight duct

Downstream straight duct connected the third corner and fourth corner together. It is a square duct with 1000 mm long as shown in Figure B-8. Five electric cartridges heaters have been positioned on both sides of the duct to rise the air temperature.
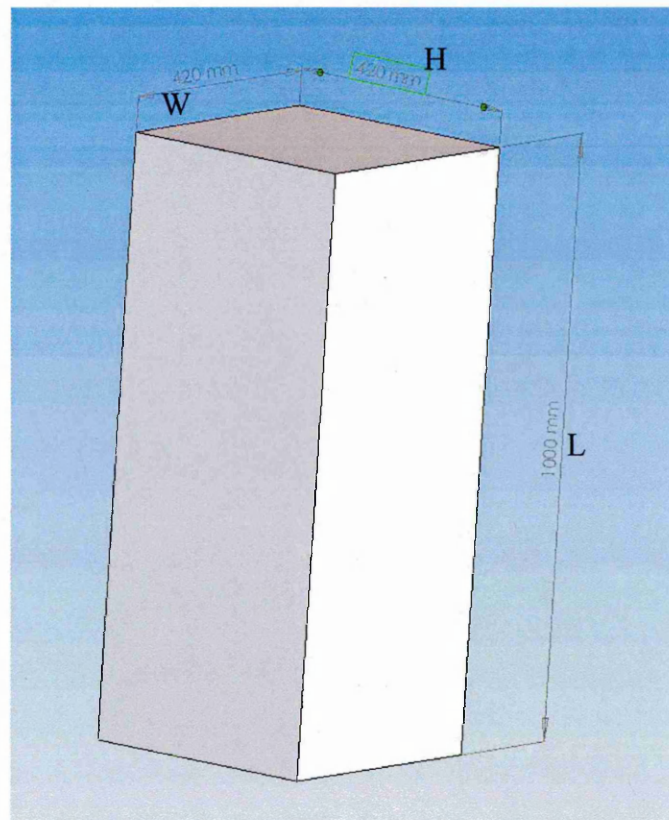

Figure B-8: Downstream straight duct dimension

Know W = H = 420 mm, L = 1000 mm and pressure loss coefficient k = 1.0.
From Equation B-5, velocity at down stream straight duct v =2.08 m/s

Using Equation B-3;

$$h = k \times \frac{v^2}{2g}$$

$$= 1 \times \frac{2.08^2}{2 \times 9.81}$$

$$= 0.22 \text{ m}$$

B.7 Fourth Corner

The fourth corner was carefully design using numerical methods and CFD code, FLUENT to reduce the pressure loss and maintain uniformity of the air flow inside the duct. The outer radius is 1056.62 mm and the inner radius is 636.62mm as shown in Figure B-9.
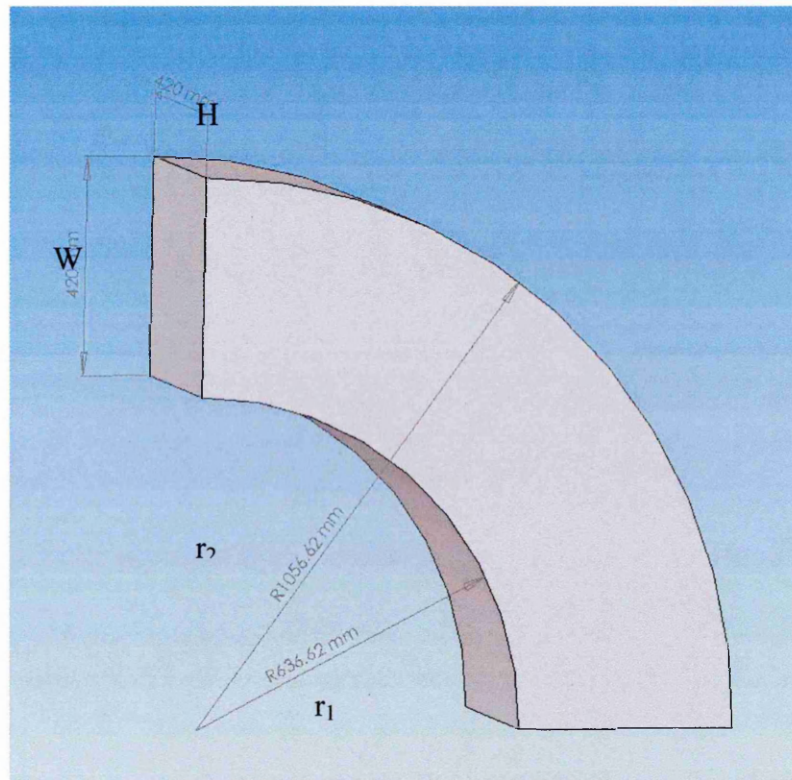

Figure B-9: Fourth corner's dimension

Given, W = H =420 mm, r_1 = 636.62 mm and r_2 = 1056.62 mm.
Using Equation B-5 velocity at fourth corner is 2.08 m/s

From Table B-2, pressure loss coefficient can be calculated in below,
$$k = c_p \times A_f$$

$$= 0.15 \times 1.0$$

$$= 0.15$$

Pressure loss at fourth corner can be defined using Equation B-3;
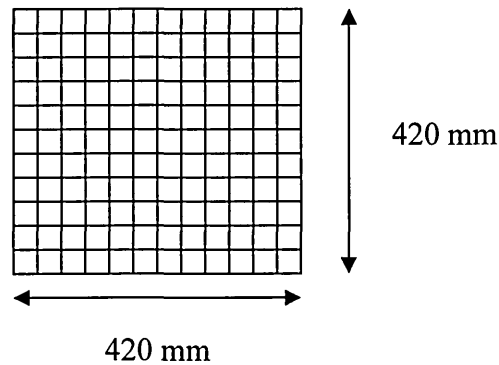
$$h = k \times \frac{v^2}{2g}$$

$$= 0.15 \times \frac{2.08^2}{2 \times 9.81}$$

$$= 0.03 \text{ m}$$

B.8 Downstream Wire Mesh

A fine wire mesh between the downstream straight duct and the fourth corner has been used to straighten the flow and also acts as a protection guide of the bifurcated fan.

Given, wire diameter = 1 mm, aperture = 6 mm.

420 mm

420 mm

The total meshed area can be calculated in below,
$420 \div 6 = 70$ number of mesh
Wire area $= \pi \times r \times h = 659.73 \text{ mm}^2$
Total wire area $= 659.73 \times 70 = 46181.41 \text{ mm}^2$

Total mesh area $= 46181.41 \times 2 = 92362.82 \text{ mm}^2$

Velocity passing through the mesh:

$$v = \frac{Q}{\left(A_{open} - A_{mesh}\right)/1000^2} \qquad \text{Equation B-7}$$

$$v = \frac{0.37}{0.08}$$

$$= 4.38 \text{ m/s}$$

179

Pressure loss can be calculated in below:

$$k = \left(1 - \frac{A_{mesh}}{A_{open}}\right)$$

$$k = \left(1 - \frac{92362.82}{176400}\right)$$

$$= 0.48$$

Pressure loss from wire mesh can be calculated using Equation B-3:

$$h = k \times \frac{v^2}{2g}$$

$$= 0.48 \times \frac{4.38^2}{2 \times 9.81}$$

$$= 0.47 \text{ m}$$

B.9 Contraction

Contraction is one of the most importance sections of the wind tunnel. Studies have been carried out to achieve an optimum design on the contraction. Figure B-10 shows a 3D contraction with contraction area ratio of 6.
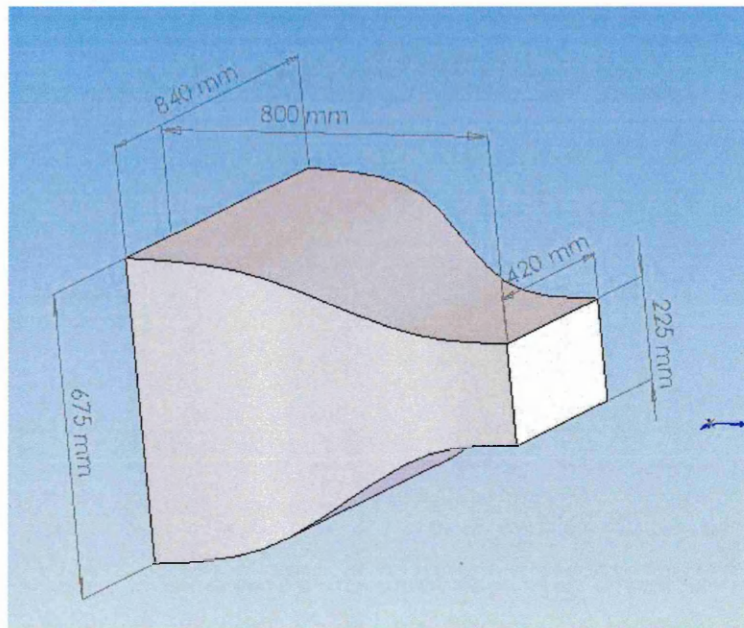

Figure B-10: CAD model shows the contraction's dimension

Contraction area ratio:

$$AR = \frac{A_{inlet}}{A_{outlet}}$$

180

$$AR = \frac{840 \times 675}{225 \times 420}$$

$$= 6$$

Using venturi flow equation, diffuser pressure loss can be written as:

$$P_{in} - P_{out} = \Delta P = \frac{1}{2}\rho v_{out}^2 - \frac{1}{2}\rho v_{in}^2 \qquad \text{Equation B-10}$$

From continuity, outlet velocity can be substituted out of the above equation as,

$$\Delta p = \frac{1}{2}\rho v_{in}^2 \left[\left(\frac{A_{inlet}}{A_{outlet}} \right)^2 - 1 \right] \qquad \text{Equation B-11}$$

Air velocity at contraction inlet can be calculated using Equation B-5;

$$v = \frac{Q}{A_{inlet}}$$

$$= \frac{0.37}{\left(\frac{840 \times 675}{1000^2} \right)}$$

$$= 0.65 \text{ m/s}$$

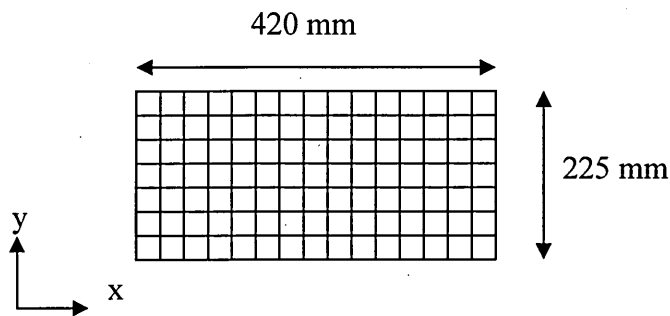Substituting AR = 6, ρ = 1.22 kg/m^3 and v = 0.648 m/s into Equation B-11:

$$\Delta P = \frac{1}{2} \times 0.648^2 \left[\left(6^2 - 1 \right) \right]$$

$$= 8.96 \text{ Pascal}$$

h = 0.75 m

B.10 Test Section Wire Mesh

A small piece of fine wire mesh has been used to straighten the flow at the test section. Given, wire diameter = 1 mm, aperture = 6 mm.

Total meshed area can be calculated in below:

X –axis:
$420 \div 6 = 70$ number of mesh
Wire area $= \pi \times r \times h = 659.73 \text{ mm}^2$
Total wire area $= 659.73 \times 70 = 46181.41 \text{ mm}^2$

Y –axis:
$225 \div 6 = 37.5$ number of mesh
Wire area $= \pi \times r \times h = 353.43 \text{ mm}^2$
Total wire area $= 353.43 \times 37.5 = 13253.59 \text{ mm}^2$

Total mesh area $= 46181.41 + 13253.59 = 59435 \text{ mm}^2$

From Equation B-7, velocity passing through the mesh is:
$$v = \frac{Q}{\left(A_{open} - A_{mesh}\right)/1000^2}$$
$$= \frac{0.37}{0.04}$$
$$= 10.49 \text{ m/s}$$

Pressure loss coefficient can be calculated using Equation B-8:
$$k = 1 - \frac{59435}{94500}$$
$$= 0.37$$

Pressure loss from wire mesh can be calculated using Equation B-3:
$$h = 0.37 \times \frac{10.49^2}{2 \times 9.81}$$
$$= 2.08 \text{ m}$$

B.11 Second corner

Second corner was created to direct air flow around the bend into the contraction section. Further more, it also acts as a settle zone to regain pressure. Figure B-11 shows that the second corner has larger bend than third corner, this is because study shows that smaller bend could create stagnant flow around the corner.
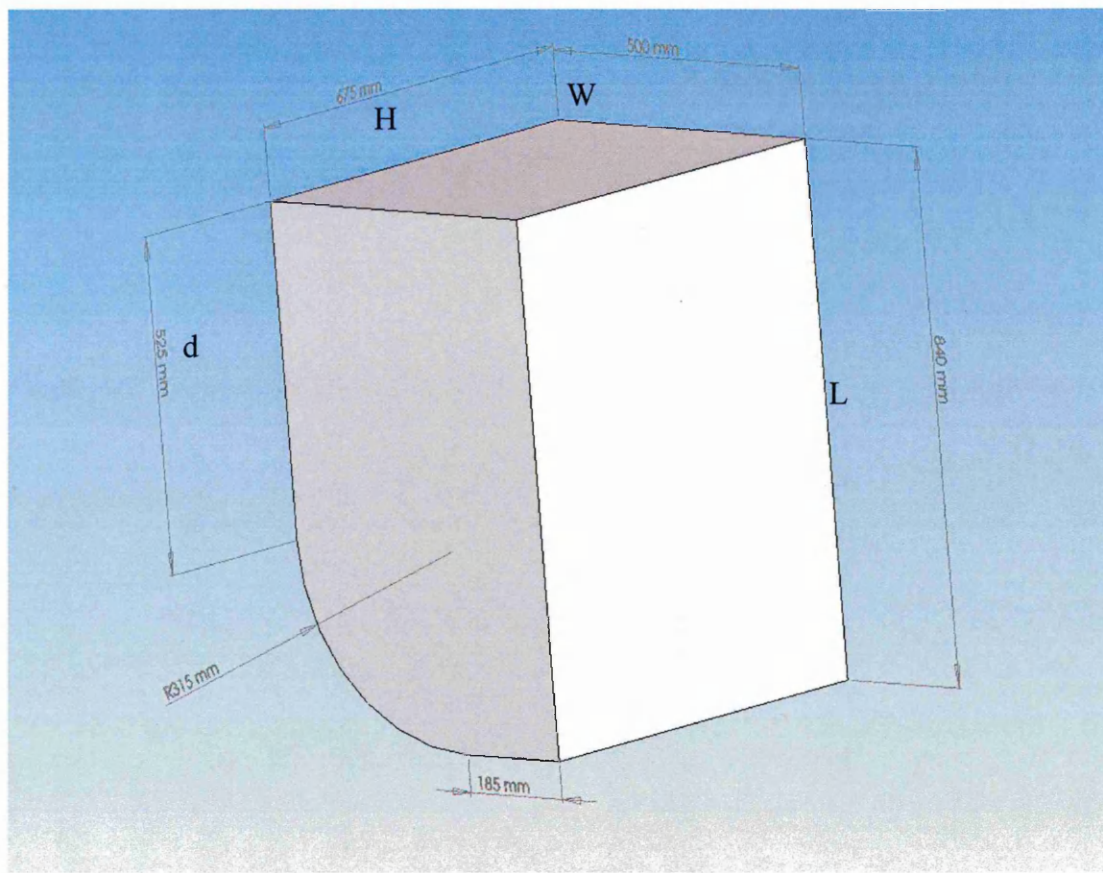
Figure B-11: CAD model shows the dimension of 2nd corner

Given, H = 675 mm, W = 500 mm, L = 840 mm and d = 525 mm, volume flow rate = 0.37 m³/s.

From Table B-2, pressure loss coefficient can be calculated in below,
$$k = c_p \times A_f$$
$$= 0.74 \times 1.37$$
$$= 1.02$$

Air velocity can be calculated using Equation B-5:
$$v = \frac{0.37}{0.34}$$
$$= 1.09 \text{ m/s}$$

Second corner pressure loss can be calculated using Equation B-3:
$$h = 1.02 \times \frac{1.09^2}{2 \times 9.81}$$
$$= 0.06 \text{ m}$$

B.12 Expansion duct

The expansion duct angle was carefully design to avoid high pressure loss. Figure B-12 shows that the expansion duct angle is 50 degree and 273.42 mm high.
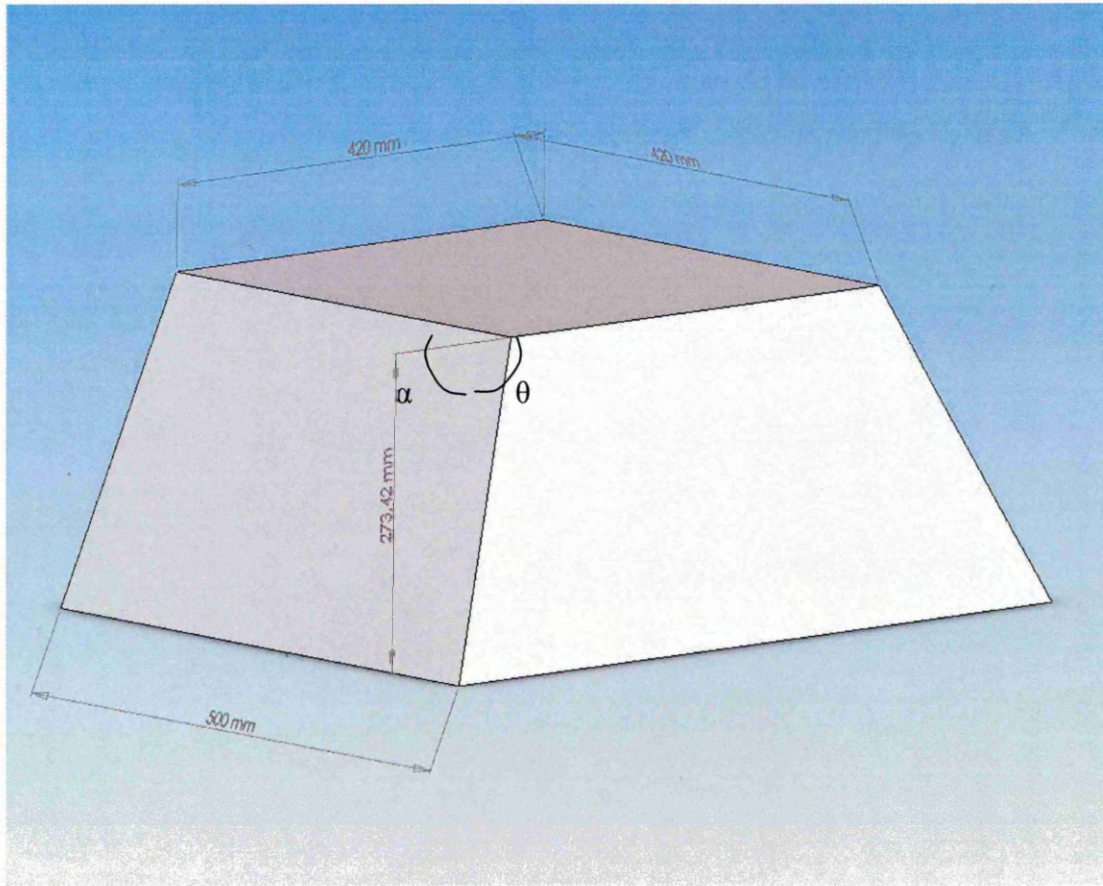

Figure B-12: CAD model shows the dimension of the expansion duct

Given, expansion height = 273.42 mm, expansion angle θ= 115°, α = 106.31°, area ratio = 1.61.

From Table B-1, pressure loss coefficient k =0.99

Using Equation B-5, air velocity can be calculated in below:
$$v = \frac{0.37}{0.18}$$
$$= 2.08 \text{ m/s}$$

Using Equation B-3, pressure loss at expansion duct can be calculated:
$$h = 0.99 \times \frac{2.08^2}{2 \times 9.81}$$
$$= 0.22 \text{ m}$$

B.13 Upstream straight duct

The upstream straight duct connected the first corner and expansion duct together. It is slightly shorter than the downstream straight duct as shown in Figure B-13.
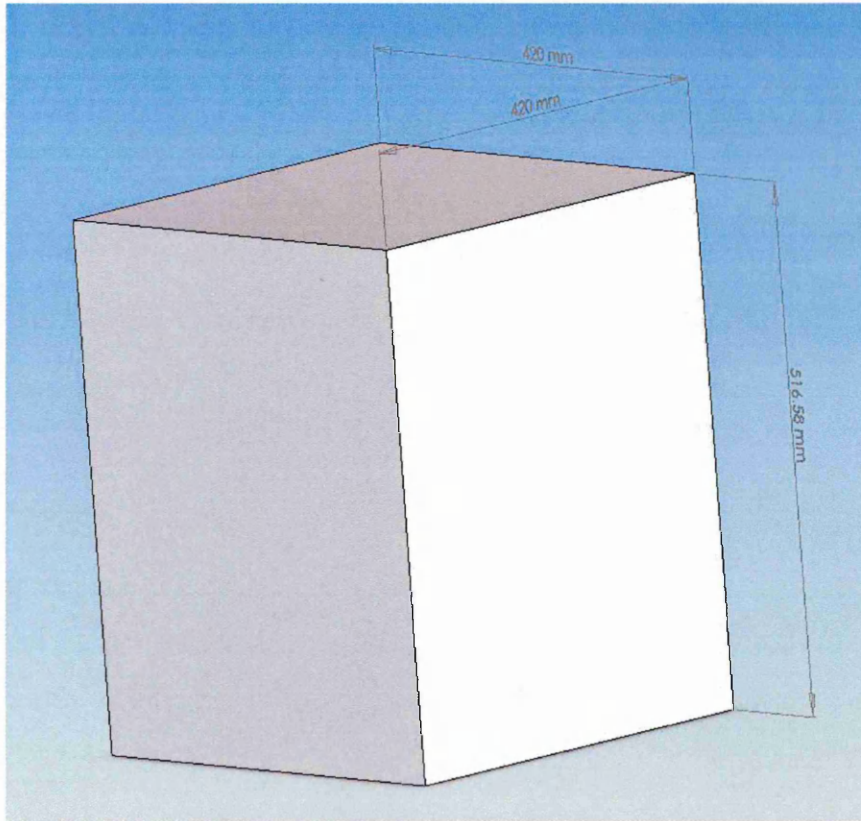

Figure B-13: CAD model shows the dimension of the upstream straight duct

Known that, upstream straight duct is a square duct (420 mm × 420 mm) and 516.56 mm long. Pressure loss coefficient k = 1.0.

Using Equation B-5, air velocity can be calculated as below:

$$v = \frac{0.37}{0.18}$$
$$= 2.08 \text{ m/s}$$

Using Equation B-3, pressure loss at first corner can be defined as:

$$h = k \times \frac{v^2}{2g}$$
$$= 1 \times \frac{2.08^2}{2 \times 9.81}$$
$$= 0.22 \text{ m}$$

B.14 First corner

The function of the first corner is the same as the fourth corner. Studies have been carried out to achieve flow uniformity in this section. It can be seen that the first corner has the same inner and outer radius as the fourth corner as shown in Figure B-14.
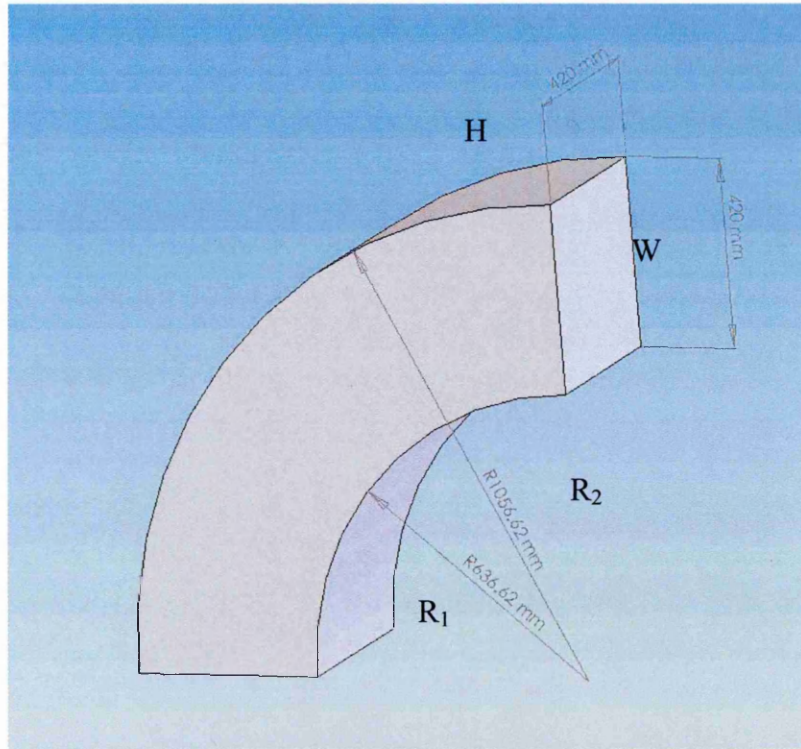
Figure B-14: CAD model shows the dimension of the 1st corner

Given, H = 420 mm, W = 420 mm, R_1 = 636.62 mm and R_2 = 1056.62 mm.

From Table (2), pressure loss coefficient can be calculated in below,

$$k = c_p \times A_f$$
$$= 0.15 \times 1.0$$
$$= 0.15$$

Pressure loss at first corner can be defined using Equation B-3;

$$h = k \times \frac{v^2}{2g}$$
$$= 0.15 \times \frac{2.08^2}{2 \times 9.81}$$
$$= 0.03 \text{ m}$$

B.15 First corner vanes

Three guide vanes were added into the first corner to enhance the flow around the 90 degree bend. The details of the design can be found in Figure B-15.
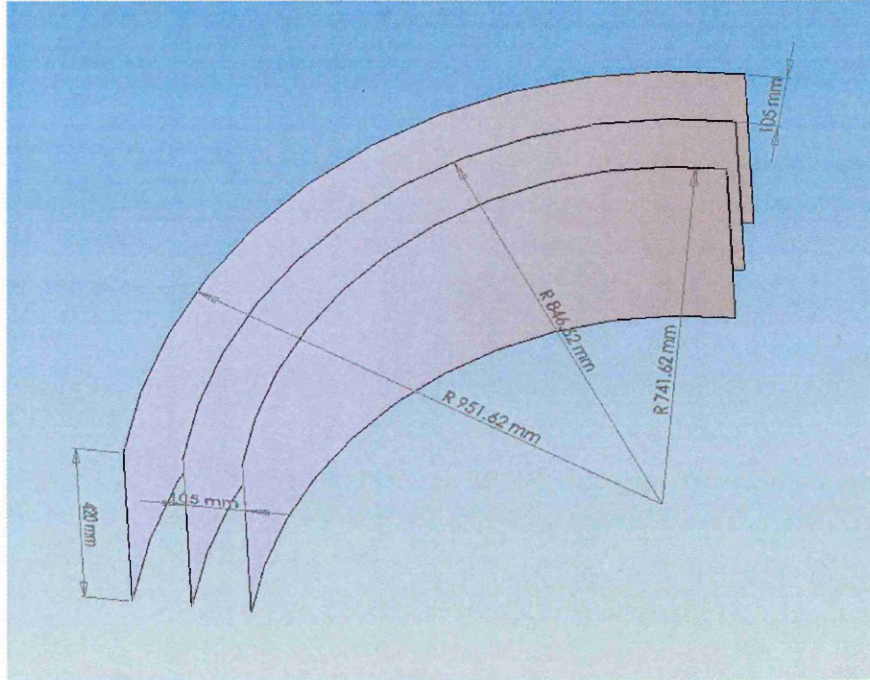

Figure B-15: CAD model of first corner guide vanes

Known that vanes width = 420 mm, each vanes has 105 mm gap between each other and the duct. The smallest vanes has radius = 741.62 mm, follow by R2 = 846.62 mm and R3 = 951.62 mm.

The vane pressure loss coefficient can be refer from Table B-3 and thus K = 0.14.

Table B-3: 90 degree bend guide vane pressure loss coefficient table

| Pressure loss coefficient K				
	Number of vanes			
$\dfrac{R_1 + R_2}{2 \times w}$	0	1	2	3
0.50	1.05	0.7	0.45	0.3
0.71	0.87	0.58	0.46	0.46
0.75	0.37	0.16	0.12	0.09
1.0	0.22	0.13	0.10	0.10

Pressure loss at 4th corner with three guide vanes can be defined using Equation B-3;

$$h = k \times \frac{v^2}{2g}$$

$$= 0.14 \times \frac{2.08^2}{2 \times 9.81}$$

$$= 0.03 \text{ m}$$

B.16 Upstream Wire Mesh

A fine wire mesh between the downstream straight duct and the fourth corner has been used to straighten the flow and it also acts as a protection guide to the specimen.

Given, wire diameter = 1 mm, aperture = 6 mm.
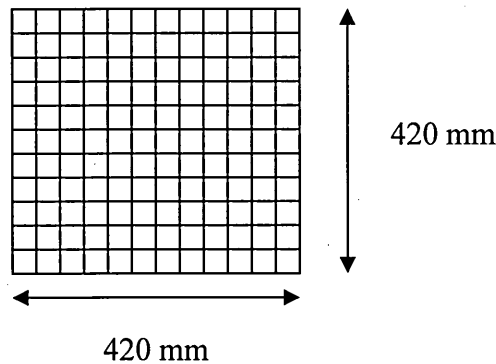
420 mm

420 mm

The total meshed area can be calculated in below,
420 ÷ 6 = 70 number of mesh
Wire area = $\pi \times r \times h$ = 659.73 mm^2
Total wire area = 659.73 × 70 = 46181.41 mm^2

Total mesh area = 46181.41 × 2 = 92362.82 mm^2

Velocity passing through the mesh:

$$v = \frac{Q}{\left(A_{open} - A_{mesh}\right)/1000^2} \qquad\qquad \text{Equation B-12}$$

$$v = \frac{0.37}{0.08}$$

$$= 4.38 \text{ m/s}$$

Pressure loss can be calculated in below:

$$k = \left(1 - \frac{A_{mesh}}{A_{open}}\right) \qquad\qquad \text{Equation B-13}$$

188

$$k = \left(1 - \frac{92362.82}{176400}\right)$$

$$= 0.48$$

Pressure loss from wire mesh can be calculated using Equation B-3:

$$h = k \times \frac{v^2}{2g}$$

$$= 0.48 \times \frac{4.38^2}{2 \times 9.81}$$

$$= 0.47 \text{ m}$$

B.17 Annular outlet

Annular outlet connects the fourth corner with the bifurcation fan. The dimension can be found in Figure B-16.
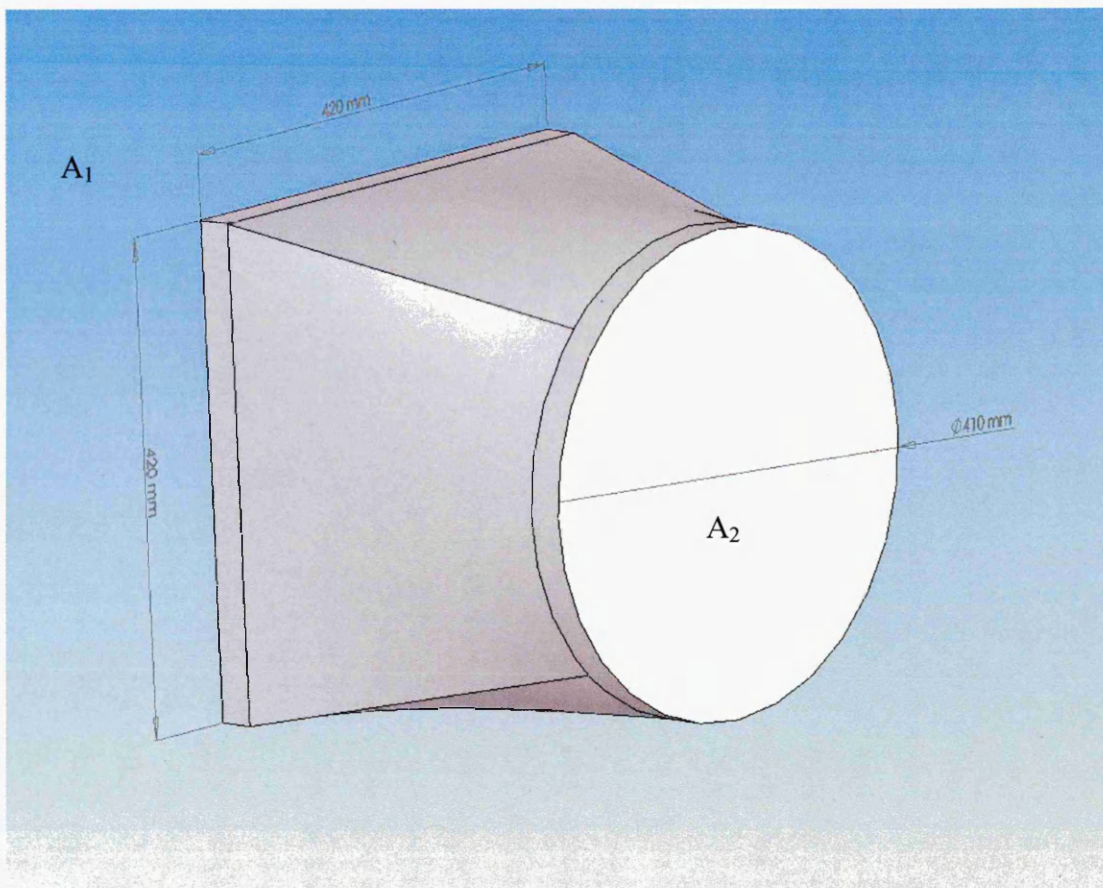

Figure B-16: CAD model of annular outlet

Given, H = W =420 mm, fan outlet mouth diameter = 410 mm and annular length = 420.60 mm.

Pressure loss coefficient can be calculated as below

$$k = \left[\frac{1}{AR^2} - 1 + k_d \right]$$

$$AR = \frac{1}{\sigma} \qquad \sigma = \frac{A_1}{A_2} \qquad k_d = 1 - c_p$$

Therefore, AR = 1.34 and k_d = 0.7. From Equation (12) pressure loss coefficient k = 0.11

Using Equation B-3

$$h = k \times \frac{v^2}{2g}$$

$$= 0.36 \times \frac{2.79^2}{2 \times 9.81}$$
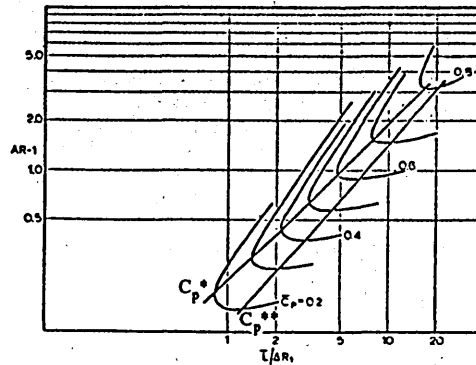
$$= 0.14 \text{ m}$$

Figure B-17: Annular Cp graph

B.18 Annular Inlet

Annular inlet connects the bifurcated fan with the first corner. The dimension can be found in Figure B-18.
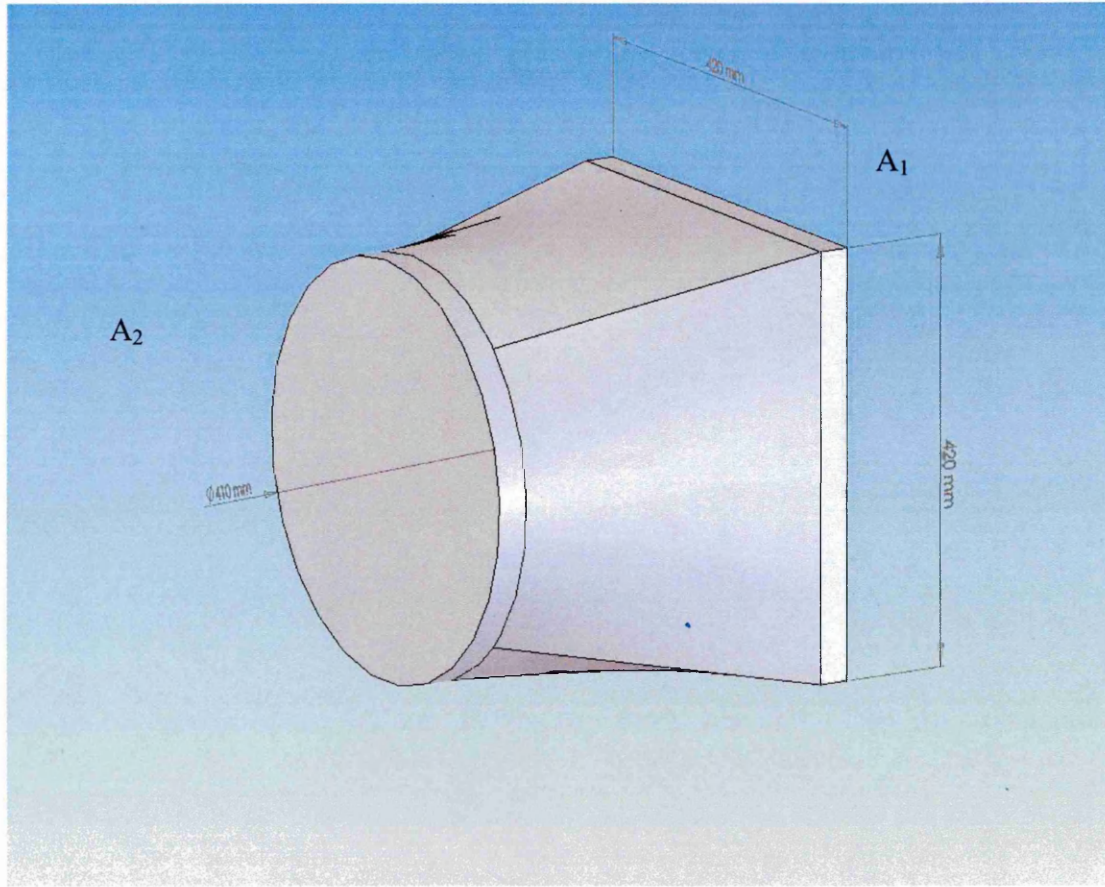
Figure B-18: Annular inlet's CAD model

Given, H = W =420 mm, fan outlet mouth diameter = 410 mm and annular length = 420.60 mm volume flow rate Q = 0.37 and ρ_{air} =1.22 kg/m^3

Annular inlet pressure head loss can be calculated using the equation below:

$$P_1 - P_2 = \frac{Q^2 \times \rho \times \left[1 - \left(\dfrac{A_2}{A_1}\right)^2\right]}{2 \times A_2^2}$$

Equation B-15

$$P_1 - P_2 = \frac{0.37^2 \times 1.22 \left[1 - (0.75)^2\right]}{2 \times 0.02}$$

$$= 2.08 \text{ Pascal}$$

$$\approx 0.17 \text{ m}$$

B.19 Pressure Loss Breakdown List

| Duct Section	Equation Used for Pressure Loss Calculation	Pressure Loss Coefficient k /with vanes	Pressure Head loss (m) without Guide Vanes	Pressure Head Loss (m) with Guide Vanes
Annular inlet	$$P_1 - P_2 = \frac{Q^2 \times \rho \times \left[1 - \left(\frac{A_2}{A_1}\right)^2\right]}{2 \times A_2^2}$$	N/A	0.17	0.17
Upstream wire mesh	$h = k \times \dfrac{v^2}{2g}$	0.48	0.47	0.47
First corner	$h = k \times \dfrac{v^2}{2g}$	0.15/ 0.14	0.03	0.03
Upstream straight duct	$h = k \times \dfrac{v^2}{2g}$	1.0	0.22	0.22
Expansion duct	$h = k \times \dfrac{v^2}{2g}$	0.99	0.22	0.22
Second corner	$h = k \times \dfrac{v^2}{2g}$	1.02	0.06	0.06
Contraction	$$\Delta p = \frac{1}{2}\rho v_{in}^2\left[\left(\frac{A_{inlet}}{A_{outlet}}\right)^2 - 1\right]$$	N/A	0.75	0.75
Test section wire mesh	$h = k \times \dfrac{v^2}{2g}$	0.37	2.08	2.08
Test section	$h = k \times \dfrac{v^2}{2g}$	0.97	0.79	0.79
Diffuser	$h = k \times \dfrac{v^2}{2g}$	0.44	0.34	0.34
Third corner	$h = k \times \dfrac{v^2}{2g}$	0.98/ 0.13	0.22	0.03
Downstream straight duct	$h = k \times \dfrac{v^2}{2g}$	1.0	0.22	0.22
Downstream wire mesh	$h = k \times \dfrac{v^2}{2g}$	0.48	0.47	0.47
Fourth corner	$h = k \times \dfrac{v^2}{2g}$	0.15	0.03	0.03
Annular outlet	$h = k \times \dfrac{v^2}{2g}$	0.36	0.14	0.14
Total pressure loss in meter :			6.21	6.02
Total pressure loss in Pascal :			73.13	70.88

Appendix C Fan's Performance Graph

COOLING DISC   John.

AFA FANS	Performance Curve
Impeller	400/110/5B/12½" @ 1600 rpm	28/09/2006 / 12:57:51

Volume	0.5775 m3/s	Efficiency (total)	51%
Static Pressure	105 Pa	Dynamic Pressure	13 Pa
Pressure Loss	0 Pa	Temperature	40 °SC continuous
Density	1.20 kg/m2	Peak Power	0.15 kW

BS848: Part 1 1980
Type D Installation

Volume in m3/s
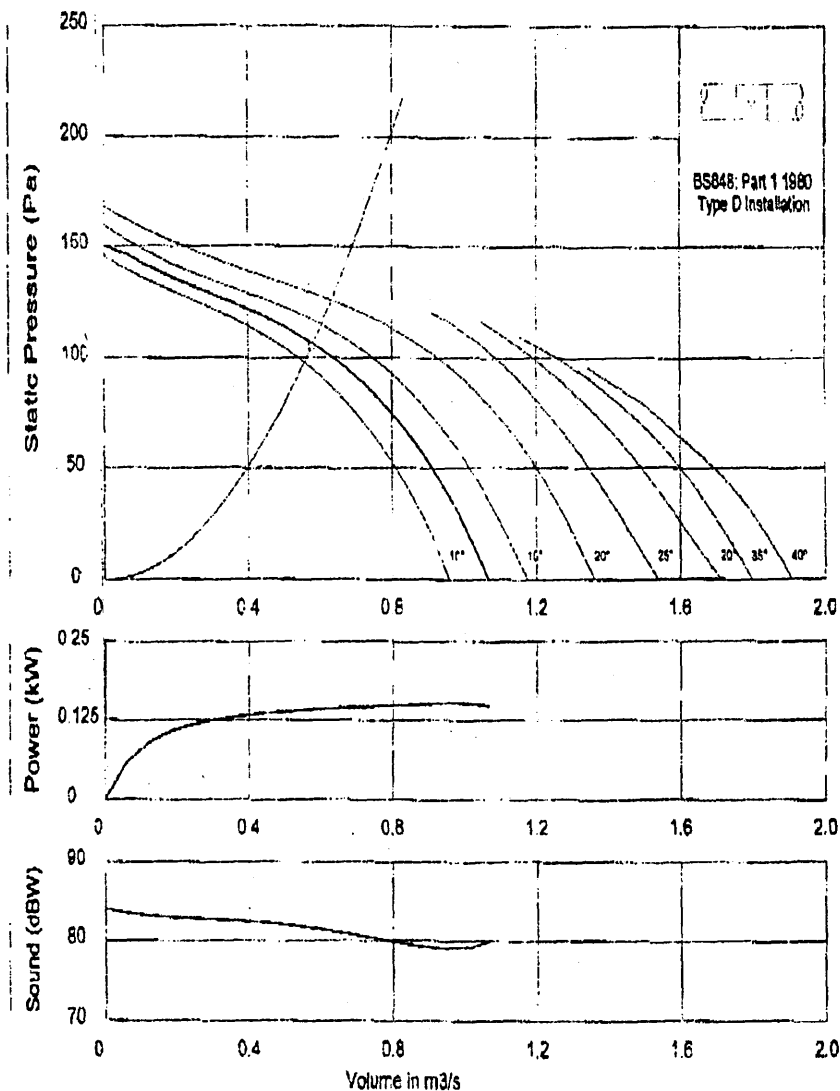
Sound Data	Average free field s.p.l.		60 dBA @ 3 dia (approximate)						
Frequency (Hz)		63	125	250	500	1k	2k	4k	8k
In-duct	[83 dBW]	79	80	70	69	68	67	63	61

Appendix D   PID Controller

D.1 Proportional action

A pure proportional control makes proportional changes to the measured error value by multiplying the error by a constant K_p. The proportional term can be written as:

$$P_{out} = K_p e(t)$$

<div align="right">Equation D-1</div>

Where, P_{out} is the proportional term, K_p is the proportional gain, e is the measured error and t is the process time. Figure D-1 shows the step response by using the proportional controller. The figure shows that the controller has relatively short rise time but high overshoot. In some applications if proportional gain is too high, it can cause the system become unstable. The drawback of proportional control is it will always retain a steady error.
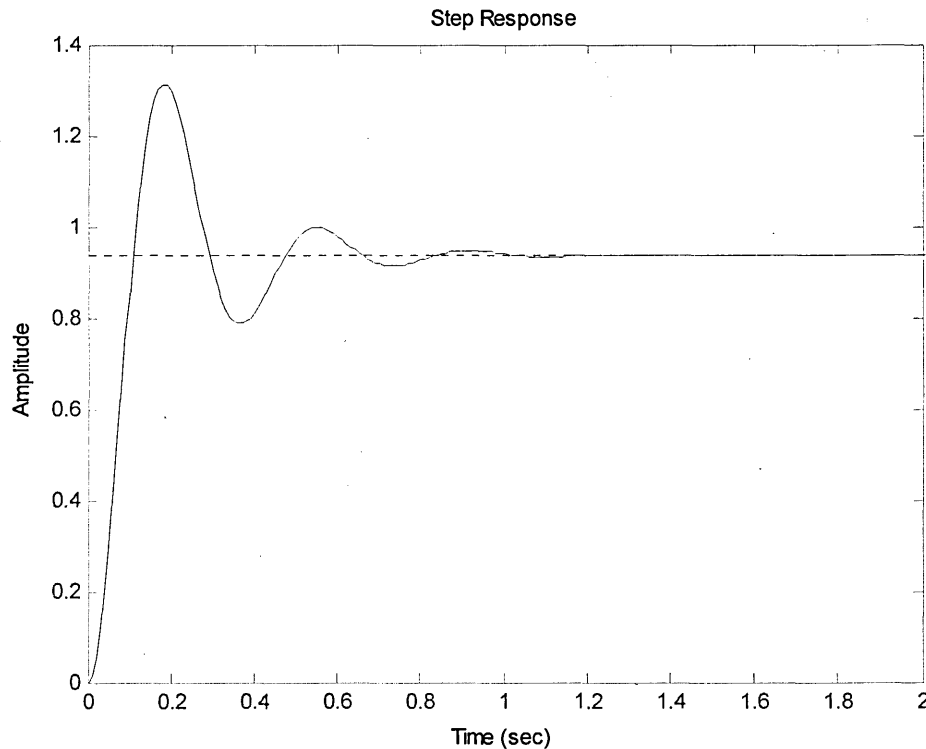

Figure D-1: Step response using Proportional control

D.2 Integral action

The main function of integral controller is to accelerates the process towards the set value and eliminate the residual of the steady state error that occurred at the proportional gain. The algorithm can be written as follow:

$$I_{out} = K_i \int_0^t e(\tau)d\tau \qquad\qquad \text{Equation D-2}$$

Where, I_{out} is the integral term, K_i is the integral gain, e is the measured error and τ is time in the past contributing in the integral response. Figure D-2 shows the step response using proportional and integral (PI) controller. The controller eliminate the steady state error but increase both the over shoot and settling time.
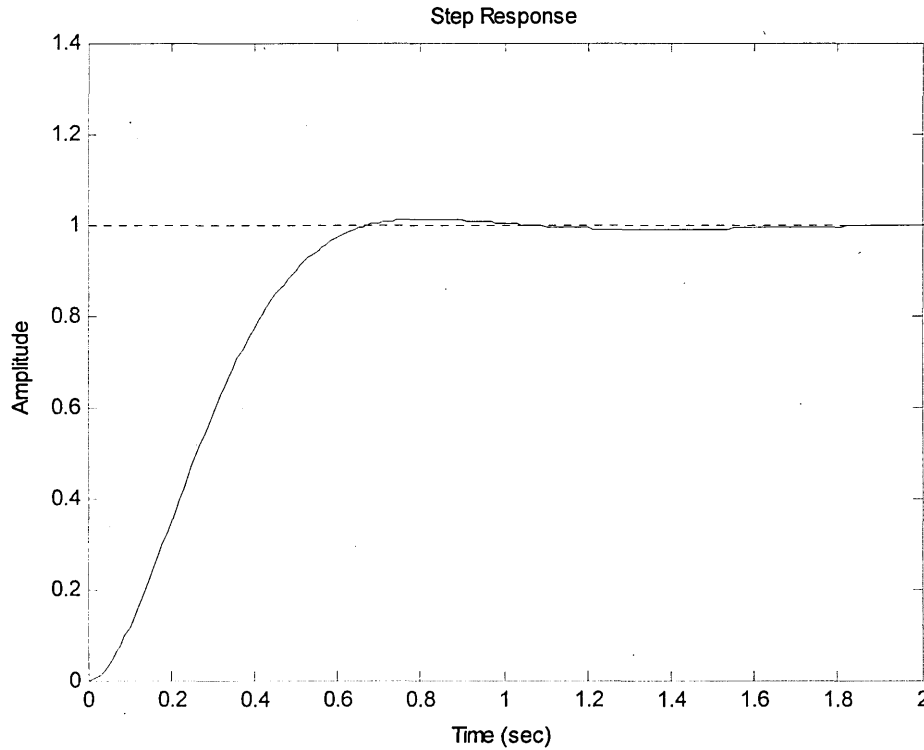

Figure D-2: Step response using proportional and integral (PI) controller

D.3 Derivative action

The purpose of derivative action is to improve the closed loop stability. The rate of change of the process error is calculated by determining the slope of the error over time and multiplying the rate of change by the derivative gain K_d. The derivative algorithm can be written as:

$$D_{out} = K_d \frac{de}{dt} \qquad\qquad \text{Equation D-3}$$

Where, D_{out} is the derivative term, K_d is the derivative gain, e is the measured error and t is time. Figure D-3 shows the step response using proportional and derivative (PD) controller.

195

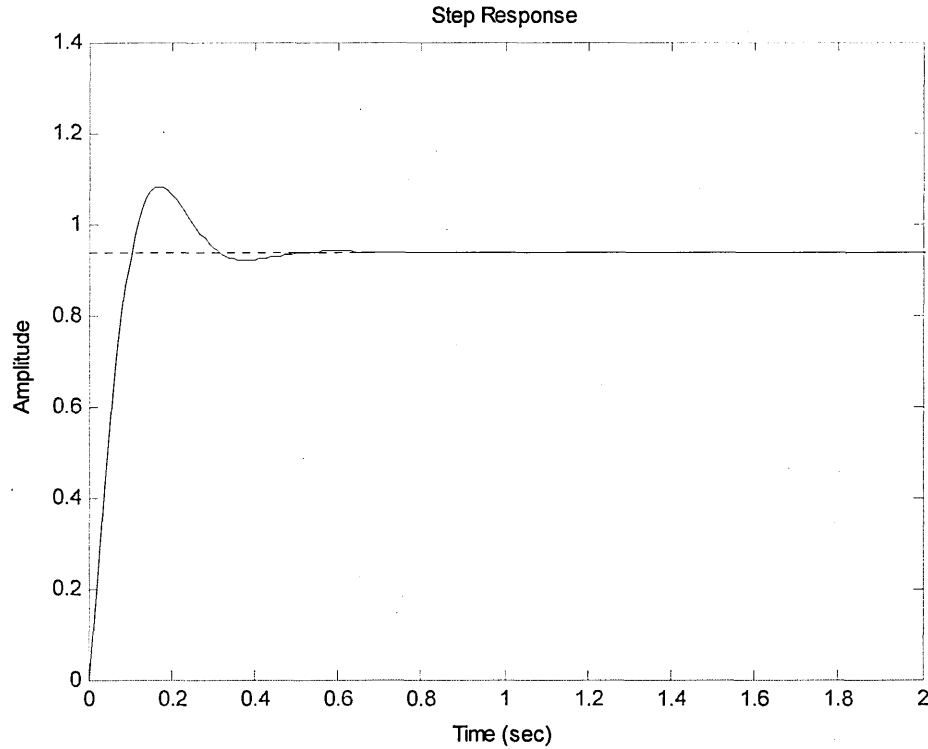The figure shows that the controller reduces the overshoot and the settling time compare to Figure D-1.

Figure D-3: Step response using proportional and derivative (PD) controller

D.4 Proportional – integral – derivative (PID) action

PID controller has three terms. Proportional (P) is corresponds to the proportional control. The larger the K_p the faster the system response but large error. The second term is the integral (I), which control the action that is proportional to the time integral of the error. Thus ensures the steady state error becomes zero. The larger the K_i the faster the steady state error can be eliminated. The third term is derivative (D) term, which decreases large overshoot. The three combined algorithms can be written as follows:

$$u(t) = K_p e(t) + K_i \int_0^t e(\tau)d\tau + K_d \frac{de}{dt}$$

Equation D-4

Appendix E   Wind Tunnel Operation Procedures

The wind tunnel was operated according to the following sequence:

E.1 Water channel operating sequence

1. Ensure that the water channel is clamped in place on the test section.
2. Ensure that the water valves are fully open.
3. Control the water flow rate from valves to meet requirement.
4. Ensure no water leakage from water channel.

E.2 Data logger operating sequence

1. Make sure all TC are connected to TC-08 data logger
2. Run recorder on computer.

E.3 Fan operating sequence

1. Ensure both hands are dry.
2. Check fan's power connection is connected to power supply.
3. Ensure pitot tube is in place.
4. Turn on wind tunnel's fan.
5. Control wind speed to desire value from potential meter controller, gradually.

E.4 Heaters operating sequence

1. Ensure both hands are dry.
2. Ensure heater controller is connected to main power supply.
3. Turn on heater controller.
4. Increase heaters power gradually.